Spectroscopy and Modelling of Catalyst Nanoparticles Using STEM-EELS





A thesis submitted for the degree of Doctor of Philosophy

James O. Sode

Linacre College, University of Oxford

Hilary 2020

Abstract

This thesis concerns the oxygen reduction reaction (ORR) in the proton exchange membrane fuel cell (PEMFC) and aims to understand the interaction of oxygen with platinum-cobalt (PtCo) catalyst nanoparticles. The techniques employed are aberrated scanning transmission electron microscopy (STEM), electron energy loss spectroscopy (EELS) and modelling through density functional theory (DFT). The comparison of certain features in the experimental and simulated EEL spectra allows for selective optimisation in catalyst design. It is imperative to optimise the design of Pt-based alloys because Pt catalysts are costly. There is also an added advantage of manifold increase in catalytic activity with PtCo alloys in particular.

In order to study the oxygen interaction, the focal point of study becomes the oxygen coverage on the surface of the PtCo alloys. This requires detailed characterisation at the nanoscale and as such, optical techniques are not ideal. Using HAADF STEM means high spatial resolution and Z-contrast, which is crucial to investigating light and heavy elements often seen in catalyst materials. However, due to the Z-dependence, elements as light as oxygen may not readily appear in the HAADF image of catalysts and therefore EELS becomes an important tool due to its large range of elemental sensitivity to chemical composition.

The most logical starting point to investigate the oxygen coverage on the PtCo alloys is to find a link between the oxidation state of the metals and the oxygen binding in the alloys. The next step is to correlate detailed features in the oxygen and metals EEL spectra and explain them through modelling. DFT modelling is not enough to fully explain these features and hence atomic multiplet theory (AMT) is another tool used to corroborate experiment, particularly in the calculation of Co spectra.

A methodology for the extraction of oxidation states using the white line ratio in the cobalt EEL signal (Co $L_{2,3}$-edge) is developed. Specifically, the PtCo nanoparticles are separated into

core and shell regions in order to highlight possible differences in the binding of oxygen on the surface compared to rest of the nanoparticle. In addition, the influence of size on the oxygen binding is also examined. The errors associated with this method as well as potential difficulties in its application are discussed. The experimental results are tied to observed features in the calculated Co and oxygen spectra from various environments using AMT and DFT.

Combining spectroscopy and modelling, it is shown that the understanding of the oxygen interaction with the PtCo alloys only increases efficiency of catalyst design. This advantage acts as a stepping stone for other studies with such nanoscale specimens like nanoparticles in the catalyst research field.

Acknowledgements

I would like to appreciate my supervisors, Dr. Rebecca Nicholls, Prof. Pete Nellist and Dogan Ozkaya for their inputs and support throughout this project. Pete and Rebecca made sure I had a solid grounding in the background knowledge required to kick off my project. They advised on the modules to study as first year foundation courses; Pete occasionally held tutorials for students in his office to test and bridge gaps in our knowledge about microscopy. In addition, meetings with Pete and Rebecca gave a detailed project path that helped build my confidence progressively through the course of the project. Rebecca has been particularly helpful in setting up small chats whenever I had a question or two about specific details of my project. She has also helped to coordinate experiments and meetings outside the department of which I am grateful.

I consider myself fortunate to have had Aakash Varambhia and Lewys Jones as a senior student and post-doctoral reasearcher, respectively. At the beginning of the project, they advised myself, as well as other new students on books to read, courses to attend, packages to download and sundry. They also formed a large part of our training on the microscopes. I am very grateful to Aakash for personal training on the microscopes all those evenings, as well as giving me a good basis to code in the Matlab and Python programming languages. All those days I would tag along to their sessions at Harwell, Lewys drove myself and Aakash and was always happy to do it. I learned a lot at those day-long sessions.

I would like to thank Dogan for his selflessness in driving me to Harwell and JMAC conferences. He has also given some advice on how to approach a DPhil project and some friendly life advice in general. I would also like to take the opportunity to highlight the contribution of Misbah Sarwar to the modelling side of my project. She gave me my first training of running DFT calculations with CASTEP. She also helped in constructing a lot of the DFT models in this thesis and is always a constant source of help when required.

I also extend thanks to Sandra Van Aert for organising the annual ATOM meeting, which gave me my first taste of presenting to an external audience. I am similarly grateful for the conferences which my supervisors and Johnson Matthey have afforded me. This allowed for networking and general feedback which I have found useful I specific parts of my project. I would also like to thank my fellow students, Colum O'Leary and Alex Sheader for support when it came to bouncing things of each other. We also travel to most conferences together which made it less lonely.

Last but not least, I will like to acknowledge the financial support from EPSRC and Johnson Matthey for three and a half years, allowing me to successfully complete this DPhil project on time.

Contents

Abstract i

Acknowledgements iii

Contents v

Glossary ix

Outline xi

1 Introduction 1

1.1 Heterogeneous Catalysts 1

1.2 The Hydrogen Fuel Cell and the ORR 2

1.3 Optimisation with Alloys 4

1.3.1 Active sites 4

1.3.2 Size effects 5

1.4 Catalyst Design 6

1.4.1 Catalyst synthesis 6

1.4.2 Core-shell 8

1.5 Conclusions 11

1.6 References 13

2 Methods of Characterisation 17

2.1 Background 17

2.2 Cyclic Voltammetry 18

2.3 Optical Spectroscopy 19

2.4 X-ray Absorption Spectroscopy 20

2.5 Atom Probe Tomography 21

2.6 Electron Microscopy 22

2.7 Conclusions 28

2.8 References 29

3 Scanning Transmission Electron Microscopy 31

3.1 The Basics of STEM 31

3.2 Bright Field STEM 32

3.3 ADF and HAADF STEM 34

3.4 Aberration Correction 39

3.5 Channelling and contamination 41

3.6 Conclusions 43

3.7 References 45

4 Electron Energy Loss Spectroscopy 47

4.1 Theory and Background 47
4.1.1 EELS Mechanism and Signals 47
4.1.2 The Spectrometer 50
4.2 Elemental Quantification 51
4.3 Fine Structure and Oxidation State 55
4.4 Conclusions 65
4.5 References 66
5 Atomic Multiplet Theory 68
5.1 Background 68
5.2 Russell Saunders and J-J Coupling Scheme 70
5.3 Calculating Transition Metal Spectra 72
5.4 Determination of Oxidation State 74
5.5 Determination of Crystal Field and Charge Transfer Effects 76
5.6 Conclusions 81
5.7 References 82
6 Density Functional Theory 84
6.1 Methods for Energy Calculations 84
6.1.1 Background 84
6.1.2 The Quantum Mechanical Method 85
6.2 The Self-Consistent Field and Energy Minimisation 87
6.3 Functionals 87
6.4 Models 88
6.5 Conclusions 92
6.6 References 93
7 Determination of cobalt oxidation states 95
7.1 Experimental Method 95
7.1.1 Outline 95
7.1.2 Sample preparation 98
7.1.3 Parameters for Imaging and Spectroscopy 100
7.1.4 Spectrum Alignment and X-ray Removal 101
7.2 PCA 102
7.3 Background Subtraction 106
7.4 Extraction of Cobalt White Line Ratios 107
7.5 Calculation of Cobalt Oxidation State 113
7.6 Comparison of methodology with MLLS 122
7.7 Error Analysis on cobalt oxidation states 127

7.8 Validity of oxidation state assignment 129
7.9 Noise correlation 130
7.10 Conclusions 133
7.11 References 135
8 Oxidation of PtCo alloys 138
8.1 Comparison of Core-Shell Oxidation in PtCo alloys 138
8.2 Effect of Co content and Acid Leaching 148
8.3 Influence of Size 153
8.4 Conclusions 156
8.5 References 157
9 Calculation of Co $L_{2,3}$-edge multiplets 158
9.1 Method and parameters 158
9.2 Interpretation of Standards spectra 159
9.3 Investigation of Crystal Field and Charge Transfer in Nanoparticles ..... **Error! Bookmark not defined.**
9.4 Conclusions 173
9.5 References 175
10 Surface modelling of O *K*-edge using density functional theory 176
10.1 Geometry optimisation and Convergence Tests 176
10.1.1 Context of calculations 176
10.1.2 Bulk Models 177
10.1.3 Optimisation of Cut-off Energy 179
10.1.4 Optimisation of *k*-point Spacing 181
10.2 Slabs 184
10.3 Analysis of oxygen sites and simulated O *K*-edge spectra 189
10.4 Conclusions 197
10.5 References 199
11 Conclusions and Future Work 201
11.1 Overview 201
11.2 Improvement in Oxidation State Analysis 201
11.3 Cobalt Multiplet Calculations 204
11.4 Robustness of DFT calculations 205
12 Appendices 207
12.1 Appendix A: Imaging and Spectroscopy Setup 207
12.1.1 Microscope alignment and spectrum imaging 207
12.1.2 Derivative parameters for obtaining spectrum energies 209
12.2 Appendix B: Python PCA and Core-shell Code 211

12.2.1 PCA denoising script 211
12.2.2 Core-shell creation script 212
12.3 Appendix C: Multiplet Software and Atomic Inputs 215
12.4 Appendix D: DFT Input Files and Executables 217
12.4.1 CASTEP input – example cell file 217
12.4.2 CASTEP input – example param file 223
12.4.3 OptaDOS input – example odi file 224
12.4.4 OptaDOS auxiliary files 225

Glossary

ADF	annular dark field
AMT	atomic multiplet theory
CCD	charged coupled device
CF	crystal field
CT	charge transfer
DFT	density functional theory
EEL	electron energy loss
EELS	electron energy loss spectroscopy
ELNES	energy loss near edge structure
EXELFS	extended energy loss fine structure
fcc	face centred cubic
FWHM	full width half-maximum
GGA	generalised gradient approximation
HAADF	high angle annular dark field
hcp	hexagonal close packed
K_{max}	plane waves cut-off value
LDA	local density approximation
LMCT	ligand-to-metal charge transfer
MLCT	metal-to-ligand charge transfer
OptaDOS	optical density of states
ORR	oxygen reduction reaction
PCA	principal component analysis
SCF	self-consistent field

SNR	signal to noise ratio
STEM	scanning transmission electron microscopy
TEM	transmission electron microscopy
XAS	X-ray absorption spectroscopy
ZLP	zero loss peak

Outline

Chapter 1 introduces heterogeneous catalysts, the hydrogen fuel cell and the problem of the ORR in the cell. The migration from common Pt catalysts to alloys and the improvement in catalytic activity is explained, with reference to various works on the optimisation of size, morphology and particle interface of the catalysts.

The general methods for characterisation are discussed in chapter 2. The non-microscopic techniques are reviewed and their advantages and limitations are highlighted. Electron microscopy is introduced, leading on to the use of STEM.

In chapter 3, STEM is introduced along with the optics and detectors paramount to achieving the desired information from the catalyst. In particular, the use of ADF and HAADF STEM in tandem with spectroscopic techniques such as EELS and EDX in deriving both structural and compositional information is briefly discussed. The use of aberration correction obtaining new levels of spatial resolution is also discussed. This chapter goes on to review few examples of imaging and detecting oxygen in catalyst particles.

Chapter 4 outlines the theory and mechanism of electronic energy loss spectroscopy. The available signals for collection are discussed and the importance of elastic and inelastic scattering are expounded. The effect of the spectrometer resolution on the fine structure and elemental quantification is presented. The use of the fine structure and quantification to determine oxygen hybridisation and oxidation state of transition metals is reviewed.

Chapter 5 focuses on AMT and its utilisation in the assignment of energy transitions in EEL spectra. The different coupling schemes used in atomic and solid state environments are described and examples of how they are used in the determination of crystal field and charge transfer effects are detailed. Examples in the determination of hybridisation and oxidation state in various transition metals is also reviewed.

The theory and methods for DFT are presented in chapter 6. The approximations made for the electronic interactions, as well as the self-consistent field (SCF) loop in the ground state energy calculation of a system, are described. The advantages and disadvantage of various functionals are briefly highlighted, along with models used.

Chapter 7 shows the workflow and data acquisition for oxidation state analysis is explained. The process for background subtraction of the O *K*-edge and Co $L_{2,3}$-edge is demonstrated. The calculation of the Co white line ratio and the methodology of assigning oxidation states using cobalt standards is also demonstrated, along with a breakdown of associated errors.

Chapter 8 takes a look at various PtCo nanoparticles and their oxidation in their cores and shells. The white line ratios and thus oxidation states in each region is analysed. The effect of size and cobalt content on the level of oxidation is discussed. The reason why the oxidation states can only be estimated in practicality as opposed to assigning absolute oxidation states is also explained.

The AMT method is applied to analyse the Co $L_{2,3}$-edge in chapter 9. The Co multiplet spectra are calculated and compared to those obtained from experiment. Examples of Co spectra are assigned and analysed for possible crystal field and charge transfer effects. The limitations of the method are discussed.

Chapter 10 focuses on the DFT modelling of the O *K*-edge in various environments and the ground state energy calculations. The bulk and surface models used are detailed as well as optimisation tests for accuracy and efficiency. The resultant O *K*-edge spectra are compared to each other and also to experiment in order to determine the oxygen interaction and geometry of the Pt and Co metals.

In chapter 11, the techniques highlighted in the previous chapters are brought together for a coherent and useful application to similar nanoparticles. The ideas for future work are discussed.

The appendices A to C make up chapter 12, providing additional information on experimental and simulation techniques/packages used in this study.

1 Introduction

1.1 Heterogeneous Catalysts

A catalyst speeds up a chemical reaction without being changed or consumed [1]. Kinetic studies of catalytic reactions show that the activation barrier is lowered, thus saving time and energy. While catalysts come in various phases, as much as 90% of industrially produced chemicals are via solid catalysts [2,3]. Solid catalysts are easy to separate from products for later use [4], favouring them over fluid catalysts. They also have rigid structural networks with planes, giving rise to selectivity, activity and stability in a chemical reaction. Catalysts are split into homogenous and heterogeneous types. The former describes the reactant, catalyst and product all having the same phase while the latter means at least one of them is in a different phase [5]. Most heterogeneous catalysts are in the solid state [3] and proceed via the Langmuir-Hinshelwood model [6]. This is where the reactants adsorb to specific planes or active sites, and in an ideal case, allowing the reaction proceed to completion at a faster rate than uncatalysed (Figure 1.1).

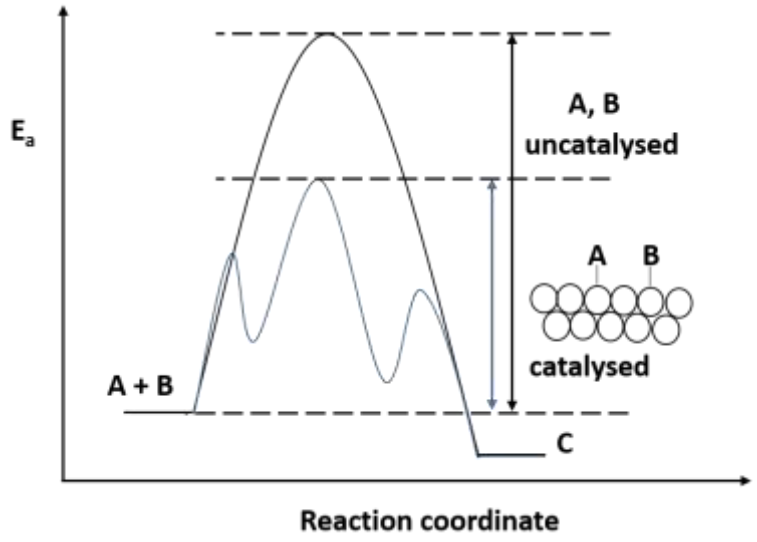


Figure 1.1. The lowering of an activation energy, E_a, through a catalyst.

Active sites are generally on the surface of the catalyst and as such, increasing the surface area of the catalyst to enhance conversion is a much-pursued goal in industry. To this end, the design of nanoparticles dispersed on a carbon-black support is often employed. The activity of the surface is dictated by the arrangement and spacing between the atoms in the surface layer of the nanoparticle [1]. A plethora of orientations including adatoms, terraces and flat planes exist on a typical nanoparticle and they all play various roles in the selectivity and activity of the catalyst. The crystallographic planes are also very crucial in the active sites for adsorbates in heterogeneous catalysis. The reaction mechanisms in heterogeneous catalysis are not fully understood. Investigative variables commonly used in research are particle size, shape, composition, adsorbate-particle interfacial interaction as well as particle-support interactions [7–10]. All of the aforementioned variables are dynamic in that they are subject to change during and or after reaction. Hence, there is a great deal to be had in understanding the correlation between all of the variables.

1.2 The Hydrogen Fuel Cell and the ORR

To combat climate change, a decrease in greenhouse gas emissions by automobiles and electricity generators is paramount. The hydrogen fuel cell is a technology that offers clean energy with less thermodynamic work and no moving parts. One of the more commonly researched hydrogen fuel cells is the PEMFC (Figure 1.2) and for efficient conversion, the interaction of oxygen with the catalyst nanoparticles within the cell is important. The mechanism of the PEMFC is to split the H_2 molecule at the anode into a proton and an electron, whereby the electron travels around the electric circuit [11,12].

$$2H_2 \rightarrow 4H^+ + 4e^- \qquad 1.2a$$

On the other hand, the proton diffuses through the membrane, usually Nafion, and onto the cathode. This is due to a combination of the porosity and the negatively charged sulfonated

groups [12,13] on the Nafion membrane (Figure 1.2), which allows only positively charged ions through it. Both electrodes are carbon-black, commonly coated with Pt nanoparticles as the catalyst to drive the splitting processes. At the cathode, the proton recombines with the electron and reduces O_2 to produce water.

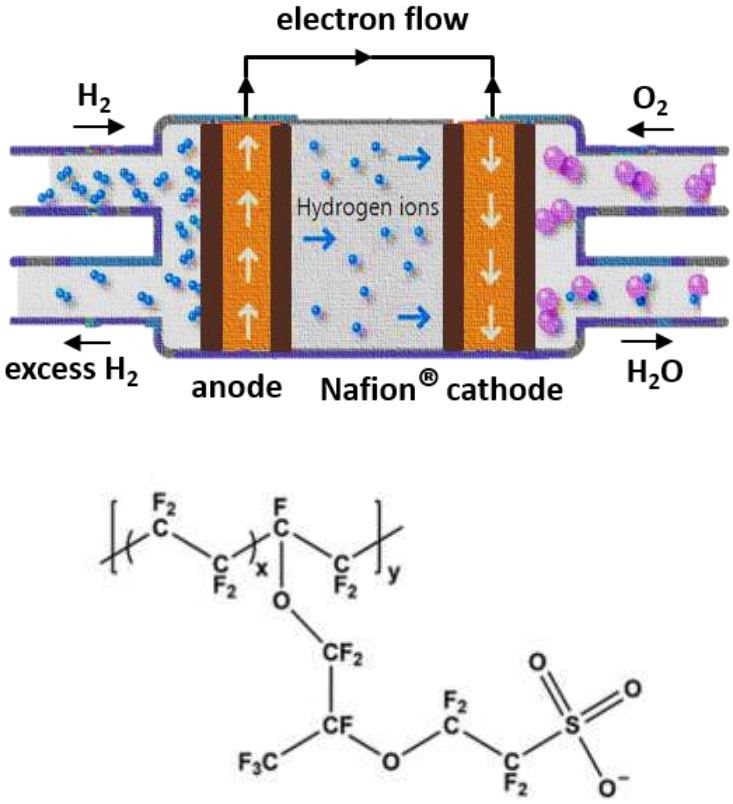


Figure 1.2. Schematic of PEMFC (top), *modified from* [12] and chemical structure of Nafion (bottom), *modified from* [14].

$$O_2 + 4H^+ + 4e^- \rightarrow 2H_2O \qquad 1.2b$$

Equations 1.2a and 1.2b are the half-cell equations for the complete ORR [12]. It is generally accepted that the ORR occurs via the dissociative four-electron pathway according to equation 1.2c [12,15,16], where * indicates an adsorption site:

$$½\ O_2 + * \rightarrow O* + H^+ + e^- \rightarrow OH* + H^+ + e^- \rightarrow H_2O \qquad 1.2c$$

The reaction in 1.2c occurs for each oxygen atom, making it a four-electron pathway. However, there is a two-electron pathway involving the formation of hydrogen peroxide radicals, which

would damage the membrane and ultimately cause the breakdown of the PEMFC [12,15]. The two-electron pathway is responsible for over half the voltage loss in the PEMFC [17]. In addition, the ORR that occurs at the cathode is generally slow [12,15,17,18]. While the anode reaction has easier electron transfer from the hydrogen, oxygen, a lot more electronegative than hydrogen, binds too strongly to the Pt catalyst, thereby inhibiting the adsorption-desorption reversibility [12,17–19]. This violates the Sabatier principle which states the catalyst should not bind oxygen and or its intermediates too strongly or weakly for optimum catalytic performance [20]. Finding a catalyst that binds oxygen by approximately 0.2 eV less than platinum would be the ideal [18].

The anode is not exempt from fault – the formation of H_2 gas from hydrocarbons leaves carbon monoxide (CO) as a by-product on the electrodes [21,22], resulting in poisoning. However, adding more water at the anode can drive the conversion of the CO to carbon dioxide (CO_2), while producing more H_2 to be used via the water-gas shift reaction (WGSR) [22]. The cathode on the other hand is not as straightforward. To improve the ORR, much of recent research has been on tuning size, composition and morphology of the Pt catalysts and hence, catalyst design is the usually the pivot for optimisation.

1.3 Optimisation with Alloys

1.3.1 Active sites

As much of research and development is heavily focused on the usage of platinum group metals (PGMs) and their alloys, the US Department of Energy (DOE) aimed to reduce platinum loading from $20gkW^{-1}$ in 2007 to less than $0.125gkW^{-1}$ by the beginning of 2020 [23,24]. The latest report, as of 2015, has the platinum loading down to $0.16gkW^{-1}$ [24], therefore the research field has been making progress. The way this has been achieved is through the optimisation of the geometry and size in Pt alloy nanoparticles. When two different metals in

a crystal interact, their electronic properties and lattice parameter can change, yielding new properties that could improve the ORR activity. In addition, manipulating the coordination of the metals can also improve the ORR and knowledge of what sites the oxygen molecule (O_2) chemisorb is required.

Early on, Lang *et al.* evidenced that O_2 chemisorption mainly occurred on thermally stable ultra-high vacuum (up to 1500K) low Miller index planes (100) or (111) in higher Miller index crystal surfaces of Pt [25]. It was demonstrated using Low Electron Energy Diffraction (LEED) that (100) and (111) sites were terraced, had a constant width and were of monatomic height. These features were thought to be important in O_2 chemisorption. Researchers such as Gambardella *et al.* and Feibelman *et al.* have since validated these findings using DFT calculations to confirm that the top of the monatomic sites are the most preferred for O_2 dissociation on Pt(111) [26,27]. The common theme is that most of the catalytic reactions occur on the surface and bulk effects of the particles are negligible. Hence, decreasing the size with the intent to increase the surface-to-volume ratio would seem the next logical step, all while keeping in mind that particles of nanometre scale behave differently.

1.3.2 Size effects

Since the ultimate goal is to decrease the Pt loading, reducing the particle size is the way to go if alloys are not considered. Decreasing the particle size means a higher surface-to-volume ratio, meaning more of the surface is available for catalysis. Catalytic reactions tend to occur on the surface of the particles rather than the bulk [28,29], so the efficiency versus Pt cost gain is high. However, since the surface-to-volume ratio is higher in smaller particles, the surface energy increases and as such, multiple structural changes occur as means of thermodynamic compensation [28]. There are systems that reduce surface energy, such as face-centred cubic (fcc) gold (Au) nanoparticles and they do this by maximising the atomic density of the Au(111) planes by forming twinned sub-units [30,31].

Conversely, Peres-Alonzo *et al.* have shown that the surface-to-volume ratio reason for very small particles having low ORR activity is not substantial. Although they found that specific activity did indeed decrease with decreasing particle size, it was observed that the proportion of terraced sites were the main source of the activity [32]. They revealed that the proportion of terrace sites were 37%, 45%, 59% and 70% for 2 nm, 3 nm, 4 nm and 11 nm particle sizes, respectively [32]. This goes to show that the way the atoms are coordinated plays a crucial role in catalytic activity.

To complicate issues further, small particles are not stable under the beam in electron microscopy (EM), a common technique for investigating catalyst nanoparticles. Early studies by Buffat and Borel have shown that Au particles decreased in melting temperature to a plateau of less than 1300K at particle diameters of 20 nm [33]. This issue of small particles melting under the beam, even at a lot lower diameters, are common theme in the catalyst research field. All this points to the need to either find new ways of studying the particles or coming up with other catalyst design methods. This has spurred the development of new design methods such as Pt alloys.

1.4 Catalyst Design

1.4.1 Catalyst synthesis

Catalyst design in the technological field generally revolves around metal and metal oxide nanoparticles; the latter for its higher redox activity and potential oxygen vacancies, which can contribute to conductivity for applications that may require it [34]. There are two types of approach: the *bottom-up* and *top-down* method. *Bottom-up* means that during synthesis, the atoms and or planes in a particle are methodically stacked to give a nanostructure for a desired catalytic outcome [34,35]. Inherent chemical forces between the atoms can also create self-assembly mechanisms that result in a large stable nanostructure. In contrast, the particle is

already formed in the *top-down* method. One of two things usually follows; either certain crystallographic planes are etched out or restructuring is induced to selectively obtain surfaces for the desired catalysis [34,35]. The common routes of catalyst design are shown below

(Figure 1).

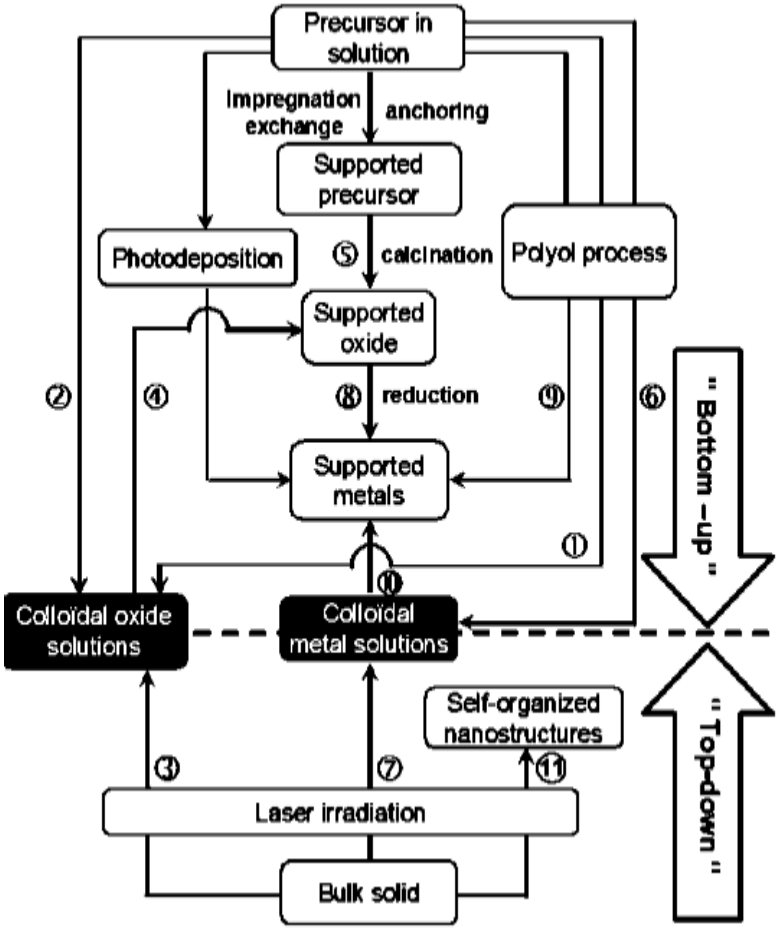


Figure 1.3. Illustration of the synthesis of metal and metal oxide catalysts via *bottom-up and top-down methods* [35].

Routes 1–7 (Figure 1.3) are usually for making colloidal dispersions. Routes 8–10 are for supported metals while 11 is the main self-assembly route [34,35]. For heterogeneous catalysts, the colloidal route is popular for catalyst synthesis. In route 1 and 2, a solvent such as polyol is used for nucleation-mediated growth of the metal precursor which allows size, shape and composition to be tuned [35–39]. However, removal of species that block metal active sites in the product such as the stabiliser i.e. polyvinylpyrolidone (PVP) is difficult [40]. Route 3 uses

irradiation of the precursor but has to be carefully controlled as it could lead to surface damage. Route 4 involves impregnating a support, for example, Pt-based colloid on carbon black, and then evaporating the solvent [34,35,41]. This type of colloid can be calcined (route 5) to remove impurities and increase crystallinity [42]. However, thermal damages or unwanted phase changes may result. Route 6 and 7 are essentially routes 2 and 3 respectively, delineated by one pair being for the metal while the other is for the metal oxide. For supported metals, reduction of a supported oxide or precursor, routes 8 and 9 respectively, are commonly used. The impregnation method in colloids can also be used (route 10). Route 11 is the prominent route for self-assembled structures such as Au spheres on single-crystalline $SrTiO_3$ support (STO) in superconductor electronics [43]. The major issue with this route is controlling the laser fluence and pulse [43].

For heterogeneous catalysis, the *bottom-up* method is the preferred and most used approach in industry. This is because it easier to implement, scale and is less costly. The problem is the obtained size, shape and composition tends to vary a lot [44]. The *top-down* method does not have this issue; however, it is difficult to scale to practical industrial use [44]. Currently, there is more focus on optimising the *bottom-up* method and much of the research is geared towards alloying and the synthesis of core-shell nanoparticles.

1.4.2 Core-shell

To reach the goal of the DOE, it is obvious that the only ways to reduce the Pt loadings is to attain a higher specific activity or mass activity of PGMs during catalysis. The PGMs are a group of six noble transition metals: Pt, iridium (Ir), rhodium (Rh), ruthenium (Ru), osmium (Os) and palladium (Pd) [45]. They have similar physical and chemical properties including corrosion resistance, high melting points, redox behaviour and structural stability [45,46]. One way the catalytic activity of PGMs are optimised is through the particle geometry. The most widely studied geometry is the core-shell. The core-shell structure, as the name suggests, is one

whereby one of the metal alloys is embedded in the other, so that the former becomes the core while latter forms the shell (Figure 1.4).

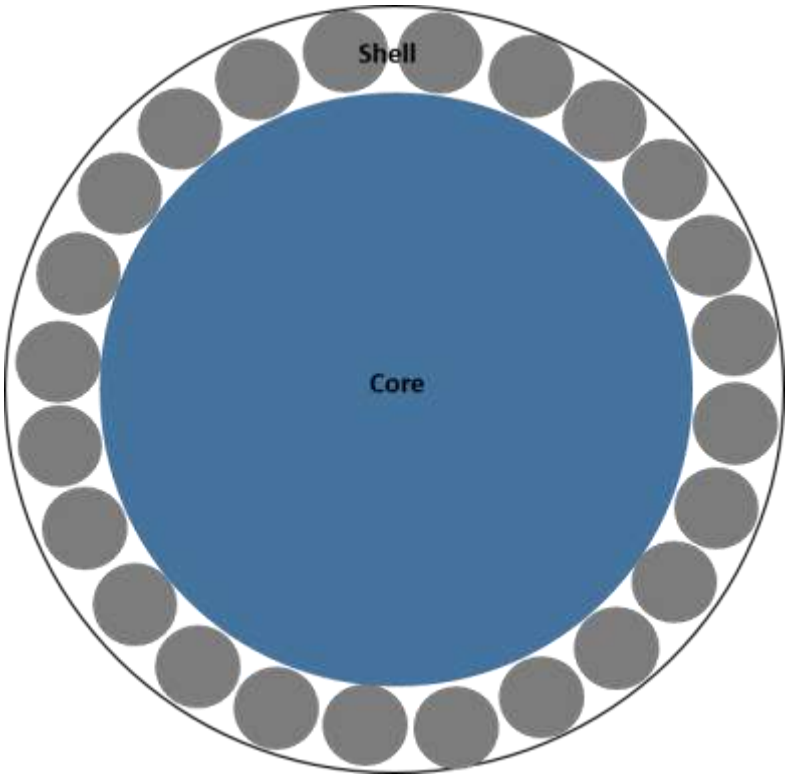


Figure 1.4. A shell layer of atoms forming the surface coverage on the core of a nanoparticle.

Zhang *et al.* showed that embedding a noble metal in the core-shell morphology increases ORR activity. They synthesised a Pt/Ir core-shell nanodentrite catalyst [47] – Ir being the noble metal. A higher mass activity than Pt black was achieved. When the 1:1 molar mixture of Pt/Ir (non-dentritic) was compared to the 2:1 molar Pt/Ir nanodentrites, the latter had an increase of 1.5 in electrochemical surface area (ECSA) along with more uniform 15 nm particle diameters [47]. While this finding was not specifically explained, it is possible that because nanodentrites are highly branched and porous, more edges and corner sites are exposed, increasing the surface area for the ORR to occur. This is corroborated by Yeo *et al.* where Au seed mediated synthesis of Pt/Au saw similarly to Zhang *et al.*, 15 nm uniform nanodentrites compared to 40 nm particles without Au and a higher mass activity by a factor of three than Pt black [48]. Yeo *et*

al. indeed explained that this phenomenon was due to increase in the exposure of edges and corners in the nanodentrites.

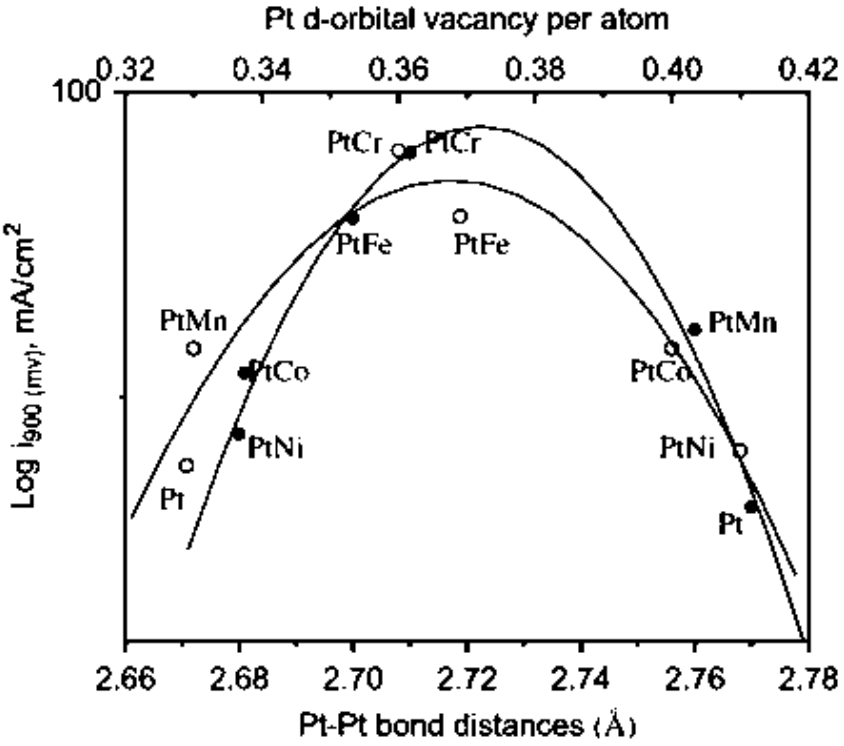


Figure 1.5. Oxygen electrode performance in PEMFCs derived from XAS, showing variation with Pt-Pt distance (•) and Pt *d*-orbital vacancy (◦). *Image reproduced from* [55].

Another benefit of the core-shell geometry is in the process of acid leaching, where in some cases, the core-shell geometry is more evident. This phenomenon is when the core-shell forms a Pt skin on the surface due to the higher acid affinity and oxophilicity of the alloying metal compared to the Pt, causing it to migrate out of the particle during the reaction cycle [49,50]. An example is the Co migration out of Pt_3Co as reported by Lopex-Haro *et al.* This was due to the Co atoms preferentially reacting with O_2 molecules in what was termed place-exchange of O and Pt atoms [49]. Additionally, if the difference in atomic radii between the Pt and alloying metal is to be considered, the resultant strain also contributes to increased ORR activity as evidenced by Gasteiger *et al.* [51]. Work by Jalan and Taylor have linked this to the variation

in Pt-Pt distances with varying alloying metals [52] and using the theory of Norvskov *et al.* [53,54], Mukerjee has found a dependence on *d*-orbital occupancy (Figure 1.5) [55,56].

From a broad perspective, two major contributions will increase the ORR in alloys. The first is strain effects on Pt-Pt distances [55,56]. This is because the radii differential enhances O_2 dissociation on the surface of the alloy. However, only PGMs closest to Pt properties are realistic candidates. For example, the two best performing alloys (Figure 1.5) are PtCo and PtNi (platinum-nickel). At a 2+ oxidation state, the Co atom has an ionic radii of 79 and 88.5 pm for high spin and low spin configurations, respectively [57]. At the same oxidation state, the Ni atom has an ionic radius of 83 pm while that of Pt is 94 pm [57]. This phenomenon causes a lattice contraction, thus lowers the Pt-Pt distance. This has been seen to increase the ORR [58].

The second contribution is electronic, driven by the alloying metal. Using a combination of XAS and X-ray emission spectroscopy (XES), Anniyev *et al.* found that Co or Ni transfers charge into the Pt 5d band which shifts it to a higher energy state [59]. Conversely, the antibonding orbitals of the Pt-O are lowered below the Fermi energy (E_F) and filled [59]. This reduces the Pt-O bonding orbital overlap. Given the fact that the population of antibonding orbitals weakens chemical bonds, the result is a weaker Pt-O bond. This together with the strain effect will lead to easier dissociation of O atoms from the Pt-alloy surface. Hence, it is deducible that oxygen binding can be controlled using bimetallics, however, this brings about a severe characterisation challenge because the size, morphology of the bimetallic, as well as the binding site of the O atoms need to be studied.

1.5 Conclusions

The use and importance of heterogeneous catalysts has been briefly summarised. The effectiveness of a catalyst has been linked to adsorption on certain planes and active sites that

increase its stability, selectivity and activity. The problem of the ORR in the hydrogen fuel cell was also introduced and it has been shown that knowledge of the mechanisms that lead to poisoning and voltage loss is paramount to improving the cell performance. Various optimisation techniques used in literature have combined size and crystal design to optimise the available active sites for catalytic conversion. The role that PGMs and the core-shell particle geometry plays in current research has been detailed and examples of observed increases in ORR have been highlighted.

The next chapter will look at methods used to traditionally characterise the particles once they are synthesised. Their advantages and disadvantages will be examined in terms of the scale of properties needed to be probed and sample preservation.

1.6 References

[1] Taylor H S 1925 A Theory of the Catalytic Surface *Proc. R. Soc. A Math. Phys. Eng. Sci.* **108** 105–111

[2] Rothenberg G 2008 *Catalysis: Concepts and Green Applications*

[3] Hagen J 2006 *Industrial Catalysis: A Practical Approach* (John Wiley & Sons)

[4] Hattori H 2010 Solid acid catalysts: Roles in chemical industries and new concepts *Top. Catal.* **53** 432–8

[5] Schlögl R 2015 Heterogeneous catalysis *Angew. Chemie - Int. Ed.* **54** 3465–3520

[6] Petukhov A V. 1997 Effect of molecular mobility on kinetics of an electrochemical Langmuir-Hinshelwood reaction *Chem. Phys. Lett.* **277** 539–544

[7] Kulkarni A, Chi M, Ortalan V, Browning N D and Gates B C 2010 Atomic resolution of the structure of a metal-support interface: Triosmium clusters on MgO(110) *Angew. Chemie - Int. Ed.* **49** 10089–10092

[8] Bratlie K M, Lee H, Komvopoulos K, Yang P and Somorjai G A 2007 Platinum nanoparticle shape effects on benzene hydrogenation selectivity *Nano Lett.* **7** 3097–3101

[9] Zhang B W, Sheng T, Wang Y X, Qu X M, Zhang J M, Zhang Z C, Liao H G, Zhu F C, Dou S X, Jiang Y X and Sun S G 2017 Platinum-Cobalt Bimetallic Nanoparticles with Pt Skin for Electro-Oxidation of Ethanol *ACS Catal.* **7** 892–895

[10] Aarons J, Jones L, Varambhia A, MacArthur K E, Ozkaya D, Sarwar M, Skylaris C K and Nellist P D 2017 Predicting the Oxygen-Binding Properties of Platinum Nanoparticle Ensembles by Combining High-Precision Electron Microscopy and Density Functional Theory *Nano Lett.* **17** 4003–4012

[11] Dupuis A C 2011 Proton exchange membranes for fuel cells operated at medium temperatures: Materials and experimental techniques *Prog. Mater. Sci.* **56** 289–327

[12] Holton O T and Stevenson J W 2013 The role of platinum in proton exchange membrane fuel cells *Platin. Met. Rev.* **57** 259–271

[13] Spry D B, Goun A, Glusac K, Moilanen D E and Fayer M D 2007 Proton transport and the water environment in Nafion fuel cell membranes and AOT reverse micelles *J. Am. Chem. Soc.* **129** 8122–8130

[14] Shi W and Baker L A 2015 Imaging heterogeneity and transport of degraded Nafion membranes *RSC Adv.* **5** 99284–99290

[15] De Morais R F, Franco A A, Sautet P and Loffreda D 2015 Coverage-dependent thermodynamic analysis of the formation of water and hydrogen peroxide on a platinum model catalyst *Phys. Chem. Chem. Phys.* **17** 11392–11400

[16] Zhang J, Vukmirovic M B, Xu Y, Mavrikakis M and Adzic R R 2005 Controlling the catalytic activity of platinum-monolayer electrocatalysts for oxygen reduction with different substrates *Angew. Chemie - Int. Ed.* **44** 2132–2135

[17] Sheng W, Gasteiger H A and Shao-Horn Y 2010 Hydrogen oxidation and evolution reaction kinetics on platinum: Acid vs alkaline electrolytes *J. Electrochem. Soc.* **157**

1529–1536

[18] Stamenkovic V, Mun B S, Mayrhofer K J J, Ross P N, Markovic N M, Rossmeisl J, Greeley J and Nørskov J K 2006 Changing the activity of electrocatalysts for oxygen reduction by tuning the surface electronic structure *Angew. Chemie - Int. Ed.* **45** 2897–2901

[19] Gracia-Espino E, Jia X and Wågberg T 2014 Improved oxygen reduction performance of Pt-Ni nanoparticles by adhesion on nitrogen-doped graphene *J. Phys. Chem. C* **118** 2804–2811

[20] Bligaard T, Nørskov J K, Dahl S, Matthiesen J, Christensen C H and Sehested J 2004 The Brønsted-Evans-Polanyi relation and the volcano curve in heterogeneous catalysis *J. Catal.* **224** 206–217

[21] Ralph T R and Hogarth M P 2002 Catalysis for Low Temperature Fuel Cells PART II: THE ANODE CHALLENGES *Platin. Mater. Rev.* **46** 117

[22] Vielstich W, Lamm A and Gasteiger H 2003 *Handbook of fuel cells. Fundamentals, technology, applications* (John Wiley & Sons)

[23] Binny D M . 2013 *Plasma Functionalization of Graphene Nanoflakes for Non-Noble Catalyst in Fuel Cells* (McGill)

[24] U.S. Department of Energy D C C A S T 2010 DOE Technical Targets for Polymer Electrolyte Membrane Fuel Cell Components | Department of Energy *http://www1.eere.energy.gov/Hydrogenandfuelcells/Pdfs/Component_Durability_May_2010.Pdf*

[25] Lang B, Joyner R W and Somorjai G A 1972 Low energy electron diffraction studies of high index crystal surfaces of platinum *Surf. Sci.* **30** 440–453

[26] Gambardella P, Šljivančanin, Hammer B, Blanc M, Kuhnke K and Kern K 2001 Oxygen dissociation at pt step *Phys. Rev. Lett.* **87** 56103–56104

[27] Feibelman P J, Hammer B, Norskov J K, Wagner F, Scheffler M, Stump R, Watwe R and Dumesic J 2001 The CO/Pt(111) Puzzle a *J. Phys. Chem. B* **105** 4018–4025

[28] Solliard C and Flueli M 1985 Surface stress and size effect on the lattice parameter in small particles of gold and platinum *Surf. Sci.* **156** 487–494

[29] Qi W H, Wang M P and Su Y C 2002 Size effect on the lattice parameters of nanoparticles *J. Mater. Sci. Lett.* **2** 877–878

[30] Elechiguerra J L, Reyes-Gasga J and Yacaman M J 2006 The role of twinning in shape evolution of anisotropic noble metal nanostructures *J. Mater. Chem.* **16** 3906–3919

[31] MacArthur K E, Young N P, Critchell J W and Kirkland A I 2012 “Ex-situ” annealing and structural transformations in gold nanoparticles *J. Phys. Conf. Ser.* **371** 1–4

[32] Perez-Alonso F J, McCarthy D N, Nierhoff A, Hernandez-Fernandez P, Strebel C, Stephens I E L, Nielsen J H and Chorkendorff I 2012 The effect of size on the oxygen electroreduction activity of mass-selected platinum nanoparticles *Angew. Chemie - Int. Ed.* **51** 4641–4643

[33] Buffat P and Borel J P 1976 Size effect on the melting temperature of gold particles *Phys. Rev. A* **13** 2287–2298

[34] Chavali M S and Nikolova M P 2019 Metal oxide nanoparticles and their applications in nanotechnology *SN Appl. Sci.* **1** 1–30

[35] Bozon-Verduraz F, Fiévet F, Piquemal J Y, Brayner R, Kabouss K El, Soumare Y, Viau G and Shafeev G 2009 Nanoparticles of metal and metal oxides: Some peculiar synthesis methods, size and shape control, application to catalysts preparation *Brazilian J. Phys.* **39** 134–140

[36] Couto G G, Klein J J, Schreiner W H, Mosca D H, de Oliveira A J A and Zarbin A J G 2007 Nickel nanoparticles obtained by a modified polyol process: Synthesis, characterization, and magnetic properties *J. Colloid Interface Sci.* **311** 461–468

[37] Li D and Komarneni S 2006 Microwave-assisted polyol process for synthesis of Ni nanoparticles *J. Am. Ceram. Soc.* **89** 1510–1517

[38] Ung D, Viau G, Ricolleau C, Warmont F, Gredin P and Fiévet F 2005 CoNi nanowires synthesized by heterogeneous nucleation in liquid polyol *Adv. Mater.* **17** 338–344

[39] Joseyphus R J, Matsumoto T, Takahashi H, Kodama D, Tohji K and Jeyadevan B 2007 Designed synthesis of cobalt and its alloys by polyol process *J. Solid State Chem.* **180** 3008–3018

[40] Donoeva B and de Jongh P E 2018 Colloidal Au Catalyst Preparation: Selective Removal of Polyvinylpyrrolidone from Active Au Sites *Chem. Cat. Chem.* **10** 989–997

[41] Gontard L C, Knappett B R, Wheatley A E H, Chang S L Y and Fernández A 2014 Impregnation of carbon black for the examination of colloids using TEM *Carbon N. Y.* **76** 464–468

[42] Lee I, Morales R, Albiter M A and Zaera F 2008 Synthesis of heterogeneous catalysts with well shaped platinum particles to control reaction selectivity *Proc. Natl. Acad. Sci. U. S. A.* **105** 15241–15246

[43] Schmidl G, Jia G, Gawlik A, Kreusch J, Schmidl F, Dellith J, Dathe A, Lin Z H, Huang J S and Plentz J 2018 Fabrication of self-assembled spherical Gold Particles by pulsed UV Laser Treatment *Sci. Rep.* **8** 1–9

[44] Rotello V 2004 *Nanoparticles: Building Blocks for Nanotechnology* (New York: Springer Science & Business Media, Inc.)

[45] Renner H, Schlamp G, Kleinwächter I, Drost E, Lüschow H M, Tews P, Panster P, Diehl M, Lang J, Kreuzer T, Knödler A, Starz K A, Dermann K, Rothaut J, Drieselmann R, Peter C and Schiele R 2000 *Ullmann's Encyclopedia of Industrial Chemistry* (Wiley)

[46] Harris D C and Cabri L J 1991 Nomenclature of platinum-group-element alloys; review and revision *Can. Mineral.* **29** 231–237

[47] Zhang G, Shao Z G, Lu W, Li G, Liu F and Yi B 2012 One-pot synthesis of Ir@Pt nanodendrites as highly active bifunctional electrocatalysts for oxygen reduction and oxygen evolution in acidic medium *Electrochem. commun.* **22** 145–148

[48] Yeo K M, Choi S, Anisur R M, Kim J and Lee I S 2011 Surfactant-free platinum-on-gold nanodendrites with enhanced catalytic performance for oxygen reduction *Angew. Chemie - Int. Ed.* **50** 745–748

[49] Lopez-Haro M, Dubau L, Guétaz L, Bayle-Guillemaud P, Chatenet M, André J, Caqué N, Rossinot E and Maillard F 2014 Atomic-scale structure and composition of Pt3Co/C

nanocrystallites during real PEMFC operation: A STEM-EELS study *Appl. Catal. B Environ.* **152**–**153** 300–308

[50] Chen S, Ferreira P J, Sheng W, Yabuuchi N, Allard L F and Shao-Horn Y 2008 Enhanced activity for oxygen reduction reaction on "Pt_3Co" nanoparticles: Direct evidence of percolated and sandwich-segregation structures *J. Am. Chem. Soc.* **130** 13818–13819

[51] Gasteiger H A, Kocha S S, Sompalli B and Wagner F T 2005 Activity benchmarks and requirements for Pt, Pt-alloy, and non-Pt oxygen reduction catalysts for PEMFCs *Appl. Catal. B Environ.* **56** 9–35

[52] Jalan V and Taylor E J 1984 Importance of Interatomic Spacing in the Catalytic Reduction of Oxygen in Phosphoric Acid. *Proc. - Electrochem. Soc.* **84**–**12** 546–557

[53] Kitchin J R, Nørskov J K, Barteau M A and Chen J G 2004 Modification of the surface electronic and chemical properties of Pt(111) by subsurface 3d transition metals *J. Chem. Phys.* **120** 10240–10246

[54] Nørskov J K, Bligaard T, Logadottir A, Bahn S, Hansen L B, Bollinger M, Bengaard H, Hammer B, Sljivancanin Z, Mavrikakis M, Xu Y, Dahl S and Jacobsen C J H 2002 Universality in heterogeneous catalysis *J. Catal.* **209** 275–278

[55] Mukerjee S, Srinivasan S, Soriaga M P and McBreen J 1995 Role of Structural and Electronic Properties of Pt and Pt Alloys on Electrocatalysis of Oxygen Reduction An In Situ XANES and EXAFS Investigation *J. Electrochem. Soc.* **142** 1409–1422

[56] Strasses P, Koh S, Anniyev T, Greeley J, More K, Yu C, Liu Z, Kaya S, Nordlund D, Ogasawara H, Toney M F and Nilsson A 2010 Lattice-strain control of the activity in dealloyed core–shell fuel cell catalysts *Nat. Chem.* **2** 454–459

[57] Shannon R D 1976 Revised effective ionic radii and systematic studies of interatomic distances in halides and chalcogenides *Acta Crystallogr. Sect. A* **32** 751–767

[58] Salgado J R C, Antolini E and Gonzalez E R 2004 Preparation of Pt-Co/C electrocatalysts by reduction with borohydride in acid and alkaline media: The effect on the performance of the catalyst *J. Power Sour.* **138** 56–60

[59] Anniyev T, Kaya S, Rajasekaran S, Ogasawara H, Nordlund D and Nilsson A 2012 Tuning the metal-adsorbate chemical bond through the ligand effect on platinum subsurface alloys *Angew. Chemie - Int. Ed.* **51** 7724–7728

2 Methods of Characterisation

2.1 Background

The relationship between the properties and performance of solid heterogeneous catalysts can be understood when the structure, size and composition is characterised at nanoscale. Adsorbates and the intermediates which subsequently form on the surface of the metal catalyst may influence the kinetics of the reaction. However, the reaction kinetics may involve a myriad of intermediates and alternative catalytic routes which makes characterisation difficult and time-consuming. Various characterisation methods used for characterising PtCo nanoparticles, the sample type of study in this thesis, will be briefly reviewed in this chapter.

Characterisation methods often fall into two categories; bulk-averaging methods and single-particle methods. Bulk-averaging methods studies the entire catalyst system and gives an average measurement. These are advantageous as the experimental time scale for this type of method does not often surpass a few hours. In contrast, the single-particle methods require probes at the atomic scale or better, therefore the information obtained is highly localised within individual particles. The importance of the probes used such as photons and electrons on the limitations of each characterisation technique is also highlighted.

Bulk-averaging methods

- cyclic voltammetry (CV)
- optical spectroscopy (OS)
- X-ray absorption spectroscopy (XAS)

Single-particle methods

- atom probe tomography (APT)
- electron microscopy (EM)

2.2 Cyclic Voltammetry

CV is an electroanalytical technique usually involving a working electrode and a reference electrode in an electrochemical cell. The working electrode potential is cycled against the reference electrode potential, which is held constant. For fuel cell catalysts, the particles are adsorbed on to the surface of the working electrode while a negative potential is firstly swept up to a potential limit known as the cathodic peak potential (E_{pc}) [59,60]. This point is where the voltage sweep was sufficient to induce reduction. At this point, all adsorbed species on the surface of the catalyst has been reduced [60,61]. After this point, a positive potential is swept to induce the reverse reaction, inducing oxidation up to an extrema known as the anodic peak potential (E_{pa}) where all the species have been oxidised. The current response as a function of the applied potential is plotted as the cyclic voltammogram. Hence, this technique is useful for monitoring the average adsorption-desorption kinetics of surface bound O_2 on a solid metal catalysts such as PGMs and consequently, the fuel cell performance.

Lai *et al.* found the voltammogram of dealloyed carbon-supported 1:1 30 wt% PtCo nanoparticles showed the highest current after 2h of dealloying. This was due to the formation of a Pt skin formed at the surface of the particles after dealloying [62]. The catalytic activity dropped after 4h of dealloying, meaning that the particles should not be acid leached for more than 2h for optimum ORR. These PtCo nanoparticles were dried and heat-treated under H_2/N_2 (hydrogen/nitrogen mix) gas to remove any possible surface oxides. The samples studied in this thesis are 20 wt% PtCo and half of them are dealloyed. They are either cobalt-rich ($PtCo_3$) or cobalt-deficient (Pt_3Co) and were exposed to air before received. As such, surface oxides may be present prior to analysis.

Apart from the formation of a Pt-skin on the surface of PtCo nanoparticles, particle size can affect the ORR and this can be measured from CV. For example, Vinayan *et al.* found that smaller Pt_3Co particles in carbon nanotubes gave a higher electrochemical surface area

(ECSA), 73 m^2g^{-1}, than larger ones [63]. The average particle size was measured to be 3.8 nm for the sample with the 73 m^2g^{-1} ECSA. On the other hand, the larger particles had a lower ECSA of 42.2 m^2g^{-1}, averaging 6.6 nm in size. This was as a result of different reducing agents used during the synthesis of the two Pt_3Co samples studied [63]. The particles studied in this thesis range ~2 – 20 nm in size. This means, the ESCAs will most likely differ significantly. Hence, any correlation with size in the alloys will be important to study. Results from CV such as the given have a substantial amount of information on the bulk characteristics of the catalyst, however, properties arising from individual atomic sites and or planes cannot be delineated.

2.3 Optical Spectroscopy

Optical techniques commonly used in heterogeneous catalysis include Infrared, Raman and UV-vis spectroscopy. Infrared and Raman can fingerprint chemical bonding from characteristic vibrations in a molecule. In UV-vis, the wavelengths absorbed are correlated to the various types of bonds in molecules [67]. All techniques involve the elastic and inelastic scattering of light or photons but utilise different regions of the electromagnetic spectrum. The three techniques mentioned are usually used for confirmation of the product particles i.e. the presence or absence of absorption signals from functional groups, which may be part of the reactants used, would indicate the degree of reaction completion. For example, from IR absorption signals, Vinayan *et al.* showed the presence of oxygen OH and C=O groups which act as anchors for the metal sites during the synthesis of Pt_3Co carbon nanotubes [63]. This type of information is important for not just precursors but also possible functional groups of oxygen intermediates which may adsorb on the surface of the catalyst post-synthesis. IR radiation is strongly absorbed by solids and thus, only a small window is available for vibrational quantification. Sharp cut-offs below 1300 cm^{-1} also make it hard to probe low vibrations [67]. Also, interpretation can become difficult if a system has many vibrational modes.

Raman spectroscopy is very similar to IR in mechanism of absorption although can give slightly different information. It can inform on the level of disorder on the carbon which supports the catalyst i.e. intensities of bands characteristic of sp^2 disordered carbon [63]. The main issues with Raman spectroscopy are that intensities from surface species are low and high energy laser beams used may damage or restructure the catalyst [67]. UV-vis has less common with IR and Raman spectroscopy. It can be used to detect surface metal distribution and morphology. Dai *et al.* demonstrated this when they discovered PtCo nanoparticles with a shell of gold atoms [64]. The major limitation with UV-vis is that the spectra tend to have broad and overlapping bands and so are not element specific [67].

Optical techniques, while cheaper and faster than most characterisation methods, have a severe flaw when it comes to studying catalytic structure used in the fuel cell – the probe. The photon wavelengths with these methods are typically 400–700 nm, while catalysts are usually 2–10 nm in diameter. This means a more detailed characterisation is required.

2.4 X-ray Absorption Spectroscopy

The more common X-ray technique for characterising nanoparticle structure is X-ray diffraction (XRD). It is faster than most spectroscopic techniques and is good for quickly identifying important characteristics of a sample such as its size, crystallinity and lattice planes [62,63]. XRD has been used to discover predominantly fcc crystallography in PtCo nanoparticles [62,63,65] and even additional phases such as face centred tetragonal (fct) under increased temperatures [65]. On the other hand, XAS can provide information on local bonding and coordination in heterogeneous solid catalysts [68]. XAS follows an absorption mechanism and the features at the absorption edge in the resultant spectrum are indicative of electronic transitions to unoccupied states [68]. Specifically, the X-ray absorption near-edge structure (XANES) gives information on the chemical environment while further upfield, the X-ray absorption fine structure (EXAFS) informs about the surrounding atoms [68].

XAS results have shown that the Co-Co bonds dissolve during electrochemical cycling of acid-treated PtCo/C nanoparticles right before the Pt-skin develops [62]. This was determined from the lower Co-Co coordination number after dealloying and just before the formation of the Pt-skin. The Co/Pt molar ratio, calculated using the Co *K* and Pt L_3 edge jumps in the XANES spectra, also dropped by ~30% after 4 h of the dealloying process [62]. Similarly, work done by Jia *et al.* revealed platinum atoms have smaller coordination numbers than cobalt atoms in dealloyed PtCo/C nanoparticles, evidencing a Co-rich core and Pt-dominated surface in the PtCo/C nanoparticles [66].

While properties such as the aforementioned can be extracted from XAS, they are not specific enough. For example, the bond distances are averages and are not enough to directly identify the atoms or their exact coordination [66]. XAS also requires synchrotron radiation facilities.

2.5 Atom Probe Tomography

APT combines 3D imaging and chemical composition measurements to reconstruct particles at atomic resolution [69,70]. The sample is usually in the form of a needle and a high voltage bias is passed to it. The high voltage and small radius of the needle produces an electrostatic field effect, inducing evaporation of the atoms from the surface [69,70]. The ions are detected in an x-y array on a position sensitive detector [69]. Along with the time it takes to arrive at the detector, the 3D image can be reconstructed [69].

There is very limited work on APT use for studying nanoparticles. One such work is where Li *et al.* revealed the average particle composition on a 40 wt% Pt/Co on a carbon support to be 93.1 ±1.7 atom % Pt and 6.9 ±0.5 atom % Co [71]. This differed from the composition of the 3:1 Pt/Co ratio which was thought to have been industrially prepared and no core-shell structure was found. As the resultant images of APT are 3D reconstructions, the distribution and particle size and morphology can be determined with higher detail than techniques which just show 2D

projections or 1D line scans of the particles. As such, APT is a clearly useful technique that provides more information than the conventional 2D projection methods. However, APT requires a lot of time and careful sample preparation to ensure accurate reconstructions [72].

2.6 Electron Microscopy

For most in-depth research involving solid fuel cell catalysts, EM techniques have given the most information. This is because electrons form the probe and due to their very small wavelength, they can probe sub-angstrom length scales, making them the optimum technique for nanoparticle characterisation. The microscopes are usually operated in two modes; scanning and transmission.

An example of the scanning mode operation is in scanning electron microscopy (SEM), where an electromagnetic lens focuses a probe of electrons that rasters across the specimen and are collected by a detector [73]. The resolution is limited by beam spreading and multiple scattering [73] and as such, most SEM are operated at low accelerating voltages, typically 10–30 kV [74]. At very low voltages, the electrons can only escape from within a few nanometres, referred to as secondary electrons, of the specimen surface and as such [73,75], topographical information can be obtained using a secondary electron detector. For example, Sievers *et al.* were able to show that alternate sputtering synthesis of PtCo had non-uniform growth [77]. SEM images taken after acid leaching revealed that the cobalt atoms grew on top of platinum atoms at edges and grain boundaries (Figure 2.1). However, this deduction was benefited from the prior knowledge of the synthetical procedure. With a typical SEM operating at 20 kV only capable of 1.5–3.5 nm resolution [78,79], the SEM has more visual appeal than depth of chemical information.

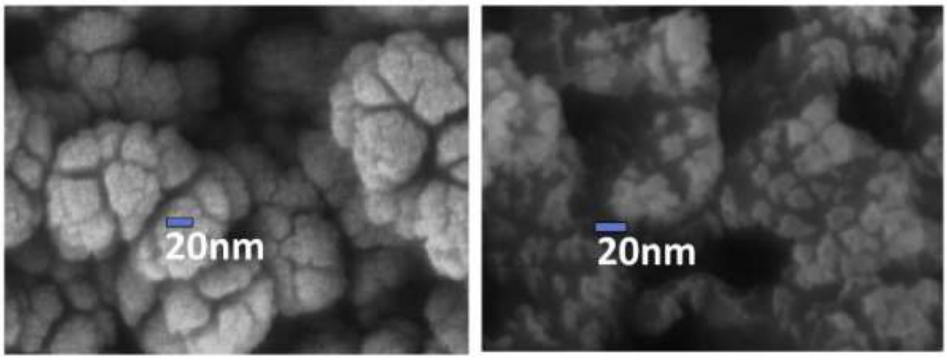


Figure 2.1. SEM image of PtCo nanoparticles formed from alternate sputtering deposition, where Pt atoms were last deposited (left) and where Co atoms were last deposited (right). *Images from* [76].

On the other hand, TEM (transmission electron microscopy) sees the electrons that have passed through the specimen in the transmission mode [68]. The interaction volume is significantly smaller than in SEM albeit not as visually informative about the morphology of a nanoparticle. TEM can be operated in bright-field (BF), dark-field (DF) optics mode, or a combination of the two. BF imaging is recorded with the full beam transmitted from the sample while DF imaging excludes the scattered beam, using an aperture. The apertures can also be used to enhance contrast in a specimen as they block beams coming from large angles. TEM can be used to study dynamic mechanisms such as dealloying in PtCo nanoparticles.

Lai *et al.* showed that PtCo nanoparticles decreased by approximately 2 nm after 4 h of dealloying [62]. Watanabe *et al.* demonstrated that TEM images could also be used to study stability, ordering and particle formation in acid-corroded ordered PtCo nanoparticles. They found before corrosion, a wide particle size dispersion of ∼2–10 nm. However, after 50 h of corrosion, particles as large as 10 nm were found and none less than 5 nm could be seen (Figure 2.2) [80]. There was no beam damage to the small particles and so Ostwald ripening was determined to have occurred, whereby small particles coalesce into larger ones. In the case of disordered PtCo, small particles less than 5 nm still remained, alluding to greater structural stability of the disordered alloy [80]. The PtCo particles to be studied in this thesis range ∼2–

20 nm and the leached particles have a similarly wide dispersion to those studied by Watanabe *et al.* and as such, Ostwald ripening does not appear to be an issue.

a

b

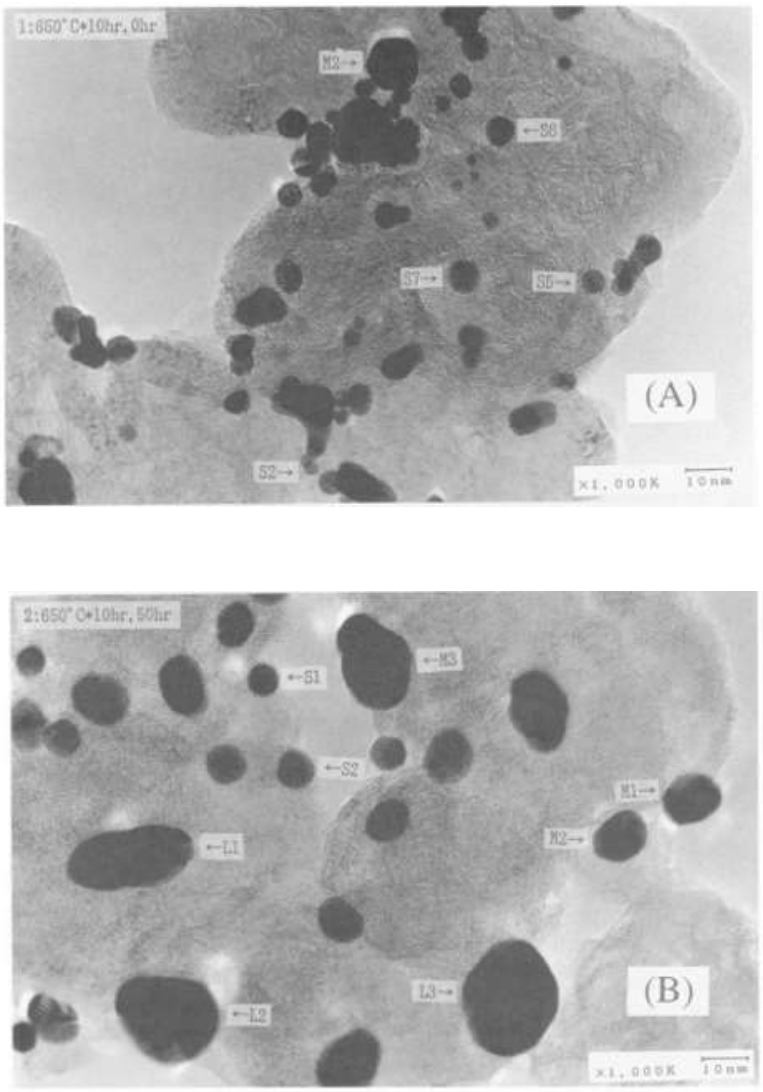


Figure 2.2. TEM image of ordered PtCo alloy (a) before and (b) 50 h after acid corrosion. *Images from* [80].

The visual information from time-dependent TEM images proves more useful than SEM images due to the detailed changes in particle chemistry which can be seen at such a small scale. More detailed information can be detected from TEM images when high-resolution TEM (HRTEM) is implemented. HRTEM uses the interference between the transmitted and diffracted beams to form phase contrast images [68]. While TEM can derive detailed information on lattice planes, quantitative information is still quite difficult due to contrast

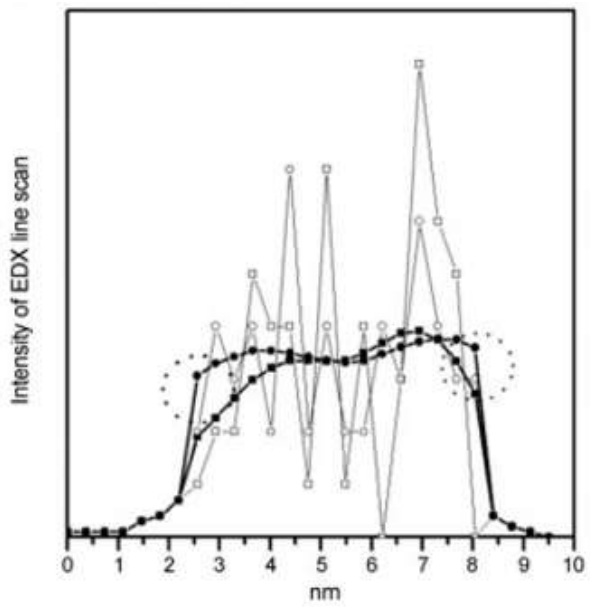
reversals observed in the images. This is because of the coherent nature of the beams that interfere to form the images [68]. Generally, exit wave reconstructions are used to corroborate TEM or HRTEM data. In addition, sample thickness can make specific elements hard to detect just from the images.

The scanning mode counterpart of TEM is STEM (scanning transmission electron microscopy). In STEM, the electrons form a convergent beam on the specimen and the point-size probe allows for very high contrast and resolution. Coupled with aberration-correction, the probe can get even smaller, which has allowed for detection of localised composition and even properties like surface roughness [10] on the particles. Like TEM, sample thickness makes it hard to distinguish elements from the STEM images and so for catalyst particles, it is commonly combined with spectroscopic methods such as EDX (energy dispersive spectroscopy). For PtCo nanoparticles, a combination of STEM and EDX has been used to see facets and Co depletion on particles with such facets. Macarthur *et al.* showed Co depleted 4–5 atomic layers into acid leached PtCo nanoparticles. This was seen mainly at the surface but not at the vertices of facetted particles [81]. Lai *et al.* also use a combination of STEM and EDX to show Co starts off enriched at the surface but decreases after dealloying (Figure 2.3) [62].

Facets and ordering in PtCo nanoparticles can also be seen from STEM HAADF (high angle annular dark) images. For example, *in situ* STEM studies have identified $L1_0$ ordered fct phases in PtCo particles less than 2 nm and some Pt_3Co ordering in larger particles, at 450 ℃ under reduction conditions (Figure 2.4a) [82]. The $L1_2$ phase is another ordering seen in Pt_3Co nanoparticles (Figure 2.4b and c) from works such as Wang *et al.* [83] and Dr Vharambhia [84], which features the same PtCo particles as those to be studied in this thesis. The study done by Dr Vharambhia also included a combination of STEM and EDX for compositional quantification, which is later referred to in chapter 8. Information such as the aforementioned

show why STEM is a very prominent tool for catalyst characterisation and a detailed look into its mechanism and optics will be reviewed in the next chapter.

a



b

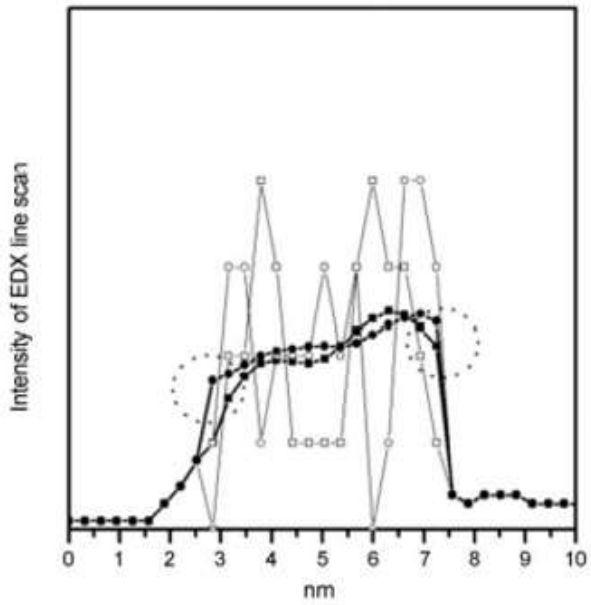
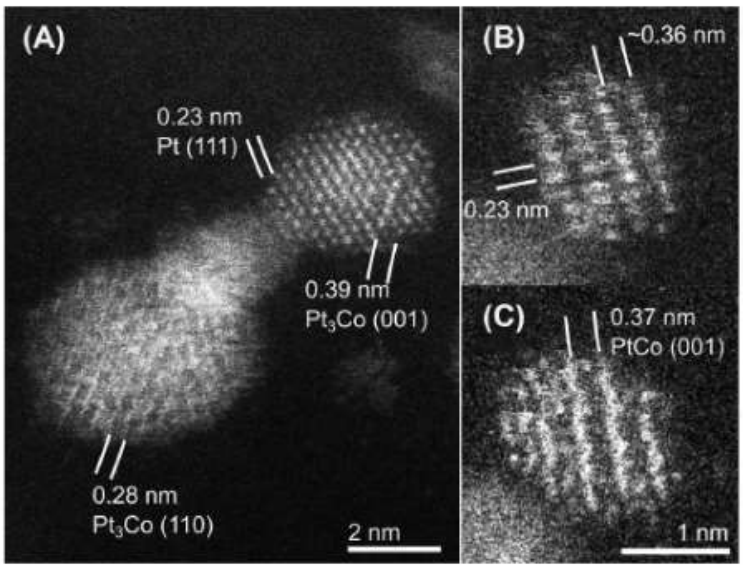
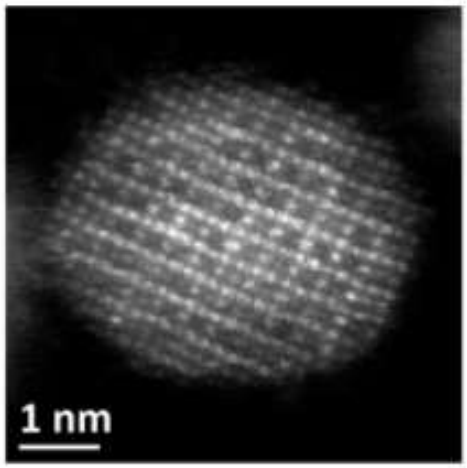


Figure 2.3. STEM-EDX cross-sectional line profile PtCo nanoparticle, taken (a) before and (b) 4 h after dealloying. Key: (□ Pt M-edge, ▪ Pt M-edge (smooth), ○ Co K edge and ● Co K-edge (smooth)). *Images from* [62].

a



b



c

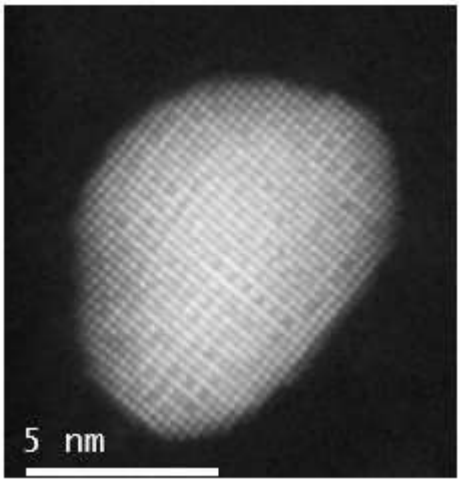


Figure 2.4. STEM-HAADF images of PtCo particles, showing (a) weak Pt_3Co ordering (inset, A) and tetragonal fct $L1_0$ ordering (inset, B and C) from [82], (b) $L1_2$ ordering of a Pt_3Co particle from [83] and (c) [88].

2.7 Conclusions

While not exhaustive, this chapter has looked into the major techniques used in the characterisation of heterogeneous catalysts. The advantages and disadvantages of bulk-averaging and single-particle methods have been discussed. The bulk-averaging methods have been shown to be limited by statistical averaging of the subject particle but this also makes them high throughput. The single-particle method in comparison gives local information but is low throughput. In the next chapter, a detailed look into STEM would show why it is the best candidate for high throughput a study and most useful for PEMFC catalysts. Furthermore, the recent improvements in the optics will be correlated to its growing popularity in the research field.

2.8 References

[59] Skoog D A, Holler F J and Crouch S R 2017 *Principles of Instrumental Analysis* (Massachusetts: Cengage Learning)

[60] Kissinger P T and Heineman W R 1983 Cyclic Voltammetry *J. Chem. Educ.* **60** 702–706

[61] Carriedo G A 1988 The use of cyclic voltammetry in the study of the chemistry of metal-carbonyls: An introductory experiment *J. Chem. Educ.* **65** 1020–1022

[62] Lai F, Su W, Sarma L S, Liu D, Hsieh C, Lee, J and Hwang B 2010 Chemical Dealloying Mechanism of Bimetallic Pt–Co Nanoparticles and Enhancement of Catalytic Activity toward Oxygen Reduction *Chem. Eur. J.* **16** 4602–4611

[63] Vinayan B P, Jafri R I, Nagar R, Rajalakshmi N, Sethupathi K, Ramaprabhu S 2012 Catalytic activity of platinume cobalt alloy nanoparticles decorated functionalized multiwalled carbon nanotubes for oxygen reduction reaction in PEMFC *Int. J. Hyd. Ener.* **37** 412–421.

[64] Dai J, Du Y, and Yang P 2006 Preparation and Characterization of Pt/Co-Core Au-Shell Magnetic Nanoparticles *Z. Anorg. Allg. Chem.* **632** 1108–1111.

[65] Koh S, Leisch J, Toney M F and Strasser P 2007 Structure-Activity-Stability Relationships of Pt-Co Alloy Electrocatalysts in Gas-Diffusion Electrode Layers *J. Phys. Chem. C* **111**, 3744-3752

[66] Jia Q, Caldwell K, Strickland K, Ziegelbauer J M, Liu Z, Yu Z, Ramaker D E and Mukerjee S 2015 Improved Oxygen Reduction Activity and Durability of Dealloyed $PtCo_x$ Catalysts for Proton Exchange Membrane Fuel Cells: Strain, Ligand, and Particle Size Effects *ACS Catal.* **5** 176–86

[67] Ma Z and Zaera F 2006 *Characterization of Heterogeneous Catalysts* ed R M Richards (Florida: Taylor & Francis (CRC Press))

[68] Williams D B and Carter B C 1996 *Transmission Electron Microscopy* (New York: Springer ScienceþBusiness Media)

[69] Miller M K 2000 *Atom Probe Tomography* (Boston, MA: Springer US)

[70] Bunton J H, Lenz D, Olson J D, Thompson K, Ulfig R, Larson D and Kelly T 2006 Instrumentation developments in atom probe tomography: Applications in semiconductor research *Microsc. Microanal.* **12** 1730–1731

[71] Li T, Marquis E A, Bagot P A J, Christian E, Theobald B R C, Sharman J D B, Ozkaya D, Moody P, Tsang S C E 2014 Atomic Imaging of Carbon-Supported Pt, Pt/Co, and Ir@Pt Nanocatalysts by Atom-Probe Tomography *ACS Catal.* **4** 695–702

[72] Yang Q, Joyce D E, Saranu S, Hughes G M, Varambhia A, Moody M P and Bagot P A J 2015 A combined approach for deposition and characterization of atomically engineered catalyst nanoparticles *Catal. Struct. React.* **1** 125–131

[73] Ul-Hamid A 2018 *A Beginners' Guide to Scanning Electron Microscopy* (Cham: Springer)

[74] Pawley J 1984 LOW voltage scanning electron microscopy *J. Microsc.* **136** 45–68

[75] Liu J 2000 High-resolution and low-voltage FE-SEM imaging and microanalysis in materials characterization *Mater. Charact.* **44** 353–363

[76] Sievers G, Mueller S, Quade A, Steffen F, Jakubith S, Kruth A and Brueser V 2014 Mesoporous PteCo oxygen reduction reaction (ORR) catalysts for lowtemperature proton exchange membrane fuel cell synthesized by alternating sputtering *J. Power Sour.* **268** 255–260

[77] Liu J 2000 Contrast of highly dispersed metal nanoparticles in high-resolution secondary electron and backscattered electron images of supported metal catalysts *Microsc. Microanal.* **6** 388–399

[78] Haibo E 2013 *Quantitative Analysis of Core-Shell Nanoparticle Catalysts by Scanning Transmission Electron Microscopy* (Oxford)

[79] Joy D C 1984 Beam interactions, contrast and resolution in the SEM ed O Johari *J. Microsc.* **136** 241–258

[80] Watanabe M, Tsurumi K, Mizukami T, Nakamura T and Stonehart P 1994 Activity and Stability of Ordered and Disordered Co-Pt Alloys for Phosphoric Acid Fuel Cells *J. Electrochem. Soc.* **141** 2659–2668

[81] MacArthur K E, Slater T J A, Haigh S J, Ozkaya D, Nellist P D and Lozano-Perez S 2016 Compositional quantification of PtCo acid-leached fuel cell catalysts using EDX partial cross sections *J. Mater. Sci. Technol.* **32** 248–253

[82] Ward M R, Theobald B, Sharman J, Boyes E D and Gai P L 2018 Direct observations of dynamic PtCo interactions in fuel cell catalyst precursors at the atomic level using E(S)TEM *J. Microsc.* **269** 143–150

[83] Wang X X, Hwang S, Pan Y, Chen K, He Y, Karakalos S, Zhang H, Spendelow J S, Su D and Wu G 2018 Ordered Pt_3Co Intermetallic Nanoparticles Derived from Metal−Organic Frameworks for Oxygen Reduction *Nano Lett.* **18** 4163−4171

[84] Varambhia A 2018 *Quantitative Structural and Compositional Studies of Catalyst Nanoparticles using Imaging and Spectroscopy in STEM* (Oxford)

3 Scanning Transmission Electron Microscopy

3.1 The Basics of STEM

Optical microscopes are often the common imaging tool deployed to investigate specimens. However, the wavelengths of photons are not small enough to probe features in nanoparticles. The Scanning Transmission Electron Microscope (STEM) uses a convergent beam to probe features on such a scale, as opposed to parallel illumination used in traditional Transmission Electron Microscopy (TEM) [85,86]. Although, it was firstly designed and constructed by Baron Manfred von Ardenne in the early 20th century [86,87], it was not until much later that Crewe *et al.* would develop the necessary high vacuum conditions required to fit a field emission gun (FEG) for the nanometre resolution required in the STEM [88–90].

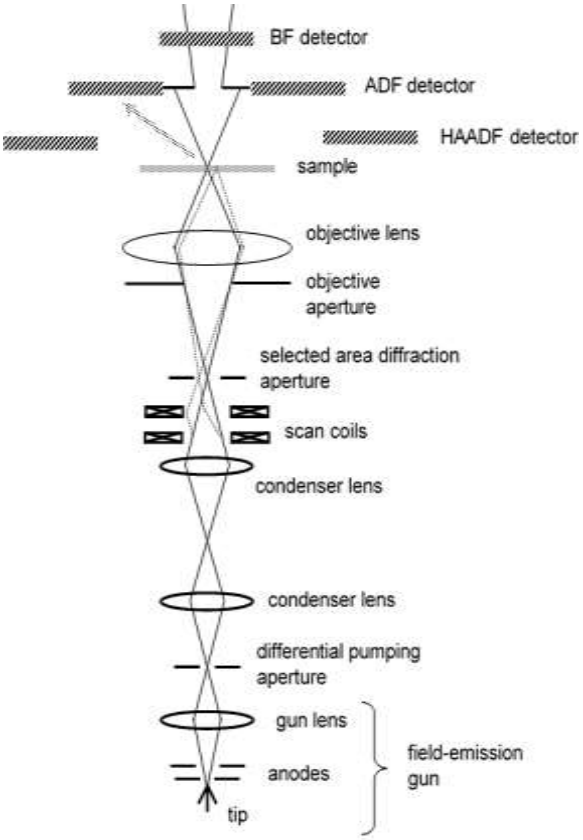


Figure 3.1. Schematic of a STEM, equipped with bright field (BF), annular dark field (ADF) and high-angle annular dark field (HAADF) detectors. *Modified from* [85].

To achieve atomic resolution, the cold field emission gun (Figure 3.1) is preferred over the Schottky thermally assisted field emission gun because of the brightness (number of electrons per unit area per solid angle) obtained [85]. As the brightness is a conserved quantity in the optics, the smaller source size would yield the better spatial resolution. The source is demagnified a further 10^2 times by the probe-forming optics – the combination of the condenser and objective lenses to obtain the sub-nanometre sized probe [85] that is rastered across the specimen by deflector coils, forming an image from the scattering that reaches the detector.

3.2 Bright Field STEM

The detector that collects the direct beam (Figure 3.2) is the bright-field (BF) disc and is made of a scintillator coupled to a photomultiplier tube [85,88]. With collection angles (β) <5 mrad, it can detect phase contrast between the overlapping Bragg discs (Figure 3.3) [78,88,91]. In the condition that the probe-forming aperture (objective aperture) is sufficiently large, the convergent beam is coherent, allowing the observation of interference patterns in the overlapping regions of the Bragg discs [85,88,91]. It should be noted that this phenomenon is only seen in crystalline specimens.

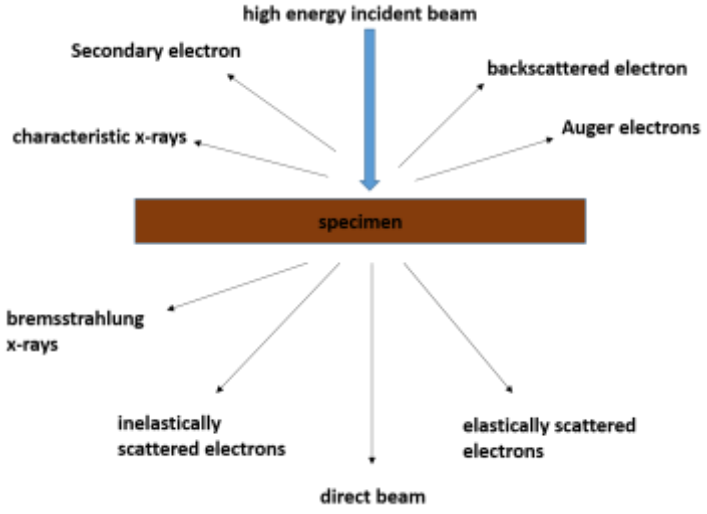


Figure 3.2. Relative directions of the scattering that is transmitted from a thin specimen.

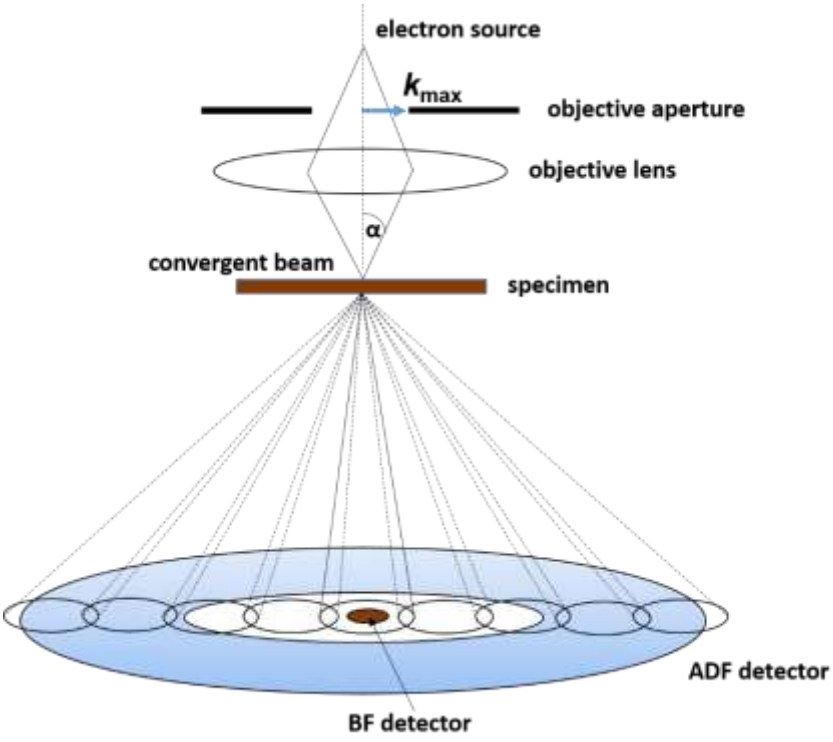


Figure 3.3. Schematic of interference patterns in Bragg discs, resulting in STEM image contrast at the detector plane. The convergence angle (α) determines how much of the illuminating beam is incident on the specimen and is related to the resolution of the image.

The image of the overlapping discs is referred to as a convergent beam electron diffraction pattern and is formed at the detector plane with the following wavefunction in equation 3.2:

$$\Psi_f(\mathbf{K_f}, R_p) = \sum_g \phi_g A(\mathbf{K_f} - g)\exp[-i(\mathbf{K_f} - g)\cdot R_p] \qquad 3.2$$

where ψ_f is the wave in the detector plane, $\mathbf{K_f}$ is the traverse component of the wave, R_p is probe position, g is a vector of the diffracted beam (each Bragg disc), ϕ_g is a sample transmission function, $A(\mathbf{K})$ is the aperture function but $\mathbf{K}$ is replaced with $(\mathbf{K_f} - g)$ to include the g diffracted beams [85,88]. The contrast that is seen in the bright-field image is then the intensity of the wave as a function of R_p at $\mathbf{K_f} = 0$ and is calculated to be in equation 3.2.1:

$$I_{BF}(R_p) = | \Psi_p(R_p) \otimes \phi(R_p) |^2 \qquad 3.2.1$$

It can be seen that the BF detector is sufficiently small in size to be sensitive to the interference

fringes i.e. the phase in the overlapping regions of the Bragg discs and is thus considered a coherent image [85,86].

According to theory of reciprocity [92], the BF STEM is equivalent to TEM and similar information about a subject specimen can be obtained. Kakinuma *et al.* showed a TEM image of a small Pt particle of ∼2 nm on a TiN (titanium nitride) support and was able to deduce its clear faceting and hexahedral shape [93]. Using high resolution BF STEM, it was observed that the Pt(111) and Ti(111) planes lay parallel to each other, with a sub-nanometre amorphous oxide layer covering the particle and support. Similarly using BF STEM, Li *et al.* revealed that the core-shell structure of a nitrogen-doped iron carbon nanotube (CNT@Fe-N-PC) fuel cell catalyst was linked to its high electrical conductivity [94]. It was posited that the graphitised shell of the nanotube gave a high ORR activity. Observations such as the aforementioned are very similar to what can be obtained from HRTEM. As with HRTEM, BF STEM also suffers from contrast reversals due to the coherent nature of the beam. However, the major issue is the contrast dependence on mass-thickness, limiting image interpretability [95].

3.3 ADF and HAADF STEM

The BF detector is small compared to the ADF detector (c.f. section 3.2, Figure. 2) and such a large detector gives rise to an incoherent image [85,88]. This is because the ADF averages over the interference fringes, eliminating any phase information. The $\phi(R_p)$ in 2.2 must then be replaced by the fraction of intensity from individual atoms scattering, $O(R_p)$, in the image formed at the detector, resulting in equation 3.3:

$$I_{ADF}(R_p) = | \Psi_p(R_p) |^2 \otimes O(R_p) \qquad 3.3$$

This means that individual atoms can be imaged as Nellist and Pennycook first demonstrated by elucidating the Pt, Al and O atomic configuration on a γ-Al_2O_3 support [91]. This is very important in catalyst systems because heavy atoms like Pt can be viewed against lighter O

atoms due to Z-contrast in incoherent imaging. Going to higher angles, typically inner angles of β = 80 mrad in a HAADF detector , yields a strong signal intensity dependence on the atomic number, Z [78,88,96]. This is advantageous because unlike HRTEM where the image formation relies on the phase contrast, the Z-contrast makes elements easier to distinguish against the support.

As the Z-contrast is proven to follow a Z^{α} dependency, where α is between 1 and 2 [97], lighter atoms (low Z) are hard to image. A technique that has been used to image lighter elements in catalysts is annular bright-field (ABF) imaging. This is usually an annular detector, usually 11–22 mrad [98], with a disc blocking the BF direct beam. Findlay *et al.* has imaged oxygen columns within the pyramidal twin grain boundary of α-Al_2O_3 support using β = 11–22 mrad ABF detector [98]. Using the same detector angles, Okunishi *et al.* imaged Sr, Ti and O atomic columns on $SrTiO_3$[001], a semiconductor used in solid oxide fuel cells. Little to no sensitivity was found with thickness and defocus ranging 10–70 nm and -20–+20 nm, respectively [99]. It was found that the ABF angles used were optimal for detecting these atoms that varied a good amount in Z. The down side of ABF imaging is that some fraction of the intensity in heavier elements must be sacrificed.

Scattering intensities from light elements may not need to be sacrificed as much when using ADF imaging. Huang *et al.* revealed oxygen vacancy ordering on $LiMn_2O_4$[100], a cathode catalyst used in lithium (Li) ion batteries. They observed Li and O atomic columns for the first time in ADF at β = 52–140 mrad after they could not discern the columns in the HAADF image at β = 92–228 mrad [100]. A difference in contrast was seen with the O atomic columns, where one set of columns had a brighter contrast than the other, evidencing oxygen vacancies in the latter [100]. While HAADF imaging is evidently not suitable for viewing lighter atoms like oxygen, the scattering from heavier elements can be used to deduce information about oxygen binding and thus, electrocatalytic activity. For example, Dai *et al.* showed that under oxygen

and annealing at 720 ℃, Pt_3Co was driven to adopt a core-shell morphology [101]. From sequential HAADF images, they found the annealing changed the Pt_3Co structure from disordered to an $L1_2$ ordered intermetallic core [101]. It was observed that simultaneous formation of a surface Pt bilayer inhibited the energetically favourable Co oxidation. It was also observed that lowering the annealing temperature to at 300 ℃ induced a Pt layer-by-layer growth, resulting in a Pt_3Co core-shell structure [101]. The core-shell morphology has also been corroborated by a myriad of researchers in enhancing the ORR in similar alloy catalysts.

The origin of the Z-contrast has been attributed to the loss of coherency due to the large angles in HAADF imaging, which in turn is attributed to lattice vibrations that attenuate the intensity of Bragg beams – referred to as thermal diffuse scattering (TDS) [85]. Albeit, it has been proven that it is not solely the large angles that cause the loss of coherency but the integration of multiple large angle scattering over the annular detector [85,102]. Incoherent Z-imaging in STEM allows for relatively unambiguous quantification of elements in catalysts systems. However, detailed quantification becomes an issue with thick and or complex specimens.

While not as challenging as HRTEM in terms of image interpretation, HAADF imaging also has a dependence on thickness and composition. Sometimes, scattering may occur beyond the outer angles of the ADF detector, yielding contrast reversals in the densest parts of the image and breaking the monotonic relationship between Z and thickness [103]. Researchers such as Ercius and Muller have introduced a technique referred to as incoherent bright-field imaging (IBF), which is basically BF imaging with larger angles, typically 0–100 mrad [103,104]. They observed that as ADF showed a sharp rise then gradual fall in image intensity through a Ta wedge specimen of 8 μm thickness, IBF showed a monotonic decrease [103]. IBF is relatively uncommon and its use is mainly for very thick specimens. The common method of obtaining quantitatively reliable data is the comparison of ADF simulated cross-sections to image intensities from experiment. The cross-section describes the probability of a scattering event

from an element and is usually given in the unit of barns (b). The cross-sections could be derived from a database or in-house calculations.

Using ADF simulations, LeBeau *et al.* have shown column-by-column atom counting in an Au wedge without a calibrated standard [105]. Their quantification was based on binning the columns by the number of atoms they could see in the ADF image – this was cross-referenced with a multislice ADF simulation. Aarons *et al.* have justified the technique used by LeBeau *et al.* with Pt nanoparticles. Since nanoparticles are very small, they have relatively few atomic columns and thus, the ADF image intensities could be compared to tabulated references. The 3D structures of the Pt nanoparticles were simulated and oxygen binding on the nanoparticles were modelled using DFT [10]. This means that tilting the specimen to numerous projections is not always required to obtain 3D constructions of nanoparticles. On the other hand, MacArthur *et al.* used the statistical estimation technique pioneered by Van Aert *et al.* [106] to determine cross-sections for a PtCo bimetallic particle [96]. The difference compared to the method used by LeBeau *et al.* is that Van Aert *et al.* uses an integration classification likelihood (ICL) criterion. The histogram of intensities from the ADF image is decomposed into an optimum number of Gaussian components using a local minima function, before comparing to simulation [106]. This is advantageous as it smears out Poissonian noise and random errors. The disadvantage as highlighted by De Backer *et al.* [107] is accurately selecting the number of Gaussians to use due to the field of view. ADF simulations get more complicated with more atoms and current models used are an ongoing improvement.

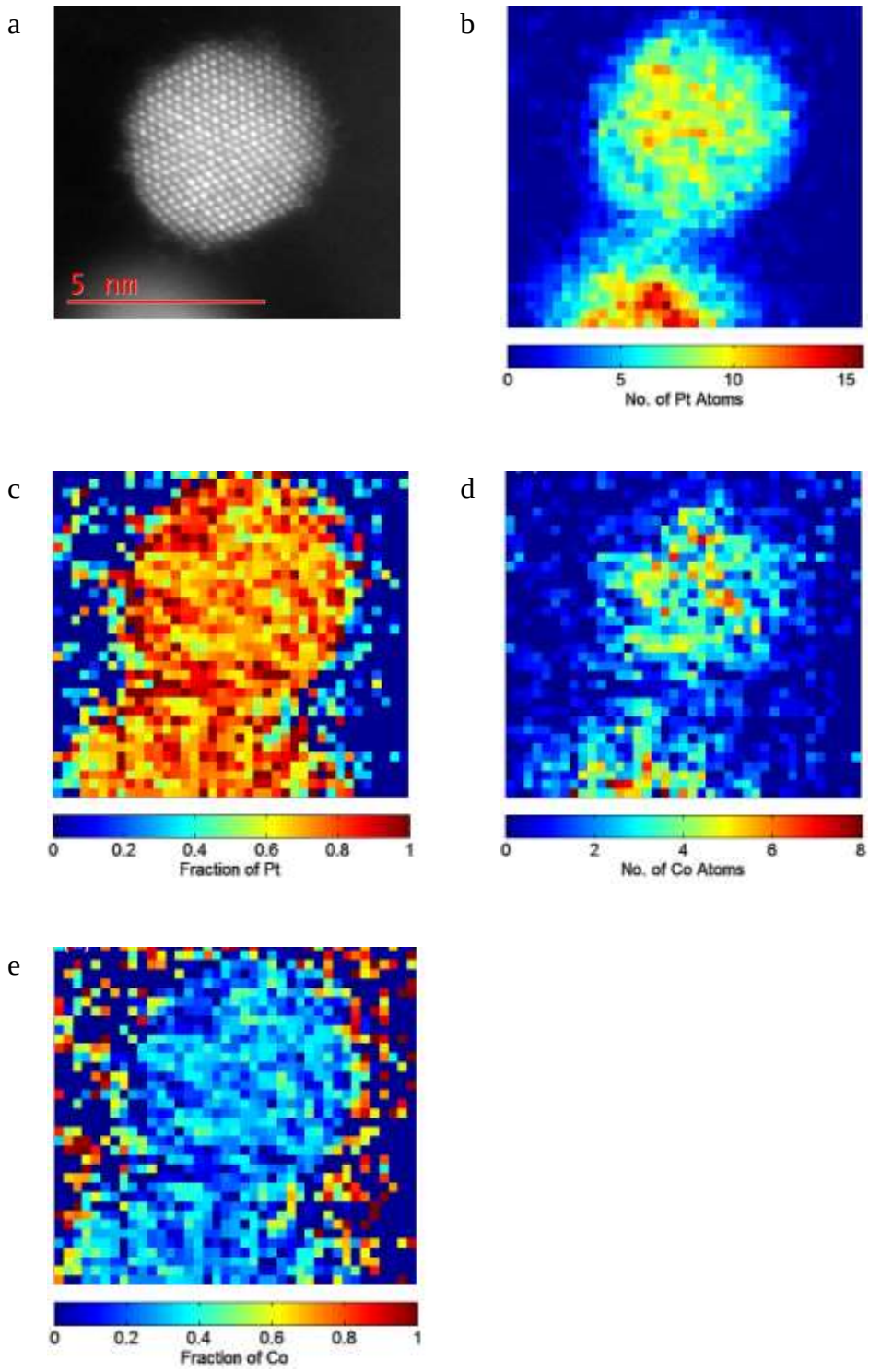


Figure 3.4. – Composition cross section analysis of a PtCo leached particle using ADF and EDX. The (a) number of Pt atoms, (b) atomic fraction of Pt, (c) number of Co atoms and (d) atomic fraction of Co atoms are shown. The composition of the particle was found to be 73±8 atPt% (Pt atomic percentage). *Images from* [96].

3.4 Aberration Correction

Intensities seen in an image can only be accurately correlated to the specimen if every point that the convergent beam forms on the specimen is projected in the resultant image. However, unlike optical lenses, this is not the case with electromagnetic lenses used in electron microscopy [97]. This due to the physics of the magnets not being able to correctly focus varying wavelengths of electrons from the gun into a spot probe. There are two main types of aberrations; monochromatic and chromatic aberrations The monochromatic aberrations are those that exist despite electrons having relatively uniform energy while chromatic aberrations are caused by electrons of non-uniform energy. Among the common monochromatic aberrations i.e. coma, spherical aberration and astigmatism, the effect of spherical aberration is most key because it is caused from the off-axis rays not being brought to the same focus as the paraxial (closest to the centre of the lens) rays (Figure 3.4) [85].

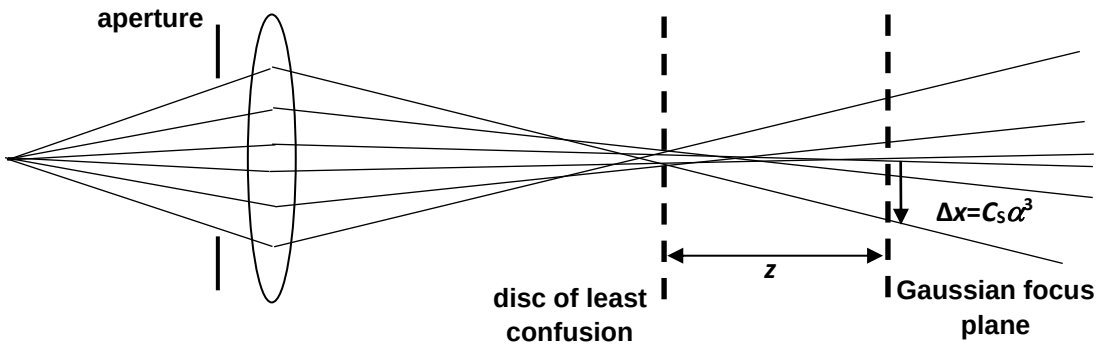


Figure 3.4. Schematic of STEM ray optic depicting spherical aberration where Δx is the displacement due to the aberration and C_s is the coefficient for spherical aberration. *Image reproduced from* [85].

The above diagram (Figure 3.4) shows that the paraxial rays are focused to a different plane (Gaussian plane) compared to the off-axis-rays. Consequently, the disc of least confusion is the smallest beam diameter that can give the optimal resolution in this case. Furthermore, the

cube dependence on the displacement infers that resolution will be most limited with larger α values. This seems counter-intuitive because a larger α means that more electrons can be focused into a small probe, yielding a higher current density and therefore increasing the signal-to-noise ratio (SNR) and resolution in images [93,108]. One solution has been to choose an optimal spatial frequency, k_{max} since it is proportional to α by a multiple of the wavelength, λ [78,85]. This function of the aperture cuts out the higher order beams in the front focal plane (FFP) and results in the optimum resolution [85].

Furthermore, optimal or Scherzer defocus [85,86] needs to be attained, given by equation 3.4:

$$\Delta f_{opt} = -0.71(\lambda^3 C_s)^{1/2} \qquad 3.4$$

Imposing the k_{max} or diffraction limited probe gives equation 3.4.1:

$$d_{diff} = 0.43(\lambda^3 C_s)^{1/4} \qquad 3.4.1$$

Looking at 2.6 and comparing the 0.43 pre-factor to 0.66 for the equivalent in TEM [70], this may contribute to the smaller probe achieved in STEM imaging. However, the advent of auxiliary lenses which correct C_s (spherical aberration coefficient) and C_c (chromatic aberration coefficient) have improved STEM imaging. These auxiliary lenses are referred to as aberration correctors. The function of the correctors are to make C_s and C_c = 0 or at least limit them without introducing corollary aberrations of their own [85,86]. Hexapole and quadropole-octupole correctors are prominent in HAADF STEM and point resolution of 78 pm, compared to an uncorrected 200 pm, has been achieved [78,109].

C_s correctors are more prominent than C_c correctors as they are harder to make and operate. Also, spherical aberration has a larger effect on resolution. Using a hexapole C_s corrector, Haider *et al.* found an improvement from 0.24 nm point resolution in the uncorrected TEM image to 0.14 nm in the aberration-corrected image of an epitaxial Si (silicon) specimen, Si(111)/$CoSi_2$, at 200kV [110]. They found that contrast delocalisation was absent at C_s = 0.05 mm [109]. Krivanek revealed BF STEM images of graphitised carbon (002) lattice planes using

a quadrupole-hexapole corrector at 100 kV. With C_s of around 0.1–0.4 mm, lattice distances of 3.44 Å could be measured [111]. More recently, Shilo *et al.* found a refractive silicon nitride thin film served as an alternative to traditional multipole correctors which have to have precise alignment and withstand electrical instabilities from external noise and power supply [112]. The Si(110) columns were observed as 138 pm-separated dumbbells in the corrected HAADF image compared to elongated intensities seen in the uncorrected image [112]. This finding means that the fabrication and addition of thin film graters in microscopes could at the very least be an extra tool for aberration correction in STEM imaging.

3.5 Channelling and contamination

Even with aberration correction, STEM imaging still has a few challenges that make compositional quantification difficult. As earlier mentioned, intensities in a HAADF image depends strongly on thickness and composition, therefore accurate cross-sections need to be matched to the intensities seen in the image. This becomes a significant issue when studying oxygen in Pt bimetallics because the Z-contrast, in addition to lensing effects, supresses the oxygen signal to the point of near absence in the ADF image. It gets worse when the complexity of mixed atomic columns are introduced.

The solution to Schrodinger's equations for a periodic potential is of the form in $\Psi_k(R) = u_k(R)\, e^{ikr}$, where a plane wave is multiplied by a periodic function specific to the specimen, u_k, to give the eigenfunction for the wave equation [68,86]. The eigenstates or Bloch states are most localised on the atomic columns due to the electrostatic pull of at the atomic sites and therefore, each subsequent atom experiences a more focused probe than it would feel if the illuminating beam interacted with it individually [85,86]. This destroys the linearity of the intensity with number of atoms in the ADF image because the scattering cross-section derived would be

significantly higher, making quantification difficult. This phenomenon is referred to as channelling [85,86] (Figure 3.5).

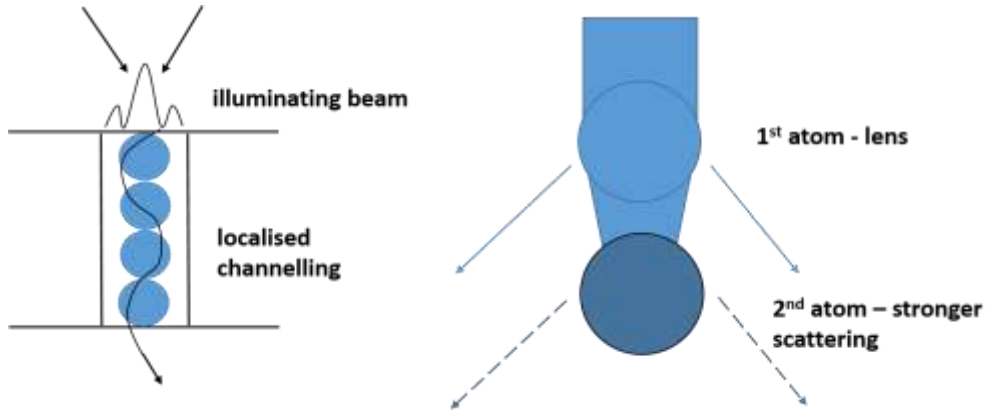


Figure 3.5. Relative directions of the scattering that is transmitted from thin specimen.

Channelling effects have been modelled using prominent methods such as the bloch wave and multislice procedures. The bloch wave method as theorised by Bethe considers that the bloch states of the incident electron and the bloch states of the specimen are in superposition and are excited by multiple-angle plane waves from the probe [78,96]. Given that this means the phases of the waves in these states are all linked, the inverting of large matrices over all the angles would be required [78,96] and this would take a lot of computation and time for this method to be practical.

Another major issue in STEM imaging is contamination of the specimen. The major source of contamination, especially with catalysts under the microscope is usually from the carbon support. This due to the cracking of the hydrocarbon bonds and redeposition under the electron beam. The redeposition creates an amorphous carbon layer clogs the STEM image and reduces its contrast. As this creates a net effect of decreased channelling, atomic columns are barely resolvable with such contamination. Contamination is also linked to the beam energy. A high accelerating voltage will bring about large collisions between the incident electrons and atoms within specimen, leading to large atomic displacements and even damage. This is referred to

as cause knock-on damage [113,114]. Conversely, too low an accelerating voltage increases the interaction time the incident electron spends within the specimen, leading to bond damage by radiolysis [113,114]. Atoms on the surface can also move under the beam and in extreme cases, holes can be drilled through the specimen if the probe retains its position for a long duration. The specimen could also see more complex phenomenon like beam-induced heating and conduction in conjugated systems.

There are ways to mitigate contamination and sample damage. To begin with, carbon supported specimens are generally plasma cleaned or baked at 80 ℃, which seems to significantly reduce the probability of contamination. Higher accelerating voltages can be used for mainly larger *Z* materials while lower voltages would favour lower *Z* specimens. If the accelerating voltage is to be held constant, constant moving of the beam away from a particular probe position will reduce sample damage. An approach that has seen increasing use is to use less dwell time and acquire multiple frames which can be summed up to boost the signal.

3.6 Conclusions

Depending on the detectors used, STEM allows a variety of signals to be collected in order to obtain the structure and composition of a specimen. The advantage of having a small and bright probe on spatial resolution has been discussed. The loss of coherence and the optics that lead to *Z*-contrast imaging has been shown to be instrumental in understanding catalyst structure in ADF and HAADF STEM. However, the sacrifice of low light elements in ADF imaging has been highlighted and auxiliary techniques such as ABF have been put forward. The non-monotonic relationship between intensity and mass-thickness in ADF imaging has also been discussed, with a brief look into IBF as a possible alternative but mainly for very thick specimens.

The improvement that aberration correction brings to image interpretation has been shown to be crucial. The higher beam currents and smaller probes boosts spatial resolution than in an uncorrected STEM microscope. However, problems such as channelling and sample damage still pose challenges to unambiguous elemental quantification. Consequently, EELS (electron energy loss spectroscopy) is introduced in the next chapter. Through the examination of transitions at specific resonant frequencies, atomic bonding states of can be identified in a wide range of elements. Such knowledge is crucial to optimising the design of catalysts and EELS is one of the most powerful tools that explores this.

3.7 References

[85] Nellist P D 2007 *Science of Microscopy* (New York: Springer)

[86] Brydson R 2011 *Aberration-Corrected Analytical Transmission Electron Microscopy* (West Sussex: Wiley)

[87] Von Ardenne M 1983 The scanning electron microscope *Mag. Phys.* **109** 553–572

[88] Crewe A V. 1983 High-Resolution Scanning Transmission Electron Microscopy *Science (80-.).* **221** 325–330

[89] Crewe A V 1963 A new kind of a scanning microscope *J. Microsc.* **2** 369–371

[90] Crewe A V, Wall J and Langmore J 1970 Visibility of Single Atoms *Science (80-.).* **168** 1338– 1340

[91] Nellist P D and Pennycook S J 1996 Direct Imaging of the Atomic Configuration of Ultradispersed Catalysts *Science (80-.).* **274** 413–415

[92] Rose H and Kisielowski C F 2005 On the Reciprocity of TEM and STEM *Microsc. Microanal.* **11** 2114–2115

[93] Kakinuma K, Wakasugi Y, Uchida M, Kamino T, Uchida H, Deki S and Watanabe M 2012 Preparation of titanium nitride-supported platinum catalysts with well controlled morphology and their properties relevant to polymer electrolyte fuel cells *Electrochim. Acta* **77** 279–284

[94] Li J C, Yang Z Q, Tang D M, Zhang L, Hou P X, Zhao S Y, Liu C, Cheng M, Li G X, Zhang F and Cheng H M 2018 N-doped carbon nanotubes containing a high concentration of single iron atoms for efficient oxygen reduction *NPG Asia Mater.* **10** 1–7

[95] Patel B, Pearson R and Watanabe M 2014 Bright field and dark field STEM-IN-SEM imaging of polymer systems *J. Appl. Polym. Sci.* **131** 1–8

[96] MacArthur K E 2015 *Quantitative Structural and Compositional Characterisation of Bimetallic Fuel-Cell Catalyst Nanoparticles Using STEM* (Oxford)

[97] Wang Z W, Li Z Y, Park S J, Abdela A, Tang D and Palmer R E 2011 Quantitative Z-contrast imaging in the scanning transmission electron microscope with size-selected clusters *Phys. Rev. B - Condens. Matter Mater. Phys.* **84** 2–4

[98] Findlay S D, Azuma S, Shibata N, Okunishi E and Ikuhara Y 2011 Direct oxygen imaging within a ceramic interface, with some observations upon the dark contrast at the grain boundary *Ultramicroscopy* **111** 285–289

[99] Okunishi E, Sawada H and Kondo Y 2012 Experimental study of annular bright field (ABF) imaging using aberration-corrected scanning transmission electron microscopy (STEM) *Micron* **43** 538–544

[100] Huang R, Ikuhara Y H, Mizoguchi T, Findlay S D, Kuwabara A, Fisher C A J, Moriwake H, Oki H, Hirayama T and Ikuhara Y 2011 Oxygen-vacancy ordering at surfaces of lithium manganese(III,IV) oxide spinel nanoparticles *Angew. Chemie - Int. Ed.* **50** 3053–3057

[101] Dai S, You Y, Zhang S, Cai W, Xu M, Xie L, Wu R, Graham G W and Pan X 2017 In

situ atomic-scale observation of oxygen-driven core-shell formation in Pt 3 Co nanoparticles *Nat. Commun.* **8** 1–8

[102] Amali A and Rez P 1997 Theory of lattice resolution in high-angle annular dark-field images *Microsc. Microanal.* **3** 28–46

[103] Ercius P and Muller D 2009 Incoherent Bright Field STEM for Imaging and Tomography of Ultra-Thick TEM Cross-sections *Microsc. Microanal.* **15** 238–239

[104] Ercius P, Weyland M, Muller D A and Gignac L M 2006 Three-dimensional imaging of nanovoids in copper interconnects using incoherent bright field tomography *Appl. Phys. Lett.* **88** 1–4

[105] Lebeau J M, Findlay S D, Allen L J and Stemmer S 2010 Standardless atom counting in scanning transmission electron microscopy *Nano Lett.* **10** 4405–4408

[106] Van Aert S, Verbeeck J, Erni R, Bals S, Luysberg M, Dyck D Van and Tendeloo G Van 2009 Quantitative atomic resolution mapping using high-angle annular dark field scanning transmission electron microscopy *Ultramicroscopy* **109** 1236–1244

[107] De Backer A, Martinez G T, Rosenauer A and Van Aert S 2013 Atom counting in HAADF STEM using a statistical model-based approach: Methodology, possibilities, and inherent limitations *Ultramicroscopy* **134** 23–33

[108] Watanabe M, Ackland D W, Kiely C J, Williams B D, Kanno M, Hynes R and Sawada H 2006 The aberration corrected JEOL JEM-2200FS FEG-STEM/TEM fitted with an Ω electron energy-filter: Performance characterization and selected applications *JEOL News* **41** 2–7

[109] Nellist P D, Chisholm M F, Dellby N, Krivanek O L, Murfitt M F, Szilagyi Z S, Lupini A R, Borisevich A, Sides W H and Pennycook S J 2004 Direct sub-angstrom imaging of a crystal lattice *Science* **305** 1741

[110] Haider M, Rose H, Uhlemann S, Schwan E, Kabius B and Urban K 1998 A spherical-aberration-corrected 200 kV transmission electron microscope *Ultramicroscopy* **75** 53–60

[111] Krivanek O L, Dellby N and Lupini A R 1999 Towards sub-Å electron beams *Ultramicroscopy* **78** 1–11

[112] Shiloh R, Remez R, Lu P H, Jin L, Lereah Y, Tavabi A H, Dunin-Borkowski R E and Arie A 2018 Spherical aberration correction in a scanning transmission electron microscope using a sculpted thin film *Ultramicroscopy* **189** 46–53

[113] Datye A K and Smith D J 1992 The Study of Heterogeneous Catalysts by High-Resolution Transmission Electron Microscopy *Catal. Rev.* **34** 129–178

[114] Egerton R F 2014 Choice of operating voltage for a transmission electron microscope *Ultramicroscopy* **145** 85–93

4 Electron Energy Loss Spectroscopy

4.1 Theory and Background

4.1.1 EELS Mechanism and Signals

EELS involves the spectral analysis of electron beam after it has scattered from the specimen. The scattering is mainly of two types; elastic and inelastic. Elastic scattering means no energy loss of the incident electron has occurred. Inelastic scattering means the incident electron has lost energy. While elastic scattering makes the most part of diffraction patterns and images, inelastically scattered electrons are the foundation of the EELS technique as they allow the probing of the unoccupied density of states (DOS), which is related to the bonding environment in a material. This gives a more detailed view of catalyst materials than any imaging technique and most other spectroscopic techniques due to the large range of elements that EELS can probe.

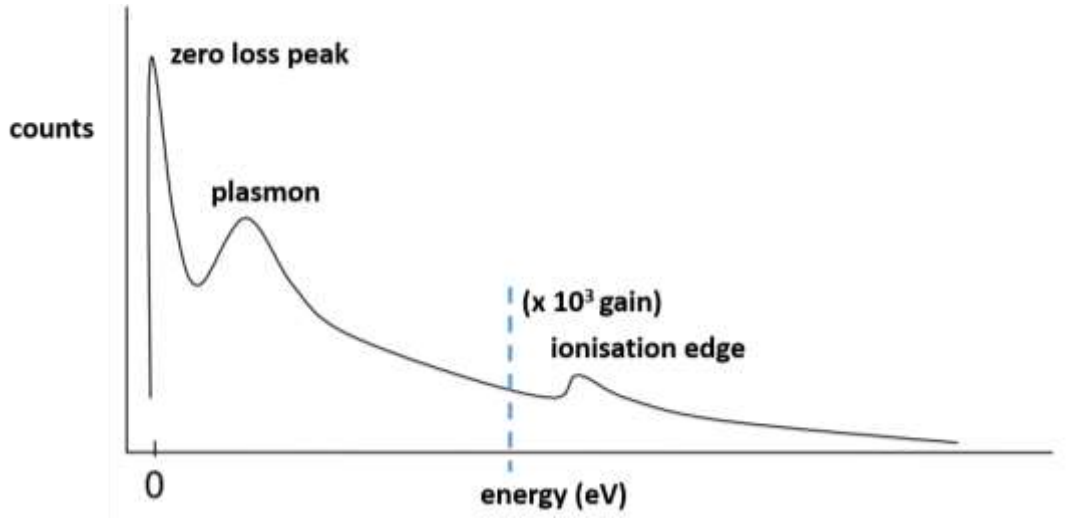


Figure 4.1. Basic features of an EEL spectrum.

Inelastic scattering is subdivided into inner and outer shell excitations. The former are excitations from the core while the latter are usually single or collective responses from non-core electrons [115]. The electrons that have lost no energy make up the zero loss peak (ZLP)

and is the main elastic signal of the EEL spectrum (Figure 1). Some 5–50 eV after the ZLP, is the plasmon signal (Figure 4.1), which is the collective electronic response of the non-core or valence band and is the bulk of the outer shell excitations. The inelastic scattering events are significantly less than the elastic scattering, dominated by the ZLP and plasmon signal, therefore the background has to be blown up by a factor of a thousand to make the features visible (Figure 4.1).

The inner shell excitations are distinguished by the ionisation edge and because this is related to the binding energy of the shell the electron was excited from, this can be used to fingerprint specific elements and their surrounding structure. The EEL spectrum, from a simplistic model, is a convolution of Gaussians and Lorentzians, describing the instrumental and core-hole lifetime broadening. These effects perturb the interpretation of the fine structure and the latter has been found to introduce extra peaks in the spectrum depending on the overlap with the valence state. The region closest to and including the ionisation edge is known as the energy-loss near-edge structure (ELNES) while those slightly further down make up the extended energy loss fine structure (EXELFS). The ELNES gives details on local geometry while the EXELFS elucidates bond distances and coordination number [115]. Their distinction is related to differences in the mean free path that the incident electron takes [68,115]. The shapes and peak intensities of the ELNES and EXELFS can be used to determine oxidation states and bonding arrangement because the shifts and position of the edge onset depends on changes in the charge on the atom and the interaction between the excited electron and the hole it leaves behind [115].

The process of EELS scattering is not a random event and is governed by rules. The scattering theory as proposed by Bethe considers that an electron incident on a specimen will scatter within an angular range, θ, as a function of the EELS collection angle, β [115,120]. The energy loss and momentum, q, transferred from the incident electron upon collision with the ejected

electron gives information about the unoccupied density of states (DOS) in the form of the fine structure. The intensity of the DOS fine structure is related to the amount of states, $N_f(E)$, and a matrix element allows for transitions into the states, $M_{i,f}(E)$ [115,116] as expressed in 4.1.1:

$$I(E) \propto \sum | M_{i,f}(E) |^2 N_f(E) \qquad 4.1.1$$

The matrix element, $M_{i,f}(E)$, governs the probability of transition of a core electron into an empty state. However, there are certain approximations made when dealing with these transitions. One of them is the dipole approximation. This approximation relates the angular-momentum quantum number, *l*, of the bound and ejected electrons [115–117] and thus, the angular and energy dependence can be extracted. The wavefunction must change symmetry with the transition $| M_{i,f}(E) |^2$ [118], with a $\Delta l \pm 1$ rule i.e. $1s \rightarrow 2p$ (l for $s = 0$, $p = 1$) and so on. Depending on the total orbital angular momentum, *j*, of subshells in the transition, which gives the subscripts in $1s_{1/2}$, $2s_{1/2}$, $2p_{1/2}$, $2p_{3/2}$, $3s_{1/2}$…, the transitions are named *K*, L_1, L_2, L_3, M_1,…accordingly and correspond to peaks in the EEL spectrum. When the matrix element is written in Dirac notation, it becomes $|\langle f| e^{i\underline{q}.\underline{r}} |i\rangle|^2$ [115,118]. A series expansion means $e^{i\underline{q}.\underline{r}}$ can be written as $1 + i\underline{q}.\underline{r} + \ldots$ where terms past the second can be ignored as $\underline{q}.\underline{r} << 1$. This is where the dipole approximation stems from.

There is also the first Born approximation which states that the incident electron is the driving field at each point in the specimen [115]. While this holds, the probability that an electron will scatter through a solid angle and lose energy in the range $E \rightarrow E + \Delta E$ is given in 4.2 as the double differential scanning cross-section (DDSC) and is related to $S(q, E)$, the dynamic form factor (DFF) in equation 4.1.1.2:

$$\partial^2\sigma/\partial E\partial\Omega = 4\gamma^2 k S(q, E)/|q|^4 a_o k_o \qquad 4.1.1.2$$

The DFF is commonly written in accordance with Fermi's golden rule as in equation 4.1.1.3:

$$S(q, E) = \sum |\langle f| e^{i\underline{q}.\underline{r}} |i\rangle|^2 \, \delta(E_i - E_f + E) \qquad 4.1.1.3$$

where σ is the cross-section, Ω is the solid angle, γ a relativistic factor, r is the position of the electron and a_o is the Bohr radius. The k and k_o are wavevectors of the incident electron before and after scattering, respectively, and $\delta(E_i–E_f + E)$ fulfils the energy conservation and is a summation over all occupied and unoccupied states [115–1118]. The DFF dictates the scattering amplitude while the DDSC governs how much of the scattering is observed. This is based on the wavefunction overlap of the initial ($<$i) and final ($<$f) states of the electron, which is related to the matrix element. All of these terms come together to create the ionisation events observed in an EEL spectrum.

4.1.2 The Spectrometer

In order to obtain an EEL spectrum, the electrons need to be separated according to their energies and analysed. There are various types of spectrometers that have been developed over the years for the high-resolution recording of EEL spectra.

The most common type of modern EEL spectrometer is the sector magnet spectrometer. It is the easiest to mount on the microscope, post-column and the design is not as complicated as some of the other spectrometers. The spectrometer uses a single-prism magnet to deflect electrons 90°, separating the electrons according to their kinetic energy at the dispersion plane (Figure 4.2) [115]. The coils are symmetrically arranged between the magnetic pole pieces in the spectrometer and helps maintain the electron trajectory during travel [115]. The design of the spectrometer is such that external magnetic fluxes and hysteresis are minimised. A drift tube voltage can also be used to control any offsets in the energy of the electrons. The sector magnet spectrometer does suffer from first-order aberrations where there is a bifocal point source at the dispersion plane [68,115]. A lens array (Figure 4.2), usually quadroples, are used as correction. Sextupoles are sometimes used when higher order aberrations are involved. At the very end of the spectrometer is the CCD detection system and this is usually composed of

a scintillator couple to a photomultiplier tube and CCD camera. This is where the spectra is collected and recorded.

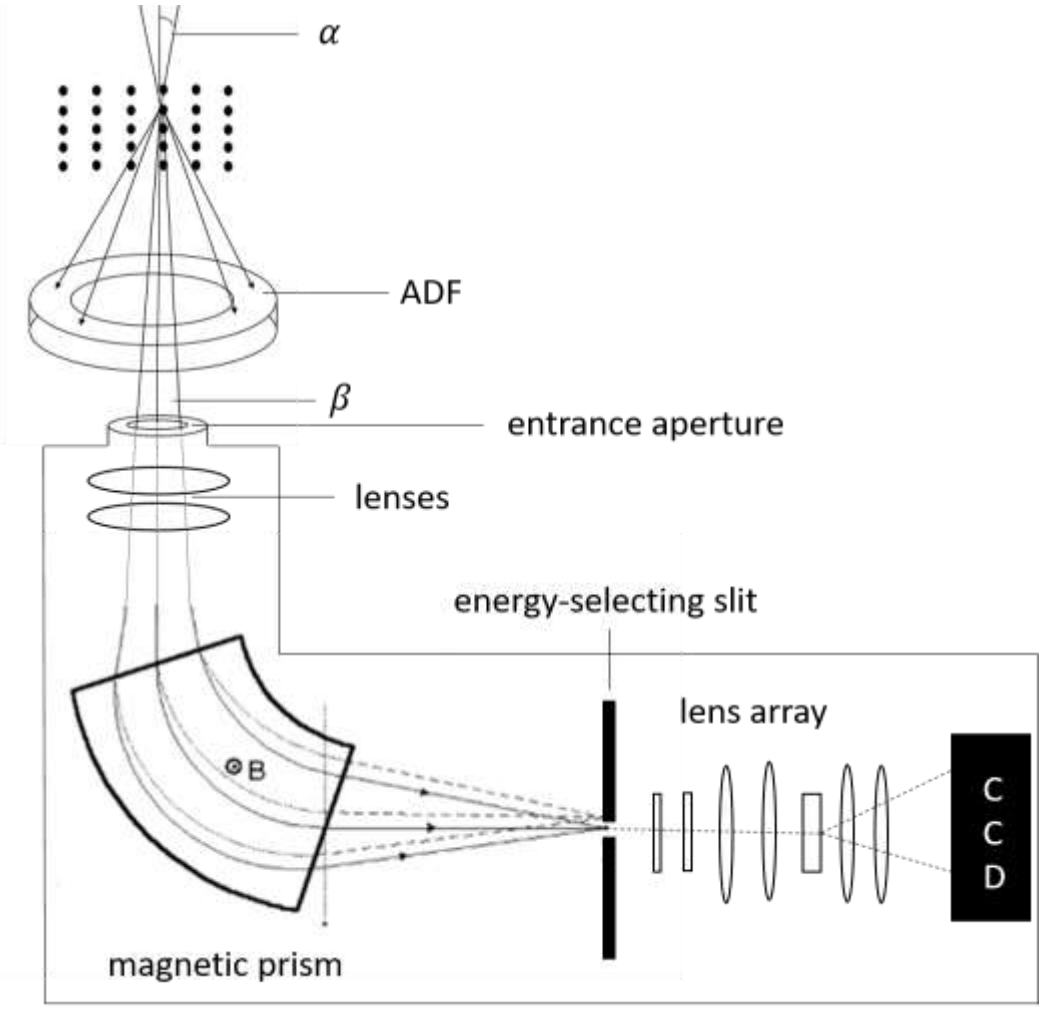


Figure 4.2. Diagram of scattering into EELS 90° magnetic sector spectrometer; B = magnetic field, α, β = convergence and collection semi-angles, respectively.

4.2 Elemental Quantification

In order to carry out elemental analysis in an EEL spectrum, it is necessary to quantify the areas under the ionisation edges of interest. For elemental quantification, only the intensities due to the ionisation events need to be considered and as such, the decreasing background in the spectrum needs to be removed. This is generally achieved by fitting a Power-Law background, $I = AE^{-r}$, due to the logarithmic relationship between the intensity and the energy loss in the

high-loss regions of the spectrum [115]. The variable E is the energy loss and A and r are fitting parameters.

For accurate quantification, knowledge of the cross-section is required. To be exact, the cross-section is commonly referred to as the partial cross-section since only a fraction of the scattering reaches the EELS detector. The ionisation intensities seen in the spectrum are derivative of these partial cross-sections and they can be used to determine elemental composition in a specimen. This is because the edge intensity is related to the number of atoms of the subject element in the specimen, and thus the composition or concentration can be calculated [115]. The concentration or atomic ratio can be determined using the formula: $N_A/N_B \approx I_A(\beta,\Delta)\sigma_B(\beta,\Delta)/I_B(\beta,\Delta)\sigma_A(\beta,\Delta)$, where A and B are two different elements, I their corresponding intensities and Δ is the integration width [115].

There are two major methods for the determination of cross-sections. Packages such as SIGMAK and SIGMAL (Figure 4.3a) use hydrogenic models to calculate the cross-sections based on work done by Egerton [119–121]. There are also those which use Hartree-Slater models based on the generalised oscillator strength (GOS), tabulated by Rez [122]. These models are implemented in the popular software, *Digital Micrograph*. The other method is the use of k-factors (Figure 4.3b), which involves measurements from standards where the elemental composition of two elements, A and B, is known and the experimental conditions are kept the same [115].

Hydrogenic models were the earliest form of deriving cross-sections and were developed in 1979 by Egerton [120]. Egerton based the calculations assuming an atomic model of hydrogen wavefunctions. A Zener screening constant, which is related to elemental Z values, was used to calculate the GOS for K shell cross-sections and the best agreements were found for $Z < 20$ and incident energies > 30 keV [120]. In 1984, Egerton found that adding relativistic effects increased the partial cross-sections by 10% at incident energies of 100 keV [120,121]. These

findings by Egerton were packaged into the SIGMAK program and is widely used to calculate *K* shell cross-sections by a myriad of researchers. For example, Joy *et al.* found 1:1 stochiometry in BN and MgO using the SIGMAK program [123].

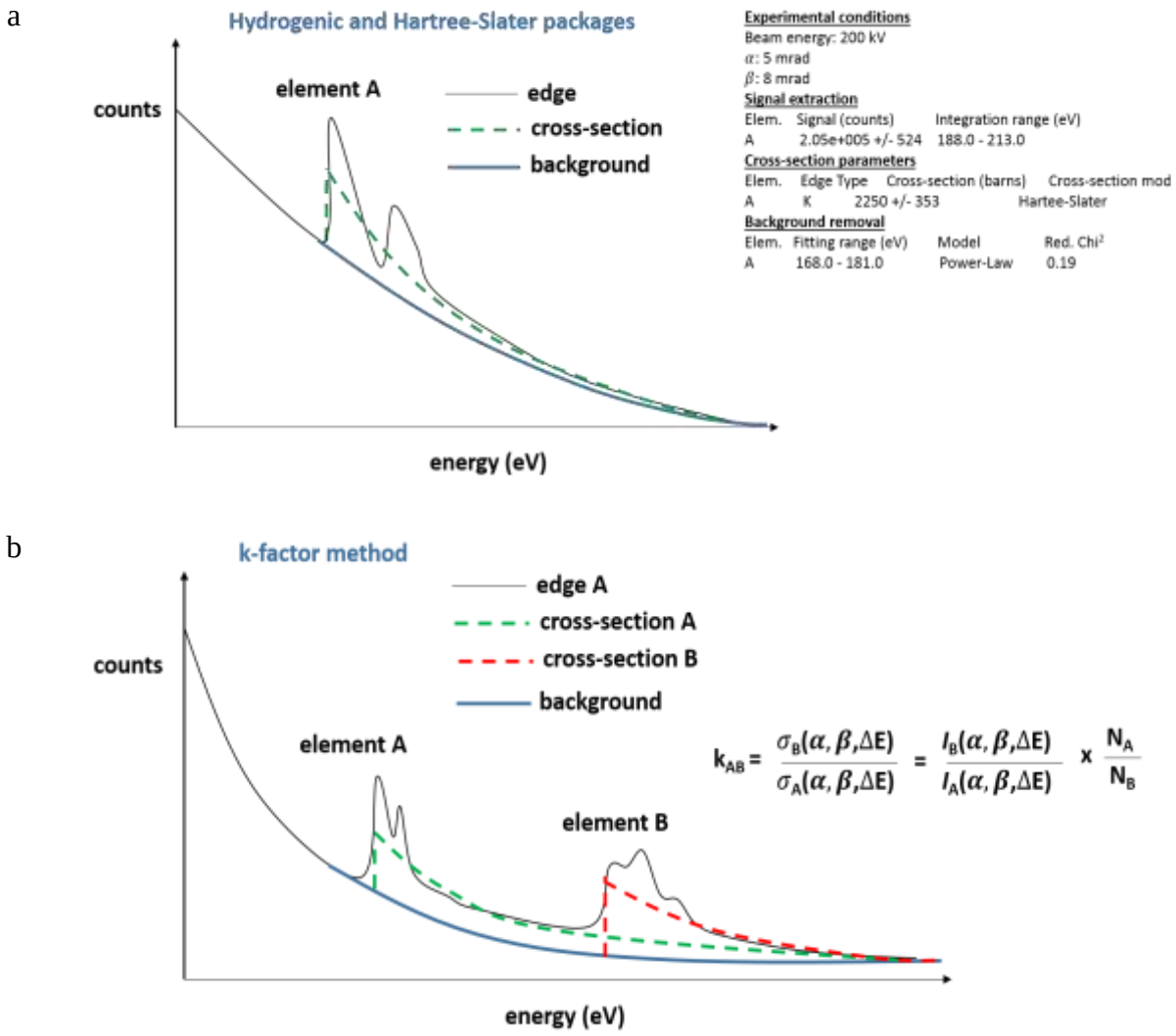


Figure 4.3. Illustration cross-section extraction using (a) hydrogenic and Hartee-Slater models and (b) the k-factor method.

The SIGMAL program was later developed my Egerton in order to incorporate *L* ionisations. Using the SIGMAL program, Allison *et al.* found that in V_6C_5, the C/V ratio was 25% lower than the known value of 0.833 in the carbide [124]. Sklad *et al.* found similar errors in the study of titanium diboride (TiB_2) [125]. When Malis and Titchmarsh compared their study of the same compound, they found that the Ti/B ratio was 0.664 compared to 1.1 measured by Sklad

et al. [126]. Work done by Grande and Ahn done on oxides also showed similar discrepancies, although thickness of the specimen was seen to play a role in the variation [127]. Consequently, it was thought that such deviations meant the SIGMAL models were still only modest in the accuracy of determining *L* shell cross-sections. Improvements by Egerton based on these errors were made and the later version of the SIGMAL package, SIGMAL2, did show better results.

The *K* transitions arise from tightly bound *s* states which give *saw-tooth* profiles, and as such, hydrogenic models best describe them. As previously discussed, *L* edges are not as straightforward. Things get more complicated with $Z > 30$ and Egerton found that the use of higher order ionisation hydrogenic models such as *M*, *N* and *O* edges were not sufficient descriptors [119]. As such Leapman *et al.* introduce Hartree-Slater wavefunctions which tends to have a sharper peak at the edge threshold than models using hydrogenic wavefunctions [128,129]. In the Hartree-Slater model, the atomic single-electron inner shell transitions are assumed due to the Hartree mean field theory, and that the transitions are thought to go into the continuum [119,129]. Rez found that *d* transitions to the continuum at low energies just above the threshold were described significantly better with the Hartree-Slater model than with the hydrogenic model [122]. Ahn and Rez found good agreement between the Hartree-Slater model and experiment for edges without delayed maxima greater than 40 eV [128]. They found a major inibitor to the accuracy of the cross-sections were solid state effects in *L* and *M* shells, albeit they found these averaged out with integration windows greater than 100 eV, observing only 10% variations in cross-section values [128].

As deducible, both the hydrogenic and Hartree-Slater models do not include solid state effects. They also do not include transitions into bound states but only sum over all unbound final states [115]. This is a major reason why higher shell cross-sections and the general fine structure vary with *L*, *M* and other higher shell ionisations. In 1987, Hofer introduced k-factors as an alternative method using a molybdenum oxide (MoO_3) thin film standard [130]. This method

used *M* edges for the determination of the partial cross-section. The thin film must contain a light element i.e. oxygen, and a heavy element i.e. molybdenum, from which the *M* cross-section is to be determined. This is because the *K* edge cross-section can be sufficiently calculated with the hydrogenic model and the unknown *M* cross-section can be measured relative to it [130]. This eliminates the requirement for thickness measurements which can skew measurements significantly [119,130]. Using this method, cross-sections from $M_{4,5}$-edges of molybdenum were accurately quantified. Using the molybdenum $M_{4,5}$-edge cross-section obtained, Hofer went on to quantify particles of molybdenum disilicide ($MoSi_2$) on holey carbon. They found the Mo/Si ratio to be accurate within 20% of the expected 33% Mo composition, using large integration windows of 100 eV. Large integration windows are thought to average out the solid state effects [130]. Lajaunie *et al.* found that the delayed maxima in $M_{4,5}$-edges contributed to errors in background subtraction and hence, cross-section accuracy. As such, based on the work done by Hofer, they have used $M_{2,3}$-edges to help distinguish between MoO_2 and MoO_3 oxides within 10% and 15% respectively, using small energy windows of 5 eV ; larger energy windows 15–20 eV brought the error down to 2% [131].

4.3 Fine Structure and Oxidation State

As earlier discussed in section 4.2, EELS experimental ionisation edges are generally quantified with atomic models, however the complete fine structure is not accurately described due to the solid state effects in the specimen. This is because the fine structure is essentially a superposition of the atomic-like edge shapes and the solid state interactions [115]. The fine structure comprises the ELNES, 30–40 eV above the edge threshold, and the EXELFS, some tens of eV beyond that [115,118]. Also previously mentioned was the ELNES giving information on local geometry while the EXELFS could be used to extract bond distances and coordination number in the surrounding regions of the atom that has undergone the ionisation.

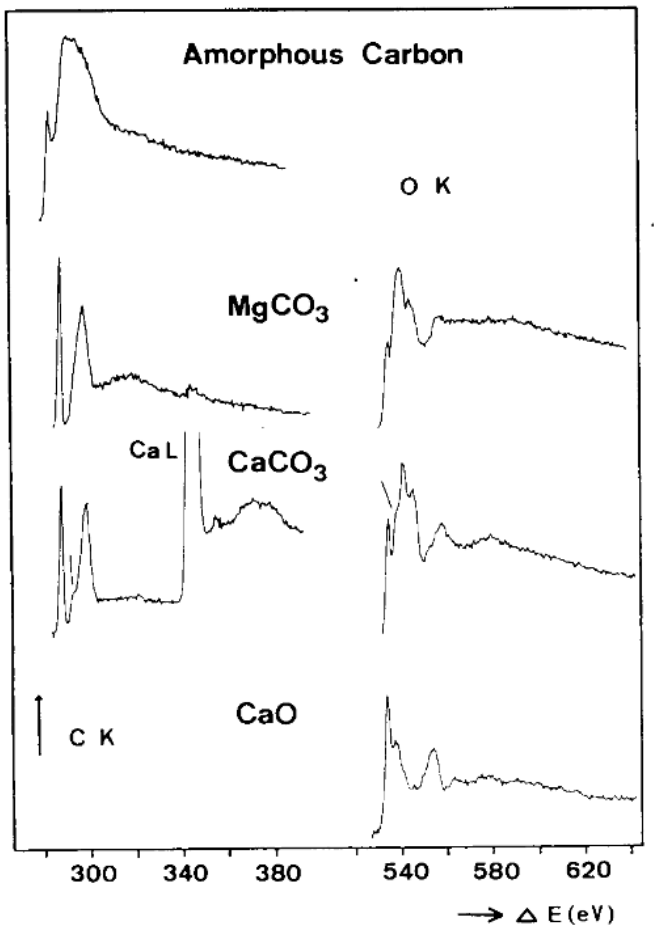


Figure 4.4. EEL spectra showing the C *K*-edges of amorphous carbon, $MgCO_3$, $CaCO_3$ and CaO, together with corresponding O *K*-edges [132].

In terms of the ELNES, the fine structure is representative of the arrangement and type of atoms within the first coordination shell. The ELNES can be thought of as arising from interference between the outgoing electron wave of the excited electron and the backscattered wave from the surrounding atoms [115]. The relatively lower kinetic energy of the electron in the ELNES region means that it samples a greater volume before energy loss, equating to a large mean free path. In contrast, the higher kinetic energy of the electron in the EXELFS region samples a smaller volume, equating to a shorter mean free path. This EXELFS structure involves the interference between the outgoing electron wave and the wave that is backscattered once from the neighbouring atomic shells [115]. For these reasons, the ELNES an EXELFS give very different information about the bonding in a specimen.

A myriad of research has gone into the procurement of fine structure information of the aforementioned sort, elucidating details more than just the chemical composition of the specimen. Hofer and Golob demonstrated that the coordination shells can be used to elucidate bonding in carbonates by comparing to the ELNES of amorphous carbon. It was shown that the σ^* transition peak of the C *K*-edge was sharper and more intense in magnesium carbonate ($MgCO_3$) and calcium carbonate ($CaCO_3$) than in amorphous carbon (Figure 4.4). The π^* peaks, although sharper, were less intense compared to that of amorphous carbon. Both peaks also had higher chemical shifts by a few eV. The chemical shift is the change in the position of a peak in the EEL spectrum, arising from a change in the electronic structure of a material. This is usually due to the changes in the relative energies of the shells closest to the Fermi level [133]. All of these features were shown to be represent the bonding of the carbon atoms to the oxygen atoms in the first coordination shell [132].

Sauer *et al.* showed that the 3D spatial arrangement could also distinguish local coordination in borate materials of different geometries. It was found that asides general shape of the ELNES, the main difference between the borate with the planar trigonal coordination of boron to oxygen atoms, vonsenite, BO_3, and the tetrahedrally coordinated rhodizite, BO_4 was the presence of the π^* peak in the former and its absence in the latter (Figure 4.5a) [134]. The experimental results were confirmed with multiple scattering (MS) theory modelling of the spectra (Figure 4.5b), using a single coordination shell of oxygen atoms [134]. In addition to the shape of the ELNES, the MS calculations also accurately predicted the chemical shift with just 0.5 eV off that from the experiment.

a

b

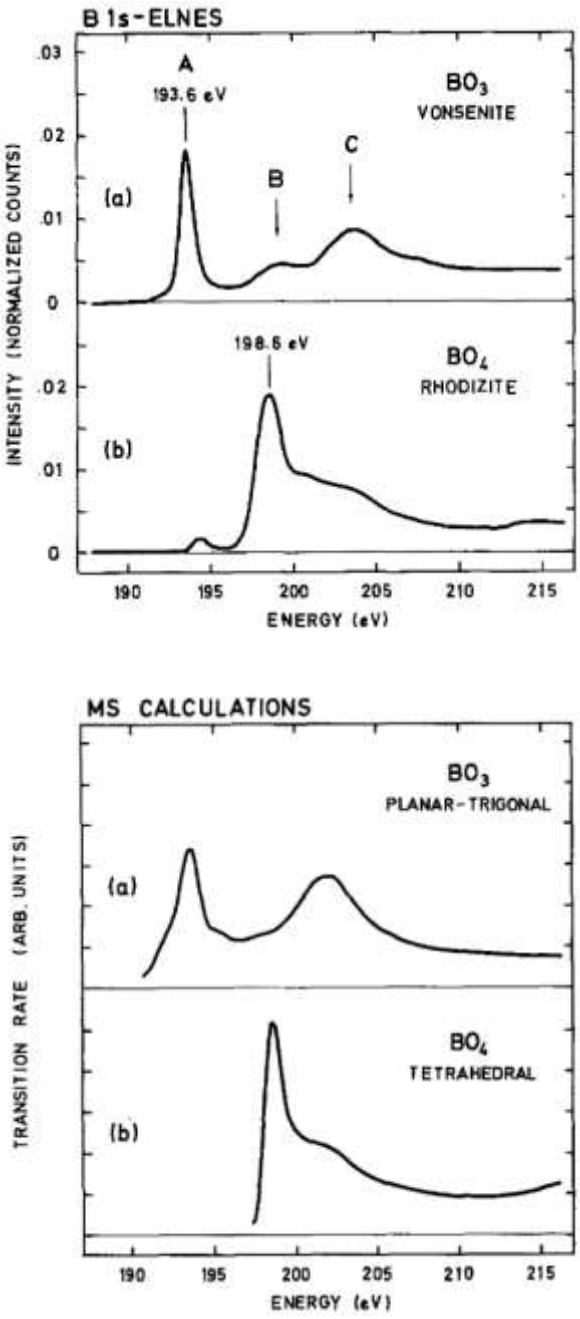


Figure 4.5. EEL spectra showing B *K*-edges of (a) vonsenite and rhodizite and (b) the corresponding MS calculated spectra [134].

The use of the first coordination shell does not always accurately describe the ELNES. Sometimes modelling of larger shell clusters is required to attain good agreement with experiment. For example, both MS and band structure calculations using seven coordination shells were needed to accurately describe the C *K*-edge of titanium carbide (TiC), evidencing

that the ELNES was dictated by medium range order between the Ti and the carbon shells [134]. While the majority of the aforementioned examples are of *K*-edges, other modelling methods for certain ionisation edges with intense features, such as white lines in $L_{2,3}$-edges exist. Such features arise from transitions to levels with a high density of unoccupied *d* or *f* final states [114] and are highly localised. The modelling generally used in these cases is AMT, which will be discussed in the following chapter.

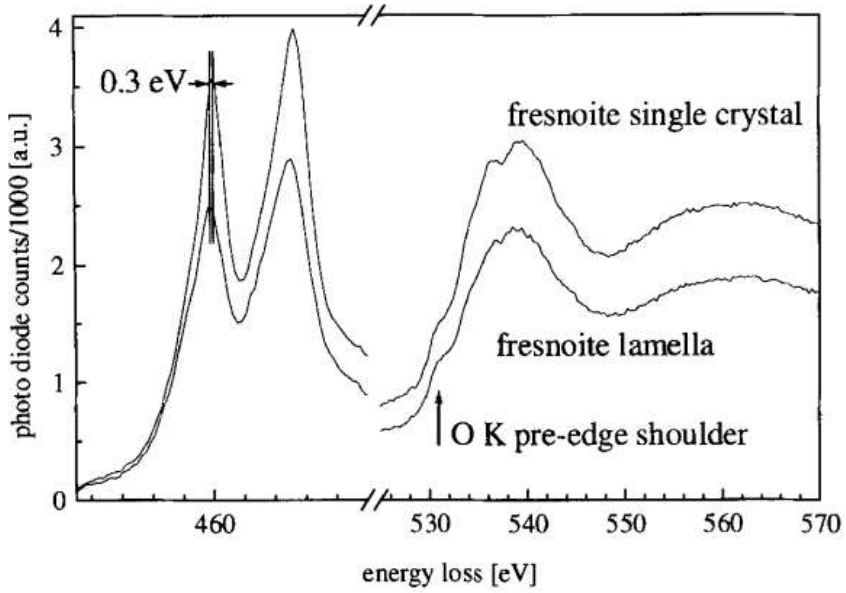


Figure 4.6. EEL spectra of Ti $L_{2,3}$-edges and O *K*-edges of a fresnoite single crystal and lamella [133].

As alluded to in section 4.1.1., changes in the charge of an atom can influence the chemical shift in the ELNES and this is usually indicative of the oxidation state of the elements in the specimen. For example, Hoche *et al.* observed that a 3.6 eV lower shift of the Ti L_3 peak of a fresnoite glass ceramic was caused by chemically induced nucleation of a lamella, introducing Ti 3+ ions into the predominantly Ti 4+ specimen (Figure 4.6) [133]. The O *K*-edge was used to confirm the proportion of Ti 3+, determined to be 10 at. %, with an approximate increase of 5% in the pre-peak intensity at the O *K*-edge threshold (Figure 4.6).

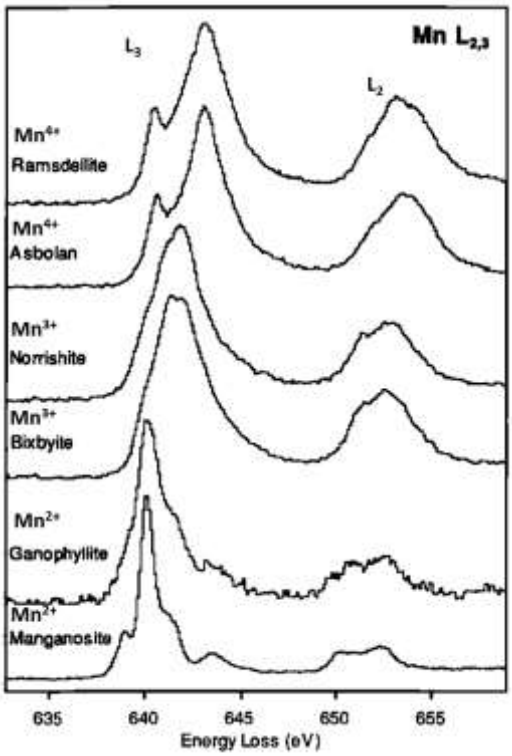


Figure 4.7. EEL spectra showing the Mn $L_{2,3}$-edges ramsdellite, asbolan, norrishite, bixbyite, ganophyllite and manganosite along with their corresponding oxidation state. *Modified from* [135]

Transition metals whereby the excited atoms have strong overlaps between excited final states and the core-hole that is left behind, can have more complicated white line features. In addition to chemical shift, they can also undergo ratio changes i.e. L_3/L_2 values in transition metals, which is related to the *d*-occupancy [114,136]. The continuum contribution to the edges are normalised and subtracted using the Hartree-Slater or hydrogenic models before quantification. The resultant L_3/L_2 values, also called white line ratios, can then be compared to standards or to literature values, thereby arriving at an oxidation state and allowing for conclusions to be made about the state of the metal. For example, comparing Mn $L_{2,3}$-edges of various manganese minerals, Garvie *et al.* showed that the detailed shape of each ELNES, together with their onsets and white line ratios, were indicative of manganese oxidation states ranging 2+ – 4+ (Figure 4.7) [135]. Similarly, Zhao *et al.* showed that the white line ratio initially increases between metallic Co (0) and CoO (2+) but decreases between CoO (2+) and Co_3O_4 (mixed valence

(2,3+)) [137]. It was also shown that the absence of an O *K*-edge (in metallic Co) can be used to identify metallic Co (Figure 4.8) if the Co $L_{2,3}$-edge is hard to distinguish. There are also characteristic peaks on the O *K*-edges of the CoO and Co_3O_4 to help distinguish between the oxides. Peak *a* arises from 1*s* transitions into the O2*p*–Co3*d* hybridised orbital while peaks *b* and *c* come from 1*s* transitions into the O2*p*–Co4*sp* hybridised orbital [137]. A gradual chemical shift is also noticeable going from the metallic Co to the Co_3O_4 oxide (Figure 4.8). A combination of these features is useful for quantifying oxidation states and estimation of the symmetry of an unknown cobalt atom.

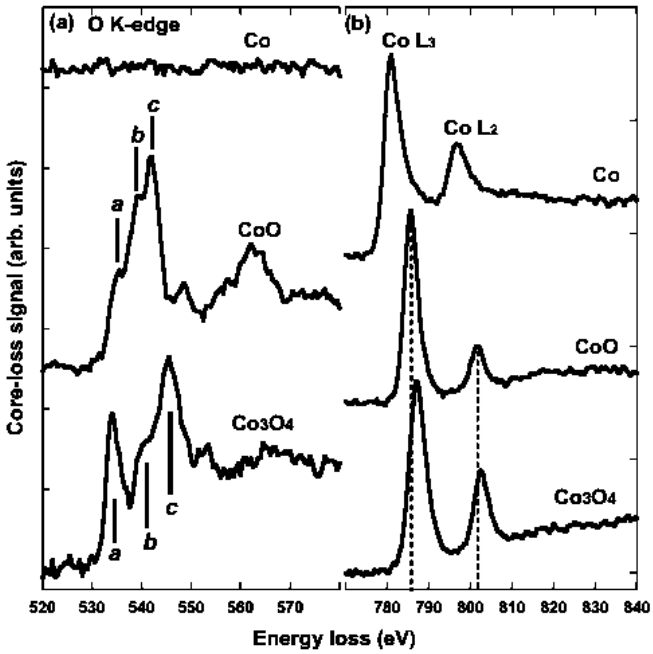


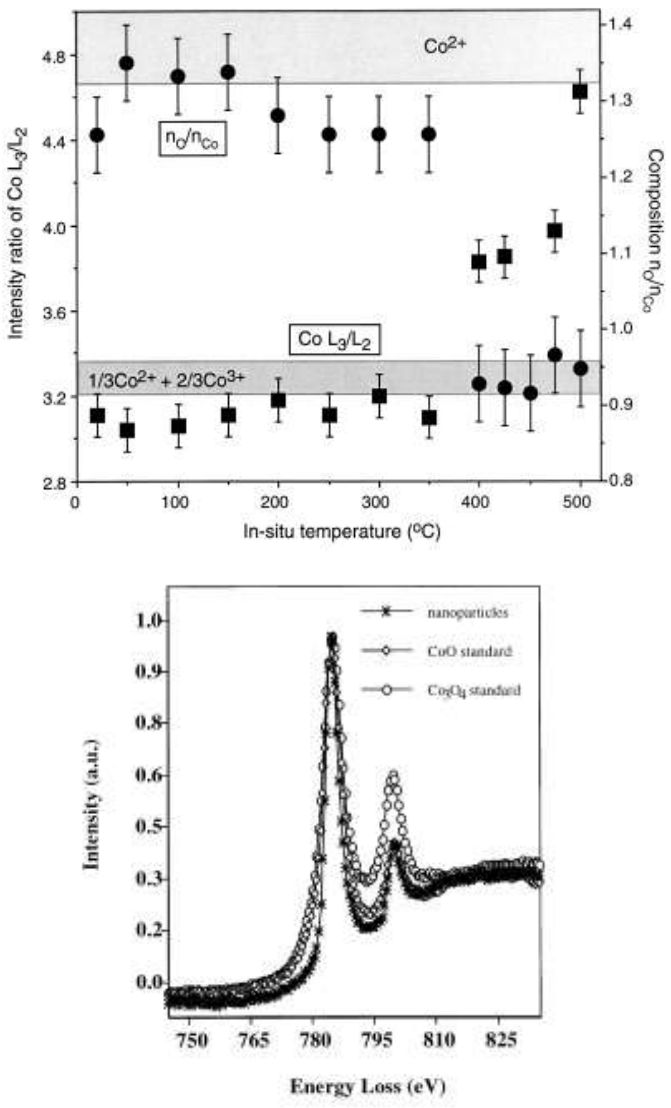
Figure 4.8. EEL spectra showing the Co $L_{2,3}$-edges and O *K*-edges of metallic Co, CoO and Co_3O_4. *Image from* [137].

The ELNES of transition metals can also be used to check for composition and commensuration with nanoparticle chemistry. Wang *et al.* was able to use cobalt edge intensities to study the composition and degree of oxidation on $CoSO_4$ (Co 2+), $CoCO_3$ (Co 2+) and Co_3O_4 (Co 2.67+) standard oxides as a function of temperature, during in situ reduction of the Co_3O_4 sample. The specimen composition, n_O/n_{Co}, was obtained by integrating the Co $L_{2,3}$-edges and corresponding O *K*-edges, using the SIGMAK and SIGMAL packages. It was

shown that above 400 ℃, the chemical composition changes from n_O/n_{Co} = 1.33±0.5 to 0.95±0.5, going from the Co 2.67+ to the co 2+ oxidation state (Figure 4.9a) [139]. This was corroborated by the increase in the white line ratios. The white line ratios are separated into two bands (Figure 4.9a), where the upper band is an average of the ratios derived from the 2+ state ($CoSO_4$ and $CoCO_3$) and the lower band represents the 2.67+ state, a mixture of 1/3 2+ and 2/3 3+ oxidation states. To highlight the match to nanoparticle chemistry, the Co $L_{2,3}$-edge intensities of a CoO nanoparticle, CoO and Co_3O_4 standards were overlaid (Figure 4.9b). It can be seen from the spectra that the nanoparticles mainly have an oxidation state of Co 2+.

a

b



Plots of (a) the variation of cobalt white line ratio and chemical composition, n_O/n_{Co}, with temperature and (b) spectra overlay of CoO nanoparticles, CoO standard and Co_3O_4 standard. *Images from* [139].

While other popular spectroscopic methods such as EDX, has been used to characterise cobalt oxides, there is little to no quantification distinguishing between the oxides. EELS is known to be better for detecting light elements where EDX falls short and as such, these types of quantification of samples that generally include a mixture of light and heavy elements is best quantified using EELS.

Table 4.1. Manganese, Iron and Cobalt ELNES $L_{2,3}$ quantification data [138,139].

	$MnCO_3$	**MnO**	**Mn_3O_4**	**Mn_2O_3**	**MnO_2**
Oxidation state	2+	2+	2+, 3+ (2.67)	3+	4+
$\Delta E(L_2-L_3)$ (eV)	11.7±0.1	11.5±0.2	11.2±0.1	10.8±0.1	10.2±0.1
L_3/L_2	4.1±0.2	3.9±0.3	2.8±0.2	2.4±0.1	2.0±0.1
	$FeTiO_3$	**FeO**	**Fe_3O_4**	**α-Fe_2O_3**	
Oxidation state	2+	2+	2+, 3+ (2.67)	3+	
$\Delta E(L_2-L_3)$ (eV)	12.8±0.1	12.8±0.1	12.9±0.1	13.0±0.1	
L_3/L_2	3.9±0.2	4.3±0.2	4.5±0.1	5.1±0.1	
	$CoCO_3$	**$CoSO_4$**	**Co_3O_4**	**$CoSi_2$**	
Oxidation state	2+	2+	2+, 3+ (2.67)	4+	
$\Delta E(L_2-L_3)$ (eV)	~15.5	~15.5	~14.5	~15.5	
L_3/L_2	5.0±0.5	4.6±0.4	3.2±0.4	2.0±0.4	

The ELNES $L_{2,3}$ data of commonly studied elements, Mn, Fe and Co are shown (Table 4.1) and the compounds of these elements were chosen because they are well known standards for the determination of the oxidation states. The Mn and Fe data were obtained from Schmid and Mader; the Co data from Zhang *et al*. The white line ratios generally increase with d-occupancy from d^0 to d^5 elements and decrease d^5 to d^{10} [141] and Mn and Fe derivatives follow this trend, however those of Co do the opposite. It is logical that white line ratios are a direct interpretation

of the oxidation state because an electron occupying a *d*-orbital reduces the number of *d*-orbitals that another electron, including its spin, can occupy. In cases where the uncertainty on the white line ratio is too high to solely determine the oxidation states i.e. $MnCO_3$, 4.1 ± 0.2; MnO, 3.9 ± 0.3 and $CoCO_3$, 5.0 ± 0.5, $CoSO_4$, 4.6 ± 0.4, the shape of the O *K*-edge is used [139,142]; when there is no distinct shape influence (for Co), standard calibrations are used [138,143].

In the Mn oxides, a clear decrease in energy difference, $\Delta E(L_2-L_3)$, which is seen with increasing oxidation state, however, it is invariant with the Fe oxides. Co valence has been very difficult to quantify and there is very limited literature on its derivatives. Nevertheless, some changes have been seen in $\Delta E(L_2-L_3)$ with oxidation states but are non-linear [143]. Additionally, peak shifts are sometimes used to aid in distinguishing between oxidation states but the spectrometer must be extremely accurate in its sensitivity to the peak positions and as such, the absolute onset energies from the resultant spectrum are not very reliable. However, what has been reliable are the trends in white line ratios comparatively across various literature with respect to the standards used but discrete L_3/L_2 values cannot always be obtained because each material is different. In cases such as this, a values would have to be extrapolated from a standard calibration curve to estimate a mixture of oxidation states in that material.

The ELNES fine structure is generally used more in research due to the vast information that can be derived from it. The EXELFS does not have as much information due to it forming the decreasing tail of the ELNES, making it harder to resolve. However, the most common deducible information from the EXELFS is bond lengths [144,145] and this is due to short-range information given by the smaller interaction volume of the incident electron. The ELNES can also be used for bond length determination, using peaks some 20–30 eV above the edge threshold, known as multiple scattering resonances (MSR) [114]. However, the EXELFS is more common due to the physics of the backscattering.

4.4 Conclusions

The mechanism of the EELS technique and basic features of an EEL spectrum have been discussed. The methods in which these features can be used to elucidate bonding characteristics as well as electronic structure has been reviewed. The development of spectrometers and the connection to energy stability have also been brought to the fore. The ELNES and EXELFS fine structure have been shown to offer significant information such as coordination, oxidation state and bond distances, which are all relevant to detailed understanding of catalyst materials susceptible to oxidation. This is important in trying to understand the chemistry of a catalyst, before and after cycling in a PEMFC. As the energy resolution and stability continually increases, EELS becomes a more prominent tool in the chemical understanding of catalyst at the sub-nanometre scale.

4.5 References

[115] Brydson R 2001 *Electron Energy Loss Spectroscopy* ed P Barlass (Oxford: BIOS Scientific)

[116] Saldin D K and Ueda Y 1992 Dipole approximation in electron-energy-loss spectroscopy: L-shell excitations *Phys. Rev. B* **46** 5100–5109.

[117] Löffler S, Ennen I, Tian F, Schattschneider P and Jaouen N 2011 Breakdown of the dipole approximation in core losses *Ultramicroscopy* **111** 1163–1167

[118] Egerton R F 1996 *R.F. Egerton. Electron Energy-Loss Spectroscopy in the Electron Microscope.* (New York: Plenum Press)

[119] Hofer F and Golob P 1988 Quantification of electron energy-loss spectra with K and L shell ionization cross-sections *Micron Microsc. Acta* **19** 73–86

[120] Egerton R F 1979 K-SHELL IONIZATION CROSS-SECTIONS FOR USE IN MICROANALYSIS *Ultramicroscopy* **4** 169–179

[121] Egerton R F 1984 *Quantitative microanalysis by electron energy-loss spectroscopy: the current status* ed O Johari (Chicago: AMF O'Hare)

[122] Rez P 1982 CROSS-SECTIONS FOR ENERGY LOSS SPECTROMETRY *Ultramicrosocopy* **9** 283–288

[123] Joy D C, Egerton R F and Mahem D M 1979 *Progress in the quantitation of electron energy-loss spectra* ed O Johari (Chicago: AMF O'Hare)

[124] Allison C, Williams W S and Hoffman M P 1984 Quantitative electron energy loss spectroscopy of vanadium carbide *Ultramicroscopy* **13** 253–263

[125] Sklad P S, Bentley J, Angelini P and Lehmann G L 1984 *Reliability of the quantification of EELS measurements* (San Francisco: San Francisco Press)

[126] Malis T and Titchmarsh J M 1985 A "k-factor" approach to EELS analysis *Inst. Phys. Conf Scm.* **78** 181–182

[127] Grande M and Ahn C C 1983 Deconvolution and quantification of energy-loss transition metal oxide spectra *Inst. Phys. Conf Scm.* **68** 123–126

[128] Ahn C C and Rez P 1985 Inner shell edge profiles in electron energy loss spectroscopy *Ultramicroscopy* **17** 105–115

[129] Leapman R D, Rez P and Mayers D F 1980 K, L, and M shell generalized oscillator strengths and ionization cross sections for fast electron collisions *J. Chem. Phys.* **72** 1232–1243

[130] F. Hofer 1987 EELS quantification of M edges by using oxidic standards *Ultramicroscopy* **21** 63–68

[131] Lajaunie L, Boucher F, Dessapt R and Moreau P 2015 Quantitative use of electron energy-loss spectroscopy Mo-M2,3 edges for the study of molybdenum oxides *Ultramicroscopy* **149** 1–8

[132] Hofer F and Golob P 1987 New examples for near-edge fine structures in electron energy loss spectroscopy *Ultramicroscopy* **21** 379–383

[133] Potapov P L and Schryvers D 2004 Measuring the absolute position of EELS ionisation edges in a TEM *Ultramicroscopy* **99** 73–85

[134] Sauer H, Brydson R, Rowley P N, Engel W and Thomas J M 1993 Determination of coordinations and coordination-specific site occupancies by electron energy-loss spectroscopy: An investigation of boron-oxygen compounds *Ultramicroscopy* **49** 198–209

[135] Höche T, Kleebe H J and Brydson R 2001 Can fresnoite (Ba2TiSi2O8) incorporate Ti3+ when crystallizing from highly reduced melts? *Philos. Mag. A Phys. Condens. Matter, Struct. Defects Mech. Prop.* **81** 825–839

[136] Scott A J, Brydson R, MacKenzie M and Craven A J 2001 Theoretical investigation of the ELNES of transition metal carbides for the extraction of structural and bonding information *Phys. Rev. B - Condens. Matter Mater. Phys.* **63** 1–12

[137] Zhao Y, Feltes T E, Regalbuto J R, Meyer R J and Klie R F 2010 In situ electron energy loss spectroscopy study of metallic Co and Co oxides *J. Appl. Phys.* **108** 1–7

[138] Garvie L A J, Craven A J and Brydson R 1994 Use of electron-energy loss near-edge fine structure in the study of minerals *Am. Mineral.* **79** 411–425

[139] Wang Z L, Yin J S and Jiang Y D 2000 EELS analysis of cation valence states and oxygen vacancies in magnetic oxides *Micron* **31** 571–580

[140] Varela M, Oxley M P, Luo W, Tao J, Watanabe M, Lupini A R, Pantelides S T and Pennycook S J 2009 Atomic-resolution imaging of oxidation states in manganites *Phys. Rev. B - Condens. Matter Mater. Phys.* **79** 11–14

[141] Schmid H K and Mader W 2006 Oxidation states of Mn and Fe in various compound oxide systems *Micron* **37** 426–432

[142] Graetz J, Ahn C C, Ouyang H, Rez P and Fultz B 2004 White lines and d-band occupancy for the 3d transition-metal oxides and lithium transition-metal oxides *Phys. Rev. B - Condens. Matter Mater. Phys.* **69** 1–6

[143] Megumi O, Kimoto K, Ebina Y and Sasaki T 2015 EELS study of Fe- or Co-doped titania nanosheets *Microscopy* **64** 77–84

[144] Cheng T, Yu H, Peng F, Wang H, Zhang B and Su D 2016 Identifying active sites of CoNC/CNT from pyrolysis of molecularly defined complexes for oxidative esterification and hydrogenation reactions *Catal. Sci. Technol.* **6** 1007–1015

[145] Bourdillon A J, El-mashri S M and Forty A J 1984 Application of TEM extended electron energy loss fine structure to the study of aluminium oxide films *Philos. Mag. A Phys. Condens. Matter, Struct. Defects Mech. Prop.* **49** 341–35260

5 Atomic Multiplet Theory

5.1 Background

Spectroscopic techniques such as EELS give detailed features in a spectrum, which are convolved by the instrumental broadening. In most transition metals, for a core-hole other than that of a 1*s* hole, there is overlap between the core-hole wavefunction and valence wavefunction and this gives rise to the fine structure [146]. A core-hole is a hole left in the core state after an electron transition into an unoccupied state. This fine structure cannot be accurately described by one-electron codes and this is where atomic multiplet theory (AMT) comes into play. AMT was originally conceived for the calculation of transition metal XAS spectra, however, due to the similar physics with EELS, it works well for the description of EEL spectra. In the previous chapter, it was seen that the hydrogenic and Hartree-Slater models commonly used to describe the edge shape were only relatively successful in predicting the general shape of the ELNES just past the threshold of the ionisation edge. It was highlighted that this was mainly the result of the solid state effects not being taken into account. These effects are due to the extra oscillations that arise from the different ways in which the core-hole and valence wavefunctions can overlap and are referred to as multiplet effects.

For final states with partially-filled 3*d* bands such as in cobalt spectra, the radial wavefunctions of the 2*p* and 3*d* holes are known to overlap to a large extent [146] and these effects are difficult to describe with one-electron codes. Excited 1*s* core electrons to the 2*p* unoccupied states of oxygen yields the O *K*-edge [115]. On the other hand, the Co $L_{2,3}$-edge is split into two dipole-allowed excitations; $2p_{1/2}$ core electrons to $3d_{3/2}$, yielding the L_2-edge, and $2p_{3/2}$ core electrons to both the $3d_{3/2}$ and $3d_{5/2}$ states (Figure 5.1) to give the L_3-edge [115]. While the white line ratio (L_3/L_2) gives the cobalt oxidation, the electronic structure of the edge is not as trivial to interpret. One-electron codes works well for systems such as oxygen and metal *K*-edges in

metal oxides but fail for $L_{2,3}$-edges, and other higher level transitions [146]. This is because the calculated DOS is not observed in the experimental spectrum and a major reason why DFT based codes fall short in the complete prediction of transition and rare-earth metal *L* edges [146,147]. These types of edges involve multiplet effects, derivative of the electron interactions and coupling of states earlier mentioned, generating a myriad of final states in the observed spectrum. The core-hole induced charge transfer and the exchange and multipole interactions between the core-hole and valence state are the configurations often amiss in the one-electron codes [147].

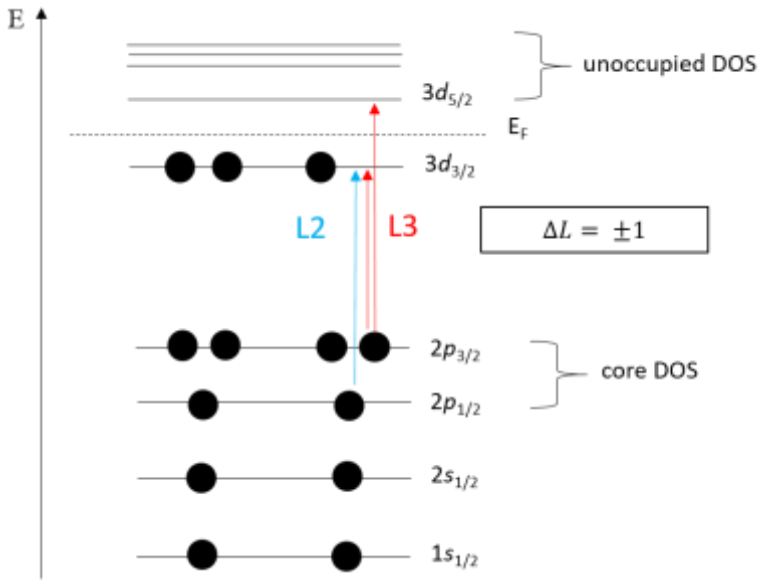


Figure 5.1. Mechanism of dipole-restricted *($\Delta L = \pm 1$)* cobalt $L_{2,3}$ excitation.

AMT calculations use an isolated atom as the starting point. The initial state configuration comprises of core and valence states. The final state configuration is the occupation of the modified core and valence states following excitation. The states in the isolated atom are degenerate but in the presence of an electric field, they split. After excitation, these states can begin to couple, giving rise to various electronic configurations. These configurations are dictated by spin-orbit coupling and Slater integrals, giving rise to multiplet effects. The Slater integrals are two-electron integrals which account the radial Coulomb repulsion between

electrons and the Coulomb exchange interaction between them [146]. The values of Slater integrals have to be of at least the same magnitude as the spin-orbit coupling for multiplet effects to be visible in the resultant spectra [146]. Crystal field effects can be added as a perturbation on the atomic result [146]. When bonding and hybridisation in the material increases, solid state effects can then be introduced as further perturbations using charge transfer parameters.

The configuration of the initial state, coupling of the final states, together with instrumentation and lifetime broadening gives rise to the full fine structure in EELS and XAS spectra. These configurations are governed by rules from what is referred to as the *Russell Saunders coupling scheme* and perturbations from crystal field and charge transfer effects in the material influence the evolution of the fine structure in the resultant spectra.

5.2 Russell Saunders and J-J Coupling Scheme

All electron states can be described by quantum numbers, *n, m, l and s*, which are the principal, magnetic, orbital angular momentum and spin quantum numbers, respectively. If the relative energies of the states can be determined, then Hund's rules can be used to derive the electronic configuration. The *Russell Saunders coupling scheme* is a rule for combining *l* and *s*, resulting in what are referred to as term symbols, which will be later expounded upon. These term symbols are used to characterise the various electronic configurations that give rise to the fine structure in EELS and XAS spectra. This coupling scheme can be used to determine the electronic configuration of the initial and final states. Starting from a free atom, the Schrodinger equation can be written as in equation 5.2 [146], where H is the Hamiltonian, p is momentum, m is electron mass, $n*$ the number of electrons, Z is the nuclear charge, e is the electron charge, r is position while i and j are indexing two different electrons. The terms in equation 5.2 are the kinetic energy, Coulomb attraction, the electron-electron repulsion and the spin-orbit coupling, respectively.

$$H = \sum_{n*} \frac{p_i^2}{2m} + \sum_{n*} \frac{-Ze^2}{r_i} + \sum_{pair} \frac{p_i^2}{r_{ij}} + \sum_{n*} \zeta(r_i) l_i \,.\, s_i \qquad 5.2$$

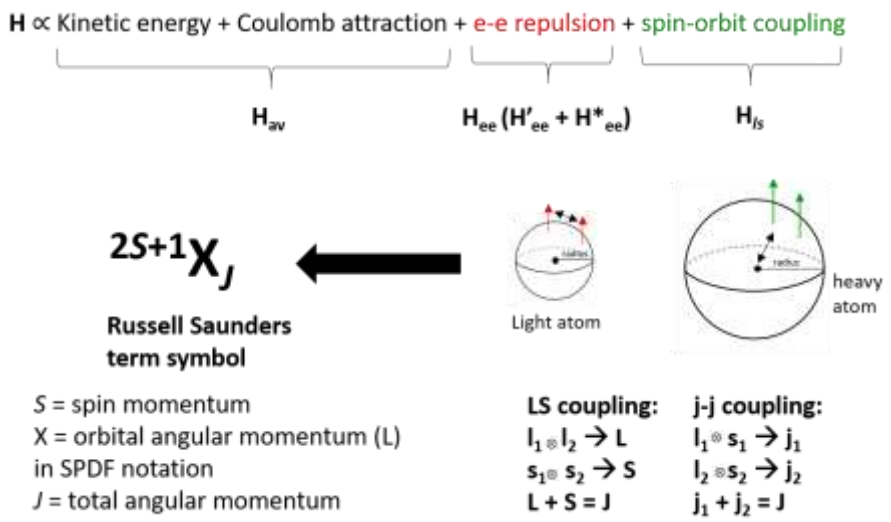


Figure 5.2. Illustration of the coupling of orbital and spin momenta to derive the Russell Saunders term symbols.

The last two terms dictate the relative energies of the initial or final state configurations and these are calculated from the Russell Saunders term symbols (Figure 5.2). Term symbols are a combination of quantum numbers which define the energy of a configuration observed in the resultant spectra. The non-spherical part of the electron-electron repulsion, H^*_{ee}, together with the spin-orbit coupling, H_{ls}, define the term symbols that contribute to the atomic spectra. The spherical part of the electron-electron repulsion, H_{ee} is added to the average Hamiltonian, H_{av} [146]. For light atoms, $H_{ee} \gg H_{ls}$ and H_{ls} can be treated as a perturbation on $H_{av} + H_{ee}$. In this case, the LS coupling scheme is used (Figure 5.2). However, for heavier or ionized elements, $H_{ee} \gg H_{ls}$ and electrons in the system become relativistic [148]. The Z and radius increase, electrons are further apart and therefore less electron interaction. More importantly, the effect of the electron-electron repulsion decreases as the spin-orbit coupling dominates. This phenomenon means that the coupling scheme will change from LS coupling to j-j coupling (Figure 5.2).

Table 5.1. The *d*-electron configurations and their corresponding orbital momentum, spin moment and ground term Russell Saunders symbols.

d^n	+2	+1	0	-1	-2	*L*	*S*	Ground symbol
d^1	↑					2	1/2	^2D
d^2	↑	↑				3	1	^3F
d^3	↑	↑	↑			3	3/2	^4F
d^4	↑	↑	↑	↑		2	2	^5D
d^5	↑	↑	↑	↑	↑	0	5/2	^6S
d^6	↑↓	↑	↑	↑	↑	2	2	^5D
d^7	↑↓	↑↓	↑	↑	↑	3	3/2	^4F
d^8	↑↓	↑↓	↑↓	↑	↑	3	1	^3F
d^9	↑↓	↑↓	↑↓	↑↓	↑	2	1/2	^2D

The term symbols are determined by total orbital momentum, *L*, and total spin momentum, *S* (Table 5.1). Summing the number of unpaired electrons, where each has a value of ½, gives *S* while *L* is arrived at by multiplying the number of electrons by the magnetic quantum number, m_l, which are the header numbers in columns (Table 5.1). A term symbol is represented as $^{2S+1}X_J$ (Figure 5.2). The term *X*, is given by the filling of electrons according to quantum number, *m*, which when added gives S, P, D, F…terms (Table 5.1). The *J* term is the total moment and is calculated as $|L-S| \leq J \leq L+S$. All term symbols are degenerate by $(2L + 1)(2S + 1)$ in the absence of spin-orbit coupling [146]. Including spin-orbit breaks the degeneracy by *J* into $2J + 1$ states [146]. In the LS coupling scheme, *L* and *S* are first coupled before being combined to give *J*. In contrast, j-j coupling involves the coupling of *l* and *s* of each electron before combining to give *j* for each electron. The individual *j* values are then combined to give *J*. An example of this calculation will be demonstrated in section 5.3.

5.3 Calculating Transition Metal Spectra

The multiplet calculations are implemented by a multiplet code, usually a version of CTM4XAS developed by de Groot. A summary of the steps in the calculation of a transition metal atomic spectrum will be demonstrated using a j-j coupling scheme since the catalysts of interest in PEMFCs are generally heavy metals.

- Trivalent Scandium (Sc^{3+}) has the $2p^6\ 3d^0$ ground state configuration for the initial state ∴ term symbol = $^1S_0$
- The calculation for the final state configuration is $2p^5\ 3d^1$ symbols are as follows:

$\boldsymbol{p^5}$			$\boldsymbol{d^1}$				
+1	0	-1	+2	+1	0	-1	-2
↑↓	↑↓	↑	↑				

- For $\boldsymbol{p^5}$, $l_1 = 2 + 0 - 1 = 1$, $2s + 1 = 2$ ∴ term = ^2P; for $\boldsymbol{d^1}$, $l_2 = 2$, $2s + 1 = 2$ ∴ term = ^2D
- The individual electron term symbols, ^2P and ^2D are further coupled:

  $l_1 = 1$, $s_1 = ½$, $l_2 = 2$, $s_2 = ½$

  $|l_1 - l_2| \leq L \leq |l_1 + l_2|$ and $|s_1 - s_2| \leq S \leq |s_1 + s_2|$ ∴ $L = 3, 2, 1$ → F, D, P and $S = 0$ or 1
- $|L - S| \leq J \leq |L + S|$ ∴ all term symbols = $^1F_3$; $^3F_{4,3,2}$; $^1D_2$; $^3D_{3,2,1}$; $^1P_1$; $^3P_{2,1,0}$
- According to the dipole selection rule, $\Delta J = +1, 0, -1$ ($\Delta J = 0$ allowed only if ground term $J \neq 0$), all term symbols will not be observed in the spectrum due to their low probability of transition
- Consequently, the allowed states are $^1P_1$, $^3P_1$ and $^3D_1$, corresponding to the three peaks observed in the spectrum (Figure 5.3)
- According to Hund's rule, the lowest energy term symbols have maximum S and only those thereof with maximum L are lowest in energy
- Hund's rule also states the lowest energy term symbol $J = |L - S|$ if the shell is half or less than half full and $J = |L + S|$ if more than half full
- Thus the relative energies in the spectrum should be $^3D_1$, $^3P_1$ and $^1P_1$, respectively
- However, the relative energies are $^3P_1$, $^3D_1$ and $^1P_1$, respectively (Figure 5.3) and this is because Hund's rule only applies for single open shells and large spin-orbit coupling can influence the order of the term symbols energies
- The relative intensities of the term symbols are given by the number of states described by that symbol

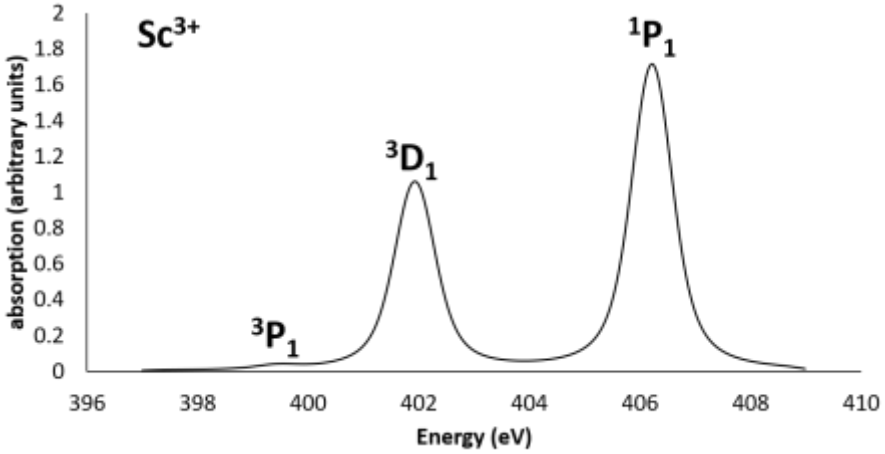


Fig. 5.3. Calculated atomic spectra of Sc^{3+} using the Charge Transfer Multiplet X-ray Absorption Spectroscopy (CTM4XAS) software by de Groot.

5.4 Determination of Oxidation State

As the oxidation state of a metal is related to its *d*-occupancy, its chemical shift and shape of the near-edge fine structure in atomic spectra can be predicted and interpreted by AMT. This has proved invaluable in the study of fuel cell catalysts. In work done by Kucheyev *et al.* on cerium oxide (ceria, CeO_2) aerogels, found that electronic properties in ceria were strongly dependent on the localisation or delocalisation 4*f* states [149]. It was found in aerogels of the same CeO_2 crystallite diameter, the aerogel with the thicker ligament, AG3, had a higher fraction of Ce^{3+} than in AG4 [149]. This can be seen from the fine structure of AG3 matching the Ce^{3+} calculated spectrum, while AG4 is a linear combination of both the Ce^{3+} and Ce^{4+} calculated spectra (Figure 5.4a). Kucheyev *et al.* also found that it was necessary to include charge transfer effects of mixed $4f^0+4f^1$ ground and $4f^1+4f^2$ final states to get a fit to experiment (Figure 5.4a and b). The notation for the charge transfer will be further explained in section 5.5. However, in order to find out the exact proportions of the Ce oxidation states, weighted average spectra from references, $CeCl_3$ and CeO_2, Ce^{3+} and Ce^{4+}, respectively, had to be used. They evidenced Ce^{3+} proportions of 95% and 40% for the $M_{4,5}$-edges (Figure 5.4a) and 90% and 50% for the $N_{4,5}$-edges (Figure 5.4b) in AG3 and AG4, respectively [149]. This was

attributed to the oxygen vacancies in the nanocrystallites present in AG3 but absent in AG4 [149]. They found that the oxygen vacancy in AG3 was accompanied by the localisation of two 4*f* electrons [149] as opposed to the forming part of the valence band in delocalisation.

a

b

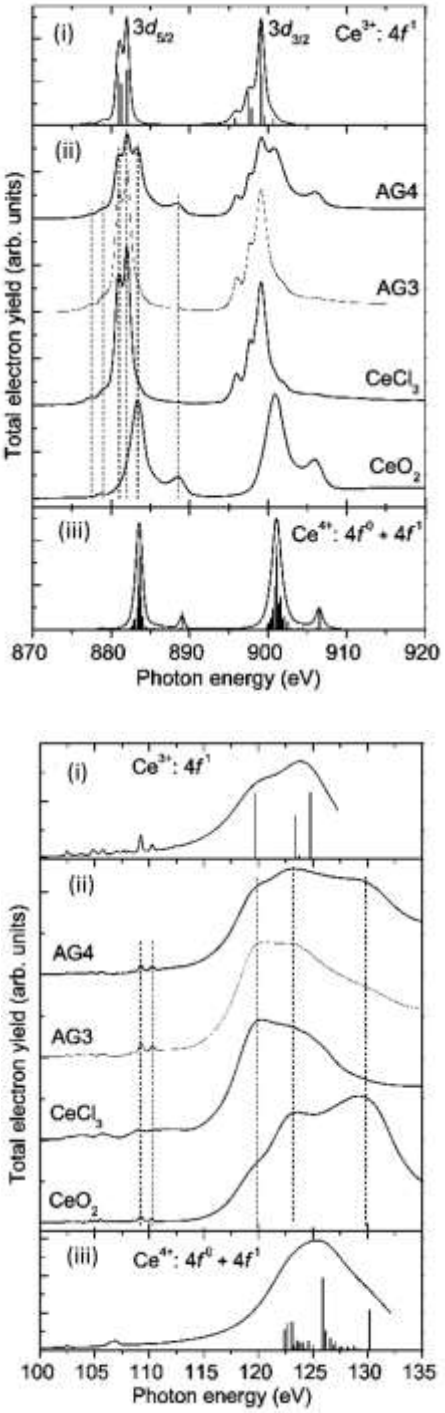


Figure 5.4. XANES spectra of (a) $M_{4,5}$-edges and (b) $N_{4,5}$-edges of AG3, AG4, reference compounds $CeCl_3$ and CeO_2, and their corresponding calculated spectra of Ce^{3+} and $Ce4^{+}$, using the Cowan multiplets code by de Groot [149].

Due to the mixture of oxidation states of the ceria aerogels, Kucheyev could not distinguish specific chemical shifts between AG3 and AG4. Using X-ray spectroscopy, Peng *et al.* have been able to distinguish between Mn^{2+}, M^{3+} and Mn^{4+} compounds. Relative to the energy of the Mn^{2+} Kβ peak, A 0.7 eV lower shift was found for Mn^{3+} while a 1.2 eV shift was found for Mn^{4+} according to multiplet calculations [150]. The Mn^{2+} also exhibited a pre-peak and pre-edge shoulder, which were less intense in the M^{3+} and Mn^{4+} spectra. This was attributed to the ^{5}P term symbol and thought to be the coupling of a spin-down from the core hole electron to four spin-up and one spin-down 3*d* electrons in the final state [150].

The relation of term symbols to the fine structure has also be delved into by other researchers such as Westre *et al.* in proving the ferric oxidation state in the iron complex, Bleomycin [151]. There is increasing use of AMT to interpret oxidation states, however, there are still some drawbacks with broadening from experiment, which make it hard to match every transition related to specific term symbols and their energies in calculated spectra. The assumption of pure state oxidation states in the reference compounds used in experiment is also a challenge in attaining congruence with calculations.

5.5 Determination of Crystal Field and Charge Transfer Effects

Crystal field and charge transfer effects are perturbations on the atomic result that yield extra term symbols and consequently, more peaks in atomic spectra such as EELS and XAS. The inclusion of the crystal field is by group theory and is based on a model of the transition metal surrounded by point charges, which represent ligands [146]. The crystal field model attempts to explain the breaking of orbital degeneracy in transition metal-ligand compounds. The nature of the ligand is important to the strength of the metal-ligand bond as this alters the energies of the relative orbitals and hence, chemical properties [152,153]. The crystal field is the energy difference resulting from the splitting of the *d*-orbitals into, for example, t_{2g} and e_g states in

octahedral symmetry, O_h (Figure 5.5a). This is mainly used to account for the symmetry of the chemical compound in which the metal resides. Charge transfer effects are included using the Anderson impurity model [146].

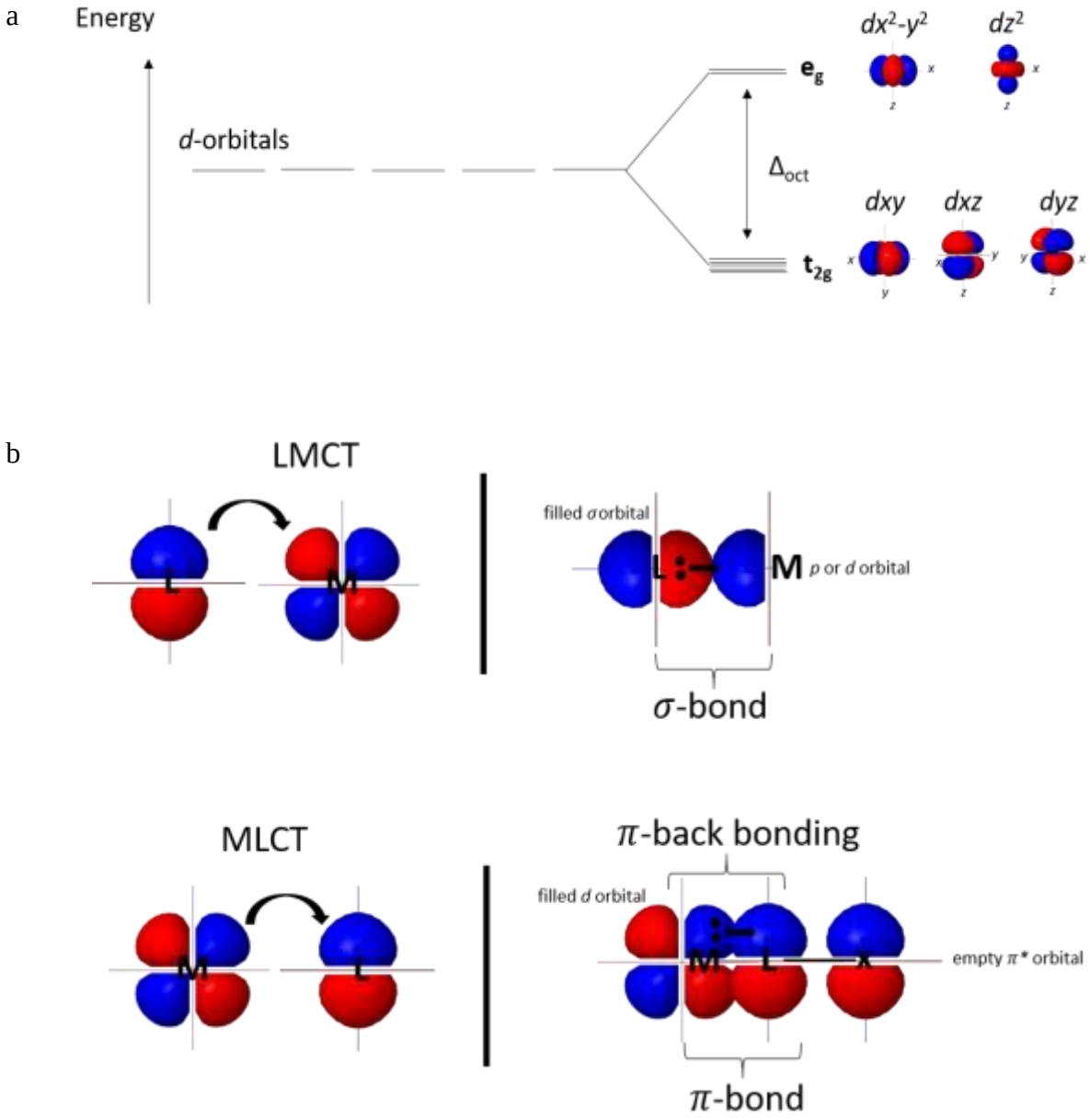
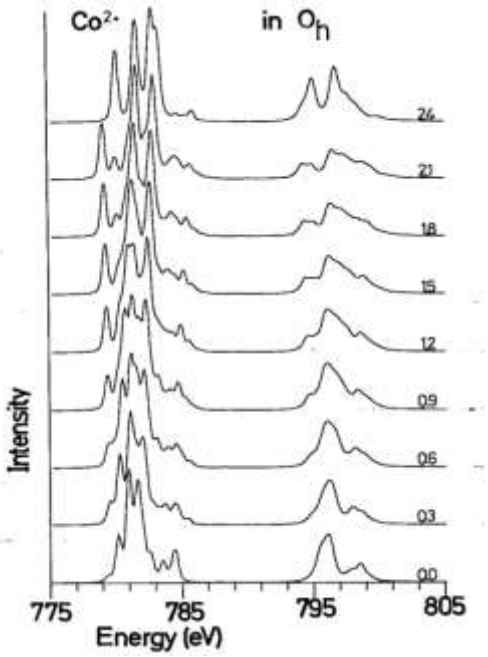


Figure 5.5. Illustration of crystal field orbital splitting in (a) O_h symmetry and (b) movement of charge in LMCT and MLCT.

The detailed theory and calculations related to crystal field and charge transfer effects can be found in work by de Groot, Kotani and Sawatzky to name a few [146,154,155]. While the crystal field uses a one electron configuration i.e. $3d^N$ to describe the ground or final states in a spectrum, the charge transfer is an added configuration and notated as $3d^N + 3d^{N+1}L$, assuming ligand-to-metal charge transfer (LMCT). The reverse would be $3d^N + 3d^{N-1}L$, denoting metal-to-ligand charge transfer (MLCT) [146,156]. LMCT usually occurs by the ligand donating its electron pair (Figure 5.5b) to the metal via σ-bonding [152,153]. Contrastingly, MLCT involves π-back bonding [152,153], where the metal donates electrons to the ligand, aided by an empty π^* orbital, *X*, on the ligand (Figure 5.5b). The *L* denotes electron or charge transfer with a hole left on the ligand [146]. Both the crystal field and charge transfer effects are brought together to give a final state spectrum.

In AMT calculations, the strength of the crystal field is controlled by a tuneable parameter in the multiplet code as shown for Co 2+ and Co 3+ by de Groot *et al*. (Figure 5.6). It was found that by varying the cubic crystal field energy, Co 2+ at 1.5 eV matched the experimental spectrum of the CoF_2 reference [157]. Recent studies using the same multiplet code report insights into the crystal field and charge transfer in nanoparticles. For example, Cui *et al.* discovered that for Co 2+ in O_h symmetry, the crystal field values increased from 0.6 eV to 0.9 eV as the sizes of cobalt nanoparticles decreased from 10 nm to 4 nm [158]. Furthermore, the suppression of MLCT peaks arising from the O2*p*–Co4*sp* hybridised orbital, where found when the surfaces of the smaller particles became oxidised [158]. The reduction in the larger nanoparticles were thought to indicate weaker Co-O, thereby making them more resistance to surface oxidation [158]. This study was a demonstration of the size dependence of cobalt nanoparticle for catalytic activity.

a



b

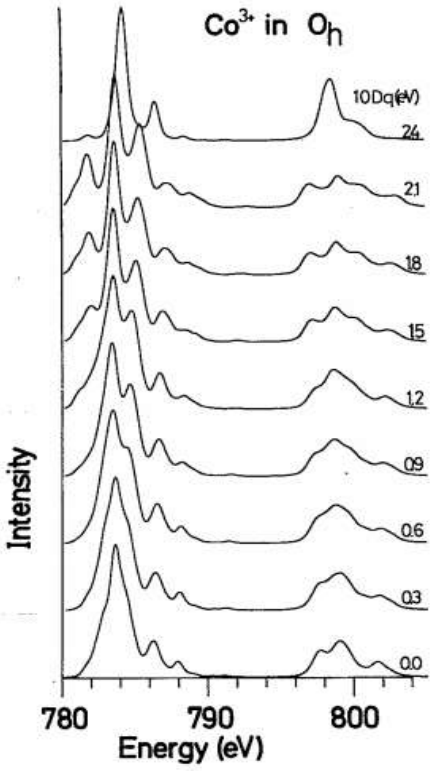


Figure 5.6. Calculated atomic spectra of (a) Co 2+ and (b) Co 3+ in O_h symmetry showing variation of cubic crystal field values from 0.1 eV to 2.4 eV [157].

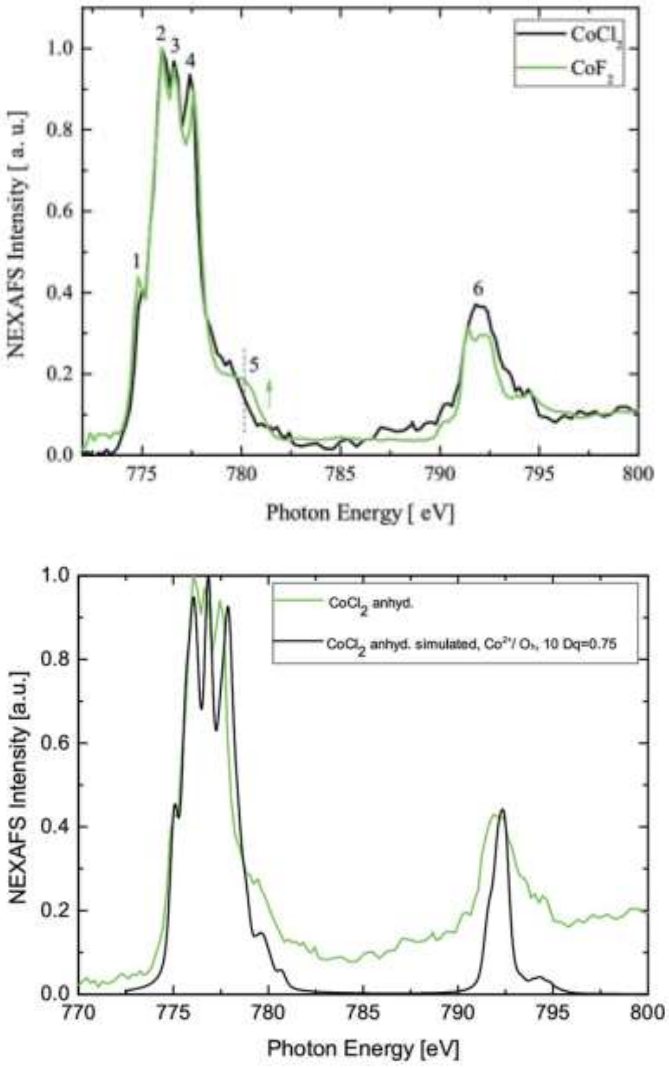


Figure 5.7. Spectra showing (a) comparison of the Co $L_{2,3}$-edges XAS of $CoCl_2$ and CoF_2 nanoparticles from experiment and (b) comparison of the CoF_2 to calculation in O_h symmetry with crystal field values of 0.75 eV [160].

The dependence of metal-O distance on the crystal field in catalyst nanoparticles has also been found by Zhong *et al.* It was found that an increase in the crystal field value from 0.7 eV to 1.0 eV correlated to a shorter V-O bond in cobalt vanium oxide ($CoVO_x$) nanoparticles [159]. This shorter V-O bond was related to longer or weaker Co-O bonds, which less oxidised and more stable Co atoms in these nanoparticles. The charge transfer was also seen to decrease from 2.2 eV to 0.5 eV [159], which means that the O2*p*–V2*sp* orbital overlap was stronger, meaning that the electrons are more localised on the Co atoms, since both metals are assumed to share oxygen atoms. Bora *et al.* showed that while charge transfer peaks are subtle when comparing

to experimental XAS spectra [160], they can show differentiate electron dynamics between similar cobalt nanoparticles. This was shown in the study of spectra from $CoCl_2$ and CoF_2 nanoparticles (Figure 5.7a and b). The transitions are labelled peaks 1–6. Peak 5 at ~780 eV was found to have a higher intensity in CoF_2 than in $CoCl_2$ (Figure 5.7a). The multiplet calculation of $CoCl_2$ was used to confirm the absence of the charge transfer feature in the $CoCl_2$ spectrum (Figure 5.7b). The higher charge transfer intensity was attributed to the higher electronegativity of the F^- anion compared to the Cl^- anion. This is logical because a fluorine atom is more electronegative than that of a chlorine and as such, more electrons from the cobalt metal would be drawn in the CoF_2 nanoparticles, inducing more charge transfer than in the $CoCl_2$ nanoparticles.

5.6 Conclusions

The use of AMT for theoretical calculations and analysis of transition metal atomic spectra has been briefly reviewed. The solid state and multiplet effects that could not be described with hydrogenic and Hartree Slater models can be accurately modelled by considering the effects of spin-orbit coupling, crystal field and charge transfer. The examples reviewed have majorly been of transition metals in coordination compounds. The hybridisation effects between the metals and the ligands have been briefly highlighted, specifically with the influence of the crystal field and charge transfer on the multiplets observed in the resultant spectrum. The examples given are predominantly of metal oxides or the like, and such complexes are dominated by σ-bonding – LMCT. However, other complicated influences such as π-bonding i.e. MLCT and back bonding could improve the reproducibility and analysis of the fine structure in atomic spectra.

5.7 References

[146] De Groot F 2005 Multiplet effects in X-ray spectroscopy *Coord. Chem. Rev.* **249** 31–63

[147] Stavitski E and de Groot F M F 2010 The CTM4XAS program for EELS and XAS spectral shape analysis of transition metal L edges *Micron* **41** 687– 694

[148] Rakowitz F and Marian C M 1996 The fine-structure splitting of the thallium atomic ground state: LS- versus jj-coupling *Chem. Phys. Lett.* **257** 105–110

[149] Kucheyev S O, Clapsaddle B J, Wang Y M, Van Buuren T and Hamza A V. 2007 Electronic structure of nanoporous ceria from X-ray absorption spectroscopy and atomic multiplet calculations *Phys. Rev. B - Condens. Matter Mater. Phys.* **76** 1–5

[150] Peng G, Wang X, Crush M M, Cramer S P, de Groot F M F, Hämäläinen K, Moore J A, Hastings J B, Siddons D P, Armstrong W H and Mullins O C 1994 High-resolution manganese X-ray fluorescence spectroscopy. Oxidation-state and spin-state sensitivity *J. Am. Chem. Soc.* **116** 2914–2920

[151] Westre T E, Loeb K E, Zaleski J M, Solomon E I, Hodgson K O, Hedman B and Hodgson K O 1995 Determination of the Geometric and Electronic Structure of Activated Bleomycin Using X-ray Absorption Spectroscopy *J. Am. Chem. Soc.* **117** 1309–1313

[152] Atkins P J and Shriver D F 2001 *Inorganic Chemistry* (New York: W H Freeman & Co)

[153] Tarr D A and Miessler G L 1991 *Inorganic Chemistry* (New Jersey: Prentice Hall)

[154] Jo T and Kotani A 1988 Narrowing Due to Valence Mixing in the 3d Core Level Spectra for Ce Compounds *J. Phys. Soc. Jpn.* **57** 2288–2292

[155] Sawatzky G A and Allen J W 1984 Magnitude and origin of the band gap in NiO *Phys. Rev. Lett.* **53** 2339–2342

[156] Ikeno H, de Groot F M F, Stavitski E and Tanaka I 2009 Multiplet calculations of L2,3 X-ray absorption near-edge structures for 3d transition-metal compounds *J. Phys. Condens. Matter* **21** 1–15

[157] De Groot F M F, Fuggle J C, Thole B T and Sawatzky G A 1990 2p X-ray absorption of 3d transition-metal compounds: An atomic multiplet description including the crystal field *Phys. Rev. B* **42** 5459–5468

[158] Cui Z, Xie C, Feng X, Becknell N, Yang P, Lu Y, Zhai X, Liu X, Yang W, Chuang Y and Guo J 2017 Revealing the Size-Dependent d−d Excitations of Cobalt Nanoparticles Using Soft X-ray Spectroscopy *J. Phys. Chem. Lett.* **8**, 319−325

[159] Zhong L, Kropp T, Baaziz W, Ersen O, Teschner D, Schlögl R, Mavrikakis M, and Zafeiratos S 2021 Improving the Catalytic Performance of Cobalt for CO Preferential Oxidation by Stabilizing the Active Phase through Vanadium Promotion *ACS Catal.* **11**, 5369−5385

[160] Bora D K, Cheng X, Kapilashrami M, Glans P A, Luob Y and Guo J H 2015 Influence of crystal structure, ligand environment and morphology on Co L-edge XAS spectral characteristics in cobalt compounds *J. Synchrotron Rad. (2015).* **22**, 1450–

1458

6 Density Functional Theory

6.1 Methods for Energy Calculations

6.1.1 Background

The fusion of experimental and modelling techniques is increasingly used for understanding chemical systems such as catalyst nanoparticles at the molecular level. Computer simulations are most widely used and the calculations for such chemical systems are generally approached in two ways – using interatomic potentials or employing quantum mechanical methods. Interatomic potentials are used to describe the potential energy of the system at various nuclear positions [161,162] and as such, they are very fast, considering that they do not take into account electron dynamics. Interatomic potentials are mostly used on large systems and out of a variety of software, GULP is most prominent for the calculations [161]. In contrast, quantum mechanical methods tries to solve the Schrodinger equation from first principles (*ab initio*) [163], meaning that different electronic interactions are explicitly focused on; the CASTEP software is one commonly used. This however requires a lot more computational effort and thus, only small systems, typically a few hundred atoms, are studied.

In order to interpret the experimental O *K*-edge spectra, a simulation of oxygen atoms in various environments of the metals is required. The calculated spectra can then be compared to experiment to determine the likely bonding environment of oxygen in the alloys. There are a few ways to simulate the experimental spectrum. A popular method is to use Green's function from multiple scattering theory. However, this method is not always accurate for the determination of bonding and so does not get the fine structure correct. This is because there are no forces, stresses or total energy calculations involved as all the parameters used are derived experimentally [164,165,166]. This means no geometry optimisations can be run to find an energy minimum. The self-consistent calculations also take longer.

An alternative method for spectral simulation, and one used in this work, calculates the spectrum from single-particle eigenenergies and dipole matrix elements as described by equations in section 4.1.1, chapter 4. However, there is a slight difference in that these calculations do not take into account the solid angle, Ω, and the relativistic factor, γ. The spectrum is calculated from the complex dielectric function $\varepsilon_1+i\varepsilon_2$, where the calculation is reduced to the imaginary part as shown in 6.1.1:

$$\varepsilon_2(\omega) = \pi e^2/\varepsilon_0 \Omega q^2 \, |<\psi^c_k| \, e^{-iq.r} \, |\psi^v_{k+q}|^2 \qquad 6.1.1$$

where Ω is the volume of the unit cell, ψ^c denotes the core wavefunction and v is that valence state [167]. The matrix elements and eigenenergies are derived from the CASTEP software and these are integrated and broadened to yield a continuous spectrum.

6.1.2 The Quantum Mechanical Method

Quantum mechanics models small scale systems by relating the wavefunction of a system to the total energy of the system via the Schrodinger equation, 6.1.3.1:

$$H\Psi = E\Psi \qquad 6.1.3.1$$

where H is the Hamiltonian that operates on the wavefunction, Ψ to yield energy, E. The Hamiltonian is composed of interactions of electrons, nuclei and combinations of the two as in equation 6.1.3.2:

$$H = \tfrac{1}{2}\sum_{i}^{electron} \frac{\nabla_i^2}{1} - \tfrac{1}{2}\sum_{A}^{nuclei} \frac{\nabla_i^2}{M_A} - \sum_{i}^{electrons} \sum_{A}^{nuclei} \frac{Z_A}{r_{iA}} + \tfrac{1}{2}\sum_{j\neq i}^{electrons} \frac{1}{r_{ij}} + \tfrac{1}{2}\sum_{A\neq B}^{nuclei} \frac{Z_A Z_B}{r_{AB}} \qquad 6.1.3.2$$

where ∇^2 is the Laplacian, M is mass of nucleus and Z, [163,168]. The number of points that would need to be to be computed for each atom is N^D where N is the number of atoms and D is the degrees of freedom i.e. 3 atoms in 3D space would need 10^9 points. There are no computers that powerful and so Kohn and Hohenberg introduced DFT, which used the particle

density, ρ at each point in space, r_1, r_2… as in equation 6.1.3.3 and 6.1.3.4, to calculate the probability of finding the particle:

$$\rho(r_1) = \sum_{i=1}^{n} \phi_i(r_1)\, \phi i^*(r_2) \qquad 6.1.3.3$$

$$\rho(r_1, r_2) = \tfrac{1}{2} \sum_{i=1}^{n} \sum_{i=1}^{n} [\phi_i(r_1)\, \phi_i^*(r_1)\, \phi_j(r_2)\, \phi_j^*(r_2) - \phi_i(r_1)\, \phi_i^*(r_2)\, \phi_j(r_2)\, \phi_j^*(r_1)] \qquad 6.1.3.4$$

where $\rho(r_1)$ and $\rho(r_2)$ are first and second order density matrices while $\rho(r_1, r_2)$ accounts for electron exchange correlation, evident from its expression in an antisymmetrised Slater determinant expressed in equation 6.1.3.4 [169]. The total electronic energy is then given by:

$$E^{elec} = \int H^N(r_1)\rho(r_1)dr_1 + \tfrac{1}{2} \iint \rho(r_1)\, 1/|r_{12}|\rho(r_1)\, dr_1 dr_2 + \tfrac{1}{2} \iint \rho(r_1)\, 1/|r_{12}|\rho^*(r_1, r_2) dr_1 dr_2 \qquad 6.1.3.5$$

Kohn and Sham went on to propose mono-electronic orbitals [170] whereby electrons cannot interact with each other, meaning that if the density of function of one electron is known at a point, it is not needed to calculate the others as it should be reproducible everywhere else – this significantly lowers computational time. Kohn and Sham introduced local effective potentials, V^{eff}, expressed in equation 6.1.3.6 and 6.1.3.7. Each non-interacting electron feels;

$$[-\tfrac{1}{2} \nabla_i^2 + V^{eff}[r]]\phi_i = \varepsilon_i \phi_i \qquad 6.1.3.6$$

$$V^{eff}[r, \rho] = V(r) + \int \rho(r')/r\text{-}r'dr + V^{XC} = V(r) + \int \rho(r')/r\text{-}r'dr + \partial E^{XC}[\rho]/\partial \rho(r) \qquad 6.1.3.7$$

where V^{XC} is the exchange-correlation potential for energy E^{XC} [170].

The calculations for these orbitals are built from basis sets. For metals and their oxides, valence electrons are modelled as free electrons. However, the core electrons behave rapidly due to their close proximity to the nucleus and hence, their wavefunctions are generally approximated by pseudopotentials. This is justified as the valence electrons are the ones involved in chemical bonding and this is generally the area of interest with catalyst materials. The wavefunctions are represented as discretely chosen plane wave basis sets in order to lower the computational cost.

Since the core is approximated by a pseudopotential, the coefficients of smaller kinetic energies become more important than larger ones and thus, a cut-off energy can be chosen for computational efficiency.

6.2 The Self-Consistent Field and Energy Minimisation

The SCF was proposed by Hartree in order to find solutions to the Hartree Product wavefunction via iteration over wavefunctions until convergence is achieved [171]. Fock developed the determinants so that the calculations followed the Pauli Principle [172] and thus, the Hartree-Fock theory was constructed. However, the Hartree-Fock theory is based on solving 3*N* variables for *n* number of electrons in a system [171]. Kohn and Sham therefore proposed that the total energy of a system can be described by ρ [170]. Since ρ is proportional to V^{eff}, which can be approximated using a functional, a series of single-particle equations, termed the Kohn-Sham equations, are then looped over in a SCF cycle to find the ground state energy of the system. Solving the Kohn-Sham equations in CASTEP searches for variational minimum energies for the subject system. The SCF approach is one whereby an initial guess is made, generating a new set of orbitals which is then used in the next iteration. This is repeated until the ground-state (least minimum energy variation) is attained. The way this is done is by approximating V^{XC} via functionals.

6.3 Functionals

Kohn and Sham introduced two main functionals to approximate the exchange correlation: Local Density Approximation (LDA) and Generalised Gradient Density (GGA). LDA assumes each point or electron in space has a homogenous electron gas (HEG) around it so that $V^{XC} \propto A[\rho(r)]^{\mu}$, where A and μ are HEG parameters that model the charge density [173]. Thus, the total exchange-correlation energy integrated over all space is given in equation 6.3.1 as:

$$E_{XC}^{LDA}[\rho] = \int \rho(r) \varepsilon_{XC}^{HEG}[\rho(r)] dr \qquad 6.3.1$$

where $\varepsilon_{XC}^{HEG}[\rho(r)]$ is the exchange-correlation energy per electron [173]. In contrast, the GGA considers that the electron density is a gradient that changes locally and is given by equation 6.3.2;

$$E_{XC}^{GGA}[\rho] = \int \rho(r)\varepsilon_{XC}^{GGA}[\rho(r), \nabla\rho(r)]dr \qquad 6.3.2$$

where $\varepsilon_{XC}^{HEG}[\rho(r)]$ is replaced with $\varepsilon_{XC}^{GGA}[\rho(r), \nabla\rho(r)]$ to represent the varying local electron density [173].

LDA overestimates binding energies and underestimates lattice parameters [173]. GGA is sometimes more accurate than LDA with improved transition state barriers, however, underestimates bond dissociation energies [173]. Hybrid functionals, based on LDA and GGA, have been introduced for improvement. For example, B3LYP by Becke is successful for organic systems [174], while PW91, developed by Perdew and Wang has gained for modelling surface and adsorbates really well [175].

6.4 Models

Using a slab model (Figure 6.1a) to study the surface interaction of oxygen in Pt(111), Feibelman *et al.* and Jacob *et al.* found fcc sites as most stable for O adsorption and Pt-O bonds of 2.00 Å and 2.01 Å respectively [176,177]. However, their bond energies differed by 50%. This is expected because LDA has been widely proven to be good for predicting geometries but overestimates binding energies and lattice parameters. Furthermore, when they compared their value to Eichler *et al.* using the PW91 GGA functional, they found a value of 3.28 eV, 0–0.25 of a monolayer Figure 6.1b.), only <5% discrepancy between their bond energies [176,177]. Again, this is expected as GGA is thought to be better at estimating binding energies and transition state barriers but found to underestimate bond dissociation energies. However, if a catalyst is highly dispersed and or prone to segregate and form clusters, they no longer have high the ordering in all the 3D directions, therefore a cluster model would be best to model the

surface adsorption interactions. Using this model via the B3LYP functional, Jacob *et al.* showed that $Pt_{9.10.9}$ was the cluster that best modelled al four binding sites (Figure 6.1c and d) [176].

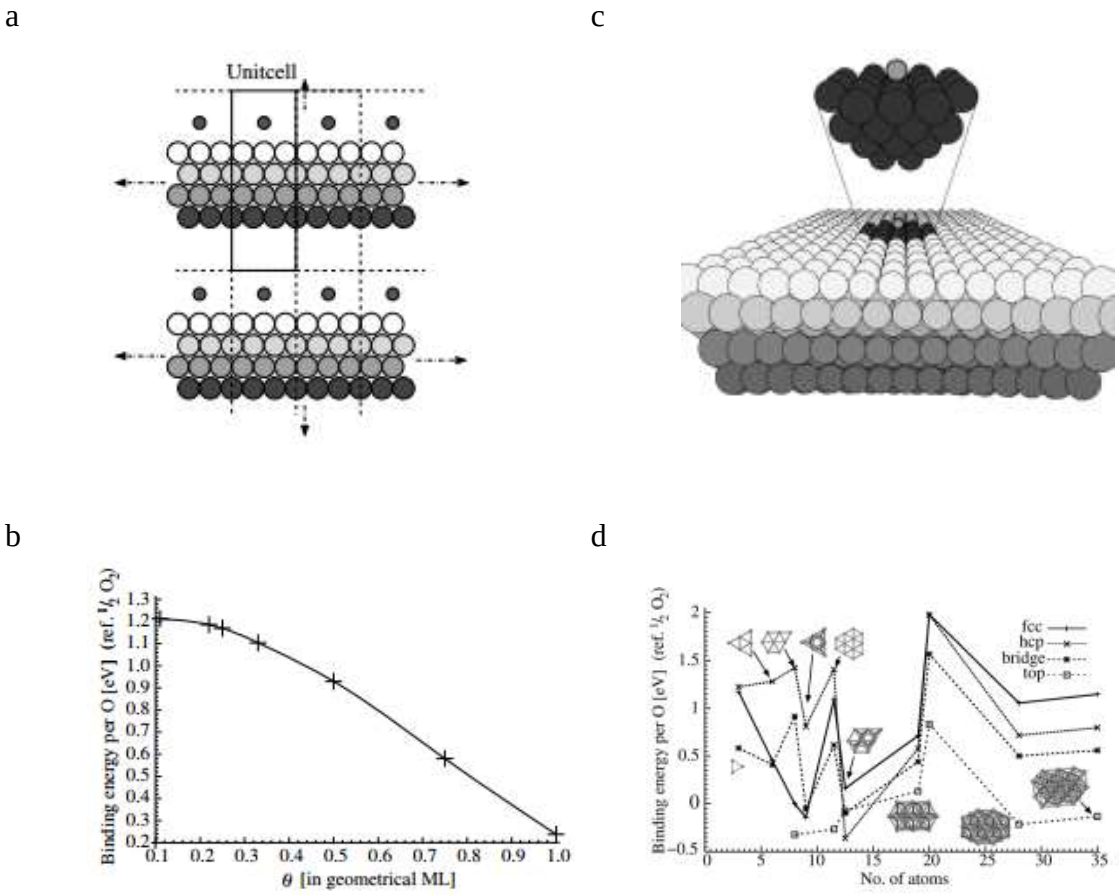


Figure 6.1. Images of (a) periodic 2D slab to model surface adsorbate (O) interaction with the adsorbent (Pt(111)); (b) binding energy varying with surface monolayer coverage; (c) a cluster model and (d) cluster models of Pt_3, Pt_6, Pt_8, Pt_{12}, $Pt_{6.3}$, $Pt_{12.8}$, $Pt_{5.10.5}$, $Pt_{9.10.9}$, $Pt_{14.13}$ at fcc, hcp (hexagonal close packed), bridge and top sites. The subscripts mean atoms per layer i.e. $Pt_{6.3}$ is 6 atoms in first layer and 3 atoms in the second layer [176].

The use of hybrid functionals has proved useful in identifying magnetic properties of a material such the switching of spin-states [178–180]. Hu and Metiu showed that Ti_2O_3 was no longer a metal by introducing a correction term (U) > 2 eV [179]. They also found that when U = 2c3 eV, their energies for the oxidation of Ti_2O_3 with oxygen were congruent with other research.

When U ≥ 2 eV, they found the lowest energy spin-state was when the spins on atom I, II, III, IV were + (spin up), - (spin down), - and + respectively (Figure 6.2).

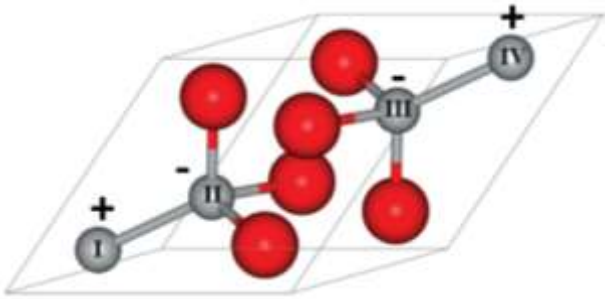


Figure 6.2. Unit cell of Ti_2O_3 showing the different spins on the oxygen atoms. *Red spheres are oxygen, grey spheres are titanium;* + = spin up, - = spin down. *Image modified from* [179].

Saqlain *et al.* also used electronic structure calculations to show that the bonding between the adsorbed O atoms and a Au/TiO_2 surface were dominated by the *p-d* hybridization of the O and Au orbitals [180]. They also found that the most favourable adsorption were two O atoms on the periphery of the Au/TiO_2 interface (Figure 6.3), with each O atom withdrawing a charge of 0.46 *e* away from the Au atom [180].

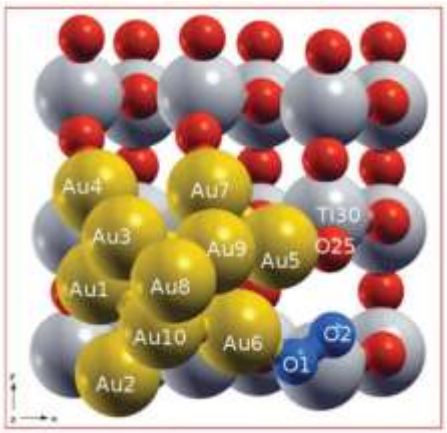


Fig. 6.3. Unit cell showing O-Au/TiO_2 crystal structure. *Red spheres are oxygen, grey spheres are titanium, gold spheres are gold; blue sphere show the peripheral adsorption of oxygen on the Au/TiO_2 surface* [180].

Specific centres of coordinated oxygen and metal in a crystal can also be modelled and their resultant spectra can elucidate active sites of oxidation. Using cluster models, Kolczewski and

Hermann demonstrated this from the comparison of calculated and XAS spectra of a vanadium pentoxide surface, V_2O_5(010). Using angle-resolved X-ray polarisation, the O *K*-edge of the singly coordinated oxygen, O(1), was shown to be derivative of $2p_x$ transitions and contribute to the low energy part of the double peak between 530–534 eV (Figure 6.4) [181]. In contrast, the triply coordinate oxygen atom, O(3), were from mainly $2p_y$ transitions and contributed to the higher energy part of the double peak [181]. The doubly coordinated oxygen atom, O(2), showed no preference to a particular direction or peak (Figure 4). This type of study can be useful in in-situ or ex-situ studies of oxygen in different coordinated environments on the surface of a metal. For example, the sites with the most adsorption and conversion of oxygen in a PEMFC alloy can be isolated using these calculations.

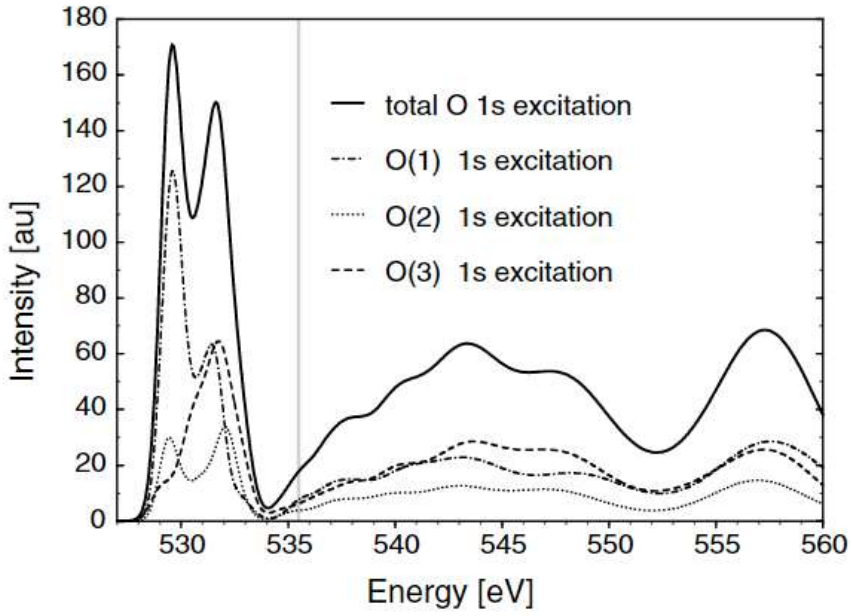


Figure 6.4. Calculated atomic spectra of $V_{10}O_{31}H_{12}$ at the oxygen centres, O(1), O(2) and O(3) [181].

The experimental *K*-edges of oxygen and most metals are often congruent with DFT, however, higher order ionisations such as *L*-edges are not accurately predicted as discussed in chapter 5. This is because DFT is a ground state code. It can only predict ground state properties but that does not mean anything in terms of the unoccupied states. In EELS and other such atomic

spectroscopy, the physics of the excitation and relaxation means that there is a core-hole potential that exists in reality after a transition that influences the initial and final state wavefunctions [182]. This perturbation is usually approximated in two ways. An electron can be removed from the core or it can be taken from the core and put in the valence band [182]. The other is the Z+1 method whereby the subject element is replaced by a heavier element [182]. This higher Z means that one can calculate the ground state energy but treat the element as a defect [182]. As neither of the two methods are dynamic calculations, they cannot completely describe the response to the potential change after a transition and as such, methods like AMT have to be invoked when interpreting spectra where this effect dominates.

6.5 Conclusions

The methods for energy calculations have been explored and their development have been briefly reviewed. The suitability of QM methods to small scale systems has been discussed. The method and equations from which the ground state energy of a system is calculated has been described and examples of work from literature have been analysed. Particularly, the comparison of calculated spectra and experimental spectra is shown to be useful in catalytic systems which have a network of oxygen-metal coordination. The examples discussed shows that DFT can be used for site-specific optimisation in the design of not just catalysts but any crystalline material.

6.6 References

[161] Gale J D 1997 GULP: A computer program for the symmetry-adapted simulation of solids *J. Chem. Soc., Faraday Trans.* **93** 629–637

[162] Jensen F 1999 *Introduction to Computational Chemistry* ed Second (Chichester: Wiley)

[163] Clark S J, Segall M D, Pickard C J, Hasnip P J, Probert M J, Refson K and Payne M C 2005 First principles methods using CASTEP *Z. Krist.* **220** 567–570

[164] Rehr J J, Kas J J, Vila F D, Prange M P and Jorissen K 2010 Parameter-free calculations of X-ray spectra with FEFF9 *Phys. Chem. Chem. Phys.* **12** 5503–5513

[165] Sorini A P, Kas J J, Rehr J J, Prange M P and Levine Z H 2006 Ab initio calculations of electron inelastic mean free paths and stopping powers *Phys. Rev. B: Condens. Matter Mater. Phys.* **74**, 1–7

[166] Moreno M S, Jorissen K and Rehr J J 2007 Practical aspects of electron energy-loss spectroscopy (EELS) calculations using FEFF8 *Micron* **38**, 1–11

[167] Morris A J, Nicholls R J, Pickard C J and Yates J R 2014 OptaDOS: A tool for obtaining density of states, core-level and optical spectra from electronic structure codes *Comput. Phys. Commun.* **185**, 1477–1485

[168] Watson G W, Tschaufeser P, Wall R A, Jackson R A and Parker S C 1997 *Computer Modelling in Inorganic Crystallography* (San Diego: Academic Press)

[169] Horenberg P and Kohn W 1964 Inhomogeneous Electron Gas *Phys. Rev.* **136** 58–64.

[170] Kohn W and Sham L J 1965 Self-Consistent Equations Including Exchange and Correlation Effects *Phys. Rev.* **140** 48–54

[171] Hartree D R 1928 The Wave Mechanics of an Atom with a Non-Coulomb Central Field Part II *Proc. Cambridge Phil. Soc.* **24** 111–132

[172] Fock V 1930 Näherungsmethode zur Lösung des quantenmechanischen Mehrkörperproblems *Zeitschrift für Phys.* **61** 126–148

[173] Segall M D, Lindan P J D, Probert M J, Pickard C J, Hasnip P J, Clark S J and Payne M C 2002 First-principles simulation: Ideas, illustrations and the CASTEP code *J. Phys. Condens. Matter* **14** 2717–2744

[174] Becke A D 1993 Density-functional thermochemistry. III. The role of exact exchange *J. Chem. Phys.* **98** 5648–5652

[175] Perdew J P, Chevary J A, Vosko S H, Jackson K A, Pederson M R, Singh D J and Fiolhais C 1992 Atoms, molecules, solids, and surfaces: Applications of the generalized gradient approximation for exchange and correlation *Phys. Rev. B* **46** 6671–6687

[176] Jacob T, Muller R P and Goddard W A 2003 Chemisorption of atomic oxygen on Pt(111) from DFT studies of Pt-clusters *J. Phys. Chem. B* **107** 9465–39476

[177] Feibelman P J, Esch S and Michely T 1996 O binding sites on stepped Pt(111) surfaces *Phys. Rev. Lett.* **77** 2257–2260

[178] Eichler A, Mittendorfer F and Hafner J 2000 Precursor-mediated adsorption of oxygen on the (111) surfaces of platinum-group metals *Phys. Rev. B - Condens. Matter Mater. Phys.* **62** 4744–4755

[179] Hu Z and Metiu H 2011 Choice of U for DFT+ U calculations for titanium oxides *J. Phys. Chem. C* **115** 5841–5845

[180] Saqlain M A, Novais Antunes F P, Hussain A, Siddiq M and Leitão A A 2017 Adsorption of oxygen and CO oxidation on Au/anatase(001) catalysts. A DFT+U study *New J. Chem.* **41** 2073–2080

[181] Kolczewski C and Hermann K 2004 Ab initio DFT cluster studies of angle-resolved NEXAFS spectra for differently coordinated oxygen at the V_2O_5(0 1 0) surface *Surf. Sci.* **552** 98–110

[182] Kostlmeier S 2001 Success and limits of common final-state approximations *Ultramicroscopy* **86** 319–324

7 Determination of cobalt oxidation states

7.1 Experimental Method

7.1.1 Outline

The interfacial chemistry of fuel cell catalysts at the nanometre scale is crucial to truly understand the ORR, the rate-limiting step of catalytic activity in Pt-based catalysts [18]. In order to achieve this, the characterisation techniques of aberration-corrected STEM and EELS are employed. The catalysts to be studied are composed of platinum, cobalt and possibly oxygen. From EELS, the O *K*-edge signal would generally be the main ELNES of interest to locate oxygen on the nanoparticles. However, given the occasionally low O *K*-edge signal, as well as the uncertainty in the Pt $M_{4,5}$-edge due to a lack of a well-defined ELNES, the cobalt white line ratios together with their relative energies become a useful alternative. The white line ratios would give the oxidation state of the cobalt atoms. This can reveal information on the strength of the oxygen bonding to the cobalt atoms.

A higher cobalt oxidation state on a particle means a stronger Co-O bond. This leaves more platinum atoms available for oxygen binding (oxygen preferentially binds to Co than Pt atoms [49,56]) and hence, catalytic activity. However, a high oxidation state means that the Co-O bond will be harder to break, therefore inhibiting desorption of oxygen intermediates. Some of these intermediates include CO which poisons the catalyst. It has been demonstrated via in-situ studies that oxygen diffuses from surface to the subsurface in Co and PtCo nanoparticles, during low and high O_2 pressures [183]. It was also found that the cobalt oxidation state increases with high O_2 pressures [183]. However, it was shown that the evolution of the highest oxidation state, Co 3+, was not affected by the oxygen diffusion, meaning Co 3+ was mainly on the surface of the particles. Co 3+ is also thought to be the most active state for CO oxidation, with the oxygen responsible for the oxidation coming from those bound to cobalt oxide phases [183,184]. The

proportion of these states can also be tuned by the percentage of platinum content [183] and higher cobalt oxidation states lower the platinum oxidation states [62,185,186], leaving more surface for platinum ORR. Thus, it is important to know what part of the nanoparticles have high oxidation states.

The experimental section of this thesis begins with the outline of the methodology (Figure 7.2) implemented for the quantification of oxidation states on the PtCo nanoparticles. The variation in the white line ratios arises from changes in the *d*-occupancy of the unoccupied state and hence, the oxidation state [137,140]. However, as there is not a one-to-one correspondence between the white line ratio and oxidation state, ambiguity arises when trying to determine oxidation states solely with the white line ratios. This has been confirmed from the measurement of cobalt standards as well as comparison to literature values [137]. Consequently, the shapes and energies of the Co $L_{2,3}$-edge, together with those of the O *K*-edge are used to estimate the oxidation states and this procedure will be discussed in this chapter.

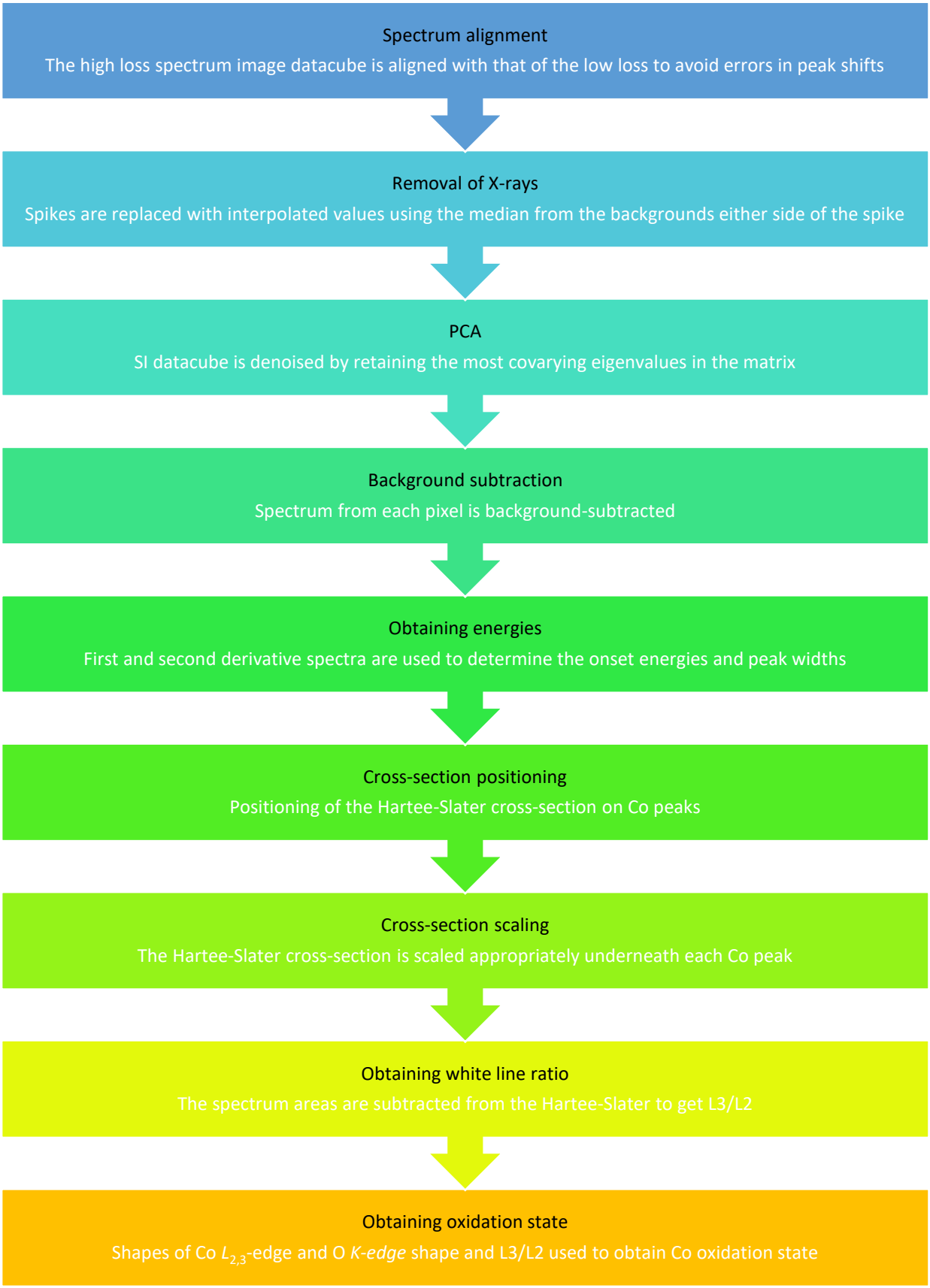


Figure 7.2. Flow chart for the methodology of deriving cobalt oxidation states.

7.1.2 Sample preparation

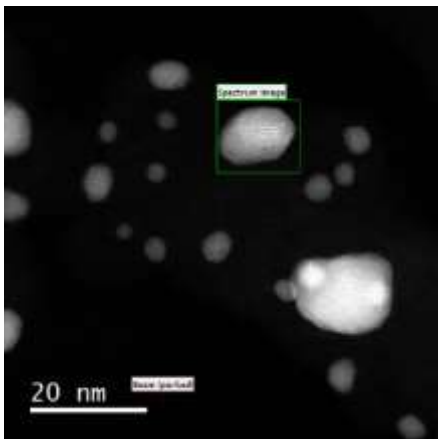
Cobalt standards were procured as references for comparison to the PtCo alloys to be investigated. The standards were air-sealed Sigma-Aldrich chemicals, provided by Christian Kuss from the Department of Chemistry, University of Oxford. These consisted of 99.9% pure powders of CoO, Co_3O_4 and $LiCoO_2$, used as references for the divalent (2+), mixed-valent (2.67+) and trivalent (3+) states of cobalt, respectively. The synthesis of a pure cobalt standard is difficult due to rapid oxidation in the presence of air and thus, a cobalt wedge, provided by Dr Aakash Varambhia at Johnson Matthey, was used as the metallic standard. The $L_{2,3}$ ratios from the metallic standard were too high compared to known metallic regions in the nanoparticles. Consequently, an average over specific metallic regions from the nanoparticles were used as the metallic reference. The fine structure was used to determine which metallic regions would be used as references.

The alloys investigated were pristine $PtCo_3$ and Pt_3Co samples. These came in an acid-leached and unleached forms and were, giving a total of four samples. The different stoichiometry has been seen to improve catalytic activity. For example, Pt_3Co has seen 200% and 300% increase in mass activity and specific activity compared to homogenous Pt and indeed disordered PtCo alloys [187]. The leached systems are also speculated to have the highest ORR and catalytic activity due to the formation of Pt skins, as well as surface strain and lattice contraction induced by the Co atoms [81,188–190] Therefore to locate oxygen coverage on these particles is paramount. These samples were industrially prepared for use in the PEMFC fuel cell and had been exposed to air prior to study, which should boost oxygen coverage for the study. The carbon-supported 20 wt% PtCo alloys were supplied by Johnson Matthey and prepared using wet chemistry. The precursor metals were co-deposited on the carbon-black support in their salt derivatives before being calcined and reduced to yield the PtCo alloy in the form of

nanoparticles. In the case of the leached particles, perchloric acid ($HClO_4$) is added to remove the cobalt from the surface of the particle.

For ease of imaging, the PtCo samples were put on a holey carbon grid. In order to maximise dispersion and minimise thickness issues, the particles were dispersed in ethanol and then crushed using a pestle and mortar. The solution was sonicated for 30 minutes before baking under vacuum at 80 °C to remove excess hydrocarbons; alternatively, the samples were plasma cleaned at 1A, 5V before being drop-casted onto the carbon grid. However, this did not eliminate contamination. It was found that simply dispersing the sample in its powdery form on the carbon grid and putting it straight into the microscope, on average, gave the least contaminated images (Figure 7.3). This also reduced contamination that resulted from the ethanol solvent in the grid mixing with the plastic material of the storage box over time.

a



b

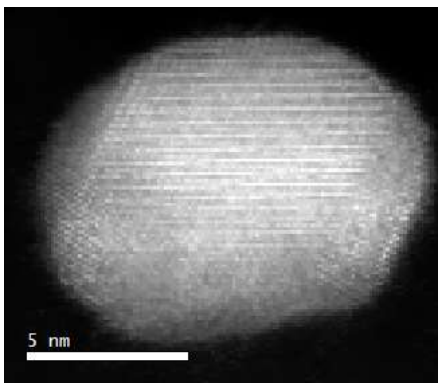


Figure 7.3. The HAADF STEM images of (a) a 600k MAG of $P_{t3}Co$ unleached nanoparticles on amorphous carbon support and (b) 6M MAG 0.05 μm FOV of a chosen particle from the 600k MAG image.

7.1.3 Parameters for Imaging and Spectroscopy

Imaging and spectroscopy were carried out on a JEOL ARM200F at 200 kV. Two instruments were used: one within the David Cockayne Centre for Electron Microscopy, University of Oxford, and the other, the Johnson Matthey owned E01 instrument at the electron Physical Science Imaging Centre (ePSIC), Diamond Light Source. Simultaneous structural and compositional data were recorded using a high angle annular dark field (HAADF) detector and a 5 mm aperture Gatan EELS GIF Quantum system in the DUAL-EELS setup. The HAADF detector inner and outer angles were ~108 and 553 mrad respectively. Most of the EELS data were acquired at convergence and collection angles of 30 and 40 mrad respectively; a few of the data at ~23 and 56 mrad respectively. The EEL spectra were recorded using dispersions of 0.25 and 0.025 eV per channel (eV/ch) for Co $L_{2,3}$-edge data with and without the O *K*-edge, respectively. At 0.25 eV/ch, the fine structure of the O *K*-edge could be used to determine the oxidation state of the oxygen and cobalt. However, the O *K*-edge is not always resolvable or may be absent and as such, at 0.025 eV/ch, the multiplets which arise on the Co $L_{2,3}$-edge at this dispersion, can also be used to determine the oxidation state.

The core-loss spectra were recorded with a pixel dwell time between 0.05 – 0.02s, whereas the low-loss spectra were recorded with a pixel dwell time between 10 – 40μs. The resolution was ±0.63 and ±1 eV as measured from the ZLP FWHM at the 0.025 eV/ch and 0.25 eV/ch dispersion, respectively. Spectrum images were acquired from thin regions with inelastic mean-free path $t/\lambda < 0.5$ according to measured EEL spectra. Particles where mainly imaged at the edge of a hole as this reduces the contributions of the carbon support and additional scattering resulting from particle overlap. However, this does introduce some stability issues due to the vibration or movement of the holey-carbon film.

The particles were found to be relatively stable under the conditions used, except with small particles, mainly <2 nm, where some sputtering, knock-on damage and particle movement

occurred, which is expected. Radiolysis did not appear to be an issue as the O *K*-edge from reference spectra was relatively well reproduced by the nanoparticle. During imaging, some knock-on damage was observed, however, this was mainly due to imaging a sample area for too long. Again, this was mostly seen for very small particles. Albeit, this was alleviated by frequent repositioning of the beam. While the oxygen cannot be distinguished from the metal atoms from imaging, it is safe to assume that it would be part of the sputtering of atoms. Given that there is not much oxygen on the particles, the beam dwell time was further reduced by approximately 20% to reduce the sputtering of oxygen atoms.

7.1.4 Spectrum Alignment and X-ray Removal

Post-experiment, the two major datasets obtained are the high angle annular dark field (HAADF) image and the spectrum image (SI). The HAADF image will be referred to in later analysis, but the bulk of the processing is implemented on the EELS SI data cube using the software, *Digital Micrograph*. Firstly, the low-loss SI was used to determine the energy shifts between different core-loss spectra. A single pixel from the low loss SI is chosen and a region of interest (ROI) drawn around the ZLP in the resultant spectrum. The offset from zero is given in eV and the spectrum shifted to 0 eV. After the correction, the offsets at each pixel in the low-loss SI are similarly applied to the corresponding pixels in the core-loss SI, giving an aligned spectrum (spectra from single pixels shown) (Fig. 7.3).

Following the spectrum alignment, X-rays from the experimental SI are removed as they may be superimposed on an important spectral edge and therefore perturb quantification and or identification of an element. The X-rays are in the form of spikes (spectra from single pixels shown) (Figure 7.4) and are removed by sifting through all image planes of the SI and identifying intensities 10 standard deviations above the local median. If the intensity is unphysical (≥10 standard deviations), the spike is removed and replaced with the interpolated background from the median of the backgrounds immediately before and after the spike

[191,192]. While there is some reduction in spatial resolution in the SI, the spectrum is easier to process analyse due to the reduction in the number of false signals following X-ray removal.

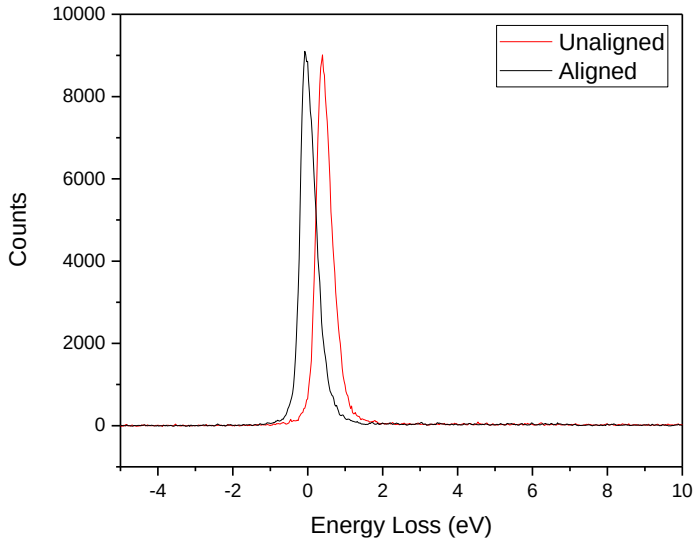


Figure 7.3. EEL spectrum of an aligned ZLP from a single pixel in the low loss SI. Spectra dispersion: 0.25 eV/ch.

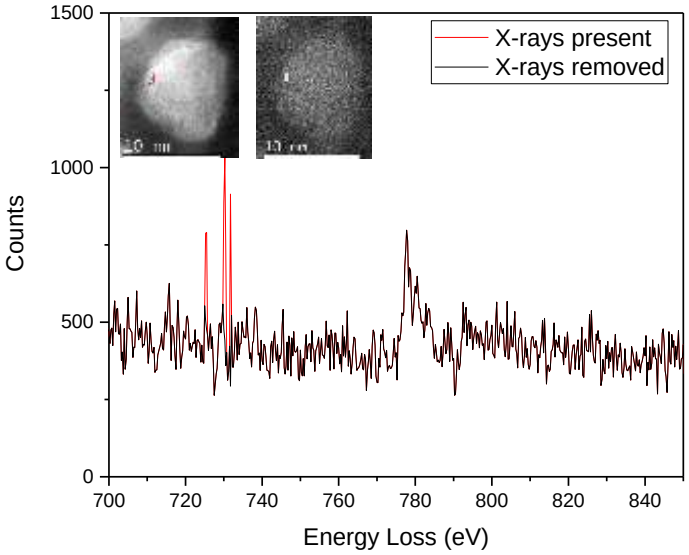


Figure 7.4. EEL spectrum from SIs showing cobalt high-loss from a single pixel probe position on the edge of a $PtCo_3$ unleached nanoparticle, before (left inset) and after (right inset) X-ray removal. Spectra dispersion: 0.25 eV/ch.

7.2 PCA

The EEL spectrum that is derived post-experiment can sometimes have very low signal-to-noise ratio (SNR). The multivariate statistical method of Principal components analysis (PCA) can be

used to separate every spectrum in the SI data cube into its additive components, segregating features of high covariance from those of low covariance i.e. noise [193]. The software, Hyperspy, has been used to carry out PCA [194]. The process is performed via singular value decomposition (SVD) [192,193], a method for decomposing the SI matrix into constituents, which makes it easier to analyse. The process is summarised in the following steps:

1. The SI is made of *a* x *b* x *c* datacube and is decomposed via SVD. The decomposition process treats the data as a matrix, *X* [195], and separates it according to the spatial amplitude, score (***t***), and the transpose of the spectral data, loading (***p'***), vectors [195]. The vectors can correlate negatively or positively and this is outputted in the form of a covariance matrix, *COV*(*x*,*y*), where *x*,*y* are two different vectors. The vectors are then arranged according to the highest covarying to the least. These are shown as eigenvalues versus the number of vectors (principal components) – the resultant plot is referred to as a scree plot (Figure 7.5a and b).
2. Next, the data is Poisson-normalised to account for shot noise since in EELS, the electron scattering process is random and the counting statistics is dominated by shot or Poisson noise.
3. The scree plot has a point where the gradient of the plot approaches zero (becomes flat) and it is often referred to as the knee of the plot (Figure 7.6a). In this case, this is approximately after the first six components and corresponds to the six loadings (Figure 7.6b) whereafter there is no significant signal in the following components. These six components are taken and reconstructed to form a PCA model. The PCA SI and the improved SNR is evident with the clear visibility of the cobalt white line edge (Figure 7.6c).

It should be noted that sometimes denoising the data using PCA may not be sufficient for a reasonable description of the SI. PCA assumes linearity, high variance above noise and that the

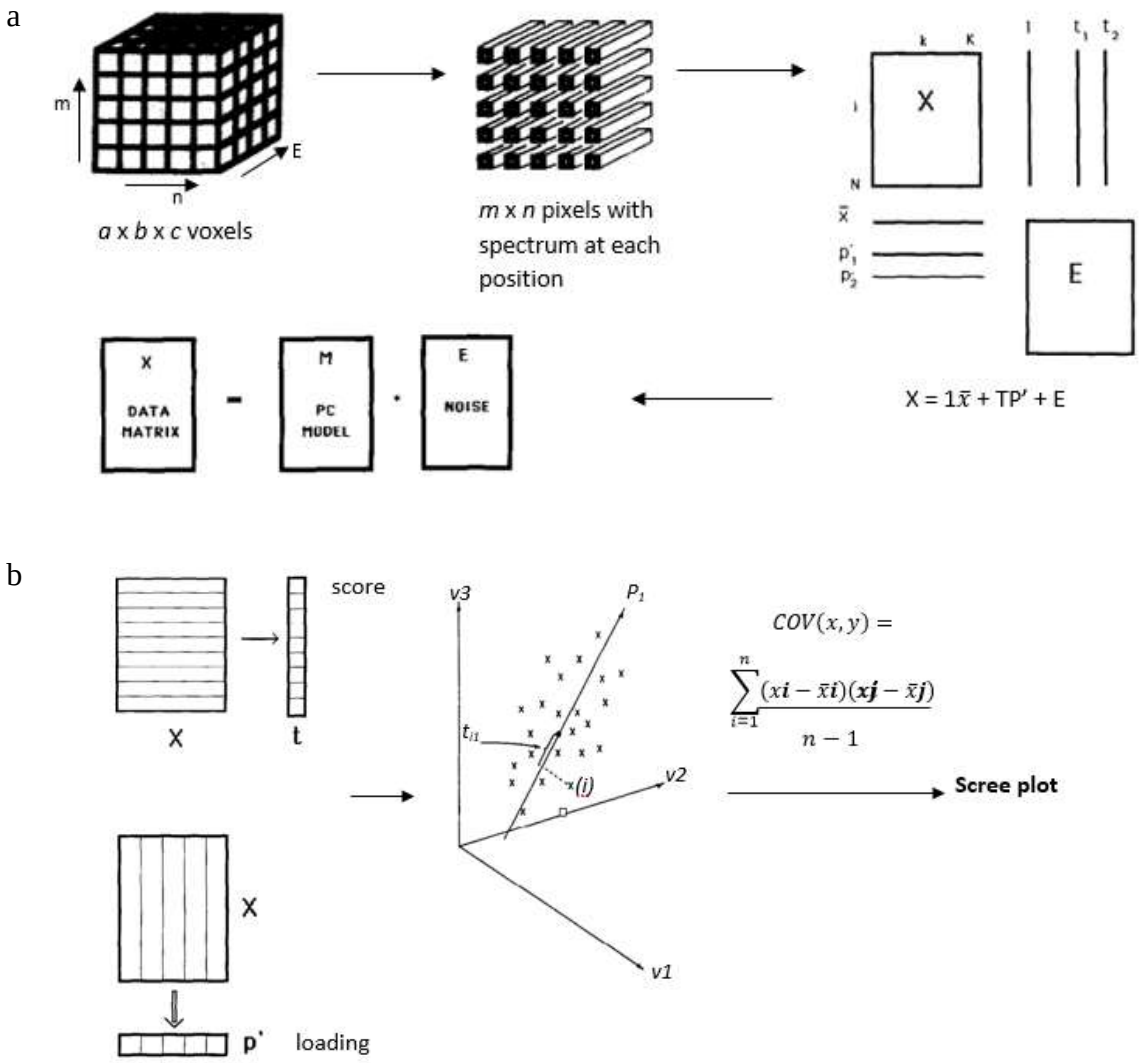


Figure 7.5. Decomposition and reconstruction of a data matrix *X* into its first two principal components (a) and illustration of variance in a score and loading vector plot (b). *Modified from* [195]. The symbol, *X*, represents the data matrix with *N* objects and *K* variables, where *i* and *k* are their row and column indices, respectively. *N* objects are assigned a scalar and projected unto a vector, *t*. The same goes for the *K* variables onto a loading (*p'*) vector. The objects represent the sample while the variables represent the measurements made on the objects.

principal components are linear; however, this is not always the case. As such other multivariate methods such as independent component analysis (ICA) and non-negative matrix factorisation (NMF) are used for more detailed analysis that does not assume mutual dependence [196,197].

In addition, it is also important to note that if any deficiencies in the detector that counts the electrons is present, it will most likely be observed in the resultant PCA model spectrum. For example, the EELS detector is made up of four quadrants glued together and so the dark/gain response varies for each quadrant. Hence, when navigating through the SI, jumps can be seen in the spectra at the specific energies corresponding to the quadrant borders. This mainly becomes a problem in very low SNR spectra. Furthermore, if there are errors in the dark/gain averaging, this could introduce correlated noise patterns in the EEL spectrum, making it hard to identify non-artefact peaks in the fine structure. This issue is discussed in more detail in section 7.9.

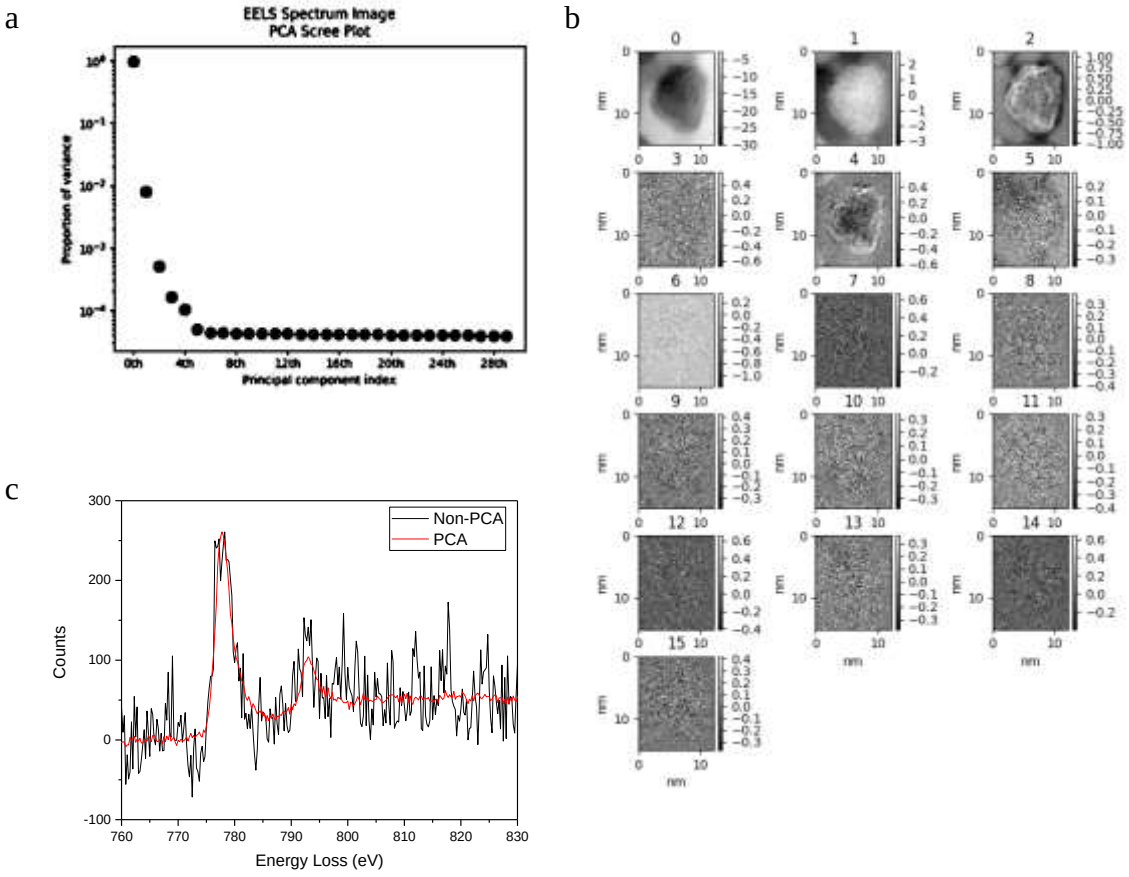
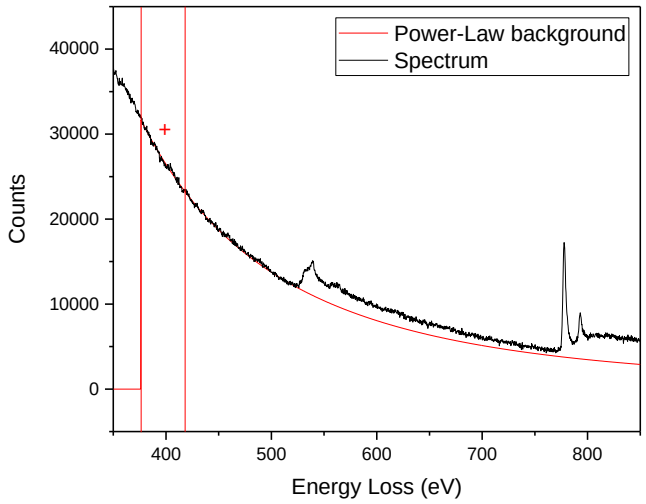


Figure 7.6. Images of (a) output scree plot with (b) their corresponding loadings and (c) comparison of cobalt white lines of Non-PCA and PCA model spectrum from a single pixel in the SI of a $PtCo_3$ unleached particle. Spectra dispersion: 0.25 eV/ch.

7.3 Background Subtraction

A region of the denoised SI which has the edges of interest is chosen and the background is subtracted (Figure 7.7a). Next, the values for the beam energy, convergence and collection angles are entered as these are related to the EELS scattering cross-sections. Using a single pre-edge window, a Power-Law background model is used to subtract the high-loss edges from the continuum contributions in the spectrum (Figure 7.7b) for accurate quantification of the ELNES. Both spectra are averaged over 50 x 50 pixels of the SIs.

a



b

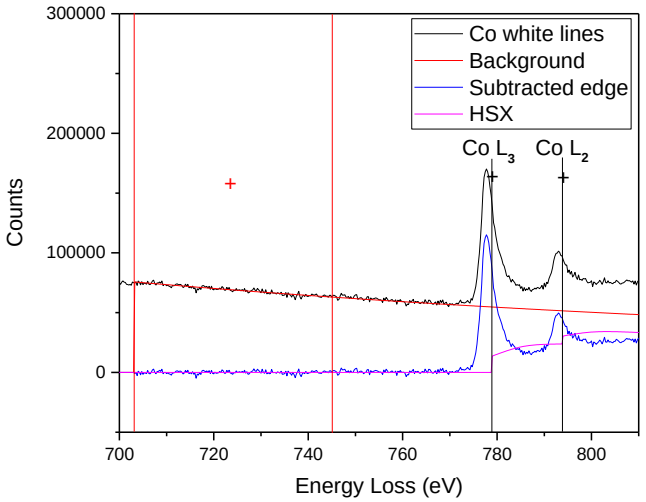


Figure 7.7. Plots of (a) background model on a $PtCo_3$ unleached particle PCA EEL spectrum and (b) non-background-subtracted illustrating the positioning of the Hartree-Slater Cross-section (HSX) on the cobalt $L_{2,3}$-edge of metallic cobalt and the resultant background-subtracted edge. Spectra averaged over 50 x 50 pixels. NB: The '+' mark the position of the HSX and the centre of the background window used for subtraction. Spectra dispersion: 0.25 eV/ch.

7.4 Extraction of Cobalt White Line Ratios

The samples used in this work are nanoparticles and such, even after PCA, the SNR remains low in some cases; this is also dependent on the region of interest in the SI. To determine the energies of the edges as accurately as possible, a consistent method is required. This is because energy windows are used to position the integration range of the white lines. In order to determine onset energies, the second derivative of the background-subtracted spectrum from the region of interest is taken. In addition, the energy width of both white lines, L_3 *w* and L_2 *w* and between (*w**), were optimised for maximum accuracy in the edge cross-section integration (Figure 7.8). The label *w** denotes the energy difference between the end of L_3 *w* and start of L_2 *w* determined by the second derivative. The onsets, indicated by the first dashed line on each peak, are read off as absolute energies from the overlaid spectra. This is where the second derivative goes to zero in the spectrum.

There are four lines either side of the white line peaks are used to determine the integration windows, L_3 *w* and L_2 *w* (Figure 7.8), for quantifying the white line ratios. These energy windows vary depending on the electronic structure of the edge but are about 10 eV on average. It should be noted that the second derivative is not a typical second derivative plot – it appears that *Digital Micrograph* applies some smoothing parameters which are encoded but illuminated to the user. An example of this is shown in the supplementary information (appendix A), where the first derivative of the first derivative does not equal the second derivative outputted by *Digital Micrograph*. However, as the method was consistent for all measurements, this was not an issue. In the case of an oxygen *K*-edge, because it has a different electronic structure, the second derivative does not generally go to zero where the spectral peak begins. Thus, the maximum of the first derivative is used to determine the onset energy. There is a library of peak positions containing EELS transitions from various elements, indexed in the Gatan Hartree-Slater General Oscillator Strength (H-GOS) tables in *Digital Micrograph*.

However, the centre of the peaks are not always at the values of the H-GOS due to an experimental chemical shift. Hence, this is corrected by taking the L_3 *w*/2 and L_2 *w*/2 (Figure 7.8) and using them as the position of the Hartree-Slater Cross-section (HSX). The spectrum shown is averaged over 50 x 50 pixels.

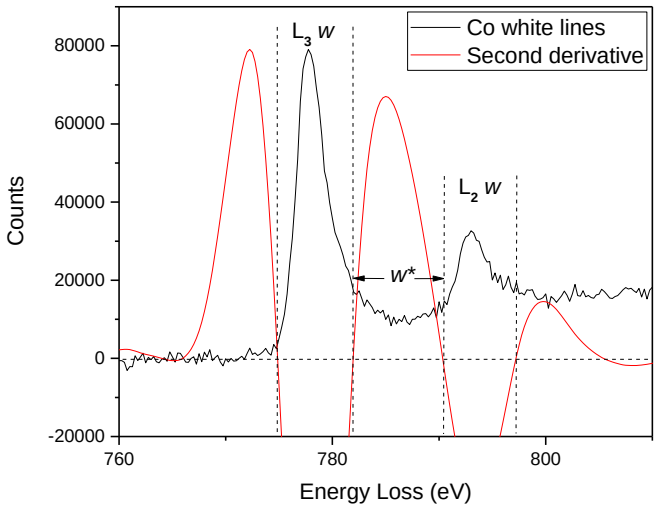


Figure 7.8. Background-subtracted cobalt $L_{2,3}$-edge of metallic cobalt EEL spectrum with second derivative spectra overlaid. L_3 *w* and L_2 *w* are the width of integration windows for each white line peak. Spectrum averaged over 50 x 50 pixels. Spectrum dispersion: 0.25 eV/ch.

The HSX is used to remove the continuum contributions specific to the $L_{2,3}$-edge from the spectrum because the post-edge background is different to that of the Power-Law. In *Digital Micrograph*, the HSX is encoded to fit to the signal. While this is fine for *K*-edges as the saw-tooth shape approximates the ELNES reasonably well, this does not work for the white-line shape of 3*d* and 4*d* transition metals. In addition, each of the white line peaks tend to have different continuum backgrounds to each other and as such, separate fits are required for each peak to account for the variation. Consequently, spectrum was imported into Excel for further quantification. In Excel, the HSX slice can then be scaled to the background as opposed to the signal by multiplying by the scaling factor required to remove the continuum contribution under each white line peak. In the case where the position of the HSX is not at the centre of one of the peaks due to the experimental chemical shift, the L_3 and L_2 peaks are treated

separately and the position of the HSX is shifted to the centre of each peak before obtaining the L_3/L_2 ratio (Figure 7.9). The spectrum shown is averaged over 36 x 10 pixels.

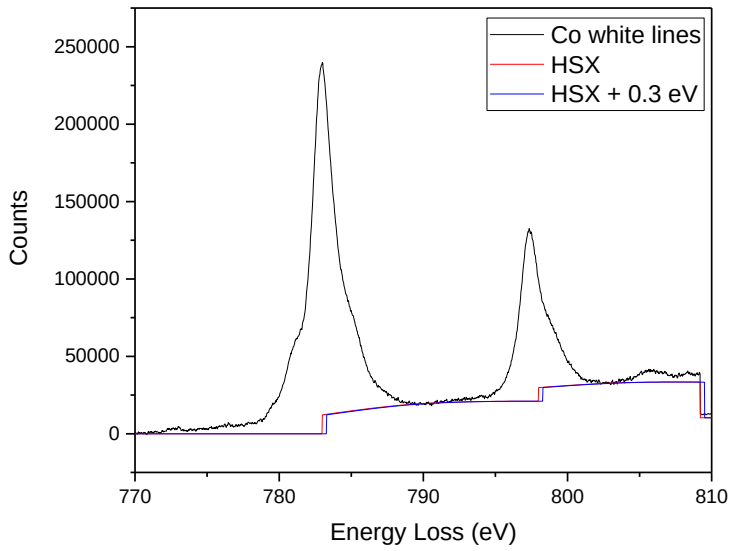


Figure 7.9. EEL spectrum showing the cobalt $L_{2,3}$-edge of a $LiCoO_2$ standard after scaling the Hartree-Slater cross-section (HSX) to fit the continuum background under each white line peak. The graph also shows the 0.3 eV chemical shift adjustment in the HSX so that each of the step-functions are at the centre of each peak. Spectra averaged over 36 x 10 pixels. Spectra dispersion: 0.25 eV/ch.

Cobalt standards of CoO, Co_3O_4 and $LiCoO_2$ were used as references for the Co 2+, Co 2.67+ and Co 3+, respectively. The CoO standard has a rock salt structure [198,199,200], with both the cobalt and oxygen both atoms in octahedral sites. The structure of the Co_3O_4 is that of a spinel, with the Co 2+ atoms in the tetrahedral sites and the Co 3+ atoms in the octahedral sites [198,200]. The Co 3+/2+ ratio is 2:1 in Co_3O_4. The oxygen atoms occupied fcc sites. $LiCoO_2$ has an improper triangular lattice, with both Li+ and Co 3+ atoms occupying octahedral sites; oxygen atoms were in fcc sites [201–204]. Knowledge of the symmetry of the sites that the cobalt atoms occupy become crucial for the modelling of cobalt fine structure and oxidation state in chapter 9. With regards to the PtCo nanoparticles, both metals are thought to be in the fcc phase [62,82]. Co nanoparticles are also thought to be fcc [205,206]. However, some reduction syntheses can lead to a hcp cobalt phase [206].

In contrast, procuring a metallic cobalt standard was not so trivial. The metallic cobalt wedge standard readily oxidised and when metallic regions were found, their ratios were significantly higher than those from the nanoparticles to be compared – by approximately 30%. Higher $L_{2,3}$ ratios in ≤ Co 2+ mean that they are more oxidised. For this reason, specific metallic regions in the nanoparticles were used as a reference instead of the standard. For data taken at the dispersion at 0.025 eV/ch, the metallic Co $L_{2,3}$-edge only has two peaks, with a delayed tail after the L_3 peak and an edge-jump just before the broad L_2 peak (see section 7.5). There is another edge-jump just after the L_2 peak. These were used to evidence the metallic state. At 0.25 eV/ch, while possible, it is more difficult to differentiate between the Co $L_{2,3}$-edges at different oxidation states and so the absence of an O *K*-edge was evidence of a metallic state.

The white line ratios were obtained by averaging over various particles from each standard and a calibration curve was plotted (Figure 7.10). All spectral data shown are averaged from 30 x 30 (metallic Co (NP)), 29 x 10 (CoO), 24 x 30 (Co_3O_4) and 36 x 10 ($LiCoO_2$) pixels. The spectra for these standards is shown later on (Figure 7.11). The errors are calculated as the standard error of the mean between the particles in that standard. The ratios from the standards were 3.1±0.1, 4.7±0.1, 2.6±0.1 and 2.40±0.01 at 0.25 eV/ch and 2.3±0.1, 4.3±0.3, 2.40±0.03 and 2.10±0.02 at 0.025 eV/ch for the metallic cobalt from nanoparticles (NP), CoO, Co_3O_4 and $LiCoO_2$, respectively. These results are in agreement with ratios from Zhao *et al*. of 3.1, 4.5 and 2.4 [137] for metallic cobalt, CoO, Co_3O_4, respectively. This also congruent with values from the EELS database, which had values of 3.4, 4.8 and 2.1 [204] for metallic cobalt, CoO, Co_3O_4, respectively. The $LiCoO_2$ white lines are not as commonly researched as the metallic cobalt and the other two oxides, however it is reported to have a white line ratio of 2.7 by Han *et al* [210], which is approximately 10% higher than the ratio found in this work. However, in comparison to other Co $L_{2,3}$-edges in literature (see Figure 7.12a and b), the value is most likely significantly lower than reported. Nevertheless, the literature values only differ

by approximately 2 – 10% from the values calculated using the developed methodology in this worked and so congruence is achieved.

The source of the ratio discrepancy between the two different dispersions is unknown. The biggest difference is seen for the metallic reference and so there may be a sample dependence which contributes to the ratio discrepancy between the dispersions. Acquiring EEL spectra at various drift tube voltages and at different dispersions according to a 'HT-adjust protocol' by Webster *et al.* has been shown to correct the onsets of Ni $L_{2,3}$-edges to within 0.1 eV [217]. While this method can correct the onset discrepancy, it is not clear if the dispersion binning is affected and hence, give more uniform ratios at different dispersions. Nevertheless, all errors were less than 10%, affording consistency in the measurements. It is clearly evident from the calibration curve that here is not a monatomic dependence between the ratio and oxidation state curve i.e. the ratio turns after Co 2+ (Figure 7.10). A similar dependence was also found in literature [137]. Consequently, the white line ratios could not be use on its own to determine the cobalt oxidation state.

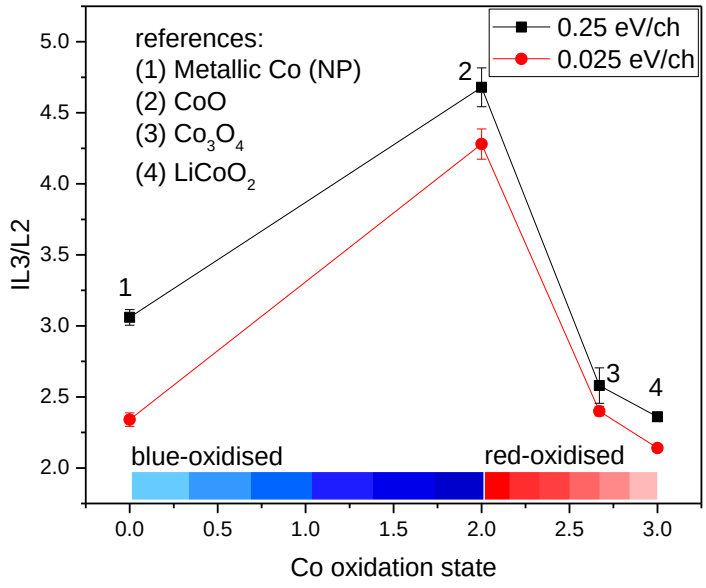


Figure 7.10. Cobalt white line ratio vs oxidation state from references at 0.025 and 0.25 eV/ch.

The edge intensities of the cobalt standards are required to be commensurate with the expected chemistry before using them for comparative study with the nanoparticles. The atomic ratios were calculated according to formula shown in chapter 4, section 4.2. The elemental analysis shows the data from the oxides are congruent with their expected stoichiometries (Table 7.1). The metallic cobalt is not included as is averaged from the nanoparticles. However, no oxygen was found from the EEL spectra used, as should be expected from metallic cobalt. From the results, the experimental ratios are 1.02:1, 1.35:1 and 2:1 compared to expected ratios 1:1, 1.33:1 and 2:1 for the CoO, Co_3O_4 and $LiCoO_2$ standards, respectively. The errors are within 10% and these are obtained directly from *Digital Micrograph* quantification package. Considering that the errors on the *K* and *L* computations are usually 5 – 10% and 10 – 20%, respectively, the stoichiometry of the standards are fairly commensurate with the expected chemistry.

Table 7.1. EELS Elemental quantification of cobalt and oxygen composition in CoO, Co_3O_4 and $LiCoO_2$ standards. Cross sections were 924±0.92b and 1189±0.119b (in barns) for the O *K*-edge and Co $L_{2,3}$-edge, respectively. The ratios shown are given relative to the oxygen. Data derived from *Digital Micrograph* software.

Standard	At. ratio O (/O)	At. ratio Co (/O)	Experimental O:Co	Expected O:Co
CoO	1.00±0.00	0.98±0.11	1.02:1	1:1
Co_3O_4	1.00±0.00	0.74±0.09	1.35:1	1.33:1
$LiCoO_2$	1.00±0.00	0.50±0.07	2:1	2:1

7.5 Calculation of Cobalt Oxidation State

As discussed in section 7.4, there is not a monatonic dependence in the reference ratio-oxidation state curve and this poses an issue in relying solely on the calibration curve for the determination of cobalt oxidation states. The onset energies of the cobalt white lines also mimic this behaviour, except the trend is inverted (Figure 7.11a). All spectral data shown are averaged from 30 x 30 (metallic Co (NP)), 29 x 10 (CoO), 24 x 30 (Co_3O_4) and 36 x 10 ($LiCoO_2$) pixels. In this case, the energy onsets have the opposite trend to that of the white line ratios i.e. the cobalt L_3 and L_2 onsets decreases by about 1.5 eV going from the metallic to the 2+ state before increasing again with oxidation state at both 0.25 eV/ch and 0.025 eV/ch (Figure 7.11a). In literature, the onsets increase with oxidation state [137] and so it appears that the slight decrease between the metallic state and Co 2+ standard, CoO, is not found. It can be seen that onset energies for both the L_3 and L_2 differ by approximately 3 eV, when comparing both dispersions. The exact reason is not known but is most likely due to slight errors in the calibration of the dispersions. It is interesting that for the L_2 at both dispersions, the onsets increase with the oxidation state right from the metallic state to the 3+ state. However, the increase between the metallic and 2+ state is approximately 0.5 eV at both dispersions and so is very minute. The errors on the onset energies are significantly less than 1% and so do not play a role in this discrepancy. This increase between the metallic and 2+ state could be due to the larger uncertainty in the cobalt L_2 onsets compared to L_3 peak. Given the inconsistencies in the white line ratios as well as varied experimental conditions used, the literature was also not fully reliable. Hence, a more detailed comparison of experimental spectra and the reference spectra was required.

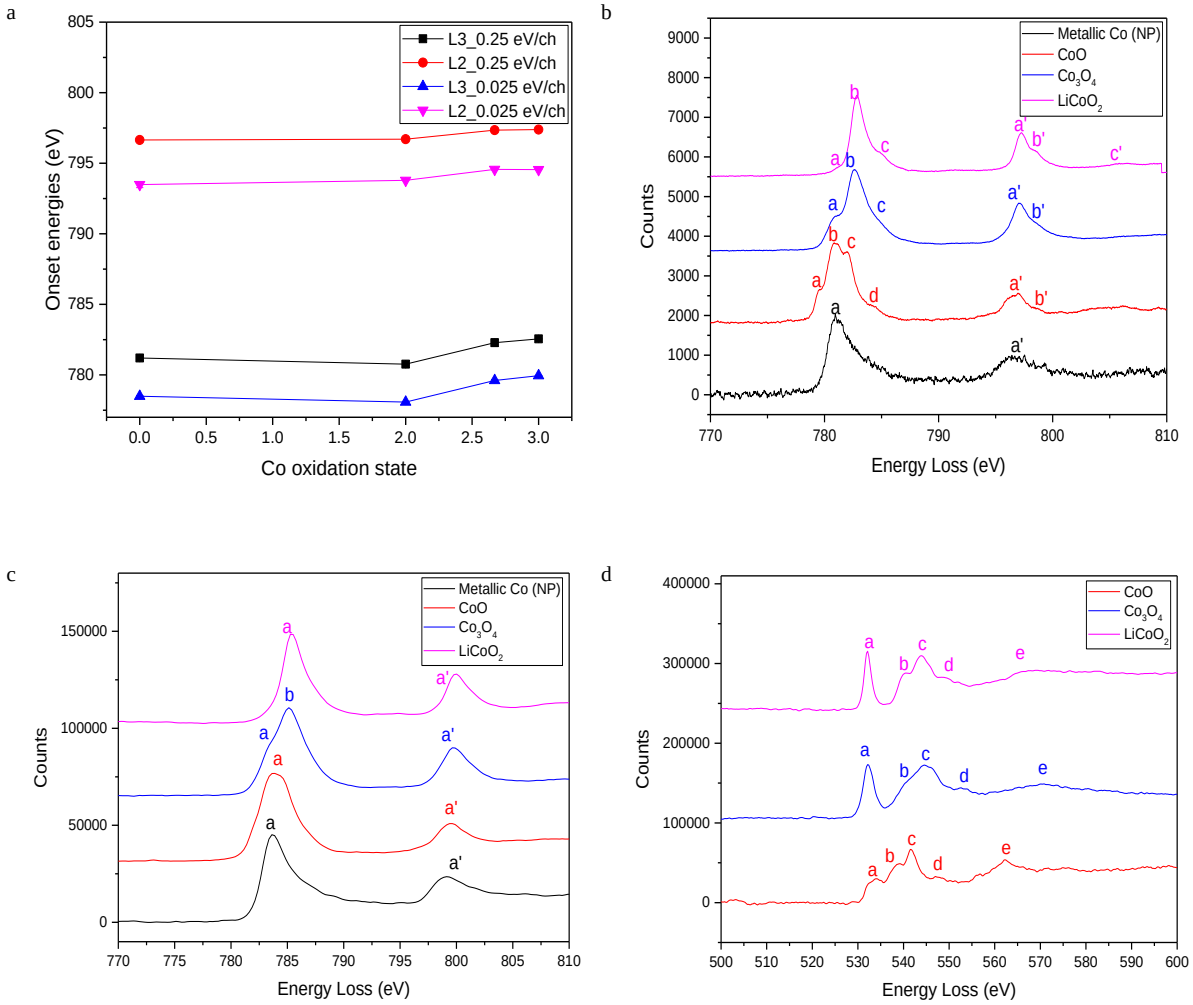


Figure 7.11. Cobalt onset energies vs oxidation state from metallic Co on nanoparticle, CoO, Co_3O_4 and $LiCoO_2$ references at (a) 0.025 and 0.25 eV/ch, (b) Co $L_{2,3}$-edge of standards 0.025 eV/ch, (c) 0.25 eV/ch and (d) O *K*-edge at 0.25 eV/ch. Spectra pixels: 30 x 30 (metallic Co (NP)), 29 x 10 (CoO), 24 x 30 (Co_3O_4) and 36 x 10 ($LiCoO_2$) pixels. NB: NP = nanoparticle.

The non-monatomic nature of the white line ratio and oxidation state can be resolved by direct comparison of the fine structure in the experimental spectrum to that of the reference standard. (Figure 7.11b and c) at the two dispersions is employed. This determines what side of the $L_{2,3}$ reference curve (Co 0 – 2+ or 2+ – 3+) would be used to estimate the oxidation state in the experimental spectrum. The Co $L_{2,3}$-edge ranges 779 – 820 eV and the peaks labelled *a* – *c'* (Figure 7.11b) and *a* – *b* (Figure 7.11c) are used for the comparison. They arise from interactions between electron configurations, dominated by electron-electron repulsion and spin-orbit coupling. These are expressed as term symbols and are discussed in chapter 9. The O *K*-edges

are also plotted and range 529 – 600 eV (Figure 7.11d). Peak *a* is a pre-peak that is derivative of the 1*s* transitions into the O2*p*–Co3*d* hybridised orbital and is sometimes called the π^* peak. Peak *b*, or the σ^* peak, and peak *c* are thought to be from the transitions into the O2*p*–Co4*sp* hybridised orbital [137,208,209]. The sources of peaks *d* and *e* are not well evidenced in literature and hence not known.

a

b

c

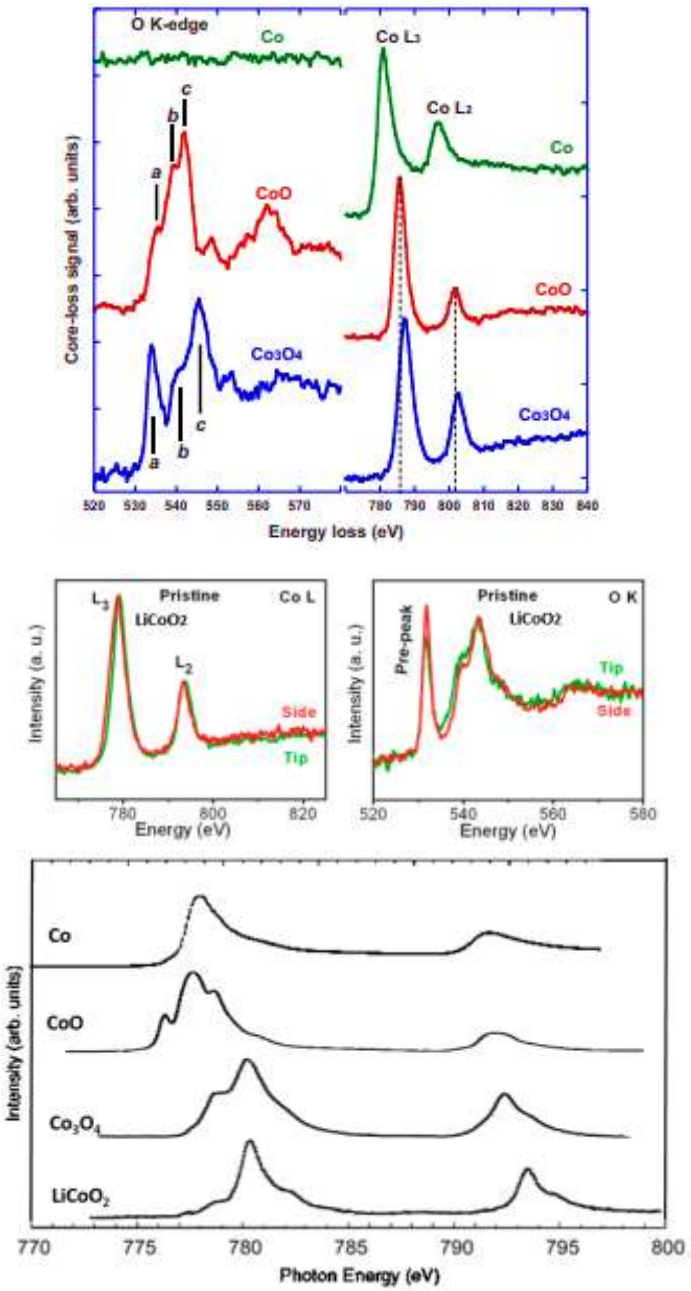


Figure 7.12. Co $L_{2,3}$-edges and O *K*-edges of (a) metallic Co, CoO, Co_3O_4 and (b) $LiCoO_2$ standards in literature. Panel a and b spectra are at low dispersion, where the Co $L_{2,3}$-edges and O *K*-edges were taken simultaneously. Panel c spectra are at high dispersion where there are no O *K*-edges. The image from panel a is taken from [137] panel b is from [210] and panel c is an overlay of individual spectra from [211–203] .

For comparison to literature, a variety of sources is used (Figure 7.12a – c) as there is no one work which has all the required spectra. While peaks *a* – *c* are commonly assigned in literature, all peaks *a* – *e* are well reproduced when comparing to literature (Figure 7.12a). Peak *a* in Co_3O_4 is slightly lower in intensity relative to peak *c* from the literature, however other literature have the peaks at the same maximum as seen in this work. The Co $L_{2,3}$-edge onsets increase with oxidation state (Figure 7.12a and c) and the peak shapes are similarly congruent with the oxides in this work. However, as earlier mentioned, the metallic cobalt was found to have a higher onset than CoO in this work, incongruent with spectra measure by Zhao *et al.* [137] (Figure 7.12a). This inconsistency is also seen when comparing the metallic cobalt spectrum by Mesilov *et al*. [222] to the oxides (Figure 7.12c). These inconsistencies are not uncommon when measuring these edges. For example, the onset of the $LiCoO_2$ is slightly lower than the other oxides and metallic cobalt (Figure 7.12b). Given that various microscope conditions used in each of the works would differ, inconsistencies between their values can be expected. For this reason, the trend is of more importance than the absolute values and that is seen to be in general, congruent with results from this work.

As mentioned earlier, relationship between the white line ratios and oxidation state is not monatomic (see Figure 7.11a) and so it is difficult to assign absolute oxidation states, particularly with only using the cobalt white line ratios. Hence the oxidation state is estimated to lie within two regimes; a blue-oxidised state (Co 0 – 2+) or a red-oxidised state (Co 2+ – 3+). In addition, the absence of an O K-edge is assumed to be indicative of a metallic state and therefore also assigned a blue-oxidised state. This nomenclature is one developed in this work for ease of analysis without imposing absolute oxidation states. Although it should be noted that all nanoparticles studied ranged Co 0 – 2.67+ and none were found to be Co 3+. After the ratios are calculated, the reference oxygen peaks from the cobalt standards labelled *a* – *e* (Figure 7.11a and b) are used to determine what side of curve to use to estimate the oxidation

state. This is done when the oxygen signal is available, which is in most cases for the particles studied. Otherwise, the cobalt fine structure is used, using the data taken at 0.025 eV/ch (see Figure 7.11b).

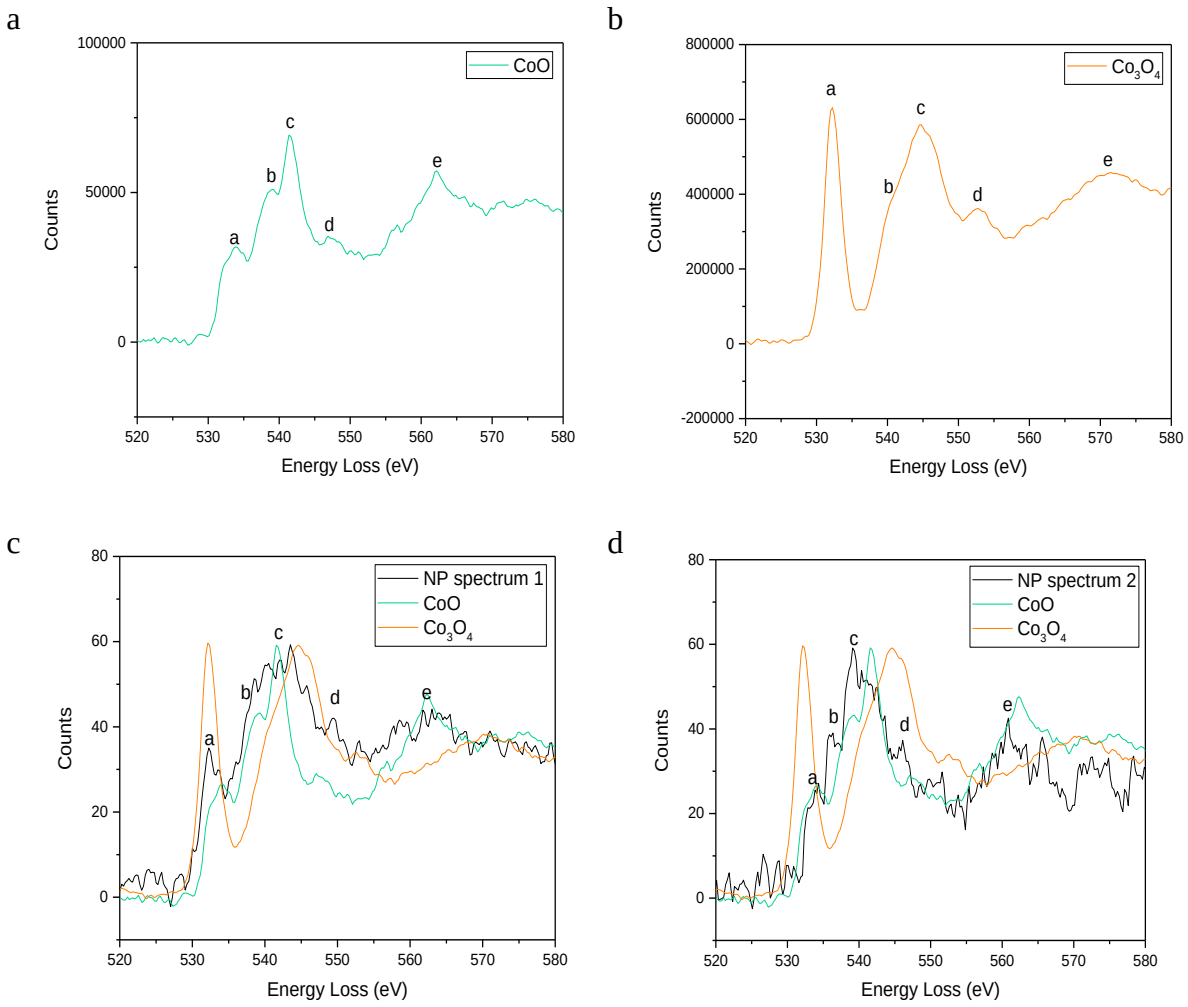


Figure 7.13. EELS O *K*-edge at 0.25 eV/ch from cobalt reference standards (a) CoO, (b) Co_3O_4, (c) NP spectrum 1, CoO and Co_3O_4 and (d) NP spectrum 2, CoO and Co_3O_4 NB: NP spectrum 1 and 2 indicate spectra taken at two different probe positions on a $PtCo_3$ unleached nanoparticle. Spectra pixels: 29 x 10 (CoO), 24 x 30 (Co_3O_4), 1 x 1 (NP spectrum 1) and 1 x 1 (NP spectrum 2). The labels in panels c and d correspond to the NP spectra.

The spectrum from the standard is used as a reference for comparison with that of the nanoparticle of interest. To demonstrate this, the O *K*-edges from the Co 2+ standard (CoO) and the Co 2.67+ standard (Co_3O_4) are compared to those from two different probe positions on a $PtCo_3$ unleached nanoparticle (Figure 7.13a – d). The spectra are averaged over 29 x 10 (CoO),

24 x 30 (Co_3O_4), 1 x 1 (NP spectrum 1) and 1 x 1 (NP spectrum 2) pixels. The Co 3+ standard is not included as no O *K*-edges from the nanoparticles indicated a Co 3+ oxidation state. After the white line ratios are calculated, the O *K*-edges from the standards (Figure 7.13a and b) are used to determine what side of the curve the oxidation state falls under. This is done through a peak-to-peak comparison.

As observable, the main peak from the standards that differentiates the states is the O2*p*–Co3*d* transitions, peak *a*. The other distinct feature, which is very useful when comparing to the very low SNR of the nanoparticle spectra, is the relative intensity of the minimum between peaks *a* and *b*, and that between peaks *d* and *e*. The intensity gap between the minimum formed by peak *a* and *b* and that formed by peak *d* and *e* in the Co 2+ standard can be compared to the same feature in the Co 2.67+ standard. The minimum formed by peak *a* and *b* and that formed by peak *d* and *e* in the Co 2+ standard have approximately, the same intensity. However, in the Co 2.67+ standard, the gap between the intensities is much higher. Comparing this gap in the Co 2.67+ to that of the Co 2+ standard reveals a 12:1 ratio in favour of the Co 2.67+ standard. In other words, the minimum formed by peak *d* and *e* is twelve times higher than that formed by peak *a* and *b* in the Co 2.67+ standard, compared to the Co 2+ standard.

It can be seen that peak *a* in NP spectrum 1 is a pre-peak, indicating that the oxidation state is between the Co 2+ and Co 2.67+ standard (Figure 7.13c). The peak is sharper and has a higher intensity compared to the Co 2+ standard. However, the peak is still significantly lower than the Co 2.67+ standard. In addition, the O2*p*–Co4*sp* transitions, peaks *b* and *c*, do not form a doublet as in the Co 2+ standard, further indicating that NP spectrum 1 is closer to the Co 2.67+. While peak *d* does not indicate much, peak *e* is clearly broad, further indicating that NP spectrum 1 is of an oxidation state closer to the mixed state. Additionally, the minimum formed by peak *d* and *e* is a lot higher than that formed by peak *a* and *b*, indicating an oxidation state between Co 2+

and Co 2.67+. In terms of what this means physically in the nanoparticles, this means the 2+ and 3+ oxidation states are mixed to give a state between a Co 2+ and a Co 2.67+ state.

On the other hand, peak *a* in NP spectrum 2 is part of the main O *K*-edge and it is also not sharp. Furthermore, there is a clear separation between peaks *b* and *c*. As with NP spectrum 1, peak *d* does not reveal much, however, peak *e* is clearly sharper in NP spectrum 2. This indicates that the oxidation state of NP spectrum 2 is closer to the Co 2+ standard. Comparing the minimum formed by peak *a* and *b* with that formed by peak *a* and *b*, it can be seen that the intensities are approximately the same, indicating that the oxidation state is between Co(0) and Co 2+. Following this analysis, NP spectrum 1 is assigned between Co 2+ and Co 2.67+ while NP spectrum 2 is assigned between the Co(0) and Co 2+ side of the calibration curve.

Another element which aids in the oxidation state analysis is the energy positions. Looking at peak *a* (Figure 7.13c and d) in NP spectrum 1 and 2, their onsets are approximately 529 and 532 eV, respectively. The energy positions of peaks *b* – *e* are slightly more uncertain, partly due to the SNR. There are other reasons why the energy position is not the most reliable indicator. Firstly, as earlier mentioned, the energy onsets mimic the white line ratios in that the onsets increase from Co(0) to Co 2+ and decreases afterwards. There is also the added reason that the nanoparticles have a mixture of states per probe position and it would be very hard to distinguish energy shifts between 2–3 eV on a nanoparticle spectrum, which has significantly lower SNR than the cobalt standards.

So far, the O *K*-edges have been used for the assignment of oxidation states. As mentioned earlier this is only possible at the 0.25 eV/ch dispersion where the oxygen signal is collected. However, at a higher dispersion of 0.025 eV/ch, the Co $L_{2,3}$-edges will be used to assign the oxidation states. The method remains the same as with the O *K*-edges. For example, the Co $L_{2,3}$-edges of the nanoparticle metallic reference (Figure 7.14a), CoO (Figure 7.14b) and Co_3O_4 (Figure 7.14c)

standards are compared to those from three different probe positions (Figure 7.14d – f) on a $PtCo_3$ unleached nanoparticle. All spectra are from single pixels. Firstly, it is observable that the fine structure from the metallic reference (Figure 7.14a), matches least to any of the spectra from the three probe positions (NP spectrum 1–3). It can be seen that the peaks *a* – *b*' from the CoO standard are well reproduced in NP spectrum 1. Specifically, peaks *a* – *d* are strongly in NP spectrum 1 are strongly indicative of a CoO-like state. However, at approximately 798 eV, peak *b*' in NP spectrum 1 is not very prominent and the entire L_2 peak is broad (Figure 7.14d) compared to the CoO standard. In addition, the position of the Co $L_{2,3}$-edge of NP spectrum 1 matches that of CoO more than Co_3O_4. For these reasons, NP spectrum 1 will assigned between the Co(0) and Co 2+ side of the calibration curve.

The position of the Co $L_{2,3}$-edges of NP spectra 2 and 3 do not match CoO as well as NP spectrum 1 did. To begin with, both the L_3 and L_2 peaks larger FWHM than the CoO standard (Figure 7.14e and f). The L_2 peak generally gets sharper and increases in intensity with oxidation state. This can be seen in NP spectra 2 and 3 with peak *a*', indicating a higher oxidation state than NP spectrum 1. While all six peaks from the CoO standard spectrum are still well reproduced in NP spectra 2 and 3, their relative intensities have changed. For example, the height of peak *c* now matches the Co_3O_4 standard more closely than the CoO (Figure 7.14e and f). Given that peaks *b* and *c* in NP spectrum 2 are about equal intensities (Figure 7.14e) indicates some sort of transition state, going from the Co 2+ state into the Co 2.67+ state. This is corroborated by the lower intensity of peak *b* compared to *c* in NP spectrum 3. While peak *a* is still present in NP spectrum 3, the lowering of peak *b* compared to *c* on the L_3, together with the slightly sharper L_2 peak (Figure 7.14f), indicates that NP spectrum 3 has the highest oxidation state of all three probe positions. As there are still four peaks, instead of three, on the L_3, the oxidation state can only be less than the Co 2.67+. For these reasons, NP spectra 2 and 3 will both be assigned between the Co 2+ and Co 2.67+ side of the calibration curve.

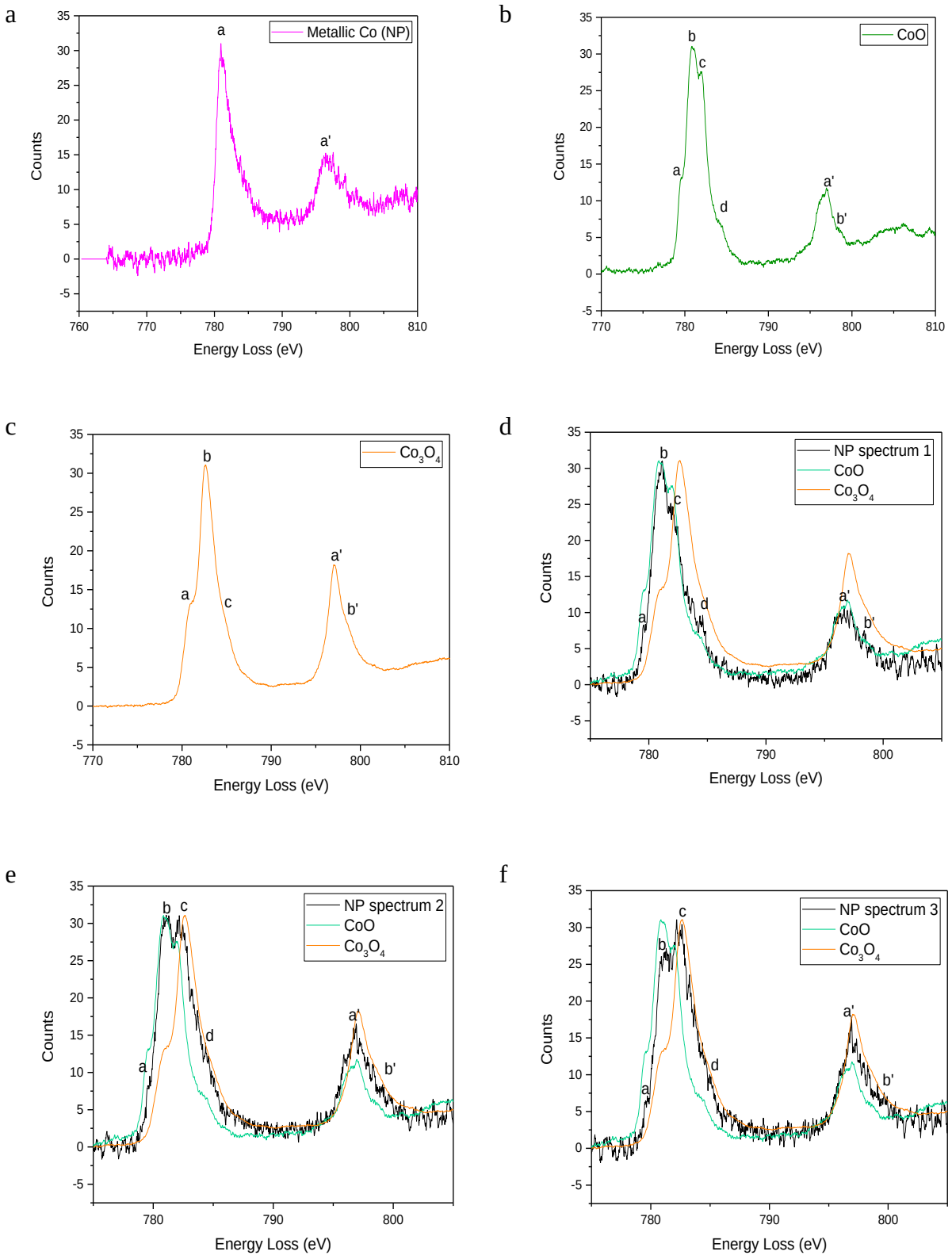


Figure 7.14. EELS Co $L_{2,3}$-edge at 0.025 eV/ch from the (a) nanoparticle metallic cobalt reference, (b) CoO standard, (c) Co_3O_4 standard, (d) overlaid CoO, Co_3O_4, NP spectrum 1, overlaid CoO, (e) Co_3O_4, NP spectrum 2 and (f) overlaid CoO, Co_3O_4, NP spectrum 3. NB: NP spectrum 1, 2 and 3 indicate spectra taken at three different probe positions on a $PtCo_3$ unleached nanoparticle. The labels in panels d, e and f correspond to the NP spectra. All spectra from single pixels.

Although the blue- and red-oxidised nomenclature is developed and used to assign oxidation states, absolute oxidation states can be obtained using the ratios from the relevant side of the curve. This can be done via interpolation from the cobalt standards calibration curve with the following calculation:

A nanoparticle between Co 2+ and Co 2.67+ with L_3/L_2 = 3.4:

Reference L_3/L_2 for Co 2+ and Co 2.67+ is 4.7 and 2.6 respectively.

$|4.7 - 2.6| = 2.1$ (L_3/L_2)

$|2 - 2.67| = 0.67$ (Oxidation State)

$|4.7 - 3.4| = 1.3$ (L_3/L_2)'

1.3/2.1 = 62% of Co 2.67+

0.62 x 0.67 = 0.4

Co oxidation state = 2 + 0.4 = **Co 2.4+**

7.6 Comparison of methodology with MLLS

A popular method for mapping oxidation states across particles is multiple linear least squared fitting (MLLS). This is done using a linear combination of reference spectra from known standards. However, there a few issues. Firstly, MLLS is only effective with a high dispersion. In other words, the only data that can be mapped are those taken at 0.025 eV/ch, the dispersion where the oxygen is absent. It would have been preferable to use the oxygen signal, however, the SNR is very low on the majority of particles for the MLLS fit. An additional problem is that most of the particles studied in this thesis are at the 0.25 eV/ch. A higher dispersion means more peaks are visible, allowing for a better fit. This is particularly vital with the Co $L_{2,3}$-edge at 0.25 eV/ch because its electronic structure is almost indistinguishable across the different oxidation

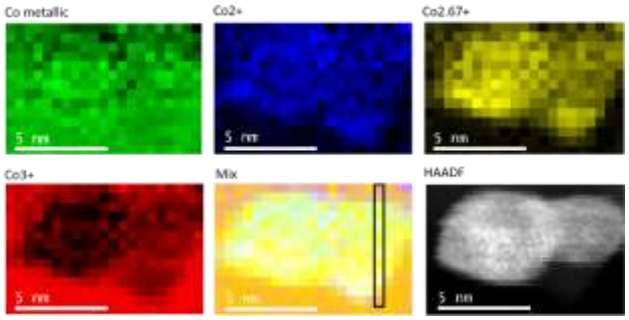
states from the reference standards. MLLS is also challenging in this case due to the low SNR on nanoparticles.

The MLLS procedure is generally implemented on non-denoised data but for parity, it has been done on the denoised data used (Figure 7.15a – f). The SI is 14 x 21 pixels in dimension. The actual dimensions are 174 x 112 pixels from the ADF but the SI was rebinned thrice to boost the EELS signal. The particles shown are $PtCo_3$ unleached particles. The largest is ~6.7 nm in diameter and is underlapped by two smaller particles of ~4.3 nm and ~3.2 nm in diameter. Specifically, the EELS data are averaged laterally from 13 x 12, 8 x 8 and 7 x 5 pixels for the 6. 7 nm, 4.3 nm and 3.2 nm particles, respectively. The number of lateral pixels used for the standards correspond to 6.5 nm, 30 nm, 18.5 nm and 53.6 nm for the metallic Co, CoO, Co3O4 and $LiCoO_2$, respectively. So in general, the sampling volume for the standards are significantly larger relative to nanoparticles compared here. The Co $L_{2,3}$-edge energy used ranges 777 – 810 eV. As perceptible from the RGB images, the MLLS also gets less interpretable with number of increasing references. This is observable in the clearer spatial variation where just three references are used (Figure 7.15c and e) for the mapping compared to all four (Figure 7.15a). Their corresponding relative percentages of the references are also shown (Figure 7.15b, d and f). These percentages are for the pixels highlighted with the black rectangle is the corresponding RGB images and are taken from the fit coefficients of each standard.

Some of the pixels in the SI could not be fit by the MLLS algorithm as they had negative coefficients for that particular standard and so were assigned 0% values. These values mainly arose from the Co 3+ reference. This is understandable because Co 3+ is the least present of oxidation states in the particles studied and so the MLLS fit had more problems when trying to fit all four standards to the SI (Figure 7.15a and b). However, when only three references are used, in the case of the fits without Co 2.67+ (Figure 7.15c and d) and Co 3+ (Figure 7.15e and f), the Co 3+ is fitted better, evident with lesser number of 0% values (Figure 7.15d and f). This

is perceptible from the more even distribution of the percentages in the bottom four pixels of the highlighted region in all four references (Figure 7.15b, d and e). However, RGB images involving the use of three references (Figure 1c and e) show more spatial variation than when all four references are used (Figure 7.15a). This finding is further solidified with the non-metallic states being clearly more identifiable when three references are used (Figure 7.15c and e) compared to when all four are used (Figure 7.15a).

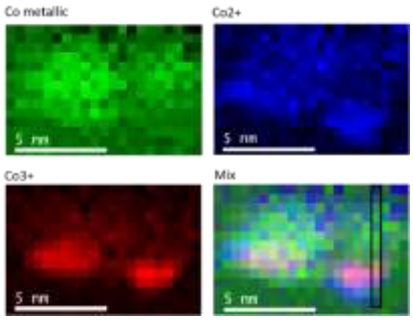
a



b

Co metallic %	Co 2+ %	Co 2.67+ %	Co 3+ %
0	77	23	0
0	67.2	32.8	0
85.6	6.8	7.6	0
98.3	0.5	1.2	0
82.8	12.6	4.6	0
98.7	0.1	1.3	0
98.7	0	1.3	0
81.5	10.9	7.6	0
96.5	0	3.6	0
0	47.8	52.3	0
0	65.9	34.1	0
89.9	8	2.1	0
0	86.9	13.1	0

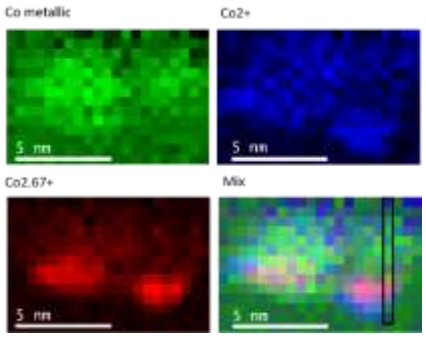
c



d

Co metallic %	Co 2+ %	Co 3+ %
0	100	0
0	100	0
91.9	7.7	0.5
98.8	1.2	0.1
87.9	11.9	0.2
99	0.8	0.2
99.2	0.6	0.2
88.3	10.2	1.4
97.8	0.9	1.4
50.3	39.1	10.6
42.3	51.8	5.9
91.8	8.2	0
0	100	0

e



f

Co metallic %	Co 2+ %	Co 2.67+ %
0	100	0
0	100	0
91.6	7.9	0.5
98.8	1.1	0.1
87.5	12.3	0.2
99.2	0.7	0.2
99.4	0.4	0.2
87.4	10.9	1.7
98.4	0	1.6
0	74.4	25.6
0	88.8	11.2
91.8	8.3	0
0	100	0

Figure 7.15. Images of (a) MLLS RGB Co $L_{2,3}$-edge 777 – 810 eV of $PtCo_3$ unleached particles for respectively for all four references, (b) without Co 2.67+ reference and (c) without Co3+ reference and (d – f) the corresponding relative percentages from each standard present in the black highlighted 12 x 1 pixels, respectively. SI is 14 x 21 pixels in dimension. Data acquired at 0.025 eV/ch.

Using the methodology developed in this thesis, the oxidation state could have also been mapped at each pixel in the SI as is implemented in the method of MLLS fitting. However, it was not trivial to obtain substantial SNR at the high dispersion used. It was also not practical to map all pixels of the SI since this would have been time-consuming, mainly due to performing a background subtraction at every pixel before calculating a white line ratio and oxidation state. Consequently, a summation over shells was the more effective approach and also more relevant to the core-shell morphology of the particles. This was done by taking the outermost 1–2 pixels around a particle. This would look like a pixel layer around the particle and is termed the *shell* while the remaining pixels on the particle is taken as the *core*.

The methodology developed in this thesis was applied to the same particle used for the MLLS (Figure 7.17a – f) and it shows more robustness in mapping out the oxidation states. The spectra from the shells are averaged over 1 pixel width radially and those from the strips are 5 x 1 pixel dimension. Spectra dispersion: 0.025 eV/ch. Whereas in the MLLS method, only three standards showed sufficient spatial variation to distinguish between oxidation states, all four standards have been in this methodology. It is perceptible that the oxidation on the particles is more distinguishable despite constraining the assignments to just blue-oxidised and red-oxidised states (Figure 7.17d). As the particles are not single-column pure states, each pixel has a mixture of oxidation states. The HAADF image is shown for reference (Figure 7.17a). The Co $L_{2,3}$-edge onsets for the sites shown ranges 778.4 – 778.9 eV for the L_3 peak and 795.5 – 795.6 eV for the L_2 peak. The Co $L_{2,3}$-edge has also been mapped out for reference (Figure 7.17b). They have been divided into shells to illustrate the variation in the level of oxidation (Figure 7.17c and d). The two larger particles, P12 (Figure 7.17e) have a smaller range of oxidation states compared to the smaller particle, P3 (Figure 7.17f).

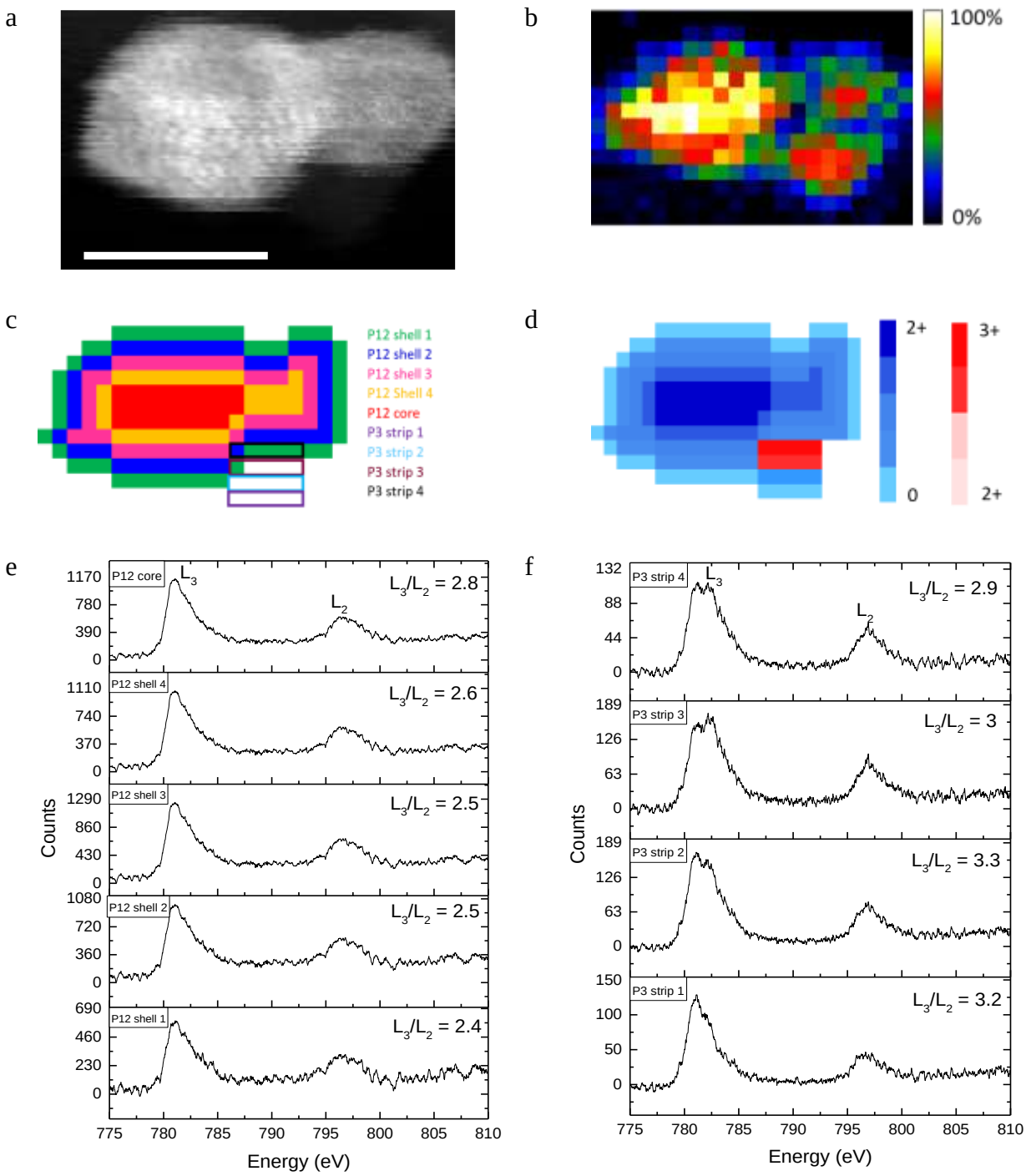


Figure 7.17. A (a) HAADF image of $PtCo_3$ unleached particles, (b) Co $L_{2,3}$-edge map at 778.3 – 800.9 eV, (c) a falsely coloured map of the particle region split into shells, (d) a colour-coded map representing the blue-oxidised and red-oxidised particles, (e) Co $L_{2,3}$-edge of shells in particle 1 and 2 (P12) and (f) in particle 3 (P3). The scattering of P3 is very small but the particle is present. Spectra pixel: width of 1 pixel (shells) and 5 x 1 (strips). Spectra dispersion: 0.025 eV/ch.

It is observable that the oxidation states generally increases as one moves inwards from edge to the centre of P12; a trend also seen in P3 (Figure 7.17d). This is corroborated by the increase in

white line ratios in the blue-oxidised states. For example, a gradual increase is noticeable from $L_3/L_2 = 2.4\pm0.2$ in the outermost shell to $L_3/L_2 = 2.8\pm0.2$ in core of P12, and from $L_3/L_2 = 3.2\pm0.1$ of strip 1 to $L_3/L_2 = 3.3\pm0.2$ of strip 2 in P3. The strips are a row of pixels chosen to analyse the oxidation state on the smallest particle, P3, since only a fraction of it is visible in the HAADF image (Figure 7.17a). Similarly, the ratio of the red-oxidised states decrease from $L_3/L_2 = 3\pm0.1$ of strip 3 to $L_3/L_2 = 2.9\pm0.1$ of strip 4 in P3, evidencing an increase in oxidation state towards the centre of the particle. The fine structure also supports the trend in the ratios as the smallest particle, P3, is the most non-metallic.

7.7 Error Analysis on cobalt oxidation states

As expected, there are various errors associated with the measurements chosen to determine the white line ratios and hence, the oxidation states. Firstly, chemical shifts in the experimental spectrum has to be accounted for in positioning of the HSX (see section 7) before calculating the white line ratio. The errors on the white line ratio using this method is between 0.9 – 3.9% from the average value. They were calculated from the standard deviations between each ratio calculated with each shift in eV required to centre the HSX at the corresponding peak.

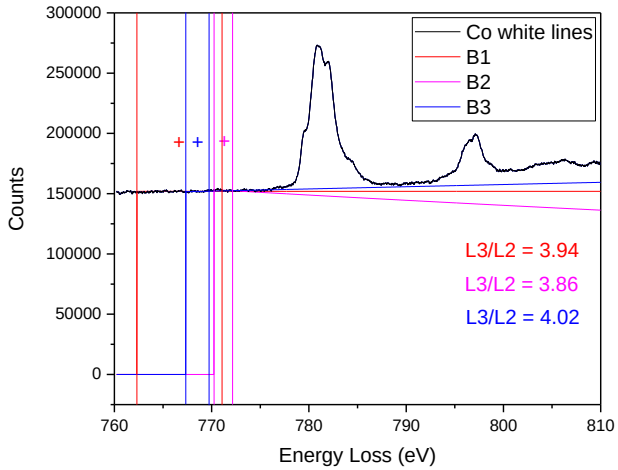


Figure 7.18. EEL spectrum of Co $L_{2,3}$-edge from a CoO standard showing different slopes (B1 – B3) used for the Power-Law background subtraction. Spectrum averaged over 24 x 35 pixels. Spectra dispersion: 0.025 eV/ch.

Another error to take into consideration is the effect of the Power-Law background subtraction on the white line ratios. This was implemented by varying the slope of the background by shifting the background window (Figure 7.18) and then taking the standard deviation from the average value. The spectrum was averaged over 24 x 35 pixels of the SI. The slopes were pushed to the limit such that the ratios were reasonable. For example, slopes less than B1 (Figure 7.18) gave less than a 90° angle with respect to the background, meaning that the slope cut into the cobalt L_2 and L_3 peak, yielding an incorrect measurement of the background and thus, the edge. Similarly, slopes greater than B3 (Figure 7.18) significantly larger than a 90° angle, which also gave incorrect results due to the large amount of background been added into the calculation of the white line ratio. The example shown here from the three different slopes pushed as far away from each other as reasonable. The resultant ratios found were 3.9, 3.9 and 4, for B1, B2 and B3 respectively, yielding a 3% error on the average of the three values. Depending on the SNR in the spectra, errors were found to be between 2 – 10%, which are within acceptable boundaries of quantification [140].

Errors in the white line ratios themselves, when everything else is constant, are calculated differently. The errors were calculated according to Varela *et al.* [140] whereby the position of the integration windows are varied and the resulting white line ratios compared. This was done by moving the integration windows 3 eV either side of the initial position of the integration windows and the standard deviation taken between the resulting white line ratios. Generally, the errors were between 1 – 9%. However, for a few nanoparticles with very low SNR, the errors were as high as 50%. It should be noted that due to the asymmetry and difference in electronic structure of each of the white line peaks, the error tends to be larger on the window shifted to the right of the peaks, introducing a larger error than there otherwise would be on the white line ratios.

The last set of errors and probably the most significant stem from the fact that not all the white line ratios from the nanoparticles lie within the standard calibration curve. This was found to be mainly an issue stemming from the metallic reference. Using the nanoparticles for the metallic reference gave approximately 30% reduction in the average white line ratio, compared to the standard. Some ratios still did not lie within the calibration curve. More detail on the source of this discrepancy is discussed further in section 7.8.

7.8 Validity of oxidation state assignment

The fact that the white line ratios from the nanoparticles do not all lie within the calibration curve poses the most problem with oxidation assignment. This was found to be mainly an issue with the blue-oxidised states; in other words, the near-metallic states (Co 0 – 2+). Despite using the nanoparticles for the metallic reference, with an approximately 30% reduction in white line ratio compared to the metallic standard, as much as 75% of the particle ratios between the Co 0 – 2+ oxidation states did not lie within the calibration curve. Compared to only 8.9 % of those between the Co 2+ – 3+ oxidation states, at first glance, it appears that the lack of a congruent metallic cobalt standard plays a major role. However, 90% of these ratios had a $\leq$10 signal-to-background-ratio (SBR), relative to the L_3 peak. As an example, the spectrum of a shell from one of the Pt_3Co leached particles studied is shown (Figure 7.19). The spectrum is averaged over 10 x 10 pixels of the SI. The SBR was found to be approximately 3.1 with a white line ratio of 2.5 ± 0.4, which is 0.6 less than the cobalt metallic ratio on the calibration curve. As observable, the fine structure has sufficient signal and SNR to be quantifiable and so ratios not lying on the calibration curve does not seem to stem from the SNR. Hence, the SBR seems to be the dominant factor in the low metallic ratios. However, it is important to note that this finding is inconclusive because there just may be some part of the physics that is not being taken into account as to why these ratios do not lie within the calibration curve.

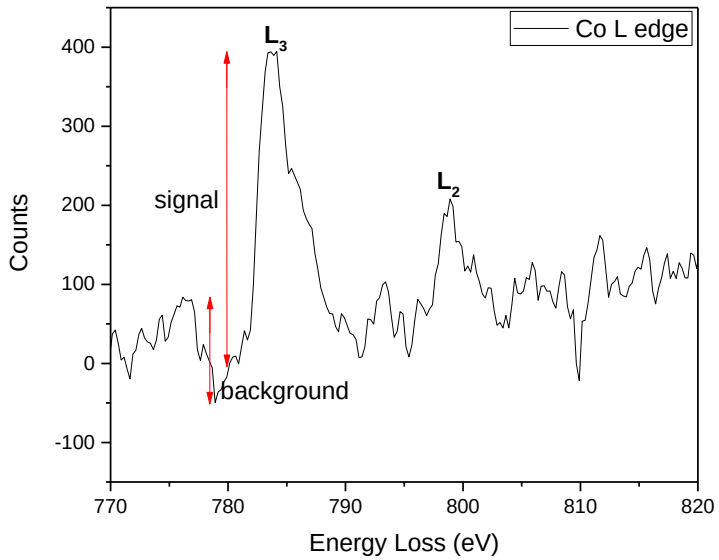


Figure 7.19. EEL spectrum of Co $L_{2,3}$-edge from shell of a Pt_3Co leached particle, showing signal and background. Spectrum averaged over 10 x 10 pixels. Spectra dispersion: 0.25 eV/ch.

7.9 Noise correlation

The determination of oxidation states proved difficult in the assignment of subtle peaks, especially in spectra with low SNR. While this is generally expected with low SNR, in this study, there appeared to be some noise correlation in the spectra (Figure 7.20) or a fixed pattern noise. The spectrum from the core is averaged over 4 x 4 pixels; that of the shell is over 25 pixels and 2 pixel widths radially. Fixed pattern noise is a repetitive patterns in the EEL spectrum not arising from the physics of the fine structure but due to incorrect dark/gain correction. This introduced further uncertainties when trying to differentiate between real spectral peaks and artefacts. This is because the noise was on the same scale as the fixed pattern noise. The noise correlation seemed to grow with a larger ROI or the number of summed spectra. This phenomenon could not be alleviated by PCA because multivariate methods only eliminate the random noise but not the systematic noise [214,215]. This systematic noise is seen in the first few principal components in PCA and permeates the entire dataset. For example, the O *K*-edge spectra of the $PtCo_3$ unleached particle from chapter 8, section 8.1 has been zoomed into to highlight this issue.

Between 550 – 600 eV, a strong correlation can be seen in the noise, precluding a confident assignment of the peak labelled *e* (Figure 7.20). Apart from subtle peaks such as *e*, this also seemed to affect peak *a*, which is related to the occupancy of the Co 3*d* states. Consequently, this made peaks at the scale of the fixed pattern noise unreliable to assign.

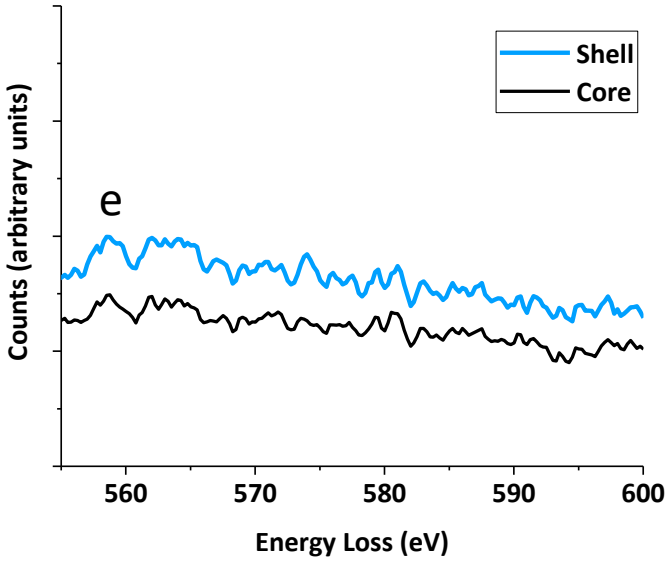


Figure 7.20. EELS O *K*-edge of $PtCo_3$ unleached particle, showing only 550 – 600 eV range. Spectrum averaged over 15 pixels (core) and 25 pixels (shell). Spectra dispersion: 0.25 eV/ch.

Given the mixture of oxidation states across the particles, the noise correlation only made the distinction between a blue-oxidised and red-oxidised state all the more difficult. To narrow down possible causes, the first few principal components were plotted separately. However, after dissecting over 30 components, it was clear that the noise correlation could not be eliminated. Individual spectra from each pixel do not appear to be correlated, however, summing a multitude of them reveals some channel-to-channel correlation. This phenomenon has also been seen by Bosman and Keast [214] and so it was likely that this systematic error originated from the raw, unprocessed data.

The raw SI was examined in order to pinpoint the source of the noise correlation. The data was unaligned and was not put through PCA. Spectra from 4 separate quadrants of the SI were plotted (Figure 7.21a and b). The spectrum from each quadrant is averaged over 10 x 18 pixels. From the spectra, it appears that peak *a* does not suffer from as much noise correlation compared to *e*, most noticeable in the dip at approximately 563 eV. While peaks *b* and *c* appear to be sufficiently distinct, peaks *d* appears to be affected by the noise correlation, evidenced by the dip at approximately 555 eV. Given that distinction between a blue-oxidised and red-oxidised state is mainly peak *a*, the assignment of the oxidation states in this format seems fairly reliable. However, the source of the noise correlation could still not be identified and this definitely reduces the validity in the assignment of absolute oxidation states.

a

b

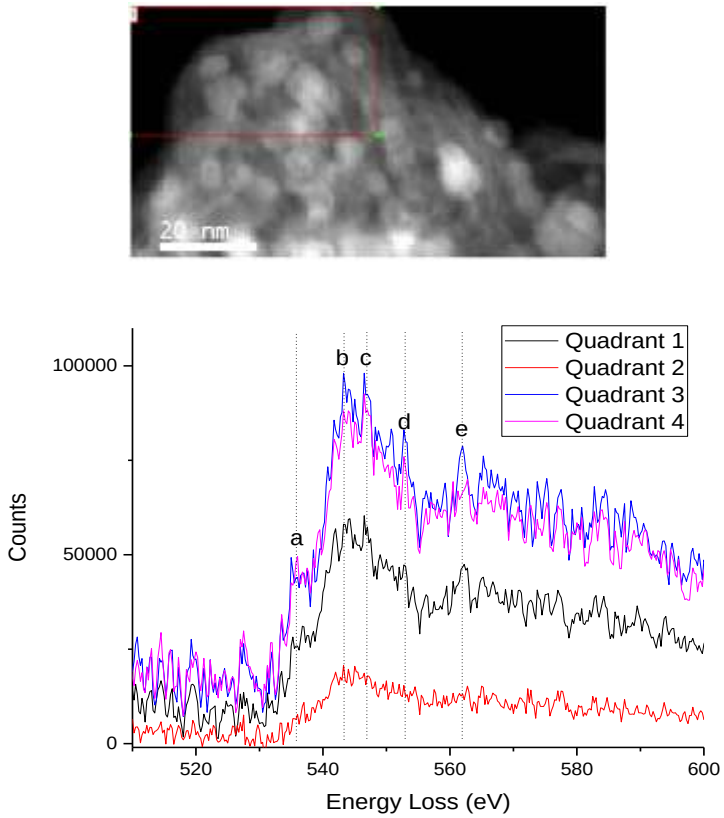


Figure 7.21. The EELS SI from (a) a $PtCo_3$ unleached and (b) O *K*-edges from each of four quadrants taken from the raw data. Spectrum from each quadrant is 10 x 18 pixels. Spectra dispersion: 0.25 eV/ch.

While the exact source of the noise correlation could not be distinguished, it does appear to be from erroneous dark and gain reference corrections. Given that the dark reference is taken just

after the spectrum image and is usually a tenth of the SI dwell time, the consensus is that the short acquisition time introduces correlated artefacts [214,215]. One method for alleviating this is binned gain-averaging [214,215], done by shifting the spectrum over a series of CCD pixels. The CCD channels are binned and aligned in order to obtain a smoother gain reference, followed by the subtraction of an average dark reference. This improves the SNR of both the energy and spatial resolution.

A related method for improving SNR, later developed is a beam-blanking method that yields a smoother background or noise variation, while improving the SNR in the EEL spectrum [200]. As earlier mentioned, the dark reference is taken long after the SI, and is only a tenth of the SI dwell time. As such, the validity of the dark reference comes into question. Consequently, a script was developed by Dr Aakash Varambhia and Dr. Lewys Jones, where after each row of pixels in an EELS SI image is acquired, the CCD stops collecting irradiation, yielding just the dark reference. As this is collected after each row, there is more acquisition time for the dark reference readout. This dark reference is then subtracted from the SI spectra and the gain reference recorded independently from the SI acquisition. Combining this with binned averaging and drift tube variation has been shown to improve the SNR and assignment of the more subtle features in the EEL spectrum.

7.10 Conclusions

The method for the extraction of cobalt oxidation states in PtCo bimetallic systems using quantitative EELS measurements has been outlined. By analysing the Co $L_{2,3}$-edge and O *K*-edge and comparing to cobalt standard references, it is shown that oxidation states in the nanoparticles containing cobalt can be estimated. The methodology developed has also been compared to the MLLS method and it appears to give more spatial variation in the mapping of oxidation states when all four standards are used as references. The white line ratio of the calibration curve from

the standards has a vertex at the Co 2+ oxidation state, introducing ambiguity either side of the curve. This is trend in the ratios is congruent with literature. The ratios were within 2 – 10% from the values calculated using the developed methodology and so congruence can be seen with literature. However, the onset energies increase between the metallic cobalt state and Co 2+ state. The opposite was seen in this study and the reason for this is still unknown.

The error in this method has been alleviated using a peak-to-peak comparison to the O *K*-edge, or when not available, to the Co $L_{2,3}$-edge at a higher dispersion. The peaks are fingerprints of specific electronic information about the density of states, indicative of the cobalt oxidation state. The majority of the errors between the white line ratios measured were below 10%; errors in their measurements i.e. background and chemical shifts were a lot lower. Considering that the samples used to demonstrate this method are nanoparticles, with some having low SNR, this method is very promising, especially for larger systems which would have a much higher SNR. The use of multi-frame spectroscopy would boost the SNR, allowing for better analysis of the fine structure, making the methodology for the extraction of oxidation states more robust.

7.11 References

[183] Zheng F, Alayoglu S, Guo J, Pushkarev V, Li Y, Glans P, Chen J and Somorjai G 2011 In-situ X-ray Absorption Study of Evolution of Oxidation States and Structure of Cobalt in Co and CoPt Bimetallic Nanoparticles (4 nm) under Reducing (H_2) and Oxidizing (O_2) Environments *Nano Lett*. **11**, 847–853

[184] Jansson J 2000 Low-Temperature CO Oxidation over Co_3O_4/Al_2O_3 *J. Cat.* **194** 55–60

[185] Aric A S, Shukla A K, Kim H, Park S, Min M and Antonucci V 2001 An XPS study on oxidation states of Pt and its alloys with Co and Cr and its relevance to electroreduction of oxygen *Appl. Surf. Sci.* **172**, 33–40.

[186] A. K. Shukla A K, M. Neergal M, P. Bera P, V. Jayaram V, M. S. Hegde M S 2001 An XPS study on binary and ternary alloys of transition metals with platinized carbon and its bearing upon oxygen electroreduction in direct methanol fuel cells *J. Electroanal. Chem.* **504**, 111–119.

[187] Wang D, Xin H L, Hovden R, Wang H, Yu Y, Muller D A, DiSalvo F J and Abruña H D 2013 Structurally ordered intermetallic platinum–cobalt core–shell nanoparticles with enhanced activity and stability as oxygen reduction electrocatalysts *Nat. Mater*. **12** 81–86

[188] Liu Z, Xin H, Yu Z, Zhu Y, Zhang J, Mundy J A, Muller D A and Wagner F T 2012 Atomic Scale Compositional Mapping and 3-Dimensional Electron Microscopy of Dealloyed $PtCo_3$ Catalyst Nanoparticles with Spongy Multi-Core/Shell Structures *J. Electrochem. Soc.* **159**, 554–558.

[189] Schulenburg H, Müller E, Khelashvili G, Roser T, Bönnemann H, Wokaun A and Scherer G G 2009 Heat-Treated PtCo3 Nanoparticles as Oxygen Reduction Catalysts *J. Phys. Chem. C* **113**, 4069–4077

[190] Yu Z, Zhang J, Liu Z, Ziegelbauer J M, Xin H, Dutta I, Muller D A, Wagner F T 2012 Comparison between dealloyed $PtCo_3$ and $PtCu_3$ cathode catalysts for proton exchange membrane fuel cells *J. Phys. Chem. C* **116**, 19877–19885

[191] Gatan Microsocopy Suite 2018. *EFTEM SI Artifact Correction. http://www.eels.info/how/spectrum-imaging/eftem-si-optimization*

[192] De la Peña F, Ostasevicius T, Fauske V T, Burdet P, Prestat E, Jokubauskas P, Nord M Sarahan M, MacArthur K E, Johnstone D N, Taillon J, Caron J, Migunov V, Furnival T, Eljarrat A, Mazzucco S, Aarholt T, Walls M, Slater T, Winkler F, Martineau B, Donval G, McLeod R, Hoglund E R, Alxneit I, Hjorth I, Henninen T, Zagonel L F and Garmannslund A. (2018, September 19). hyperspy/hyperspy: HyperSpy v1.3.2 (Version v1.3.2). Zenodo. http://doi.org/10.5281/zenodo.1221347

[193] De la Peña F, Berger M H, Hochepied J F, Dynys F, Stephan O and Walls M 2011 Mapping titanium and tin oxide phases using EELS: An application of independent component analysis *Ultramicroscopy* **111** 169–176

[194] De la Peña F, Prestat E, Fauske V T, Burdet P, Jokubauskas P, Nord M, Garmannslund A. (2019, September 6). hyperspy/hyperspy: HyperSpy v1.5.2 (Version v1.5.2). Zenodo. http://doi.org/10.5281/zenodo.3396791

[195] Wold S, Esbensen K and Geladi P 1987 Principal Component Analysis *Chem. Int. Lab. Sys.* **2** 37–52

[196] De la Peña F 2010 *Advanced methods for Electron Energy Loss Spectroscopy core loss analysis* (Paris-Sud)

[197] Astakhov S A, Stögbauer H, Kraskov A and Grassberger P 2006 Monte Carlo Algorithm for Least Dependent Non-Negative Mixture Decomposition *Anal. Chem.* **78** 1620–1627

[198] Meyer W, Hock D, Biedermann K, Gubo M, Muller S, Hammer L, and Heinz K 2008 Coexistence of Rocksalt and Wurtzite Structure in Nanosized CoO Films *Phys. Rev. Lett.* **101** 1–4

[199] Nam K M, Shim J H, Han D, Kwon H S, Kang Y, Li Y, Song H, Seo W S and Park J T 2010 Syntheses and Characterization of Wurtzite CoO, Rocksalt CoO, and Spinel Co_3O_4 Nanocrystals: Their Interconversion and Tuning of Phase and Morphology *Chem. Mater.* **22** 4446–4454

[200] Greenwood N N and Earnshaw A 1997 *Chemistry of the Element* (Oxford: Butterworth-Heinemann)

[201] Xiong F, Yan H J , Chen Y, Xu B, Le J X, Ouyang C Y 2012 The Atomic and Electronic Structure Changes Upon Delithiation of $LiCoO_2$: From First Principles Calculations *Int. J. Electrochem. Sci.* **7** 9390–9400

[202] Hertz J T, Huang Q, McQueen T, Klimczuk T, Bos J W G, Viciu L and Cava R J 2008 Magnetism and structure of Li_xCoO_2 and comparison to Na_xCoO_2 *Phys. Rev. B* **77** 1–11

[203] Qian D, Hinuma Y, Chen H, Du L, Carroll K J, Ceder G, Grey C P and Meng Y S 2012 Electronic Spin Transition in Nanosize Stoichiometric Lithium Cobalt Oxide *J. Am. Chem. Soc.* **134** 6096–6099

[204] EELS DATABASE 2020. *EELS Database: Oxygen. https:// https://eelsdb.eu/spectra*

[205] Kitakami O, Sato H, and Shimada Y 1997 Size effect on the crystal phase of cobalt fine particles *Phys. Rev. B* **56** 849–853

[206] O'Shea V A D, de la Piscina P R, Homs N, Aromi G and Fierro J L G 2009 Development of hexagonal closed-packed cobalt nanoparticlesstable at high temperature. *Chem. Mater*. **21** 5637–5643

[207] Webster R W H, Craven A J, Schaffer B, McFadzean S, MacLaren I and MacLaren D A 2020 Correction of EELS dispersion non-uniformities for improved chemical shift analysis *Ultramicroscopy* **217** 1–6

[208] De Groot F M F, Grioni M, Fuggle J C, Ghijsen J, Sawatzky G A and Petersen H 1989 Oxygen 1*s* X-ray-absorption edges of transition-metal oxides *Phys. Rev. B* **40** 5715–5722

[209] Suntivich J, Hong W T, Lee Y, Rondinelli J M, Yang W, Goodenough J B, Dabrowski B, Freeland J W and Shao-Horn Y 2014 Estimating Hybridization of Transition Metal and Oxygen States in Perovskites from O K-edge X-ray Absorption Spectroscopy *J. Phys. Chem. C* **118** 1856–1863

[210] Han B, Qian D, Risch M, Chen H, Chi M, Meng Y S and Shao-Horn Y 2015 Role of $LiCoO_2$ Surface Terminations in Oxygen Reduction and Evolution Kinetics *J. Phys. Chem. Lett.* **6** 1357−1362

[211] Yoshimatsu K, Wadati H, Sakai E, Harada T, Takahashi Y, Harano T, Shibata G, Ishigami K, Kadono T, Koide T, Sugiyama T, Ikenaga E, Kumigashira H, Lippmaa M, Oshima M and Fujimori A 2013 Spectroscopic studies on the electronic and magnetic states of Co-doped perovskite manganite $Pr_{0.8}Ca_{0.2}Mn_{1-y}Co_yO_3$ thin films *Phys. Rev. B* **88** 1−6

[212] Mesilov V V, Galakhov V R, Gubkin A F, Sherstobitova E A, Zakharova G S, Uimin M A, Yermakov A Y, Kvashnina K O and D. A. Smirnov D A 2017 X-ray Diffraction and X-ray Spectroscopy Studies of Cobalt-Doped Anatase TiO_2:Co Nanopowders *J. Phys. Chem. C* **121** 24235−24244

[213] Galakhov V R J 2021 X-Ray Spectroscopy of Cobaltites *Phys. Met. Metallogr.* **122** 83–114

[214] Bosman M and Keast V J 2008 Optimizing EELS acquisition *Ultramicroscopy* **108** 837–846

[215] Haruta M, Fujiyoshi Y, Nemoto T, Ishizuka A, Ishizuka K and Kurata H 2019 Extremely low count detection for EEL spectrum imaging by reducing CCD read-out noise *Ultramicroscopy* **207** 1–6

8 Oxidation of PtCo alloys

8.1 Comparison of Core-Shell Oxidation in PtCo alloys

To recap, the samples to be studied are a matrix of four alloys: $PtCo_3$ uleached, $PtCo_3$ uleached, Pt_3Co unleached and Pt_3Co leached. In order to study and compare the oxidation across the alloys, the methodology developed in chapter 7 is applied here. While the methodology for both the 0.25 eV/ch and 0.025 eV/ch dispersions are implemented here, the majority of the particles presented here were taken at the 0.25 eV/ch dispersion and as such is the predominant method used in this chapter. Due to the limitations of the methodology expressed in sections 7.4 – 7.8, this prohibited the assignment of absolute oxidation states to all the particles studied. As some of the ratios from the particles do not lie on the calibration curve, this also limits the sample size for study.

Considering the ratio differences between dispersions, it is better to err on the side of caution in assigning absolute oxidation states. Instead, the blue-oxidised (Co 0 – 2+) and red-oxidised (2+ – 3+) terminology introduced in chapter 7, section 7.5, has been implemented here. However, some particles were still able to be assigned oxidation states and this is discussed in section 8.3. As mentioned in chapter 7, section 7.5, all nanoparticles studied ranged Co 0 – 2.67+ and none were found to be Co 3+. This is congruent with literature where oxygen atoms are found to adsorb on Co 2+ metal centres on cobalt nanoparticles. States higher than Co 2+ were attributed to Co-O charge transfer and no Co 3+ metal centres were found [216].

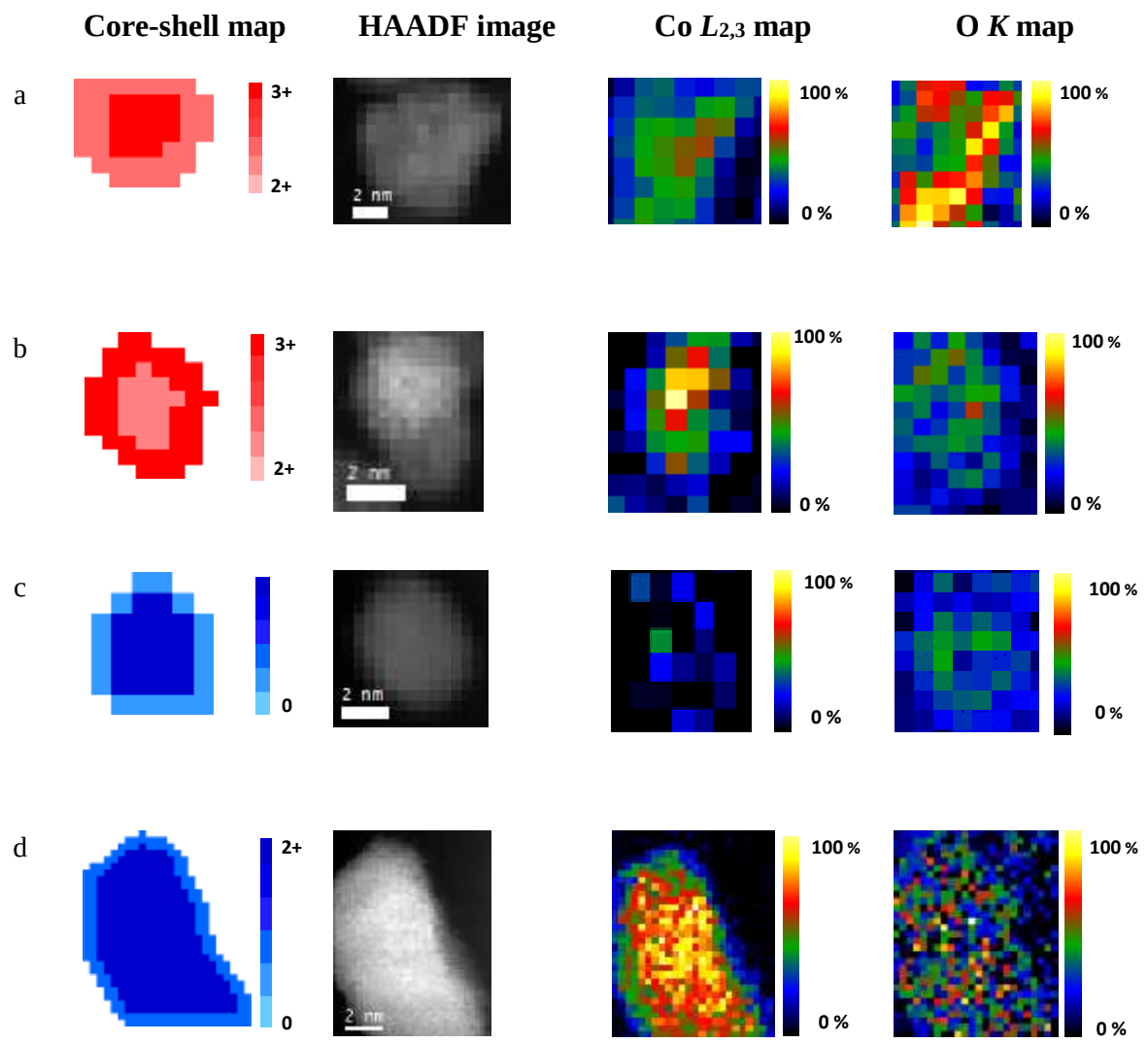


Figure 8.1. Experimental data of (a) $PtCo_3$ unleached, (b) $PtCo_3$ leached, (c) Pt_3Co unleached and (d) Pt_3Co leached particles. Left to right: cobalt core-shell map, HAADF image, cobalt $L_{2,3}$-edge RGB map and oxygen K-edge RGB map. NB: The colour scalebars on the Co $L_{2,3}$ and O K maps are absolute intensities from *Digital Micrograph*. Data acquired at 0.25 eV/ch.

An example of each of the four PtCo sample types are shown (Figure 8.1a – d). The particles are medium-sized, approximately 6 – 11 nm. Their HAADF images are shown for cross-correlation with the cobalt core-shell and elemental RGB maps. The corresponding spectra for each particle is also presented for comparison (Figure 8.2a – d). The core-shell maps are separated by pixel layers. As described in chapter 7, section 7.6, the outermost 1– 2 pixels of the particle form the shell while the rest is taken as the core. Particles with lower SNR have 2 layers as the shell. Since the pixels are rebinned to maximise SNR before the core-shell map is

created, the total number of pixel layers on the shells of the unbinned data is actually 4–8 pixels. In terms what this means atomically, given that the bond lengths of in the Pt_3Co and $PtCo_3$ fcc lattices are 275 pm and 260 pm, respectively, they can be substituted for the atomic diameters. The bond lengths were derived from crystal lattice models after relaxation using DFT (see chapter 10, Table 10.1 for crystal models/lattice parameters and references used).

The pixel size changes depending on the time spent on the particle i.e. size of the particle or stability of the particle may require using a larger or smaller pixel size. This means the pixel size varies for the particles and is limited by the STEM settings. The pixel size for all particles studied ranged between $2.89 \times 10^4 - 3.36 \times 10^5$ pm^2 in square pixels. This translates to 170 – 580 pm in pixel length and width. Assuming a pixel width of 170 pm per pixel, each pixel layer is 680 pm$\pm$170 pm. Hence, the number of atoms is 680 pm/275 pm and 680 pm/260 pm for the Pt_3Co and $PtCo_3$ samples, respectively. This gives 2.5 atoms for the Pt_3Co samples and 2.6 atoms for the $PtCo_3$ samples, per pixel layer. In other words, the width of each shell comprises 2.5 – 5.0 atoms for the Pt_3Co samples and 2.6 – 5.2 atoms $PtCo_3$ samples at the pixel width of 170 pm. These would be equivalent to 8.4 – 16.9 atoms for the Pt_3Co samples and 8.9 – 17.9 atoms $PtCo_3$ samples at a pixel width of 580 pm.

The Co $L_{2,3}$-edge ranges 778.5 – 781.9 eV for the L_3 peak and 793.8 – 797.9 eV for the L_2 peak (Figure 8.2a – d). The peaks labelled *a* and *a'* are the 2*p* to 3*d* transitions while *b* and *b'* are 2*p* to 4*s* transitions [137]. The O *K*-edge for all four samples ranges 530.1 – 534.8 eV with a tail reaching ~600 eV. As mentioned in chapter 7, peak *a* is a pre-peak represents O2*p*–Co3*d* transitions while peaks *b* and *c* arise from O2*p*–Co4*sp* hybridised transitions. The consensus is that the pre-peak intensity increases with higher cobalt oxidation state due to the increased number of unoccupied Co 3*d* states available for electron transitions [137,208,209]. This can be seen where peak *a* decreases going from the $PtCo_3$ unleached particle to the Pt_3Co leached particle (Figure 8.2a – d) and this is representative of all particles studied.

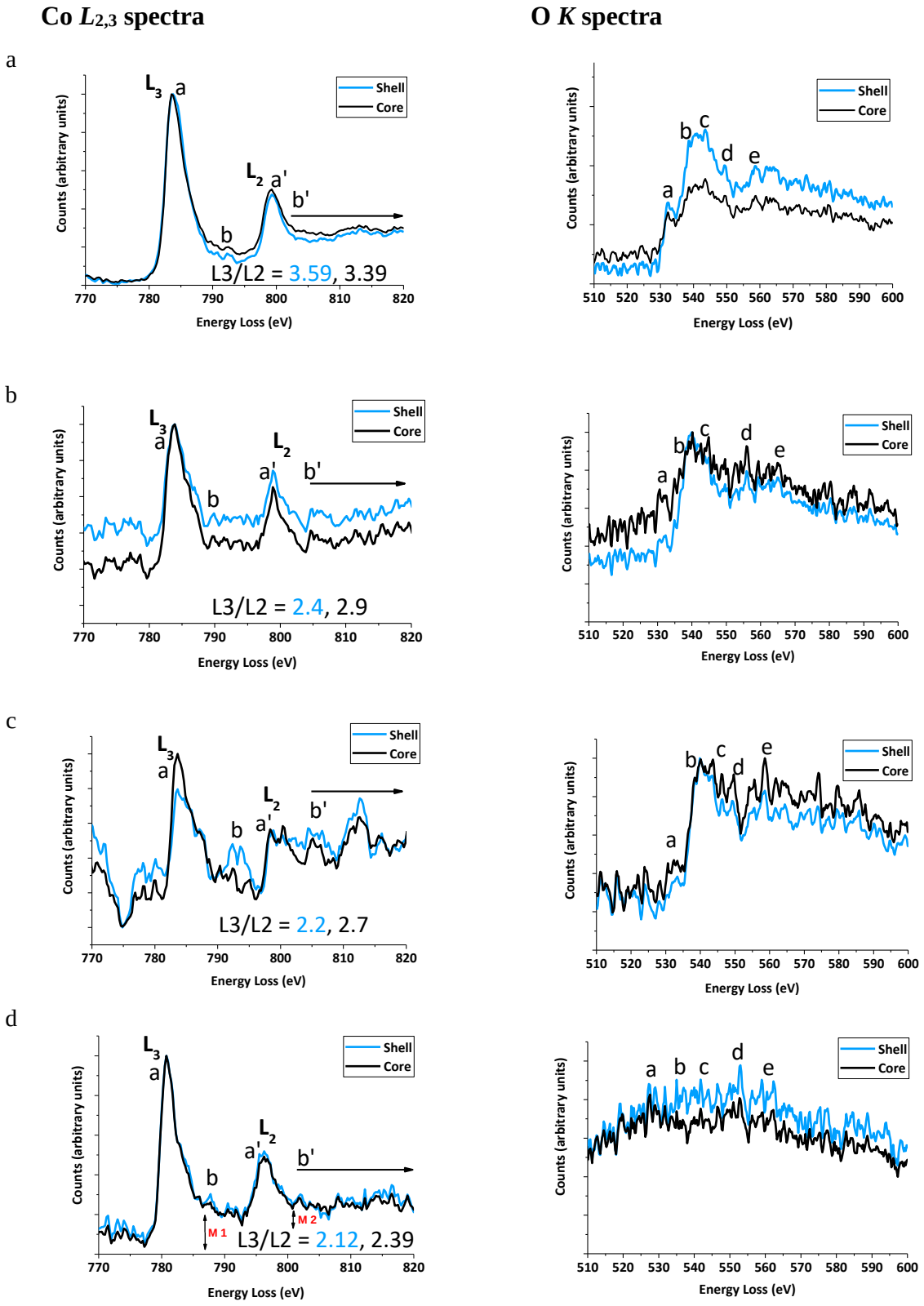


Figure 8.2. O *K*-edges of particles in figure 8.1; (a) $PtCo_3$ unleached, (b) $PtCo_3$ leached, (c) Pt_3Co unleached and (d) Pt_3Co leached particles. The Co $L_{2,3}$-edge and O *K*-edge spectra with normalised counts. NB: $L_{2,3}$ ratio is increases between the oxidation states 0 – 2+ but decrease between 2 – 3+. Spectra pixel: 7 x 8 ($PtCo_3$ unleached), 10 x 8 ($PtCo_3$ leached), 7 x 6 (Pt_3Co unleached) and 30 x 25 (Pt_3Co leached). Spectra dispersion: 0.25 eV/ch.

The white line ratios in the core and shell of the $PtCo_3$ unleached particle are L_3/L_2 = 3.4±0.3 and 3.6±0.3, respectively (Figure 8.2a). A peak-to-peak comparison to with the standards, according to the methodology (see chapter 7, section 7.5), showed this particle to be red-oxidised. Peak *a* in the $PtCo_3$ unleached O *K*-edge spectra (Figure 8.2a) is strong evidence of being red-oxidised, as well as the significantly higher minimum formed by peak *d* and *e* with that formed by peak *a* and *b*, indicating that the oxidation state is between Co 2+ and Co 2.67+. The $PtCo_3$ leached particle also exhibit these features, albeit to a lesser degree, and so is also red-oxidised. However, the $PtCo_3$ leached particle has lower ratios in the core and shell with L_3/L_2 = 2.9±0.1 and 2.4±0.3, respectively, compared to the $PtCo_3$ unleached (Figure 8.2b). Since the white line ratio decreases with oxidation state between the 2+ and the 3+ state [137], the $PtCo_3$ leached particle so is more oxidised than the $PtCo_3$ unleached. For the $PtCo_3$ unleached particle, peaks *b* – *e* (Figure 8.2a) are fairly similar to the Co 2.67+ or Co 3+ standards, despite the lower SNR in the nanoparticles spectra. However, the intensity of peak *a* is not as high as the Co 2.67+ or Co 3+ standard. Thus, this peak could be indicative of contamination; possibly oxygen bound to amorphous carbon. The core is found to be more oxidised than the shell in the $PtCo_3$ unleached particle, but the opposite is true in the $PtCo_3$ leached. Comparing their white line ratios alone, it is seen that the $PtCo_3$ unleached particle is less oxidised than the $PtCo_3$ leached particle. However, this is not easily differentiated by the O *K* edge alone. This is why a combination of the ratios and the fine structure is important for the assignment of oxidation states.

In contrast, the cobalt in the Pt_3Co leached and unleached particles are more metallic in nature and are blue-oxidised (Figure 8.1c and d, 8.2c and d). In the Pt_3Co unleached O *K* spectra (Figure 8.2c), while the minimum formed by peak *d* and *e* is significantly higher than that formed by peak *a* and *b*, peak *a* is on the same level as noise and so the oxidation state assignment is very difficult. As the sharpness and intensity of peak *a*, is a major feature of red-oxidised states, this

particle is assigned as blue-oxidised. At the 0.25 eV/ch dispersion, the peaks in the fine structure of the cobalt is not used. However, the presence of metallic cobalt is usually evidenced by a high continuum edge jump [137,217], in the energy range between peaks *b – a'* and after peak *b'* in the Co $L_{2,3}$-edge (Figure 8.2a, c and d). This is mainly seen in the Pt_3Co particles. The Pt_3Co leached particle has been used to illustrate this (Figure 8.2d). Specifically, the higher the M1/M2 ratio, the more metallic the spectrum; the similar M1 and M2 are, the more oxidised the spectrum. The reason this is also noticeable in the red-oxidised $PtCo_3$ unleached particle (Figure 8.2a) is most likely because not enough of the cobalt is strongly oxidised, evident from the Co $L_{2,3}$-edge and O *K*-edge RGB maps (Figure 8.1a).

It is also noticeable that while the core has more area oxidised than the shell of the $PtCo_3$ unleached particle, the ratios show the opposite (Figure 8.1a). This points out that a larger area of oxygen distribution is not always tantamount to a higher oxidation state. It is also interesting to highlight the distinct shape of the $PtCo_3$ leached Co $L_{2,3}$-edge compared to the other three particles (Figure 8.2b). The intensities of M1 and M2 are approximately the same and the L_2 peak is larger, corroborating the red-oxidised state of the $PtCo_3$ leached particle. Essentially, when a large proportion of the cobalt is strongly oxidised on a particle, this fine structure is strong evidence of a very non-metallic oxidation state. Again, at this dispersion, the cobalt fine structure is not used, but becomes a useful tool when the features are that prominent.

The core and shell white line ratios of the Pt_3Co leached and unleached particles are L_3/L_2 = 2.4 ± 0.1, 2.1 ± 0.2 and 2.7 ± 1.2, 2.2 ± 0.6, respectively. The error on the Pt_3Co unleached core is very high and because the fine structure is very noisy, this state is not as reliable. This means that the cores are more oxidised than the shells, however, both particles are still less oxidised than the $PtCo_3$ particles. The majority of the particles studied are core-shell with a cobalt-rich core; less so when leached. For particles that are oxidised, the oxygen tends to aggregate at the cobalt core for particles. The amount of oxygen variation is particle dependent. For example,

after integrating the O *K* edge and Co $L_{2,3}$-edge intensities and subtracting their cross sections, the corresponding intensities in the shell and core can be divided by the sum of the two to obtain the ratio of cobalt and oxygen distribution of a given nanoparticle. This gave 30%, 29%, 58% and 85.3% oxygen distribution in the cores for the $PtCo_3$ unleached, $PtCo_3$ leached, Pt_3Co unleached and Pt_3Co leached particles, respectively. Across all 80 particles measured, more than half had over 50% oxygen distribution in the core of the particle. As earlier mentioned, a larger area of oxygen surface coverage does not always mean a higher oxidation state. This can be seen from in the $PtCo_3$ unleached particle where the core oxygen distribution is calculated to be 30% but is more oxidised than the shell. The reason for this is unknown. It is also noteworthy that the Pt_3Co particles have a much larger error i.e. ≥10% compared to ≤10% in the $PtCo_3$ particles. While this is due to low SNR, this is also worsened by a lower cobalt content. However, the low cobalt content could also be the cause of the low SNR. For this reason, in addition to the fact that the leached system also has a significantly lower cobalt content, the shape of the O *K*-edge becomes vital as added confirmation of the oxidation states as opposed to solely using the white line ratios.

Going back to the O *K*-edge map of the $PtCo_3$ particle and comparing it to the Co $L_{2,3}$-edge RGB map (Figure 1a), most of the cobalt-rich core is not oxidised. This could mean that the platinum is preferentially oxidised, given that the O *K*-edge map shows oxygen on the shell but the cobalt core-shell map shows the core to be more oxidised than the shell. It could also be due to a possible surface contaminant but this is unlikely as a trend would be seen. Furthermore, while the peaks *b* – *d* of the $PtCo_3$ unleached core O *K*-edge are significantly more intense than those of the shell, it is not clear that this is indicative of a higher oxidation state. Similarly, in the Pt_3Co unleached particle O *K*-edge spectra, it is observable that in the core, the intensity of the O2*p*–Co4*sp* transitions, beyond peak *d*, are reduced relative to those in the shell (Figure 8.2c). This is also accompanied by a change in electronic structure of the Co $L_{2,3}$-edge. Again, the

source of this is unknown and it is unclear what it means in terms of the oxidation state. A better SNR would have allowed for a more detailed analysis. The SNR of the O *K*-edge spectra is also poor in the Pt_3Co particles compared to the $PtCo_3$ particles (Figure 8.2a – d). This appears to be due to the low cobalt content in the Pt_3Co particles, since it is known that oxygen forms a stronger bond to cobalt than platinum metals [56]. It follows on that the leached alloys have a worse O *K*-edge SNR due to this correlation. This could obviously influence the assignment of oxidation states as a result of a poorly resolved edge fine structure.

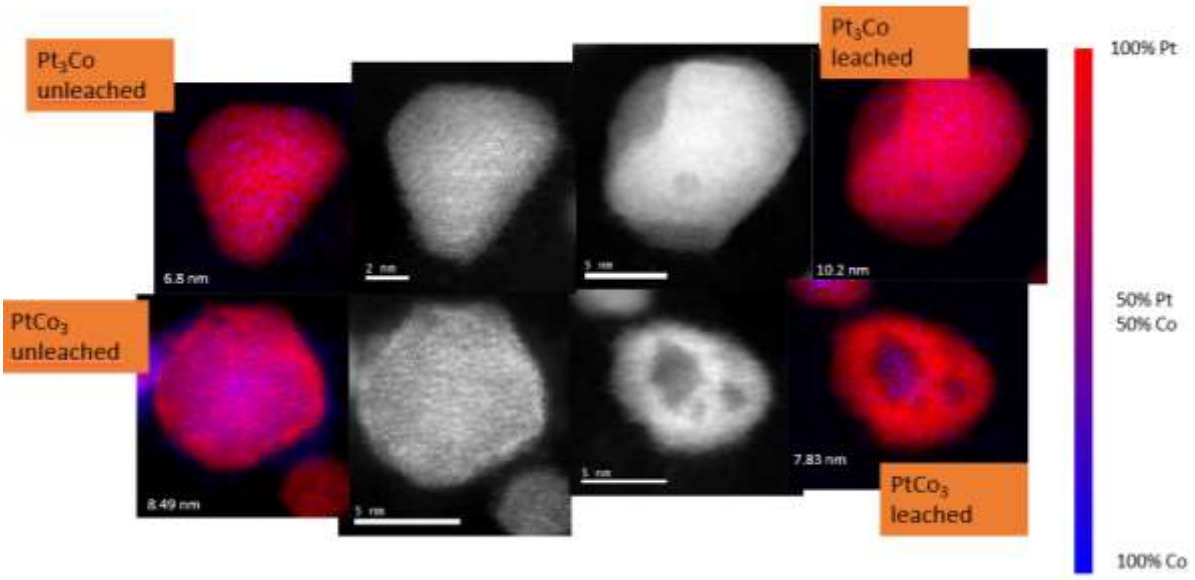


Figure 8.3. HAADF and RGB images of the PtCo sample matrix.

Across the sample matrix, oxidation was found to vary depending on sample type and particle size. A total of 80 nanoparticles across the sample matrix (Figure 8.3) were studied; 28 $PtCo_3$ unleached, 18 $PtCo_3$ leached, 18 Pt_3Co unleached and 16 Pt_3Co leached. Within this sample, data from $PtCo_3$ unleached particles were the most interpretable, followed by $PtCo_3$ leached and Pt_3Co unleached, then Pt_3Co leached particles, respectively. This was mainly due to the amount of cobalt content limiting the signal-to-noise ratio (SNR) obtained from the Co $L_{2,3}$-edge signal. The majority of the particles studied have a core-shell morphology, where it is cobalt-rich at the centre of the particles. This is more pronounced with the $PtCo_3$ particles compared to the Pt_3Co since the latter is cobalt-deficient. Compared to the unleached, the leached particles tend to have

more divots and concavity, which is a result of acid leaching (Figure 8.3). The leached particles form Pt skins (see $PtCo_3$ leached in Figure 8.3) when cobalt is leached (see chapter 1, section 1.4.2) and this is also evident, particularly in $PtCo_3$ particles.

As there is so much variation of cobalt and oxygen coverage and oxidation, even between particles of the same sample type, a schematic of the major types of oxygen, cobalt and platinum distribution found across the sample matrix is shown (Figure 8.4). No atomic ordering is inferred here as the data are not at atomic resolution to ascertain distinct forms of ordering within the nanoparticles. There are four major types of Pt/Co distribution that is seen. While there was no Pt EELS signal collected, previous work using a combination of cross-sections obtained from EELS, EDX and ADF simulations have been implemented on the particles by Dr Aakash Varambhia [88]. Knowledge of where the Pt resides in the PtCo particles has been used to corroborate the models shown.

The schematic looks at a Pt_3Co unleached (Figure 8.4a–c), Pt_3Co leached (Figure 8.4d–f), $PtCo_3$ unleached (Figure 8.4g–i) and $PtCo_3$ leached (Figure 8.4j–l) particle. Their corresponding HAADF images, Co $L_{2,3}$ map and O *K* map for visual reference (Figure 8.4a, d, g and f) along with the models of estimated Pt/Co distribution (Figure 8.4b, e, h and k) and where oxygen atoms are located on them (Figure 8.4c, f, i and l). The Pt, Co and O atoms are blue, green and red, respectively. The first type of distribution is the Pt-Co core-shell morphology and this is common to the majority of all particles studied, not just the Pt_3Co unleached (Figure 8.4b). This is congruent with what is seen in literature [88,96]. Minimal $L1_0$ ordering can also be seen where the cobalt signal appears to be coming from alternating rows of atoms in the Co $L_{2,3}$ map of the Pt_3Co unleached particle.This ordering of apparent alternating of Pt and Co row of atoms has also been seen in EELS studies by Wang *et al.* in Pt_3Co/C nanoparticles [185] and by Ma *et al.* in PtCo/C nanoparticles [218]. Comparison to the O *K* map shows that the oxygen atoms reside where the Co atoms are located (Figure 8.4c) and again, this is seen for most particles. As of

writing, there is no spectroscopic work in literature on where oxygen atoms are located on these particles.

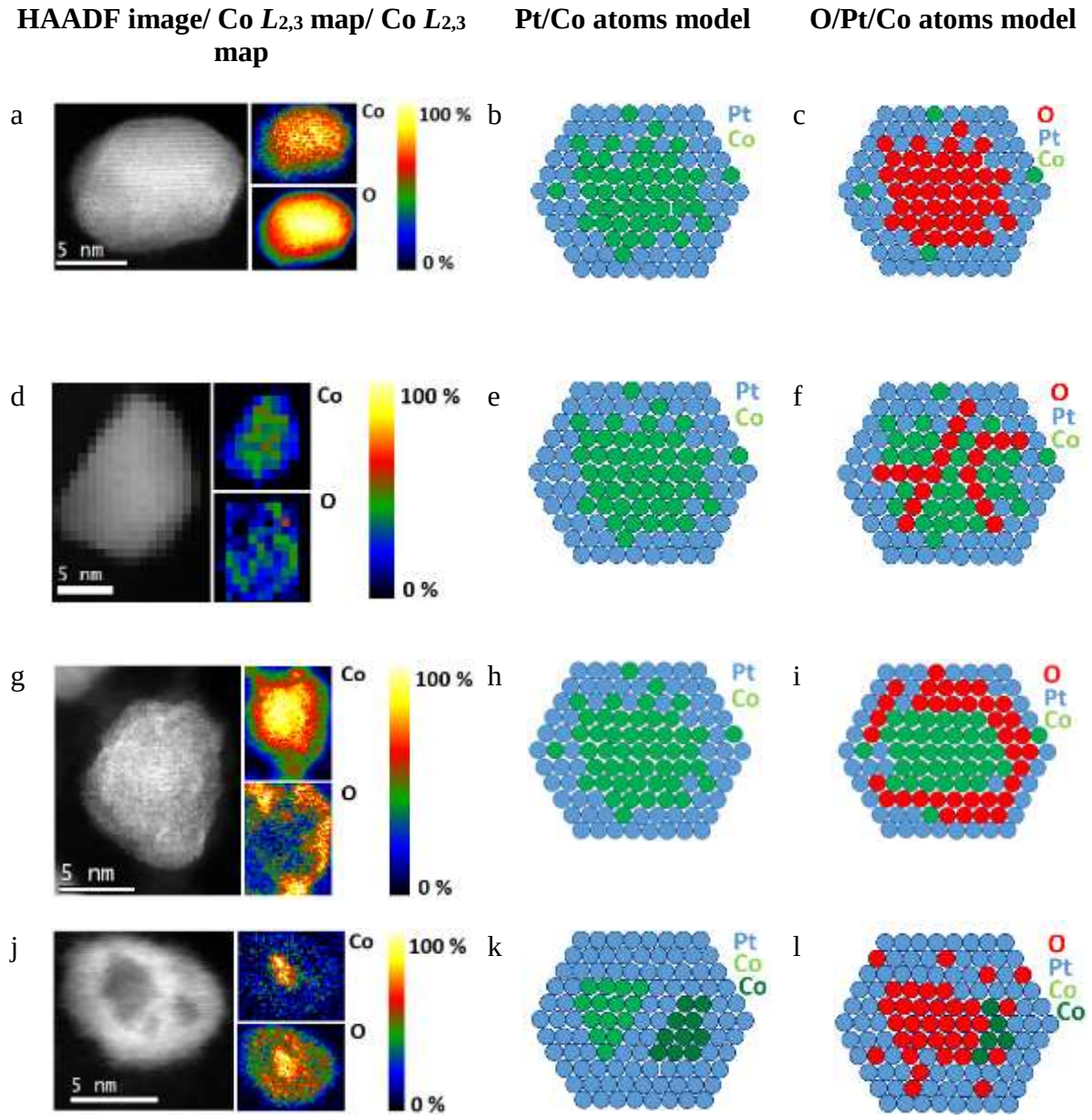


Figure 8.4. Schematic of four major cobalt, oxygen and platinum distribution found on the nanoparticles. Shown are the HAADF image, Co $L_{2,3}$ map, O *K* map, model of Pt and Co distribution and model of Pt, Co and O distribution in a (a–c) Pt_3Co unleached, (d–f) Pt_3Co leached, (g–i) $PtCo_3$ unleached and (j–l) $PtCo_3$ leached particle. The Pt, Co and O atoms are blue, green and red, repectively.

The second type of elemental distribution involves the same Pt-Co core-shell morphology, however, the oxygen atoms seem to preferentially oxidise certain facets or terraces/steps (Figure

8.4d and f). This corroborates findings of rows of metal oxides forming on not just the surface, but towards the middle of the nanoparticle [219]. Computational works have also found PtCo-O binding which shows oxygen atoms adsorbing on surfaces including top sites, facets and vertices [10,84,205]. While this type of distribution is shown here for the Pt_3Co leached particle, this was seen more on the $PtCo_3$ leached and unleached particles. The reason for this is unknown.

The third type of distribution is where the oxygen atoms preferentially bind on the edges/surface of the particle as illustrated with a $PtCo_3$ unleached particle (Figure 8.4g–i). The oxygen atoms appear to reside in the Pt-rich shell formed around the particle, where there is less cobalt (Figure 8.4i). Some large particles are know to have (111/100) facets favourable to oxygen binding [88]. Added to the fact that most particles >10 nm were found to have large metallic cores, this preferential oxygen binding at the edges seen is logical. A $PtCo_3$ unleached particle is used to illustrate the fourth type of distribution (Figure 8.4j–l). This particle appears to be a snapshot of a stage where oxygen adsorption is heavily favoured to the extent that it has completely leached out portions of cobalt (dark green atoms, Figure 8.4k), inducing the formation of a large Pt-rich shell. The oxygen atoms thus have a high surface coverage and adsorption on the particle (Figure 8.4j and l). The segregation of Co atoms has to the Pt-rich shell is well documented to be induced by strong oxidative or acidic conditions, where the shell becomes very active for ORR due to subsurface cobalt within the Pt-rich shell of leached particles [220,222,223].

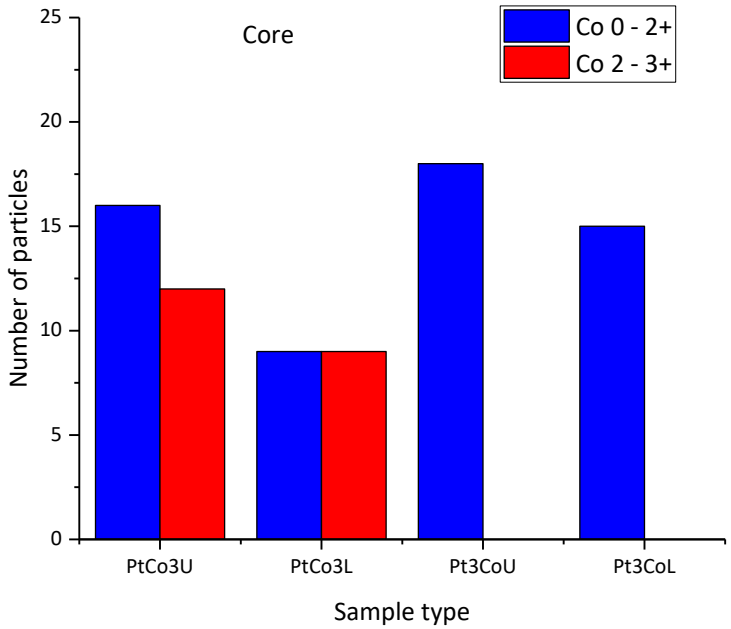
8.2 Effect of Co content and Acid Leaching

As earlier mentioned in section 8.1, the examples given are not wholly representative of the trend across the four alloys. There is variation in the proportions of oxidation across the four sample types. As mentioned in section 8.1, not all of the white line ratios lie on the calibration curve. Hence, the safest way to classify the oxidation is to use the blue-oxidised and red-oxidised nomenclature. Column charts showing the proportion of oxidation in the cores and shells, across

the four sample types, is shown (Figure 8.4a and b). Firstly, the cores of the $PtCo_3$ particles are both blue-oxidised and red-oxidised while those of the Pt_3Co are only blue-oxidised (Figure 8.4a). Only the $PtCo_3$ particles exhibit a higher oxidation state than 2+ in the column chart. This is understandable due to the higher cobalt content. As mentioned in section 8.1, oxygen forms a stronger bond to cobalt than platinum metals and thus, a higher oxidation states is expected with increased cobalt content. This appears to be the case across the particles studied (Figure 8.4a and b). In the cores, only ~43% of the $PtCo_3$ unleached particles are red-oxidised compared to 50% in the $PtCo_3$ leached sample. A 7% difference may be small, but this highlights some effect of an oxidative environment going from the unleached to the leached system in the $PtCo_3$ particles.

The chart for the distribution of oxidation in the shell of the particles also allude to a higher cobalt content being proportional to a higher oxidation state (Figure 8.4b), however, there is another trend. With 50% of the particles both red and blue-oxidised, the $PtCo_3$ unleached sample shows a more even distribution between the low and high oxidation states (Figure 8.4b). This indicates a higher degree of oxidation at the shell of the particles compared to the core. The $PtCo_3$ leached sample shows an even higher degree of oxidation with ~64% red-oxidised. The Pt_3Co unleached sample remains blue-oxidised. On the other hand, the Pt_3Co leached sample shows ~8% of the particles to be red-oxidised. This further corroborates the effect of a strongly oxidising environment in the leached alloys. However, based on this finding alone, it is unclear if the acid leach process leads to oxidation, or that the acid leached particles are more prone to oxidation when exposed to oxygen.

a



b

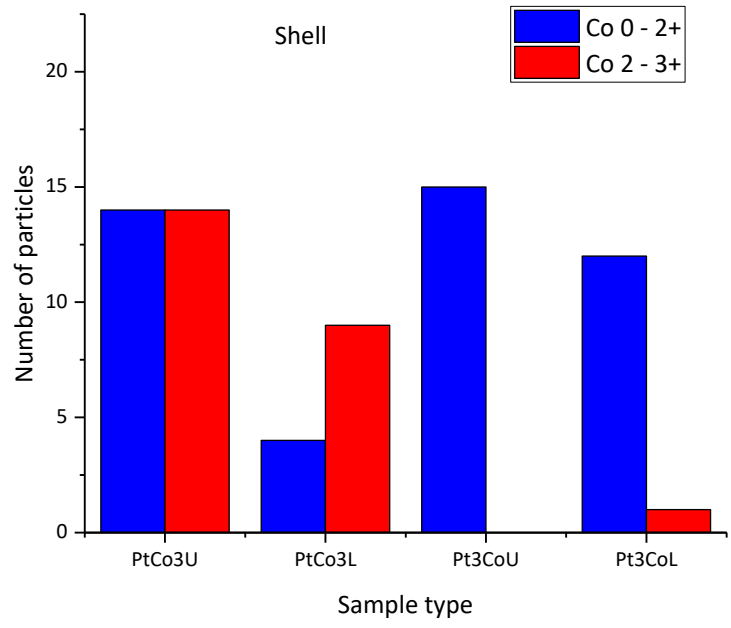


Figure 8.4. Relative proportions of oxidation with sample type in the (a) core and (b) shell. NB: $L_{2,3}$ ratio increases between the oxidation states 0 – 2+ but decreases between 2 – 3+.

From the 80 particles studied, it was found that the O *K*-edge RGB maps of heavily leached particles show the least spatial correlation to the Co $L_{2,3}$-edge RGB map. This means the oxygen is not always where the cobalt atoms are aggregated. An example of this phenomenon was shown earlier where there was an inverse relationship between the O *K*-edge and the Co $L_{2,3}$-edge RGB maps (c.f. section 8.1, Figure 8.1a). There also exists a phenomenon where the regions of the particle, usually the core, that have cobalt aggregation still have the highest O *K*-edge coverage, however the platinum shell also has substantial oxygen coverage. This phenomenon is mainly observed in the extremely leached particles, which show divots where the cobalt has been leached out (Figure 8.4a – f). Literature has shown that these features in acid leached PtCo alloys increases the Pt surface area for oxygen binding, thus boosting the catalytic activity at least two-fold [12,62,221]. In fact, the highest catalyst activity reported was a $PtCo_3$ leached system yielding four-fold oxygen reduction specific activity [203]. This was put down to a possible ligand and strain effects caused by the Co being driven to the surface of the particle.

he findings from the $PtCo_3$ leached system suggest that it would be the best for obtaining high oxidation states since it has the highest proportion of red-oxidised particles in both the core and shell, in comparison to the other three samples. The $PtCo_3$ unleached system can have the same functionality as its leached counterpart, albeit to a lesser degree because the O atoms will not be as tightly bound. Conversely, the Pt_3Co unleached sample could be seen as the most useful if a catalyst with the least amount of poisoning is desired. Similarly, the Pt_3Co leached sample could be put forward since only the shell can be red-oxidised, albeit to a low degree. This could be useful if the desorption of oxygen-based intermediates is the goal. Another approach would be prioritising the leached samples since the largely leached samples suggest full metal oxygen coverage of both the cobalt and platinum.

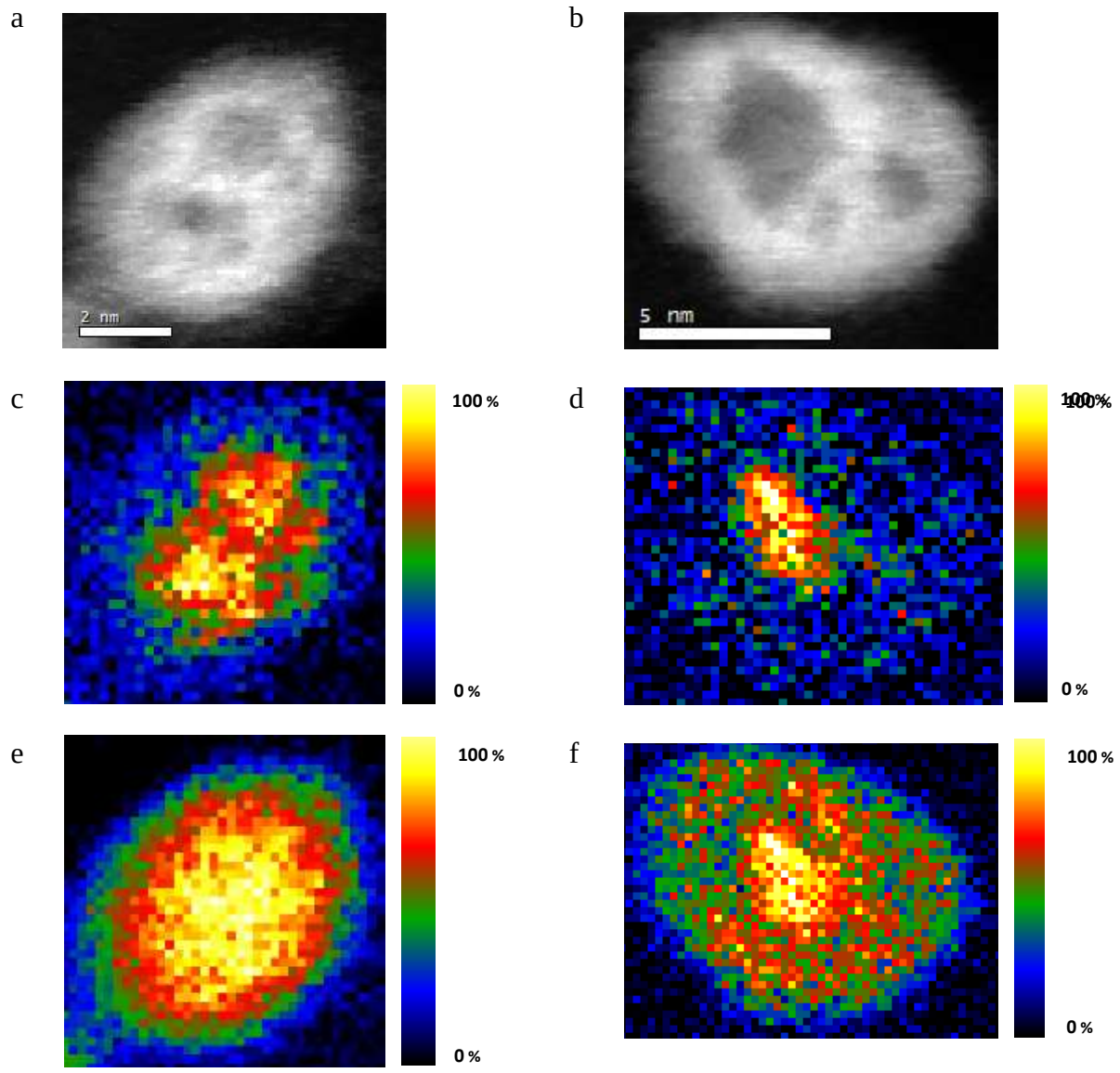


Figure 8.4. Experimental data of $PtCo_3$ leached particles. The (a and b) HAADF images, (c and d) cobalt $L_{2,3}$-edge RGB maps and (e and f) oxygen *K*-edge RGB maps. NB: The colour scalebars on the Co $L_{2,3}$ and O *K* RGB maps are normalised to the maximum value. from *Digital Micrograph*. Data acquired at 0.25 eV/ch.

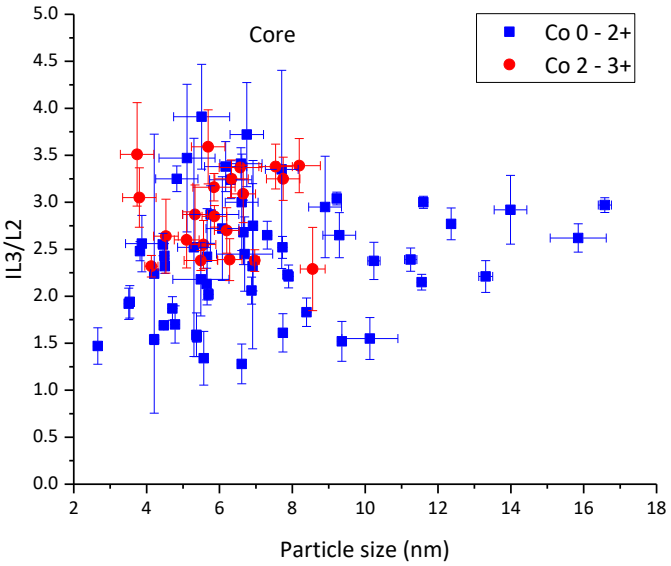
The findings from the $PtCo_3$ leached system suggest that it would be the best for obtaining high oxidation states since it has the highest proportion of red-oxidised particles in both the core and shell, in comparison to the other three samples. The $PtCo_3$ unleached system can have the same functionality as its leached counterpart, albeit to a lesser degree because the O atoms will not be as tightly bound. Conversely, the Pt_3Co unleached sample could be seen as the most useful if a catalyst with the least amount of poisoning is desired. Similarly, the Pt_3Co leached sample could be put forward since only the shell can be red-oxidised, albeit to a low degree. This could be

useful if the desorption of oxygen-based intermediates is the goal. Another approach would be prioritising the leached samples since the largely leached samples suggest full metal oxygen coverage of both the cobalt and platinum.

8.3 Influence of Size

To investigate the influence of size, the variation of the cobalt white line ratio with particle size in the core and the shell across all eighty particles is shown (Figure 8.5a and b). Again, for reasons mentioned in section 8.1, all of the particles were not assigned absolute oxidation states. However, for particles with white line ratios that were within the calibration curve, oxidation states have been assigned (Figure 8.6) as proof of concept. The errors on the size of the particles are one pixel dimension and so the size measurements are sufficiently robust for analysis. There is no strong correlation between the size and white line ratio, however, there are some noticeable points. In the core, between the size range ~10 – 15 nm, the oxidation state variation with size behaves similar to the smaller particles (Figure 8.5a). However, in the shell (Figure 8.5b), two particles >15 nm are red-oxidised compared to their blue-oxidised core (Figure 8.5a). This could mean that certain facets or terraced sites on the very large particles preferentially bind to oxygen. According to literature, it is expected that smaller particles are more surface-rough [10,203] and become more spherical than their larger counterparts due to the surface-to-volume effect [10,222]. This phenomenon has been known to increase oxygen binding strength [10]. However, the red-oxidised particles >15 nm (Figure 8.5b), may allude to a possible surface energy barrier that is broken to allow favourable oxygen binding in very large particles.

a



b

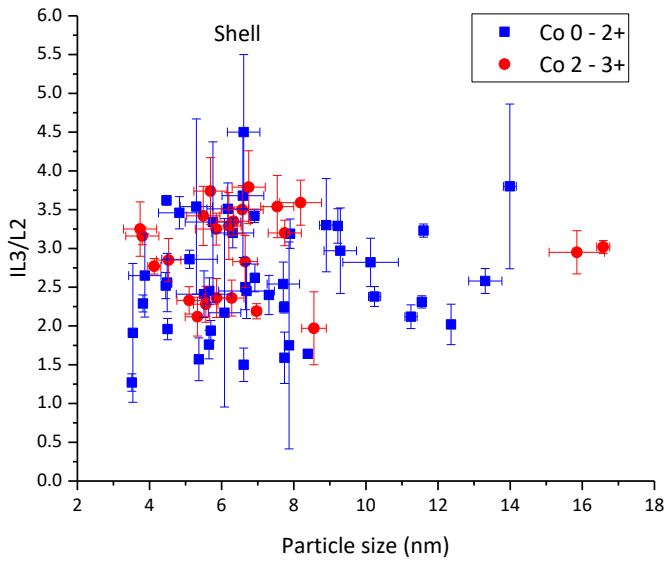


Figure 8.5. Variation of cobalt $L_{2,3}$ ratio versus particle size in the (a) core and (b) shell. NB: $L_{2,3}$ ratio increases between the oxidation states 0 – 2+ but decreases between 2 – 3+.

For the particles that lay within the calibration curve, calculated oxidation states were assigned (Figure 8.6). The smaller particles, <10 nm, no apparent trend of oxidation state with size in the core of the particles is observed. However, it appears that a gradual increase in oxidation state occurs as the particles get larger than 12 nm in the shell of the particles. Again, this alludes to the possibility that at sufficiently large particle sizes, the shells of the particles see preferential oxidation as compared to the core. However, this point is inconclusive considering the small number of data points and that not all of the particle ratios are plotted in the figure. It is

interesting to see a bimodal distribution of oxidation states, particularly in the particle sizes <10 nm. It is observable that there are little to no oxidation states between 0.5+ and 2.5+. This may highlight the fact that Co + is not known to be stable and hence, the absence of a Co+ standard. In contrast, this phenomenon may have nothing to do with the chemistry and is possibly an artefact or systematic error due to the lack of a Co + standard for comparison.

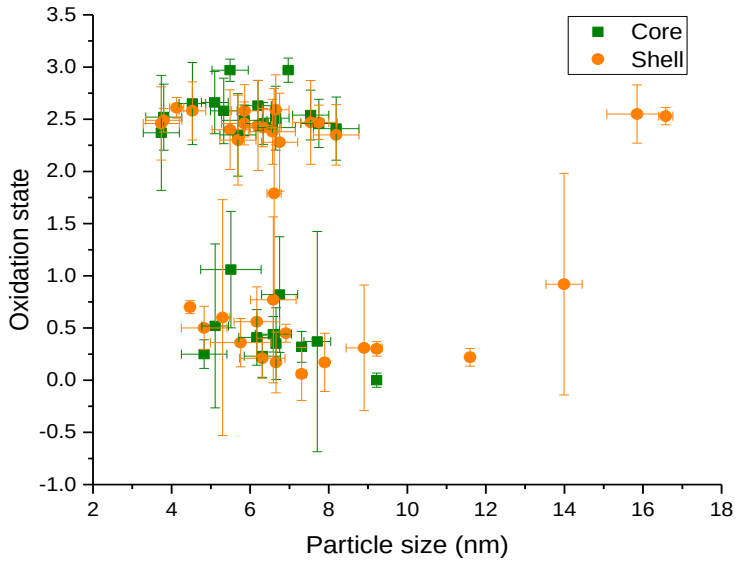


Figure 8.6. Variation of cobalt oxidation state versus particle size in the core and shell.

Nonetheless, the surface-to-volume effect is corroborated by the fact that smaller particles in this study showed larger and more evenly distributed regions of oxidation compared to localised regions of oxidation observed in the very large particles. Most of the smaller particles also had higher oxidation states than the larger particles. Again, this can be explained by the fact that smaller particles are heavily under-coordinated, thereby increasing the oxygen binding to the metals in the alloy [32,203]. The very large particles were mainly found to have ordered metallic cores, with oxygen coverage restrained toward the shells of the particles. This could mean that larger particles may be more cost-efficient alloys. Given that the oxygen coverage was found to be faceted and toward the shells of the large particles, they can be designed with cores full of

the cheaper metal, cobalt in this case, while the costlier platinum is restricted to the surface of the alloy.

8.4 Conclusions

In summary, the O *K*-edge and Co $L_{2,3}$-edge has been used to estimate the cobalt oxidation state from four types of PtCo alloys. The electronic structure of the O *K*-edge has been used for verification because the white line ratios alone are insufficient in determining the cobalt oxidation state. All oxidation states of cobalt were found to lie between the metallic (Co(0)) and the mixed valence state (Co 2.67+). However, absolute values of oxidation states are not assigned due to discrepancies, mostly with white line ratios of a significant amount of metallic states not lying within the calibration curve. Nonetheless, it has been demonstrated that the cobalt-rich samples generally have higher oxidation states as well as larger areas of oxidation compared to the cobalt-deficient alloys. Across the sample matrix, four distinct type of elemental distribution and oxygen coverage has been highlighted and is mainly congruent with literature. These include cobalt surface segregation, the formation of Pt-skins and possible facet oxygen binding. It has been further shown that smaller particles have a more even distribution of oxygen coverage over the surface compared to larger particles, which have their oxygen coverage mostly in the shell of the particles. Lastly, it has been shown that the leached particles show a higher degree of oxidation compared to the unleached particles. The next step from this work would be the modelling of the O *K*-edge and Co $L_{2,3}$-edge in various environments in order to compare their electronic structures to the experimental spectra.

8.5 References

[216] Lien H, Chang S, Chen P, Wong D P, 5, Chang Y, Lu Y, Dong C, Wang C, Chen K and Chen L 2020 Probing the active site in single-atom oxygen reduction catalysts via operando X-ray and electrochemical spectroscopy *Nat. Commun*. **11**, 1–7

[217] Henderson G S, de Groot F M and Moulton B J 2014 X-ray absorption near-edge structure (XANES) spectroscopy *Rev. Miner. & Geochem.* **78** 75–138

[218] Ma Y, Kuhn A N, Gao W, Al-Zoubi T, Du H, Pan X and Yang H 2015 Strong electrostatic adsorption approach to the synthesis of sub-three nanometer intermetallic platinum–cobalt oxygen reduction catalysts *Nano Energy* **79**, 1–7

[219] Van Spronsen M A, Frenken J W M and Groot I M N 2017 Observing the oxidation of platinum *Nat. Commun.* **8**, 1–6

[220] Noh S H, Seo M H, Seo J K, Fischerc P and Han B 2015 First principles computational study on the electrochemical stability of Pt–Co nanocatalysts *Nanoscale* **5**, 8625–8633

[221] Ball S C, Hudson S L, Thompsett D, Theobald B 2007 An investigation into factors affecting the stability of carbons and carbon supported platinum and platinum/cobalt alloy catalysts during 1.2 V potentiostatic hold regimes at a range of temperatures *J. Power Sour.* **171** 18–25

[222] Wang C, Wang G, Vliet D, Chang K, Markovic N M and Stamenkovic V R 2010 Monodisperse Pt_3Co nanoparticles as electrocatalyst: the effects of particle size and pretreatment on electrocatalytic reduction of oxygen *Phys. Chem. Chem. Phys.* **12** 6933–6939

[223] Sarwar M, Gavartin J L, Bonastre A M, Lopez S G, Thompsett D, Ball S C, Krzystala, Goldbeck G and French SA 2020 Exploring fuel cell cathode materials using ab initio high throughput calculations and validation using carbon supported Pt alloy catalysts *Phys. Chem. Chem. Phys.* **22** 5902–5912

9 Calculation of Co $L_{2,3}$-edge multiplets

9.1 Method and parameters

In chapters 7 and 8, the cobalt white line ratio has been used to provide information on the oxidation state of the atom. In this chapter, the use of the fine structure within the cobalt edge to provide additional information about the bonding environment is investigated. AMT calculations are used to investigate how different parameter which describe the bonding environment effect the spectrum. To implement these calculations of the Co $L_{2,3}$-edge multiplets, the semi-empirical code, CTM4XAS, developed by de Groot [146,147], is used. The basis of the model are atomic calculations, onto which other perturbations such as crystal field and charge transfer can be added. The principal part for multiplet calculation in the CTM4XAS code is the inclusion of the core and valence spin-orbit coupling, core-hole induced charge transfer and the core-valence two-electron integrals [146,147,224]. Firstly, the atomic parameters are included for the calculation of the spectrum (see appendix 12.4 for details). Rather than just using these parameters blindly, calculations were also carried out for congruence with experimental spectra. While Gaussian and Lorentzian broadening were also included to simulate experimental spectra, separate broadening of each of the cobalt white lines to account for the large uncertainty such as a lower SNR and SBR on the L_2 peak, was not done. This was mainly for simplicity, but also, nuance differences between the L_2 peak in experiment spectra and calculated spectra were more conspicuous than any effect of separate broadening of the white lines.

As symmetry is the basis of crystal field theory, the crystal field parameters are notated using point group symmetry. The alloy particles are fcc and since the cobalt in the Co 2+ and Co 3+ standards occupy octahedral sites (see chapter 7, section 7.4), the O_h symmetry is used for all calculations. The crystal field represents the difference splitting between the *d*-orbitals in O_h

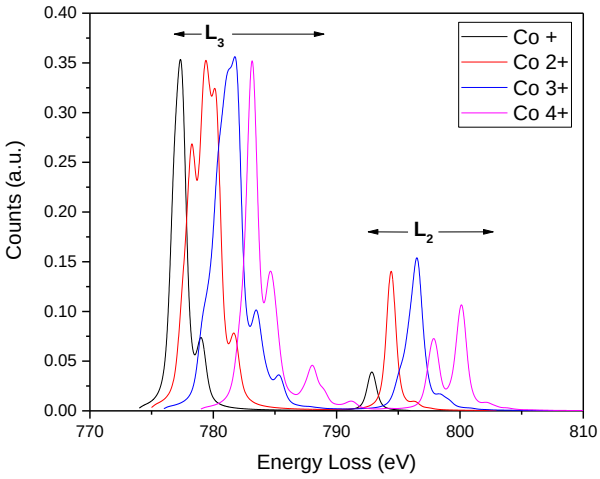
symmetry, namely, the t_{2g} and e_g states. There are inputs which allow for the variation of the crystal field strength, which can take any non-negative integer value in eV, and this controls the extent to which the ground state term symbol is split into its crystal field components. There are also initial and final state parameters, which take values in eV.

The charge transfer parameters are split into the charge transfer energy, Δ, Hubbard energy, U_{dd} and core-hole potential, U_{pd} or Q; all possible values are inputted in eV. These are tuneable parameters and have been determined from a combination of 3*d* series trends and XPS experiments [146]. The hopping parameters, *T*, comprise the last set of parameters. There are divided into four main types: $T(b_1)$, $T(a_1)$, $T(b_2)$, $T(e)$, denoting the symmetry of electron hopping in $dx^2\text{-}y^2$, dz^2 (e_g orbitals) and dxy, dxz/yz (t_{2g} orbitals), respectively, in O_h symmetry [146,147]. There are separate charge transfer parameters to simulate the LMCT and MLCT and these have also been implemented in these calculations.

9.2 Interpretation of Standards spectra

The cobalt oxidation states from experiment range Co(0) – Co 3+ in both the standards and nanoparticles. However, the CTM4XAS code does not include the option to calculate metallic states and as such, Co(0) is not included in the calculated spectra. It is also important to point out that Co 1+ and Co 4+ are not found experimentally as they are generally energetically unstable. However, they have been included in the calculations for completeness. The CTM4XAS code is programmed for calculations of pure oxidation states and as such, the mixed state, Co 2.67+, is not included in the calculation. However, the spectra of pure states can be linearly combined to obtain spectra of mixed states (as discussed later).

a



b

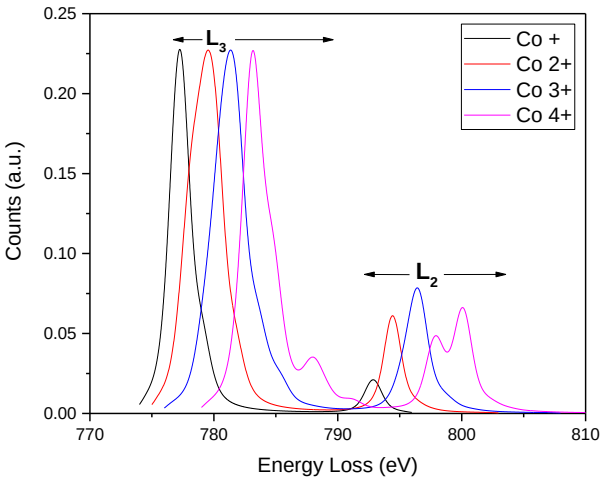


Figure 9.1. Calculated Co $L_{2,3}$-edge oxidation states ranging 1 – 4+ at Gaussian = Lorentzian broadening = (a) 0.52 eV and (b) 0.98 eV.

The calculated spectra of the oxidation states were done at 0.52 eV (Figure 9.1a) and 0.98 eV (Figure 9.1b) Gaussian and Lorentzian broadening to simulate the experimental data at dispersions of 0.025 eV/ch and 0.25 eV/ch, respectively. There is a clear chemical shift going from Co + to Co 4+ in both sets of spectra. The splitting of each of the L_2 and L_3 peaks is seen to increase from Co + to Co 4+ (Figure 9.1a and b). This is expected as the charge on the atom increases. The Co 2+ and Co 3+ calculated spectra will be the focus as these are within the range of oxidation states found in the experimental spectra. The white line ratios were found to decrease going from Co + to Co 4+ in the calculated spectra (Table 9.1 compares the Co 2+ and 3+ ratios). This observation was difficult to compare with the experimental data because

there were no Co + or Co 4+ oxidation states. Furthermore, as mentioned in the chapter 7, while the white line ratios do decrease after Co 2+, it increases going from Co(0) to the Co 2+ oxidation state.

Table 9.1. L_3/L_2 ratio, $E_{L3,\ L2}$ edge onsets and energy difference, *d*E from Co 2+ and Co 3+ standards and calculated spectra.

	L_3/L_2	E_{L3} (eV)	E_{L2} (eV)	*d*E (eV)
CoO_0.025 eV	4.3±0.1	778.10±0.02	793.80±0.04	15.70±0.03
$LiCoO_2$_0.025 eV	2.10±0.02	780.00±0.02	794.60±0.02	14.60±0.02
CoO_0.25 eV	4.7±0.1	780.80±0.03	796.70±0.03	15.9±0.1
$LiCoO_2$_0.25 eV	2.40±0.03	782.60±0.02	797.40±0.1	14.80±0.02
Co 2+ calculated	6.2	777.5	794.1	16.7
Co 3+ calculated	3.9	778.8	794.9	16.1

The calculated spectra were compared to the standards, CoO and $LiCoO_2$, used in experiment for the Co 2+ and Co 3+ oxidation states (Figure 9.2a–d). The calculated spectra appear to reasonably congruent with experiment. However, the most incongruent of the comparisons were the Co 3+ and $LiCoO_2$ spectra at the 0.52 eV broadening (Figure 9.2b). The peaks at ~784, 786 and 787 eV in the calculated spectrum does not appear to be present in the experimental spectra. In addition, at the 0.98 eV broadening (Figure 9.2c), the shape of the L_3 peaks in the Co 2+ and CoO spectra are slightly different, mostly noticeable about their maximum at ~780 and ~785, respectively. Another noticeable incongruence is the small doublet of peaks ranging ~791 – 796 eV, seen in the panel showing the Co 3+ and $LiCoO_2$

spectra at the 0.98 eV broadening (Figure 9.2d). These peaks in the $LiCoO_2$ spectrum do not appear to be present in the calculated Co 3+ spectrum. The calculated spectra shown so far has only used the atomic parameters as inputs. It turns out that the addition of crystal field and charge transfer as extra perturbations to the calculated spectra reproduced these experimental spectra better and this is shown later on.

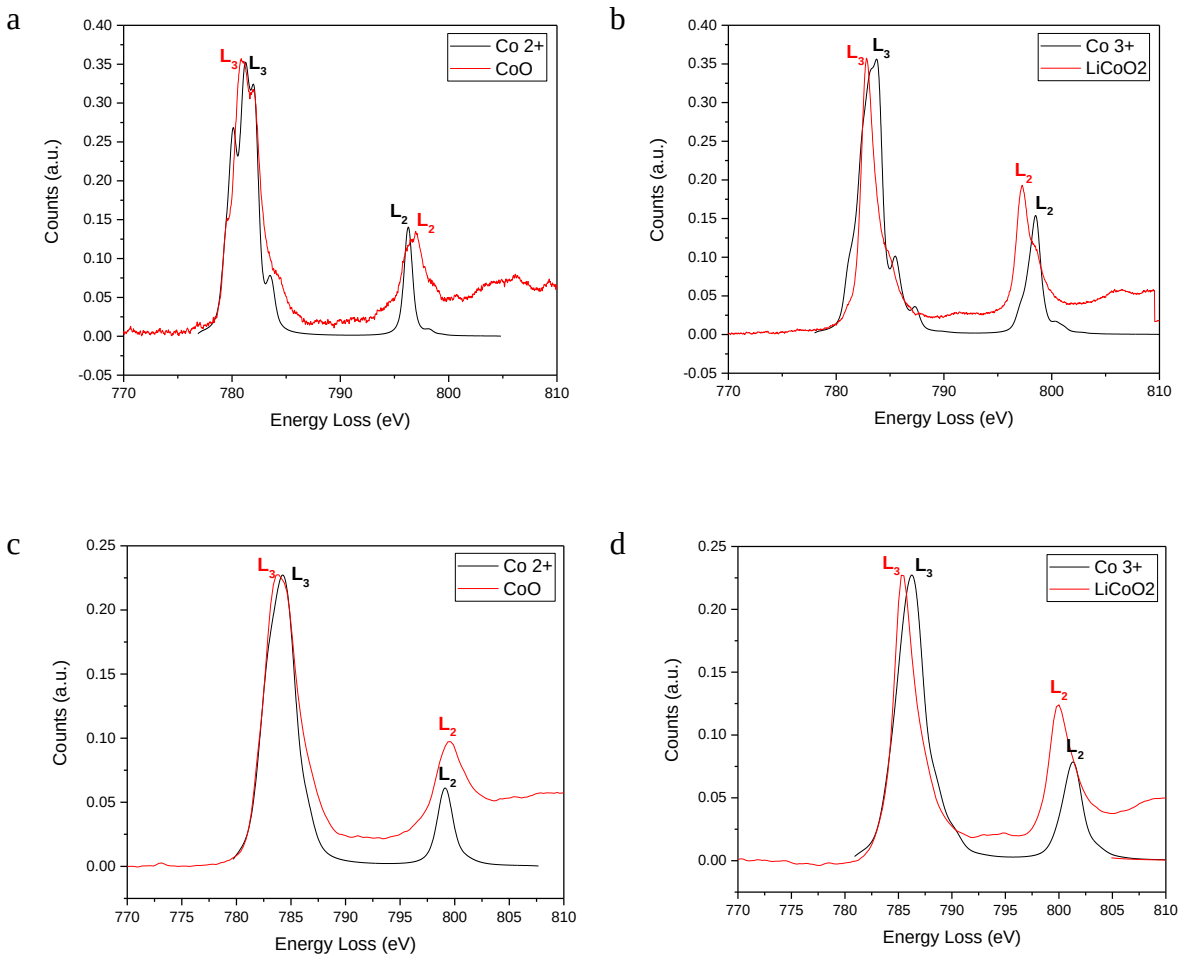
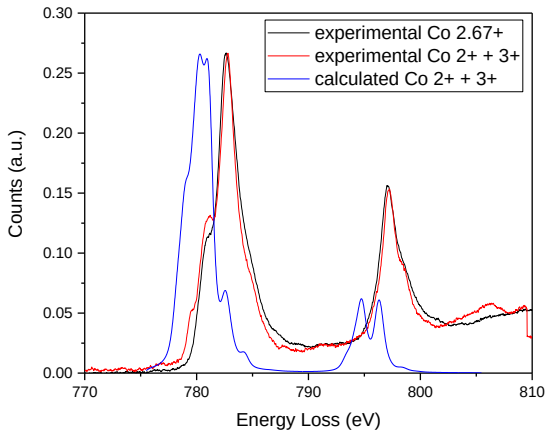


Figure 9.2. Comparison of experimental and calculated Co $L_{2,3}$-edge for (a) Co 2+ and CoO standard at Gaussian = Lorentzian broadening = 0.52 eV, (b) Co 3+ and $LiCoO_2$ standard at Gaussian = Lorentzian broadening = 0.52 eV, (c) Co 2+ and CoO standard at Gaussian = Lorentzian broadening = 0.98 eV and (d) Co 3+ and $LiCoO_2$ standard at Gaussian = Lorentzian broadening = 0.98 eV. NB: broadening is for calculated spectra. Spectra have been aligned to the same onset. Experimental spectra dispersion: 0.025 eV/ch (panels a and b) and 0.25 eV/ch (panels c and d).

a



b

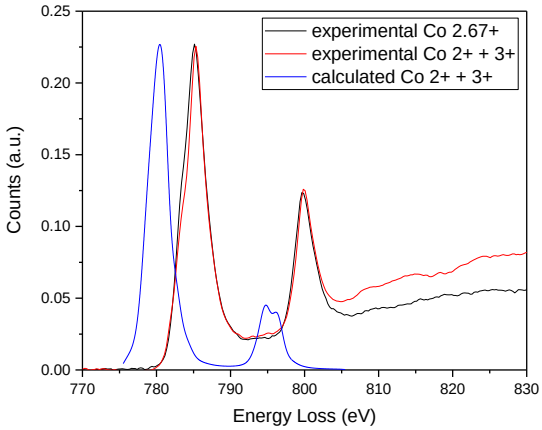


Figure 9.3. Comparison of EEL spectra from Co_3O_4 standard, linear combination of CoO and $LiCoO_2$ standards and linear combination of calculated Co 2+ and Co 3+ at the (a) 0.025 eV/ch and (b) 0.25 eV/ch dispersions. The broadenings on the calculated spectra are 0.52 and 0.98, respectively.

As mentioned earlier, the CMT4XAS code cannot model the Co 2.67+ state, however, a linear combination of the states is possible. The Co 2+ and Co 3+ states were linearly combined by adding the Co 2+ and Co 3+ in a 2:1 Co 3+/Co 2+ ratio. Results for both for the calculated and experimental spectra are shown (Figure 9.3a and b). While the difference between the Co 2.67+ standard and the linearly combined mixed state, Co 2+ + Co 3+, is not much, there are some distinct features not common to both fine structures. For example, at the 0.025 eV/ch dispersion, there is a pre-peak at ~779 eV on the L_3 peak in the linearly combined state which is absent in the Co 2.67+ standard (Figure 9.3a). The peak immediately after, ~781 eV, is common to both spectra but the intensity is higher in the linearly combined spectrum. The contrast is less obvious at the 0.25 eV/ch dispersion, possibly due to the broadening. A close

look at the L_3 peak, ~783 eV, shows that the linearly combined state has slightly less intensity than the individual mixed state (Figure 9.3b). The calculated spectra are more distinct from the experimental spectra at both the 0.52 and 0.98 eV broadenings. This is most noticeable on the splitting of the L_2 peaks into doublets of approximately equal intensities (Figure 9.3a and b). The reason for the discrepancy in the calculated spectra could be due to insufficient experimental parameters. However, it is not clear with the experimental spectra. It may be due to the different symmetries of the cobalt in the standards.

As mentioned in chapter 7, section 7.4, the cobalt atoms in both the CoO and $LiCoO_2$ standards occupy octahedral sites, however, those in the Co_3O_4 standard are mixed. The Co 2+ atoms sit in tetrahedral sites while the Co 3+ atoms take the octahedral sites. Therefore, it is logical that the symmetry of the site may have a sufficient effect on the spectrum to produce a difference in the fine structure of the cobalt edge. To test this, a spectrum of Co 2+ in tetrahedral symmetry, D_{4h}, was calculated. This was then added to the Co 3+ in O_h with charge transfer energy of Δ = -3 eV to get a closer match to the physical model of the Co_3O_4 compound. The lower broadening, 0.52 eV, was used because any distinct features would be more noticeable than with the larger broadening of 0.98 eV. The tetrahedral symmetry has two more crystal field parameters than in octahedral symmetry. The parameters are *D*t and *D*s and represent tetragonal parameters for further splitting of the crystal field. The spectrum with (Co 2+ D_{4h} * + 3+ O_h) and without (Co 2+ D_{4h} + 3+ O_h) these parameters are plotted (Figure 9.4). The results show closer matches for both spectra (Figure 9.4) compared to the calculated spectrum which had the Co 2+ in O_h symmetry and Co 3+ without charge transfer in O_h symmetry (Figure 9.3a). For example, the L_3 and L_2 peaks are more symmetrical (Figure 9.4). The doublet splittings at ~780 eV and ~796 eV in the Co 2+ + 3+ O_h spectrum (Figure 9.3a) are no longer present. However, the shoulder peaks either side of the main intensities on the L_3 and L_2 peaks are still

not well described. Nevertheless, this improved match shows the importance of the symmetry in the models used.

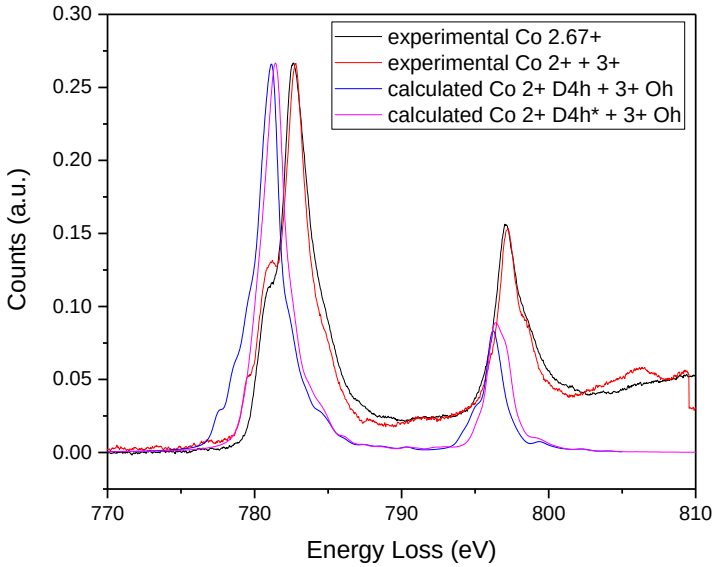


Figure 9.3. Comparison of EEL spectra from Co_3O_4 standard, linear combination of CoO and $LiCoO_2$ standards at the 0.025 eV/ch dispersions, linear combination of calculated Co 2+ D_{4h} (one tetrahedral parameter) + Co 3+ O_h with CT = -3 eV and linear combination of calculated Co 2+ D_{4h}^* (three tetrahedral parameters) + Co 3+ O_h with CT = -3 eV. NB: The calculated spectra have 0.52 eV broadening.

The absolute values of the white line ratios from the calculated spectra were found to be higher than those of the standards (Table 9.1). For example, Co 2+ and 3+ have ratios of 6.2 and 3.9, respectively, while the standards were 4.7±0.1 and 2.40±0.03 at 0.25 eV/ch, respectively. At 0.025 eV/ch, the ratios were 4.3±0.1 and 2.10±0.02 for the Co 2+ and 3+ in the standards, respectively. In the calculated spectra, the Co 2+ and Co 3+ $L_{2,3}$-edge energies ranged ~778 – 795 eV, however, their absolute values differed by 2 – 3 eV compared to experimental values. The energies difference values, *d*E, differed by ~1 eV. While the code was not built for precise energy calculations, the slight imprecision means that absolute values cannot be compared with experiment. This is also the case for the discrepancies with the white line ratios. Nevertheless, the relative trends in all cases are congruent with experimental data.

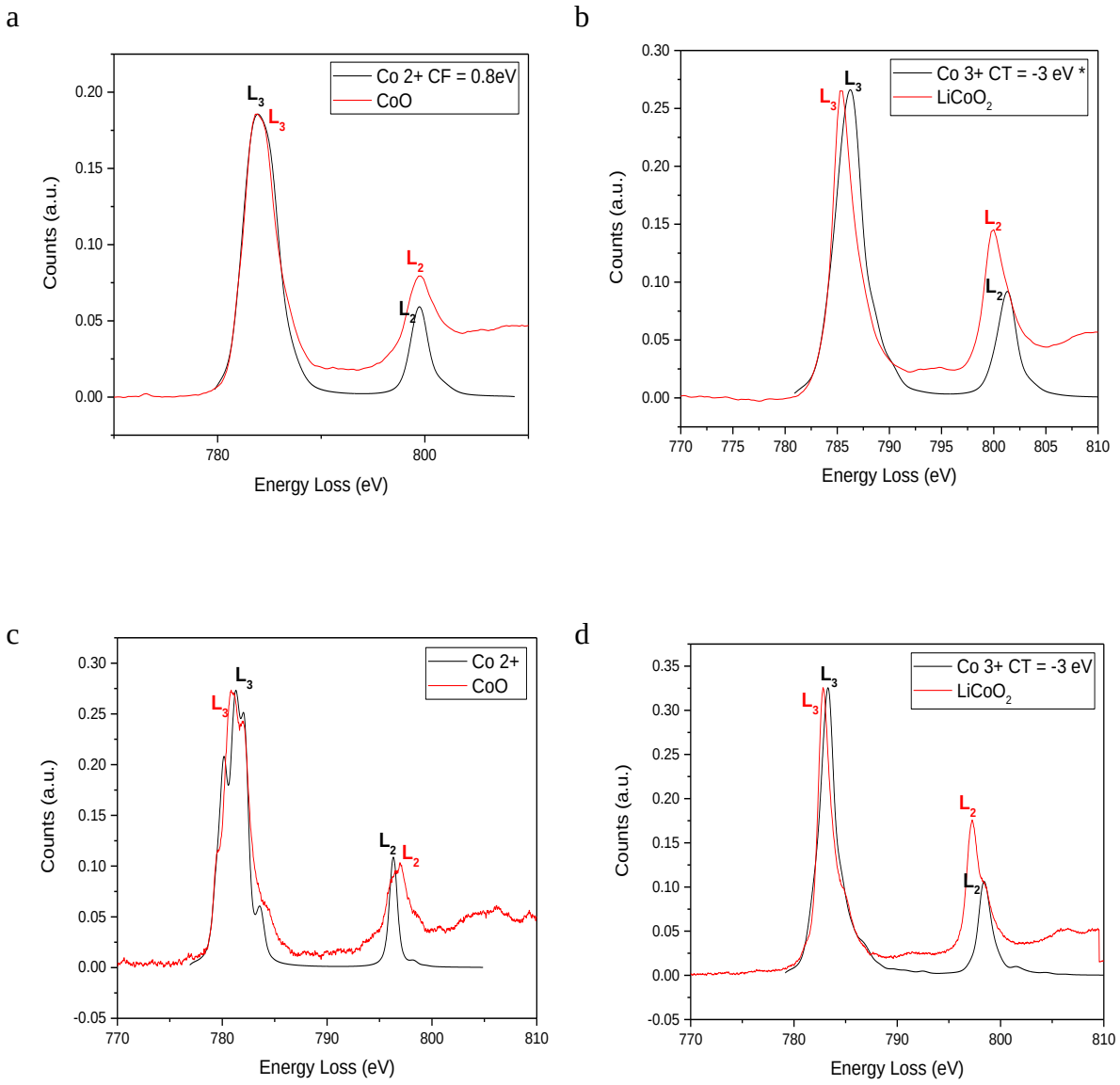


Figure 9.4. Experimental (red) and calculated (black) Co $L_{2,3}$-edge. The (a) Co 2+ standard and Co 2+ with crystal field, CF = 0.8 eV, (b) Co 3+ standard and Co 3+ with charge transfer, CT = -3 eV*, (c) Co 2+ standard and Co 2+ without crystal field and (d) Co 3+ standard and Co 3+ with charge transfer, CT = -3 eV. Gaussian = Lorentzian broadening = 0.98, 0.88, 0.59 eV and 0.52 eV for calculated spectra in panels a, b, c and d, respectively. Spectra have been aligned to the same onset. Experimental spectra dispersion: 0.25 eV/ch (panels a and b) and 0.025 eV/ch (panels c and d).

As earlier discussed, the use of just the atomic parameters in the calculated spectra were not enough to get sufficient congruence with some parts of the experimental data spectra and as such, crystal field and charge transfer parameters were introduced. In chapter 5 (see section 5.5, Figure 5.5), it is seen that varying the value of the crystal field in the calculation can have a large effect on the fine structure, effecting the shape and onset of the Co $L_{2,3}$-edge. In this

study, a crystal field value of 0.8 eV was required to accurately model the fine structure of the Co 2+ standard at 0.25 eV/ch (Figure 9.4a) while a charge transfer energy of Δ = -3 eV and 0.88 eV Gaussian and Lorentzian broadening was required for the Co 3+ standard (Figure 9.4b) at the same dispersion. It is important to mention that only the Co 2+ standard at 0.025 eV/ch (Figure 9.4c) did not require the crystal field and charge parameters for a better fit to experiment. This is odd because the calculations should not be dispersion dependent.

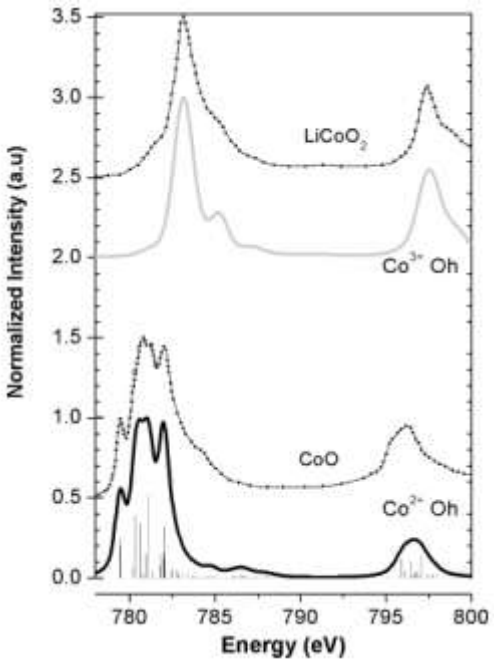


Figure 9.5. Overlay of Co $L_{2,3}$-edges of CoO and LiCoO2 reference samples (dotted lines) and calculated multiplet spectra of Co 2+ and Co 3+ in octahedral symmetry. Image modified from [225].

Comparing with the Co 2+ calculated spectrum from de Groot and co. [225], all six peaks from their calculations (Figure 9.5) are fairly well reproduced (Figure 9.4c). However, with a crystal field value of 0.6 eV, 0.4 eV Gaussian and 0.8 Lorentzian broadening on the L_2 peak (double that of the L_3), the L_2 peak was broader than the spectrum calculated here, which had broadenings of 0.52 eV. The spectra at 0.52 eV broadening calculated in this work is easier to compare to literature as the peaks are less broadened than the spectra at 0.98 eV broadening. In addition, the peaks at ~781 eV and 784 eV on the L_3 had slightly broader and lower

intensities compared to the Co 2+ spectrum here. This is also true comparing to the CoO reference spectrum (Figure 9.5) and the experimental Co 2+ standard, CoO, spectrum in this thesis. This was most likely due to the addition of Δ = 3 eV charge transfer in the spectrum, which is absent the Co 2+ spectrum calculated here. However, decreasing the broadening and increasing the crystal field to 0.75 eV matches the Co 2+ calculated spectrum here very well as the peaks at ~781 eV and 784 eV intensity increased [159].

The Co 3+ standard at 0.025 eV/ch required Δ = -3 eV and 0.52 eV Gaussian and Lorentzian broadening on the Co 3+ calculated spectrum for congruence (Figure 9.4d). Comparison with the Co 3+ calculated spectrum from de Groot and co. (Figure 9.5), all five peaks were reproduced fairly well. Again, due to the higher Lorentzian broadening of 0.8 eV on the L_2, it was slightly broader than that in the Co 3+ calculated spectrum here. However, the peaks at ~785 eV and 787 eV on the L_3 were sharper than those in the Co 3+ calculated spectrum here. This is also true comparing to the $LiCoO_2$ reference spectrum (Figure 9.5) and the experimental Co 3+ standard, $LiCoO_2$, spectrum in this thesis. A crystal field value of 1.9 eV and of Δ = 4.5 eV charge transfer was used. Further research shows that decreasing the crystal field value to 1 eV [226] gave an almost perfect match with the L_3 in the Co 3+ calculated spectrum here. The take away from these comparisons with literature is that all spectra require crystal field and charge transfer to correctly simulate the experimental spectra. The addition of crystal field and charge transfer effects were found to be useful in relation to some of the nanoparticles. For example, a nanoparticle spectrum from the core of a $PtCo_3$ unleached particle is shown to have Co 2+ crystal field effects (Figure 9.6) despite having a fraction of Co 3+ (as determined experimentally from O *K*-edge). While crystal field and charge and transfer effects were required to model the Co 2+ and Co 3+ in the standards, only some of the nanoparticles exhibit these effects.

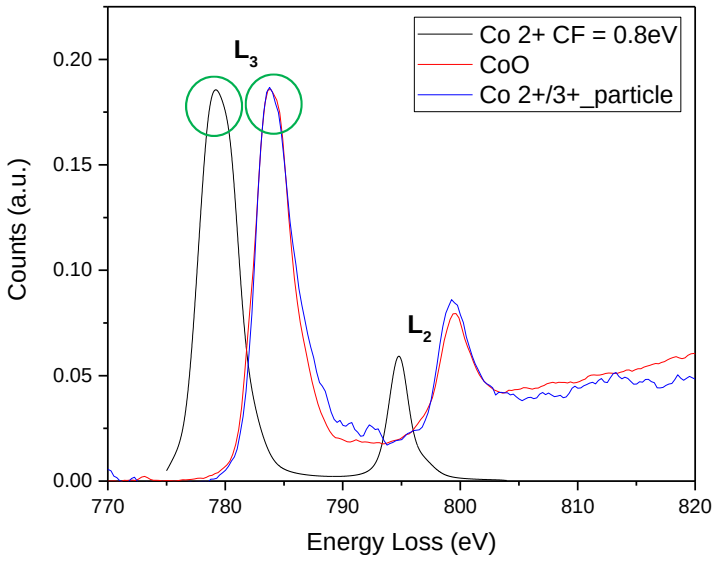


Figure 9.6. Calculated (black), standard (red) and a $PtCo_3$ unleached nanoparticle (blue). The calculated spectrum was at Gaussian = Lorentzian broadening = 0.98 eV while the experimental spectra were taken at 0.25 eV/ch. NB: Counts scaled to that of calculated spectrum.

9.3 Investigation of Crystal Field and Charge Transfer in Nanoparticles

Crystal field and charge transfer effects were visible across 55 of the 80 nanoparticles investigated. The CTM4XAS code does not output information on features belonging to the different sets of *d* orbitals that give rise to them and as such, individual calculations were made using the charge transfer hopping parameters to determine these features. The Co 3+ standard has been used to illustrate this since its spectrum had inherent charge transfer, evidenced by calculation (see section 9.2, Figure 9.2b and d). These calculations were done at broadenings of 0.59 eV and 0.88 eV to compare to both experimental dispersions.

The Co 3+ standard spectrum has been reproduced in the calculations and it can be seen that the e_g orbitals exert a slight chemical shift of ~1 eV, as well as a larger contribution to the high energy side of the L_3 and L_2 peaks at ~782 eV and ~797 eV, respectively (Figure 9.7a and c).

On the other hand, the t_{2g} orbitals make up the bulk of the low energy side of the L_3 and L_2 peaks at ~781 eV and ~796 eV, respectively (Figure 9.7b and d). The chemical shifts are similar to those exerted by the e_g orbitals. This is congruent with the relative energies of the *d* orbitals in an octahedral crystal field.

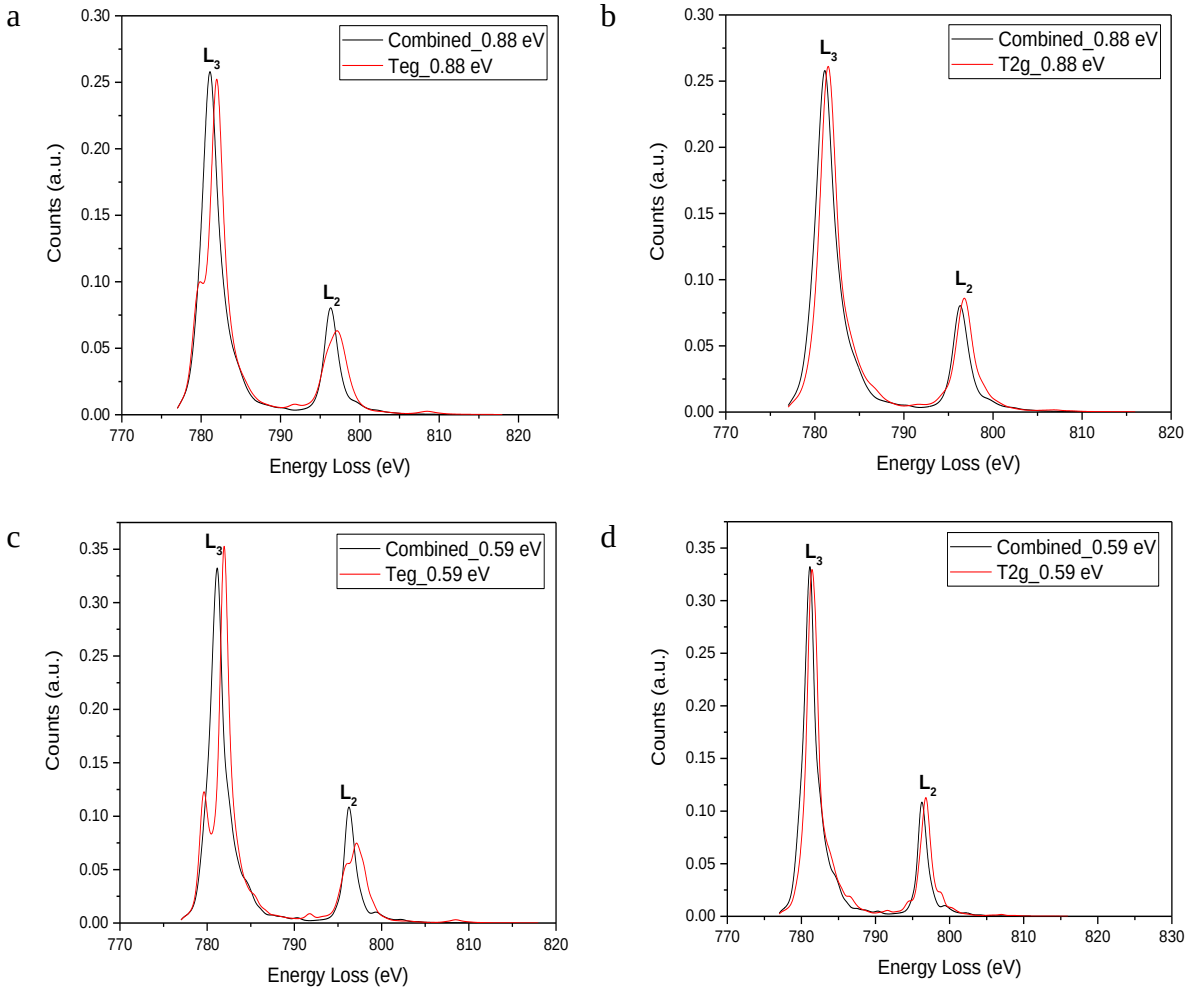


Figure 9.7. The calculated spectra of Co $L_{2,3}$-edge of Co 3+ with charge transfer, CT = -3 eV (black) and (a) e_g state (red) at Gaussian = Lorentzian = 0.88 eV, (b) t_{2g} state (red) at Gaussian = Lorentzian = 0.88 eV, (c) e_g state (red) at Gaussian = Lorentzian = 0.59 eV (red) and (d) t_{2g} state (red) at Gaussian = Lorentzian = 0.59 eV.

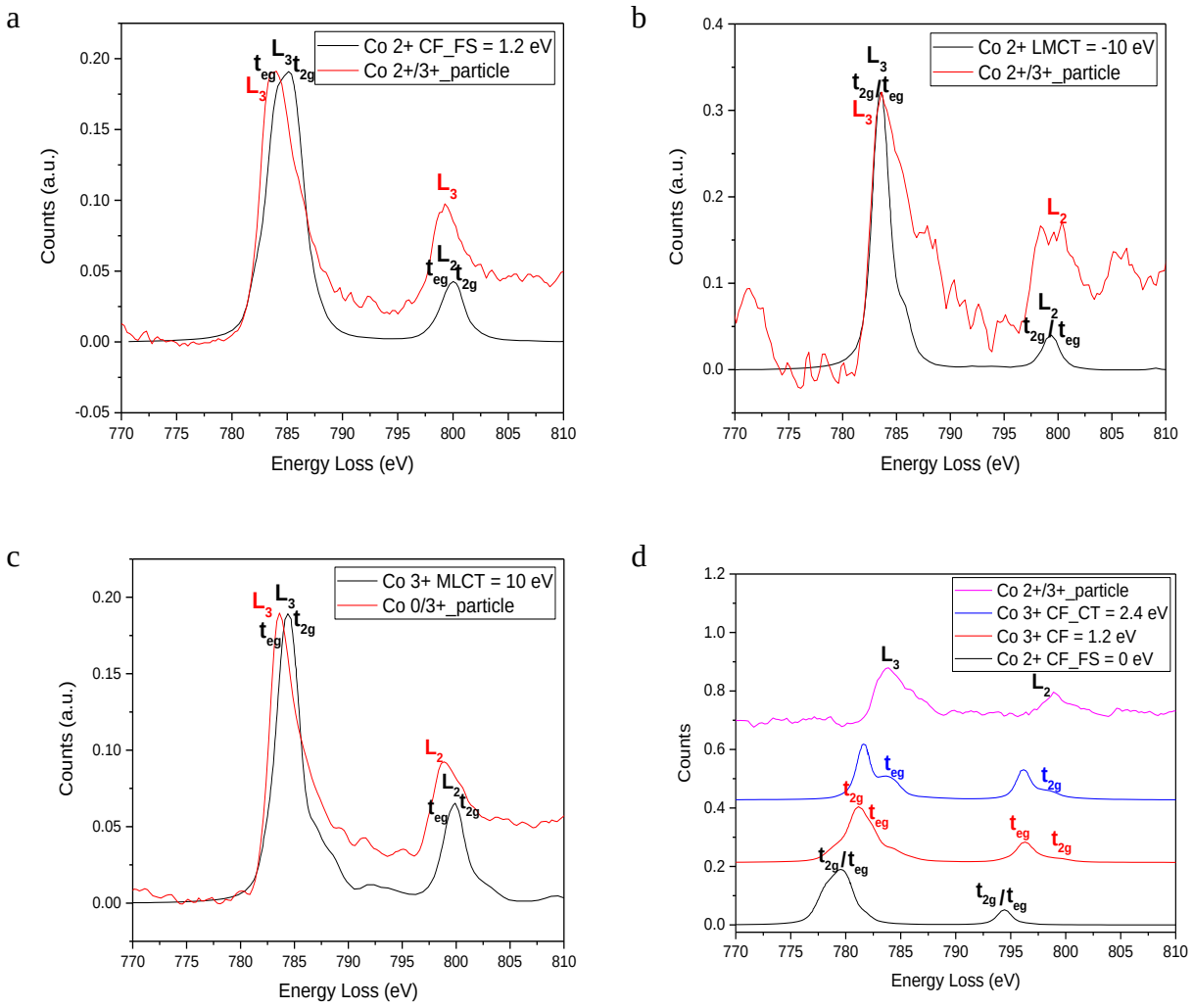


Figure 9.8. The calculated Co $L_{2,3}$-edge of (a) Co 2+ CF_FS (final state) = -3 eV (black) and a $PtCo_3$ unleached nanoparticle (red); (b) Co 2+ LMCT = -10 eV (black) and a Pt_3Co unleached nanoparticle (red); (c) Co 3+ MLCT = 10 eV (black) and a $PtCo_3$ unleached nanoparticle (red) and (d) Co 2+ CF_FS = 0 eV (black), Co 3+ CF = 1.2 eV (red), Co + CF_CT = 2.4 eV (blue) and a $PtCo_3$ leached nanoparticle (pink). All spectra shown are from the cores of the nanoparticles due to higher SNR. All calculated spectra broadenings are Gaussian = Lorentzian = 0.98 eV to match the experimental dispersion of 0.25 eV/ch on the nanoparticles.

Further calculations showed a range of features on the nanoparticles. These features were difficult to assign due to low SNR. The spectra from the cores of the nanoparticles were chosen due to higher SNR. Some evidence of Co 2+ final state effects (only final state crystal field parameter used) of 1.2 eV were found on a $PtCo_3$ unleached particle of Co 2+/ 3+ composition (Figure 9.8a). It is interesting to see that the e_g orbitals were on the lower energy side of the white line peaks while those of the t_{2g} were on the higher energy side. From a simple atomic crystal field model, e_g orbitals are generally higher than t_{2g}, however, their relative energies

may change as more orbitals or states interact. The multiplets code does not allow a detailed analysis of which exact states or term symbols give rise to the e_g and t_{2g} orbital distribution, thus spectra is labelled according to where the orbitals are most dominant.

Some evidence of Co 2+ LMCT Δ = -10 eV was found on a Pt_3Co unleached particle of Co 2+/ 3+ composition at ~797 eV (Figure 9.8b). The distribution of the e_g and t_{2g} contributions were of approximately equal proportions on both of the white lines. This was determined by solely including either the $T(b_1)$ and $T(a_1)$ to see the effects of just the e_g orbitals, or $T(b_2)$ and $T(e)$ for the t_{2g} orbitals on the L_3 and L_2 peaks. The intensities arising from the e_g orbitals were seen to change in the same position as those from the t_{2g} orbitals on both the L_3 and L_2 peaks. Another $PtCo_3$ unleached particle of Co 0/ 3+ composition showed features congruent with Co 3+ MLCT at Δ = 10 eV (Figure 9.8c). Once again, the e_g and t_{2g} orbitals were on opposite sides of their expected relative energies. Despite the predominantly metallic cobalt composition, multiplet features ranging 789 – 793 eV can be seen on the tail of the L_3 and also at ~800 eV of the L_2 peak, indicating the presence of Co 3+ charge transfer. A few particles showed effects from multiple configurations. For example, $PtCo_3$ leached particle of Co 2+/ 3+ composition showed evidence of Co 2+ final state of 0 eV, Co 3+ CF (crystal field value) of 1.2 eV and Co 3+ CF of 2.4 eV with a LMCT of Δ = -3 added (Figure 9.8d). From these effects, the Co 3+ CF of 2.4 eV with a LMCT of Δ = -3 showed the most influence on the particle. Particularly, the e_g feature at ~786 eV and that of the t_{2g} at ~801 eV on the particle. This shows strong evidence of charge transfer and may be have something to do with strong Co-O bonds formed in a leached system.

For all four sample types, including crystal field and charge transfer effects in the calculated spectra improved the match with some of the experimental spectra. For example, out of all $PtCo_3$ unleached particles measured, 61% showed this improvement. Similarly, 61% of the

Pt_3Co unleached particles also showed improvement. The number of Pt_3Co leached was slightly higher with 63% showing an improved match. The largest improvement was seen in the $PtCo_3$ leached samples, where 78% of the particles measured showed a better match. The higher percentage in the leached systems may be indicative of higher crystal field and charge transfer effects compared to unleached systems. This may be due to the chloride anions in the perchloric acid used for the acid leaching. Chloride anions are weak field ligands [227,228] which can affect *d*-orbital splittings. However, it is more likely the higher oxidation states in the leached systems mean higher crystal field and charge transfer effects. In the spectrochemical series, the Co 3+ cation is a strong field ligand [227] and will induce more *d*-orbital splittings than the much weaker field Co 2+ cation.

No clear trend between the calculated cobalt spectra and the oxygen fine structure could be found. This is complicated by the fact that each pixel of the SI is a site containing a mixture of oxidation states with no knowledge of the precise composition. This is also limited by the SNR of the both the O *K*-edge and Co $L_{2,3}$-edge on some of the nanoparticles. Further limitations include the lack of output of the term symbols from the code. This would have eliminated estimates of the relative energies of the term symbols and subsequently gave more detail on orbital interactions that create the multiplets.

9.4 Conclusions

The AMT calculations have reproduced the Co $L_{2,3}$-edge for the Co 2+ and Co 3+ standards fairly well. It was found that the mixed state is not simply a sum of the Co 2+ and Co 3+, inferring that the symmetry of the site effects the spectrum strongly enough to be picked up in the fine structure. The physical form of the Co 2.67+ standard is where the Co 2+ atoms sit in tetrahedral sites and Co 3+ atoms in octahedral sites. A linear combination of separate calculated spectra of Co 2+ in tetrahedral symmetry and Co 3+ in octahedral symmetry showed

a closer match to the experimental spectrum of the Co 2.67+ standard than when both cations are in octahedral symmetry. However, it still did not fully match the experimental spectrum of the Co 2.67+ standard. The fine structures of the Co 2+ and Co 3+ standards were more accurately reproduced when crystal field and charge transfer effects were added. While some evidence of crystal field and charge transfer effects in the Co $L_{2,3}$-edge spectra across the nanoparticles studied was found, the assignments were not very conclusive due to low SNR. It appears that the leached systems have the most spectral features congruent with these effects – this has not been investigated in depth. A theory is that the chloride ligands from the perchloric acid, used for the leaching process, together with higher amounts of the Co 3+ cation, may cause changes in the crystal field and charge transfer to arise. Although the calculations showed that the fine structure can be affected by parameters such as charge transfer and crystal field strength, it can be difficult to decouple the effects of the different parameters. In addition, the low SNR of the nanoparticles made comparison of subtle features difficult to interpret.

There were many limitations that could be improved upon based on the code. Firstly, the inability to calculate the spectrum of metallic cobalt meant no multiplet features could be compared to experimental data. More complex, is the addition of continuum contributions to model the edge jump between the white lines. This would have enabled a more precise comparison with experimental spectra. The values of the white line ratios varied from experiment – this is expected as literature also have slightly different values. However, the trend was found to be congruent with experiment. The CTMXAS code could improve the results and analysis if extraction of term symbols from non-lanthanide elements were included.

9.5 References

[224] Sherrill C D and Schaefer H F 1999 The Configuration Interaction Method: Advances in Highly Correlated Approaches *Adv. Quantum Chem.* **134** 143–269

[225] Morales F, de Groot F M F, Glatzel P, Kleimenov E, Bluhm H, HAvecker M, Knop-Gericke A and Weckhuysen B M 2004 In Situ X-ray Absorption of Co/Mn/TiO_2 Catalysts for Fischer-Tropsch Synthesis *J. Phys. Chem. B* **108**, 16201–16207

[226] De Groot F M F and Turner T S 2004 In Situ X-ray Absorption of Co/Mn/TiO_2 Catalysts for Fischer-Tropsch Synthesis *Phys. Rev. B* **108**, 6090–6102

[227] Shriver D F and Atkins P W 2001 *Inorganic Chemistry* (Oxford: Oxford University Press)

[228] Tsuchida R 1938 "Absorption Spectra of Co-ordination Compounds. I *Bull. Chem. Soc. Jpn* **13** 388–400

10 Surface modelling of O *K*-edge using density functional theory

10.1 Geometry optimisation and Convergence Tests

10.1.1 Context of calculations

Following the calculation and analysis of the cobalt fine structure across the nanoparticles, the oxygen spectra needs to be simulated for comparison to experiment and to see, if any, the influence of cobalt on the oxygen spectra. The calculations are built on previous work done on platinum and cobalt systems by Dr. Misbah Sarwar at the Johnson Matthey Sonning Common centre. In her work [10,206], the energy descriptors used to study these systems were the segregation and binding energy. In this thesis, the oxygen binding energy is the descriptor which will be used to study the oxygen interaction on the metal surfaces. More importantly, the optimised structures of oxygen bound to these metal surfaces would be used to simulate oxygen EEL spectra, which has not been previously studied. The software used to run the DFT calculations is CASTEP [161]. CASTEP is used to calculate the matrix element but requires another software, OptaDOS [167], to obtain the EEL spectra. Apart from the calculations on the CoO and Co_3O_4 which were run by Dr Rebecca Nicholls, all calculations have been run by the author at the Materials Department, University of Oxford.

In order to calculate the oxygen binding on the PtCo alloys, a model crystal of the alloy is required. Essentially, the bulk properties of the crystal is the first point of reference. In reality, the number of atoms in the crystal is relatively large and so it is computationally not feasible to model the real system. However, the relatively infinite system can be used to model a finite system if the model is set up correctly. Once the bulk properties have been optimised, the model used for the surface interaction is referred to as a slab. The slab is a surface cut from the bulk, onto which liquid or gas molecules such as O_2 adsorb. In a real world system, surfaces behave

different to the bulk because they have lower coordination to neighbouring atoms and this difference can lead surface relax and or reconstruction. This then gives more realistic chemical properties for study of adsorbed species such as O_2 on the metal surface.

10.1.2 Bulk Models

Crystal models of the pure systems, platinum and cobalt, were obtained from the Crystallography Open Database (COD) and the Inorganic Crystal Structure Database (ICSD). The crystal structures were the ground state structures at room temperature. To ensure that calculations were as accurate as possible for oxygen adsorption on the metal surfaces, properties such as lattice constants, bond lengths and space group of the systems were checked in literature for consistency with the models used. The PtCo alloys are known to have cubic close packed (ccp) or fcc symmetry. While the platinum bulk used was an fcc crystal [229] the hexagonal close packed (hcp) cobalt bulk was found to be more thermodynamically stable at room temperature than the fcc [230] and so the hcp structure [231] was used for the cobalt bulk.

All crystals can be represented by a repeating unit cell. The computational time can be reduced by using primitive, instead of conventional unit cells. However, to better depict the symmetry of the atoms, the bulk models are shown in an expanded version of the conventional unit cells (Figure 10.1a – e). The platinum and cobalt bulk models (Figure 10.1a and b) are the first calculations done as they are the pure systems. The platinum cell vectors are $a = b = c = 3.92$ Å while the cell angles are $\alpha = \beta = \gamma = 90°$. The cobalt cell vectors are $a = b = 2.52$ Å and $c = 4.07$ Å while the cell angles are $\alpha = \beta = 90°$ and $\gamma = 120°$. The cell vectors and angles were constrained such that the former were allowed to relax but the latter were fixed. The cell angles for the bulk are common knowledge and are known from literature and as such, it was computationally efficient to fix them. The cell vectors on the other hand tend to vary slightly so they were allowed to relax during the calculation.

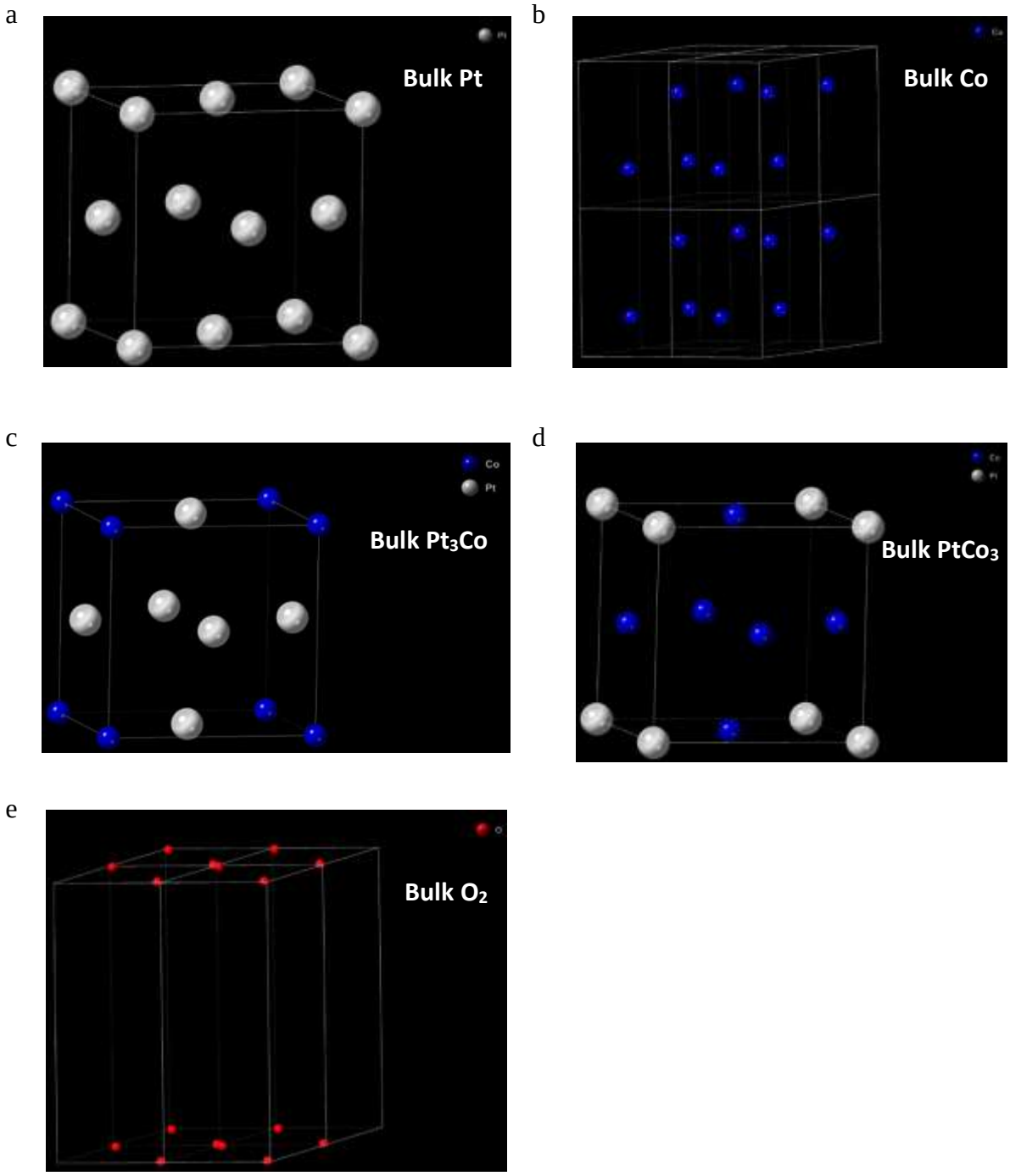


Figure 10.1. Crystal model unit cells for (a) bulk Pt, (b) Co, (c) Pt_3Co, (d) $PtCo_3$ and (e) O_2. The models were obtained from COD and ICSD and the images produced in the crystal viewer software, Jmol. NB: Pt atoms are grey, Co atoms are pink and O atoms are red.

There are two atoms in the cobalt bulk unit cell and so cobalt can be ferromagnetic i.e. spins aligned on both atoms (↑↑) or antiferromagnetic where they are unaligned (↑↓). For the alloys, the bulk platinum conventional unit cell is used as a starting point for the geometry optimisation, substituting the platinum atoms for cobalt accordingly (Figure 10.1c and d). In

the case of the Pt_3Co alloy, the platinum atom at the corner of the cell is replaced with a cobalt atom. Conversely, the three nearest neighbours of the corner platinum atom are replaced with cobalt atoms. This ordered alloy model was chosen as opposed to the disordered alloy because it is less computationally intensive due to the symmetry reducing the number of calculations. In addition, it is easier to orient the spins in aligned and non-aligned states using the ordered model. The cell vectors are $a = b = c = 3.92$ Å while the cell angles are $\alpha = \beta = \gamma = 90°$.

In order to model the oxygen bulk, a slightly different approach was taken. The oxygen being a molecule meant careful consideration had to be taken for the modelling. The oxygen molecule, O_2, is not a periodic crystal but because CASTEP requires periodicity, the O_2 molecule was modelled with large unit cell vectors (Figure 10.1e) in order to minimise any interaction with its own periodic image. The oxygen cell vectors are $a = b = 11.23$ Å and $c = 30$ Å while the cell angles are $\alpha = \beta = 90°$ and $\gamma = 120°$. The hexagonal cell was used as it is more computationally effective than having the same spacing on a square lattice. The distance between the oxygen atoms in O_2 were 1.21 Å, the confirmed bond length by experiment [232]. Lastly, O_2 is diamagnetic and was therefore modelled with a spin of 2 but not with any magnetised direction as in the case of the cobalt.

10.1.3 Optimisation of Cut-off Energy

CASTEP is a one-electron code which replaces the core electrons and nucleus with a pseudopotential. The calculations used in this study are on-the-fly ultrasoft pseudopotentials [233,234,235], which are pseudopotentials generated during the calculation rather than pulling from a pre-set library database. These are implemented with the Perdew-Burke-Ernzerhof (PBE) functional. The number of plane waves used in the calculation depends on K_{max}, a cut-off energy value related to the number of plane waves. The more plane waves used, the more accurate but computationally intensive a calculation becomes. A value of K_{max} where

increasing it does not affect the value of the property of interest is the goal of the optimisation. In this case, these properties are the total energy and bond length.

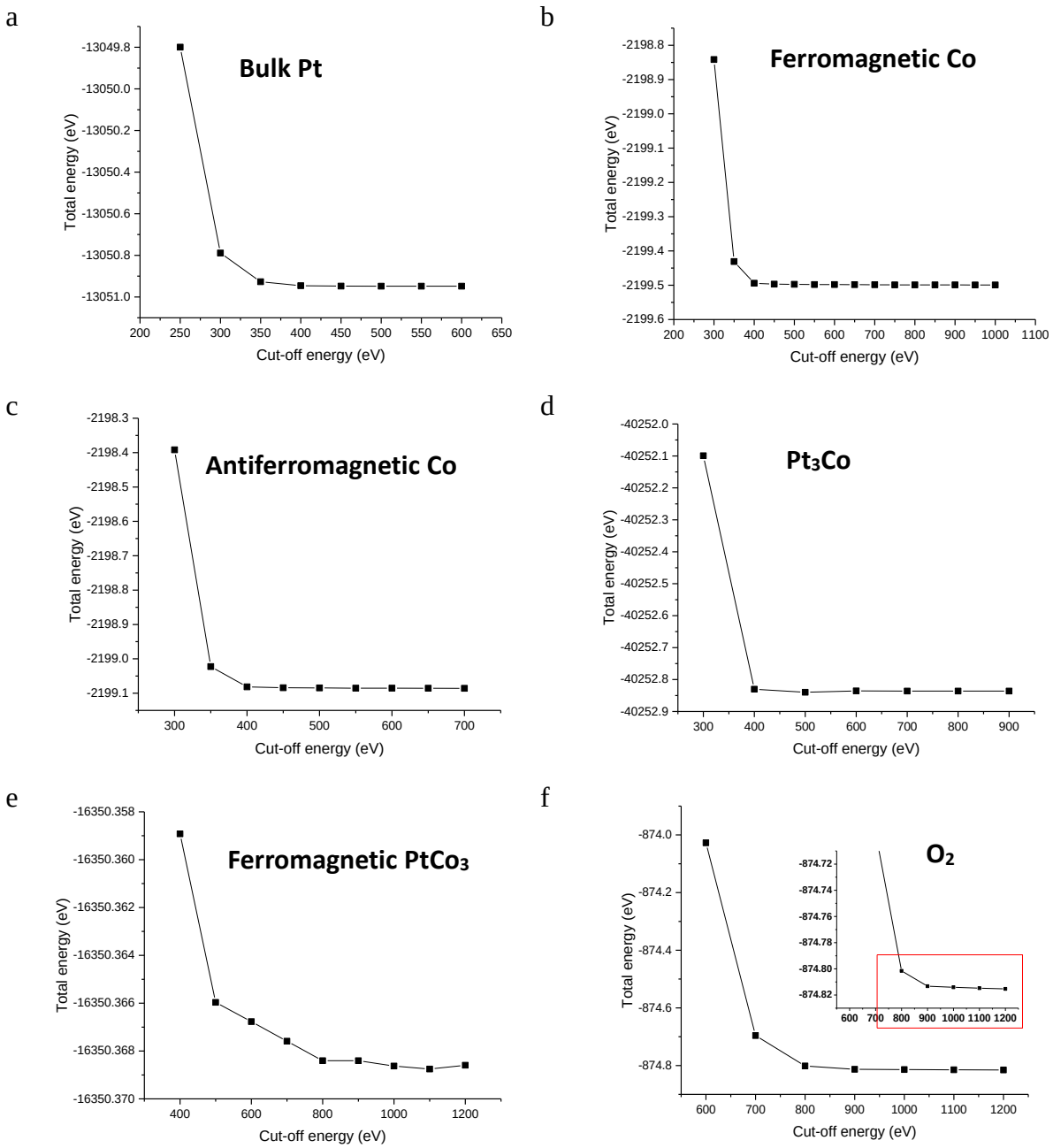


Figure 10.2. Variation of the total energy of (a) bulk Pt, (b) ferromagnetic Co, (c) antiferromagnetic Co, (d) Pt_3Co, (e) ferromagnetic $PtCo_3$ and (f) O_2 (inset: zoom) with cut-off energy at a k-point spacing of 0.04 $Å^{-1}$.

As shown by the graphs, the total energy decreases with the number of plane waves (Figure 10.2a – f). There is an initial large decrease at very low energy plane waves, followed by smaller decreases and then an eventual plateau. The optimised values of K_{max} were 450, 550,

700 for Pt, ferromagnetic Co, antiferromagnetic Co and Pt_3Co, respectively. Both ferromagnetic $PtCo_3$ and O_2 had higher values at 1000 eV. The Pt has the lowest K_{max} while O_2 has the highest K_{max}, congruent with previous work done by Dr Misbah Sarwar. It is important that the cut-off values are chosen after at least two data points that show a plateau in the variation of the total energy in order to minimise the possibility of a metastable state. In order to optimise K_{max}, another parameter, referred to as *k*-points, is required. The *k*-points are points in reciprocal space, *k*, of the crystal which determine the sampling size. They can be specified as a grid or spacing. In this work, a *k*-spacing of 0.04 $Å^{-1}$ was used. The *k*-spacing itself is also optimised with respect to the K_{max} values and this will be shown in the next section.

10.1.4 Optimisation of *k*-point Spacing

In addition to K_{max}, the value of the property of interest also needs to be converged with respect to the k-point spacing. As briefly discussed in the section 10.1.3, in the reciprocal space of any crystal, the number of points chosen determines how broadly or thinly the crystal is sampled. Ideally, all *k*-points or *k*-space would like to be sampled, however, this is not practical due to the computational cost. Generally, the total energy tends to decrease as the number of *k*-points increases, although not always. Since *k*-spacing was used, the total energy is expected to decrease as *k*-spacing decreases. However, the trend with the number of points sampled is still the same because a smaller *k*-spacing is equivalent to a larger number of *k*-points.

The bulk Pt, ferromagnetic Co and antiferromagnetic Co graphs all show the total energy decreasing as *k*-spacing decreases (Figure 10.3a, b and c). However, the opposite trend is seen for the Pt_3Co and ferromagnetic $PtCo_3$ plots (Figure 10.3d and e). Nevertheless, it is clear that all the graphs show a plateau, evidencing convergence. The first instance of this is seen at approximately 0.04 $Å^{-1}$ in all of the plots. The graph of bulk O_2 has not been included because an examination of how the total energy varies with *k*-points or *k*-spacing was not required. This

is because for non-periodic systems such as liquid or gas molecules, the unit cell is large enough for a single *k*-point to suffice. Thus, the plots of the total energy versus plane wave energy and the bond length in section 10.1.3, done at the *k*-spacing of 0.04 $Å^{-1}$, was sufficient to ascertain convergence of the O_2 bulk.

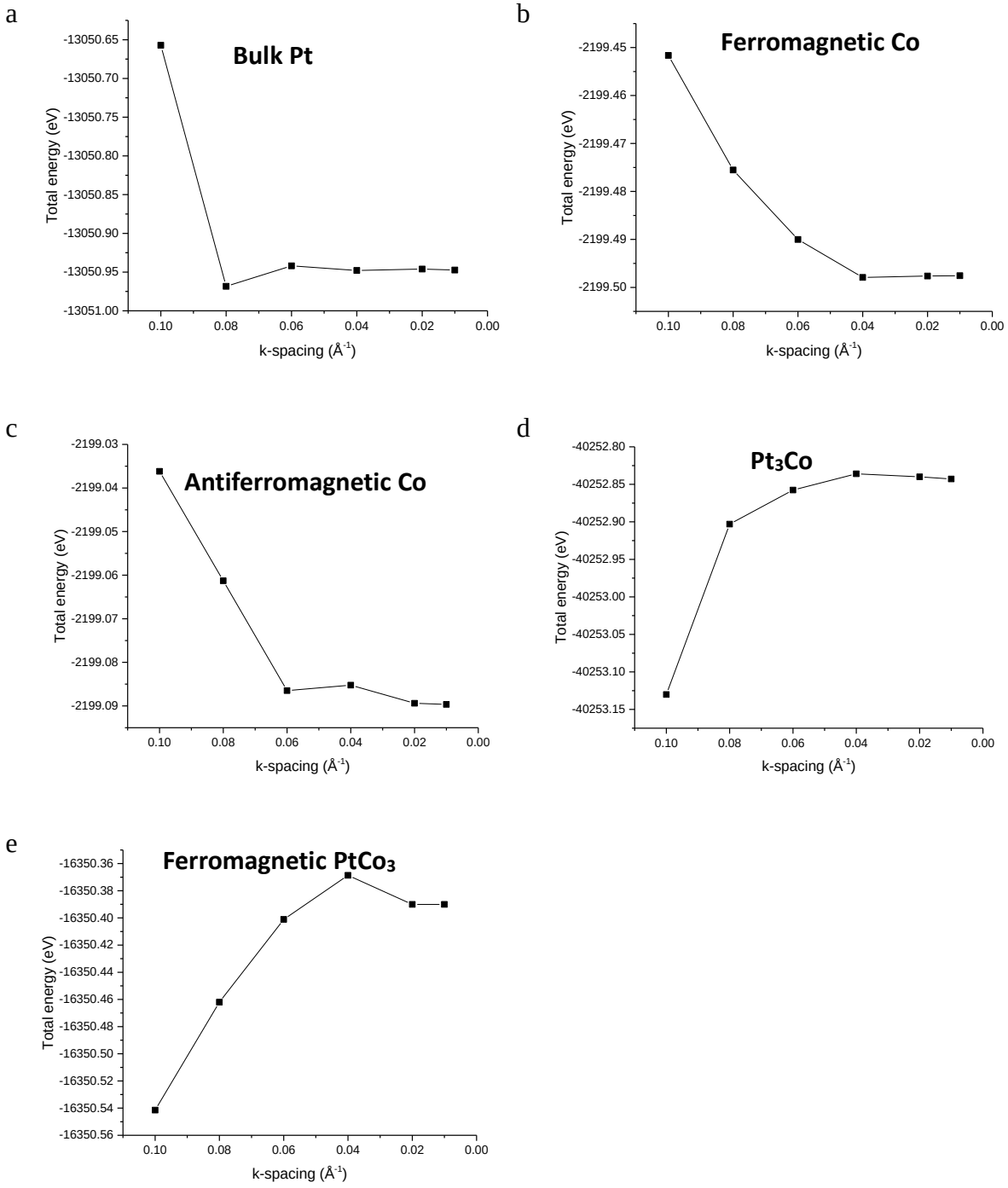


Figure 10.3. Variation of the total energy of (a) bulk Pt, (b) ferromagnetic Co, (c) antiferromagnetic Co, (d) Pt_3Co and (e) ferromagnetic $PtCo_3$ with *k*-spacing.

Table 10.1. Values of *a*, *b*, *c* lattice vectors and bond length (*bl*) from bulk Pt, ferromagnetic Co, antiferromagnetic Co, Pt_3Co, ferromagnetic $PtCo_3$ and O_2 before (expt./init.) and after (calc.) geometry optimisation at their K_{max} values. Expt. = experiment. Init. = initials. Experimental parameters compared for Pt [229], Co [231], Pt_3Co [236] and $PtCo_3$ [237].

	***a* (Å)**	***b* (Å)**	***c* (Å)**	***α* = *β***	***γ***	***bl* (Å)**
Pt calc.	3.97	3.97	3.97	90	90	2.81
Pt expt.	3.92	3.92	3.92			
ferromagnetic Co calc.	2.52	2.52	4.03	90	120	2.48
ferromagnetic Co expt.	2.52	2.52	4.07			
antiferromagnetic Co calc.	2.46	2.46	3.96	90	120	2.50
antiferromagnetic Co expt.	2.52	2.52	4.07			
Pt_3Co calc.	3.88	3.88	3.88	90	90	2.75
Pt_3Co expt.	3.85	3.85	3.85			
ferromagnetic $PtCo_3$ calc.	3.67	3.67	3.67	90	90	2.60
ferromagnetic $PtCo_3$ expt.	3.67–3.89	3.67–3.89	3.67–3.89			
O_2 calc.	11.23	11.23	30	90	120	1.22
O_2 init.	11.23	11.23	30			

Along with the total energy, the lattice parameters and bond lengths are also expected to converge with increasing plane wave energy. Although not shown, at the *k*-spacing of 0.04 $Å^{-1}$, the lattice parameters and bond lengths had the exact trend as the total energy variation. The final values from each of the bulk calculations are tabulated (Table 10.1). The values before geometry optimisation are also shown for comparison. The Pt, Pt_3Co and ferromagnetic $PtCo_3$ had $a = b = c$ values of 3.97, 3.88 and 3.67 Å, with bond lengths of 2.81, 2.75 and 2.6 Å, respectively. It is important to mention that with the $PtCo_3$ bulk, there are eight different

arrangements of the spins on the Co atoms, and these were all modelled. However, the only arrangement which converged was the ferromagnetic type, where all the spins are aligned in the same direction. The ferromagnetic Co and antiferromagnetic Co bulks had $a = b$ values of 2.5 and 2.46 Å, respectively; their c values were 4.03 and 3.96 Å, respectively. For the O_2 bulk, the $a = b$ and c values did not change from their inputs values of 11.23 and 30 Å, respectively. Since O_2 is a molecule, such high values for the vectors were used to avoid it interacting with its mirror image. However, the bond length optimised to approximately 1.22 Å, congruent with the 1.21 Å value in literature [232].

10.2 Slabs

To study the adsorption of oxygen on the metal surface, the bulk properties are not sufficient descriptors. Hence, a slab with vacuum is set up as the surface model. The optimisation on the bulk then serve as a reference point for calculations on the slab. A slab is a layer of atoms cut from the bulk crystal in a specific direction or plane. The slab model used in this study was a 4x4 surface comprising 80 atoms in 5 layers (Figure 10.4a – f). The crystallographic direction of the surface is important and for Pt and its alloys, the Pt(111) plane shows the most activity for the ORR. This Pt(111) plane has been found to have the lowest surface energy and largest facets [238]. Although terrace and edge sites are known to have a high affinity for oxygen adsorption, the Pt(111) surface is the most thermodynamically favoured for the dissociative oxygen adsorption [26,27,239,240], which is the accepted pathway in which the ORR proceeds [12,26,27,206,239]. Besides, a lot of the steps and vertices sites which favour oxygen adsorption are top and bridge sites [26,241]. In literature, the common sites studied are the top, bridge, hcp, and fcc sites [26,27,176,178,242,243]. The top site as an oxygen atom or molecule placed directly on top of, but not bonded to, an atom from the slab surface (Figure 10.5a). The bridge site has the oxygen atom or molecule between two atoms from the slab surface (Figure 10.5b). The hcp and fcc sites is where the oxygen atom or molecule ‘sits’ on an atom in the

second (Figure 10.5c) and third (Figure 10.5d) layer of the slab, respectively. These hcp and fcc sites tend to be 3-fold hollow sites, where 'hollow' means there are no atoms directly above the atom the oxygen 'sits' on.

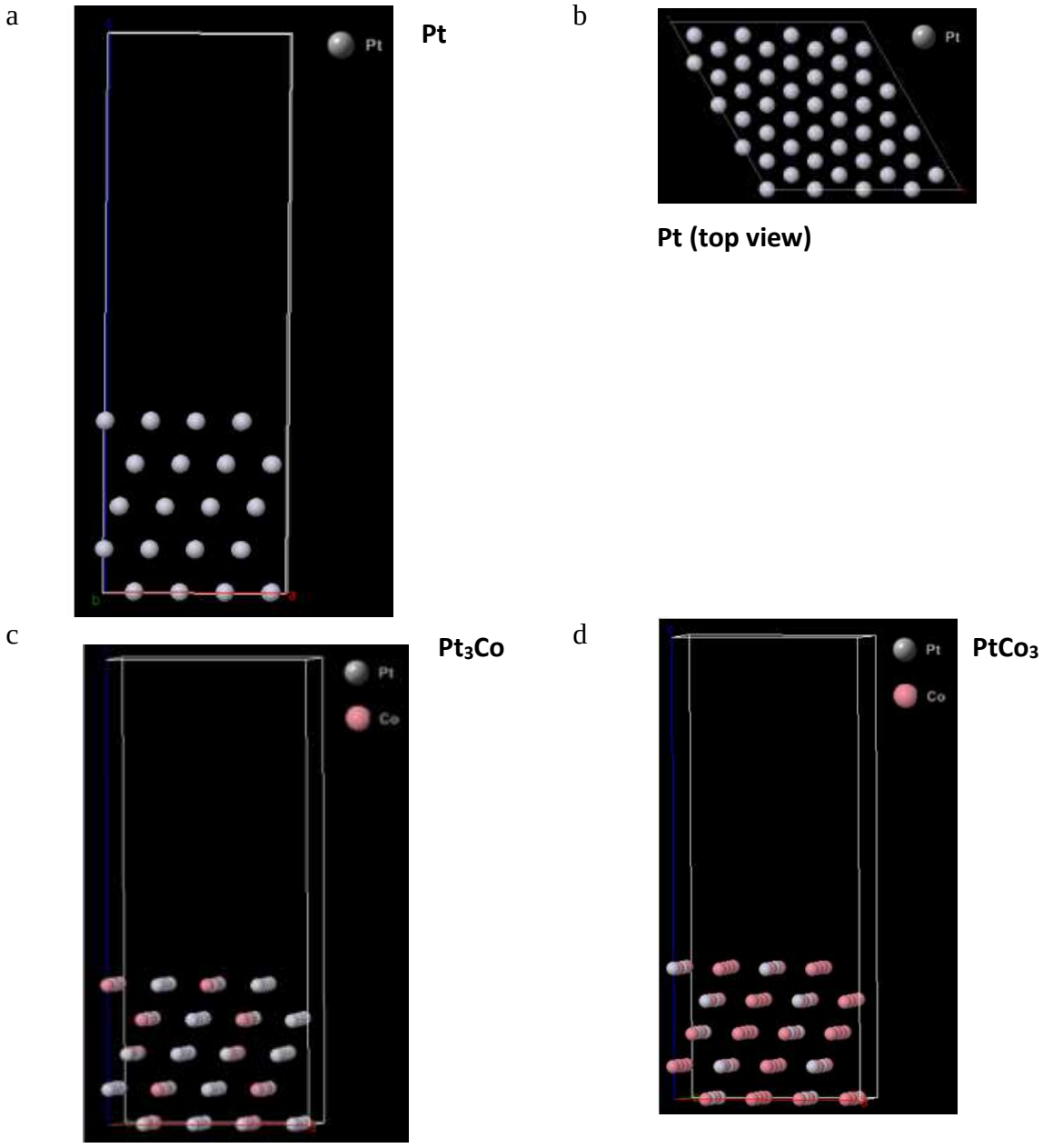


Figure 10.4. Slab models for the (111) surfaces of (a) Pt, (b) Pt (top view), (c) Pt_3Co and (d) $PtCo_3$. NB: Pt atoms are grey and Co atoms are pink. Panel a is looking down the [110] direction, panel b is looking down the [111] direction, panels c and d are looking down the [110] direction slightly rotated to the left by 30°.

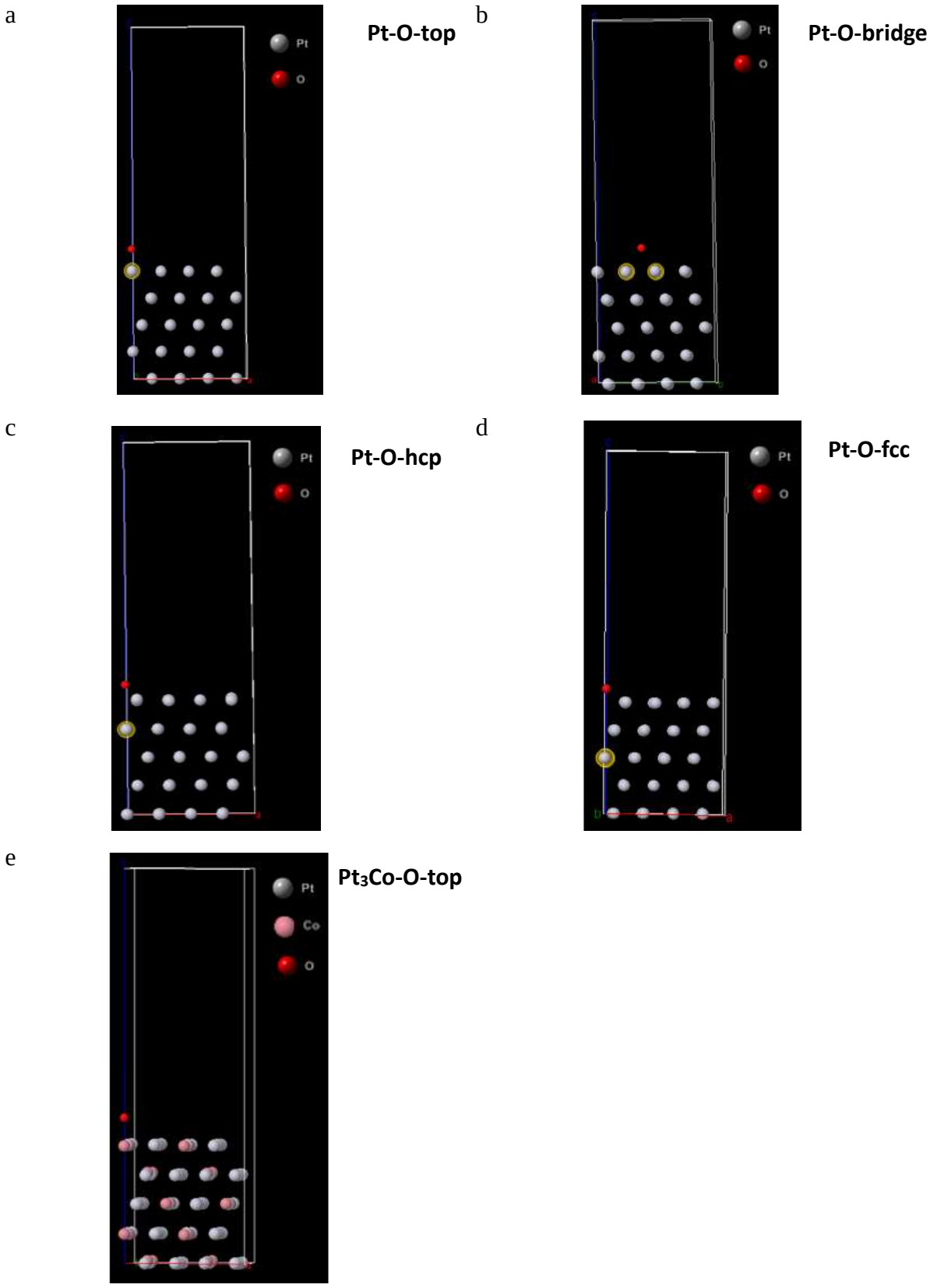


Figure 10.5. Slab models for the (111) surfaces of oxygen atom adsorbed on (a) Pt top site, (b) bridge site, (c) hcp site, (d) fcc site and (e) Pt_3Co with Co top site. NB: Pt atoms are grey, Co atoms are pink and O atoms are red. Panels a – d are looking down the [110] direction and panel e is looking down the [110] direction slightly rotated to the left by 30°.

The slabs cut from the bulk show the setup of the Pt and alloys surface models (Figure 10.4a – d). Since the O_2 bulk had the highest cutoff energy of all the bulk systems, 1000 eV was initially used to run the geometry optimisation calculations on the slabs. However, due to computational time, 800 eV, also acceptable according to the convergence curve (see section 10.1.3, Figure 10.2e), was the cutoff energy used to run all the slab calculations. Unlike the bulk calculations, both the cell vectors and angles were fixed. The positions of the atoms in the bottom two layers of the slab were also fixed to mimic the bulk properties, while the rest are not to allow for surface influence. The Pt atoms are all coloured grey (Figure 10.4a and b) while the Pt_3Co and $PtCo_3$ alloys have the Co atoms coloured pink (Figure 10.4c and d). The slabs consist of 5 layers in the fcc order of ABCAB, which are the repeat patterns of stacking. The cell vectors for the Pt slab where $a = b = 11.23$ Å and $c = 30$ Å for the vacuum perpendicular to the surface of the slab. The cell vectors for Pt_3Co and $PtCo_3$ slabs where $a = b = 10.98$ and 10.37 Å, respectively, with $c = 30$ Å. Once the slabs were geometry optimised, the oxygen atoms were added in the top site (Figure 10.5a), bridge site (Figure 10.5b), hcp site (Figure 10.5c) and fcc site (Figure 10.5d) of the Pt slab output cell and alloy output cells.

As the calculations proceeded, it was quickly realised that not all of the desired calculations could be run due to computational time. The alloys in particular took a long time to set up correctly and converge. Since the overarching aim of the study is to examine the influence of cobalt on the oxygen binding and spectra, calculations on the Pt_3Co slab (Figure 10.5e) were prioritised. In addition, only the top site could be run on the Pt_3Co slab. The top site was chosen as it had the lowest calculation time. Furthermore, the atom chosen for the top site was a Co atom instead of a Pt atom – the top site calculation on the Pt slab was deemed sufficient to study the influence Pt on the oxygen binding.

Table 10.2. Values of *a*, *b*, *c* unit cell vectors, input and output O-metal bond lengths (O-M *bl*) from Pt(111), Pt(111) O_top site, Pt(111) O_hcp site, Pt(111) O_fcc site, Pt_3Co (111) and Pt_3Co(111) O_Co_top site slabs after geometry optimisation.

	***a* (Å)**	***b* (Å)**	***c* (Å)**	**Input O-M *bl* (Å)**	**Output O-M *bl* (Å)**
Pt(111)	11.23	11.23	30	N/A	N/A
Pt(111) O_top site	11.23	11.23	30	1.83	1.81
Pt(111) O_hcp site	11.23	11.23	30	2.07 2.07 2.07	2.06 2.06 2.06
Pt(111) O_fcc site	11.23	11.23	30	2.07 2.07 2.07	2.05 2.05 2.05
Pt_3Co (111)	10.98	10.98	30	N/A	N/A
Pt_3Co(111) O_Co_top	10.98	10.98	30	2.18	1.86 2.07 2.07

The cell vectors and O-metal bond lengths recorded from the geometry optimised slabs are displayed (Table 10.2). As observable, the values for the cell vectors remained the same, showing that the lattice parameters are quite robust during geometry optimisation. The P-O bond lengths were found to increase in the order: Pt(111) O_top site < Pt(111) O_fcc site < Pt(111) O_hcp site < Pt_3Co (111) O_Co_top, with values of 1.81, 2.05, 2.06 and 2.07 Å,

respectively. The Co-O in Pt_3Co (111) O_Co_top was 1.86 Å. The results for the bridge site has not been included because it failed to converge. This may not be strange giving that Yang *et al.* and Xu *et al.* found that the bridge site on Pt(111) was merely a transition state and not a thermodynamically stable state in itself [242,244]. The next step is to compare the energies and spectra of the sites that have converged.

10.3 Analysis of oxygen sites and simulated O *K*-edge spectra

The analysis of the oxygen binding on the metal surfaces begins with a look at the most thermodynamically favourable sites of oxygen adsorption. As mentioned in section 10.1.1, the descriptor for this study is the binding energy or more specifically, the adsorption energy. The adsorption energy is described in equation 10.3:

$$E_{ads} = E_{O/slab} - E_{slab} - E_O \qquad 10.3$$

where E_{ads} is the adsorption energy, E_{slab} is the slab energy, E_O is the half of the energy of an isolated oxygen molecule and $E_{O/slab}$ is the energy of the slab with the oxygen atom adsorbed on a site [245].

Table 10.3. Values of E_{slab}, E_O, $E_{O/slab}$ and E_{ads} for Pt(111) O_top site, Pt(111) O_hcp site, Pt(111) O_fcc site and Pt_3Co(111) O_Co_top site after geometry optimisation.

	E_{slab} (eV)	E_O (eV)	$E_{O/slab}$ (eV)	E_{ads} (eV)
Pt(111) O_top	-1044055.71	-874.80	-1044493	0.11
Pt(111) O_hcp	-1044055.71	-874.80	-1044493.89	-0.78
Pt(111) O_fcc	-1044055.71	-874.80	-1044494.29	-1.18

Pt_3Co (111) O_Co_top	-805035.57	-874.80	N/A	N/A
Pt_3Co (111) O_Co_fcc	-805035.57	-874.80	-805474.34	-1.38

The calculated adsorption energies for an oxygen atom on the four sites studied are presented (Table 10.3). For the Pt(111) slab, the results show that the stability of the sites are in the order Pt(111) O_fcc > Pt(111) O_hcp > Pt(111) O_top with E_{ads} = -1.18, -0.78 and 0.11 eV, respectively. It is well known that an O atom preferentially binds to 3-fold hollow fcc sites and these results match the trend in literature [242,244,246,247,248]. The values of E_{ads} in the literature tend to range 3 ≤ 5 eV. For example, Yang *et al.* found E_{ads} = 4.76, 4.35 and 3.28 eV for the fcc, hcp and top site, respectively [242]. Similarly, Ma and Balbuena found E_{ads} = -4.48, -4.05 and -3.14 eV for the fcc, hcp and top site, respectively [247]. A few other works have reported similar values. However, the values for E_{ads} are slightly different to the calculated results in this thesis. The reason for this may be due to the difference in system used to study the sites i.e. the number of atoms, the simulation package and the libraries within. For example, the majority of the works in literature used 2x2 unit cells and a variation of software packages and these can affect the absolute values of the adsorption energies.

Comparing to other facets favourable for oxygen binding, E_{ads} values of -4.31 eV and -3.56 eV have been found for the hollow and top sites on Pt(100), respectively by Gu and Balbuena [249]. Similarly, Deskins *et al.* recorded E_{ads} values of -4.31 eV and -3.17 eV for the hollow and top sites on Pt(100) [250]. These values are similar to the fcc, hcp hollow sites and top site found by Ma and Balbuena. Following the trend of the E_{ads} values in this thesis, the hollow sites are also more favourable for oxygen adsorption than the top site on the Pt(100) surface. Furthermore, this trend is also seen on terraced sites of Pt(111) in literature. Kolb *et al.* reported E_{ads} values of -1.14 eV, -0.68 eV and 0.14 eV for the fcc-terrace, hcp-terrace and top-terrace sites on Pt(111) [251]. This trend found by Kolb *et al.* is in even more agreement with the

results found in this thesis and suggests that top sites are not as favoured as the hollow sites for oxygen binding on the Pt(111) surface.

The values of E_{ads} on the Pt(111) sites in literature are generally either all positive or all negative. Sometimes, the negative of the formula used in this study (equation 10.3) is used to calculate E_{ads} in some works in literature and so the absolute values are more important in this respect. However, the values of E_{ads} calculated in this study are a mixture of both positive and negative values i.e. -1.18, -0.78 and 0.11 eV for the fcc, hcp and top sites, respectively. This evidences that while the O atom prefers to be bonded to a Pt atom on the surface of the Pt(111) slab in the case of the fcc and hcp sites, it is more stable as part of an O_2 molecule relative to the top site. Although not published, this finding is congruent with previous test calculations done with Dr Misbah Sarwar, which gave -3.38, -2.97 and 2.28 eV on the fcc, hcp and top sites, respectively. It can be seen that there is also a variation in the absolute values compare to those in this study, however, this can be explained by the smaller cell used (2x2) and the different version of CASTEP used.

The calculated adsorption energy for an oxygen atom on $Pt_3Co(111)$ O_Co_top site failed to converge. Looking into literature, it was found that the top site collapses into the favourable fcc site [206,244]. Consequently, the calculation for the $Pt_3Co(111)$ O_Co_fcc site was run and this was the result obtained for the oxygen atom on the alloy (Table 10.3). With E_{ads} = -1.38 eV, the $Pt_3Co(111)$ O_Co_fcc site had the lowest adsorption energy out of all the slab calculations. The $Pt_3Co(111)$ O_Co_fcc site has a lower E_{ads} than the most stable site on the pure platinum slab, Pt(111) O_fcc (E_{ads} = -1.18 eV), making it the most stable out of all the slab calculations. This is not surprising as $Pt_3M(111)$, where M is a metal with a 3*d* outer shell, are known to have a more negative E_{ads} than Pt(111) due to their stronger affinity for oxygen [246]. For an effective replacement of the Pt catalyst, one that binds approximately 0.2 eV weaker than Pt is desired [10,18]. Out of all the slab calculations, only the Pt(111) O_top binds

weaker. However, in addition to the positive value of E_{ads} at this site, it binding the O atom 0.89 eV and 1.29 eV weaker than the hcp and fcc sites, respectively, is not favourable. On the other hand, while the $Pt_3Co(111)$ O_Co_fcc site has a more negative E_{ads} than Pt(111) hcp and fcc sites, it only binds the O atom stronger by 0.6 eV and 0.2 eV, respectively. This means it is the next favourable site for the ORR after the Pt(111) hollow site. However, if more PtCo slabs and site calculations had been run, a more favourable site for the ORR may have been found.

Now that the relative energy stability of the oxygen at different sites is known, spectral core-hole calculations are implemented at these sites to study their influence on the O *K*-edge fine structure. In addition to the oxygen calculations at various sites, the experimental standards, CoO and Co_3O_4, were also simulated for a more accurate and complete study of the O *K*-edge fine structure. The calculation of the CoO and Co_3O_4 were done without core-holes, however, according to literature [137], the effect is not significant. The calculated EELS O *K*-edge spectra were computed using the OptaDOS code with adaptive broadening. A DOS spacing of 0.01 eV and a Gaussian broadening of 2 eV to mimic the instrumental broadening and 0.1 eV Lorentzian broadening for the finite lifetime, were used. A Gaussian broadening of 1 eV was initially used to match the resolution from the experimental spectra, however, a broadening of 2 eV best matched the experimental spectra (Figure 10.6).

The edge onsets have been aligned to the Fermi energy, E_F, at 0 eV for ease of peak comparison and it is clear that peaks *a* – *d* (see chapter 7, section 7.5 for peak details) from the standard have been reproduced. However, peak *e* does not appear to be reproduced. In the calculated spectra, there is a peak at approximately 33 eV but due to its sudden drop off, it is likely not a real peak. There is also a cut-off at approximately 35 eV, which is due to insufficient amount of bands used in the calculations. This does not seem to be an issue as the transitions beyond 35 eV are relatively small and do not form a significant part of the O *K* fine structure. In

addition, there is a peak *d*' at approximately 26 eV from the calculated spectra which seems to match the peak at approximately 25 eV in the CoO standard (Figure 10.6). This peak was not labelled in the CoO standard because the origin of the peak was unknown. However, given that this peak is reproduced in the calculated spectra, and in literature [137], it seems reasonable that the peak is a real part of the fine structure.

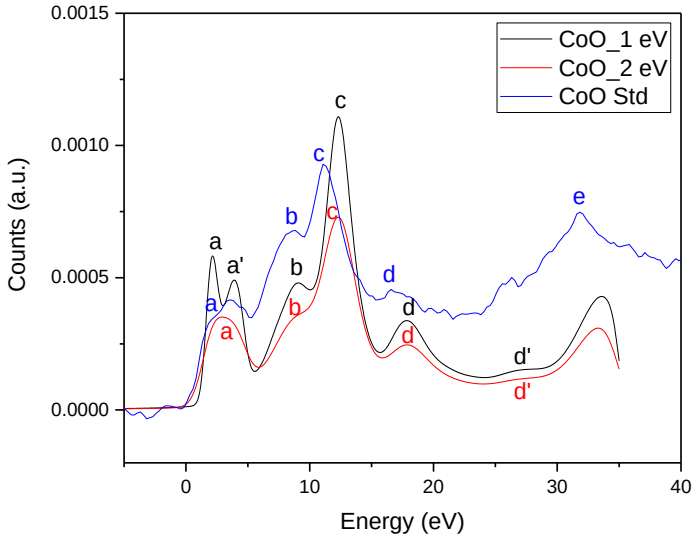
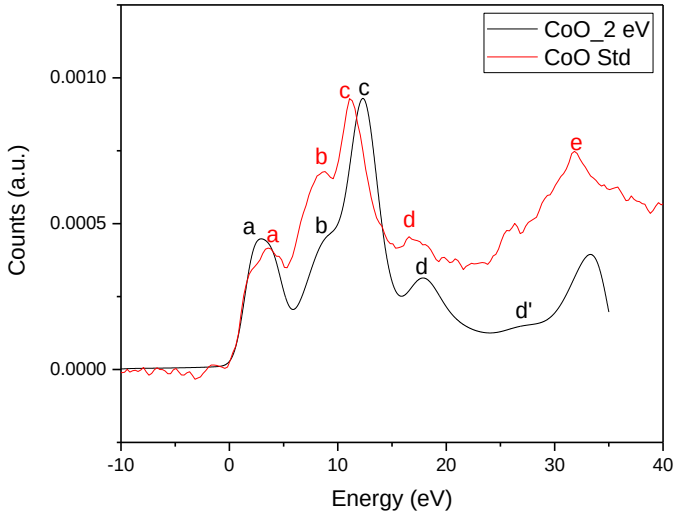


Figure 10.6. Comparison of calculated O *K*-edges for CoO at a Gaussian width of 1 eV (a), 2 eV (b) and CoO standard from experiment at 0.25 eV/ch (c). NB: The labels are for the CoO standard and edge onsets have been aligned to the Fermi energy at 0 eV.

The results of the calculated O *K*-edges for CoO and Co_3O_4 also show good agreement with the CoO and Co_3O_4 experimental standards (Figure 10.7a and b). While the edge onsets have been shifted so that the calculated and experimental spectra align, the relative peak positions within the O *K* fine structure itself have been well reproduced. Overall, a slight shift to higher energies is noticeable for the calculated CoO spectrum compared to the CoO standard. For example, ignoring peak *a* since the onsets have been aligned, peak *b* in the calculated CoO spectrum (Figure 10.7a) is shifted higher by approximately 0.5 eV. The shift is more noticeable with peaks *c* where the shift is approximately 1.5 eV. Peaks *d* and *d'* are shifted by approximately 1 eV. It should be noted that these shifts depend on the alignment of the spectra.

For example, the onsets i.e. peak *a*, has been used to align the spectra, however it could have been any of the peaks since the energies from the calculations are not absolute.

a



b

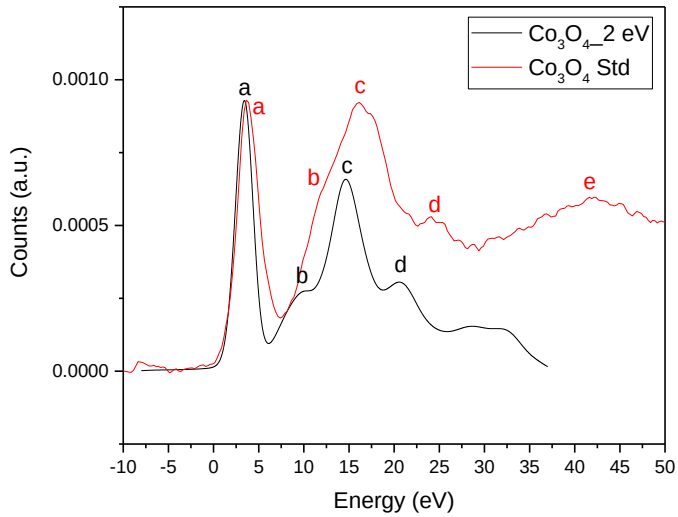
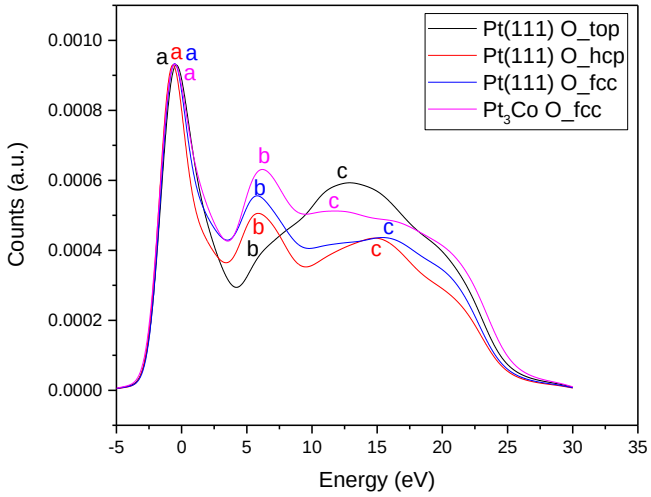


Figure 10.7. Comparison of O *K*-edges for (a) calculated CoO at a Gaussian width of 2 eV with CoO standard and (b) calculated Co_3O_4 at a Gaussian width of 2 eV with Co_3O_4 standard. NB: The edge onsets have been aligned to the Fermi energy at 0 eV.

Contrastingly, the calculated Co_3O_4 spectrum shows shifts to lower energies, approximately 2 eV for peaks *b* – *d*, compared to the Co_3O_4 standard (Figure 10.7b); again, peak *a* is where the onset is aligned. Again, the peak above approximately 30 eV is likely not real due to insufficient bands and has therefore not been labelled. However, the most noticeable difference between the calculated and experimental spectra is the variation in the relative intensities. The variation

is more prominent in the Co_3O_4 spectra than those of CoO. For example, in the calculated spectra, peak *a* is a lot larger compared to peak *b* in the experimental standards (Figure 10.7a and b). The same can be seen with peak *b* compared to peak *c*. However, looking at peaks *a* – *d* for both the calculated and experimental spectra, no peaks are unexpectedly larger or smaller than the other. It should be noted that any analysis due to the relative intensities is not robust because the CoO and Co_3O_4 calculations were run without core-holes, which affect the distribution of intensities in the spectra.

a



b

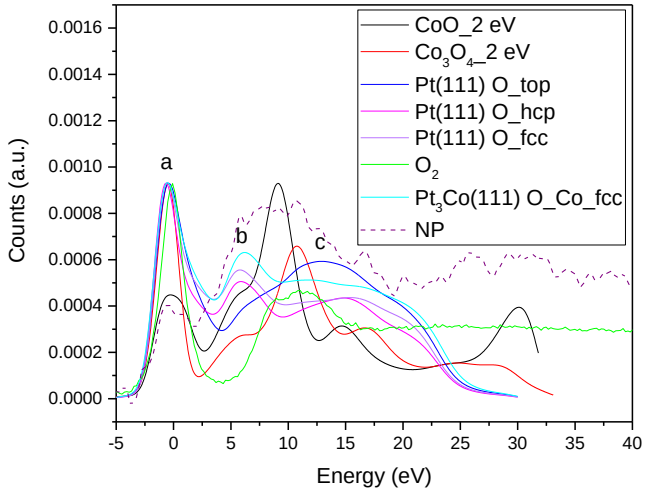


Figure 10.8. Calculated O *K*-edges for (a) Pt(111) O_top, Pt(111) O_hcp, Pt(111) O_fcc, Pt_3Co(111) O_Co_fcc at a Gaussian width of 2 eV and (b) molecular O_2, calculated CoO and Co_3O_4 at a Gaussian width of 2 eV. The spectra have been aligned by their onsets and the labels in panel b refer to Pt(111) O_top, Pt(111) O_hcp, Pt(111) O_fcc and a $PtCo_3$ unleached experimental (NP) spectra. The molecular O_2 spectrum is from the EELS database.

The calculated O *K* fine structure for the oxygen on the slabs evidently look quite different to that of NP, which is a spectrum from the shell region of a $PtCo_3$ unleached nanoparticle, those of the calculated CoO and Co_3O_4 (Figure 10.8a and b). This finding suggests that the calculated CoO and Co_3O_4 and hence, the experimental O *K*-edges, arise from bulk-like bonded oxygen atoms within the nanoparticle rather than oxygen on the surface. However, considering the surface is a smaller area compared to the whole nanoparticle and that EELS is a transmission technique, the surface O *K*-edges could be suppressed by those arising from the bulk-like bonded oxygen atoms. An experimental spectrum of molecular O_2 at 0.21 eV/ch has also been obtained from the EELS Atlas [252] for further comparison (Figure 10.8b).

All spectra have been aligned by their onsets and the peak labels refer to spectra from the slabs. The fine structures for Pt(111) O_top, Pt(111) O_hcp, Pt(111) O_fcc and Pt_3Co(111) O_Co_fcc seem to reproduce peaks *a* – *c* from the CoO and Co_3O_4, albeit the shapes and relative intensities are quite different (Figure 10.8a). It is not totally convincing that the peaks at approximately 22 eV are real. The Pt(111) O_top O *K* fine structure is noticeably distinct compared to Pt(111) O_hcp, Pt(111) O_fcc and Pt_3Co(111) O_Co_fcc. This may be due to symmetry of the hcp and fcc sites being more similar compared to the top site. It is interesting that the Pt(111) O_top O *K* fine structure is most similar to molecular O_2 (Figure 10.8b). This may be indicative of the O atom on the top site preferring to be a molecule rather than on the slab, as supported by the adsorption energy (Table 10.3). Overall, the O *K* fine structures from the pure platinum slabs are fairly similar to the alloy, with the exception of slight differences. In the O *K* fine structure of Pt_3Co(111) O_Co_fcc, peaks *a* and *b*, at ~ 2.5 and 6 eV, respectively, are shifted higher than those of the Pt(111) O_top, Pt(111) O_hcp and Pt(111) O_fcc sites (Fig. 10.8a). In contrast, peak *c* in Pt_3Co(111) O_Co_fcc, at ~ 11 eV, is downshifted relative to the other three sites in the pure platinum slabs. In addition, peak *b* in the Pt_3Co(111) O_Co_fcc fine structure has the highest intensity, relative to peak *a*, when comparing to the

other three sites. These two features seem to be the most noticeable in distinguishing between the O *K* fine structure of the alloy and those of the pure platinum slabs.

A comparison of spectra from the different sites with the calculated CoO and Co_3O_4 spectra is shown (Figure 10.8b). The Pt(111) O_top, Pt(111) O_hcp, Pt(111) O_fcc and Pt_3Co(111) O_Co_fcc onsets were not aligned with those from the calculated CoO and Co_3O_4 spectra (Figure 10.8b) because the former were core-hole calculations while the latter were not. The differences between the calculated O *K*-edges of Pt(111) O_top, Pt(111) O_hcp, Pt(111) O_fcc, Pt_3Co(111) O_Co_fcc and those of the calculated CoO and Co_3O_4 indicate that oxidation state changes are less important than the influence of the symmetry where the O atom is placed on the slab. In addition, it is known from literature that peak *a* results from O2*p*–metal 3*d* hybridisation and peaks *b* and *c* are a result of O2*p* and metal 4*sp* hybridisation. As peak *a* is very strong in all of the sites calculated, this indicates a dominant hybridisation between the O2*p* and Co3*d* orbitals rather than between the O2*p* and metal 4*sp* orbitals.

10.4 Conclusions

A computational approach has been used to study the oxygen binding and its stability on the surface of Pt and PtCo catalysts. From the calculations done on the Pt(111) slabs, an O atom located on the fcc site was found to be the most energetically stable, followed by the hcp site. These findings were congruent with previous works as 3-fold hollow sites on Pt(111) surfaces are generally found to be the most thermodynamically favoured sites. These findings were also congruent with literature. Comparison to other planes favourable for oxygen binding such as Pt(100) and terrace sites had the same trend as fond in this thesis, suggesting that top sites are not as favoured as the hollow sites for oxygen binding on the Pt surface. The top site was found to be the least stable site and the adsorption energy suggested that the environment of the O atom in the top site is similar to a molecular configuration. The adsorption energy was also

positive, inferring that O adsorption is not stable on the Pt slab. Calculation on the bridge site of the Pt(111) slab was also attempted but this failed to converge. These findings on the top and bridge site calculations were also in line with findings from previous works. For computational reasons, only the top and fcc site on the Pt_3Co slab cold be run. However, the top site did not converge, which was congruent with previous work as it is found that the O atom on the top site collapses into the more favourable fcc site. The fcc site on the $Pt_3Co(111)$ slab was found to be the most energetically stable for O atom adsorption out of all the slab calculations run. It was found to be the most favourable site for the ORR outside of the Pt(111) hollow sites.

Surface simulations were also run to distinguish between spectra from the different sites and also between bulk oxides. The O *K* spectra showed that oxygen bonding environments on the surface of the Pt(111) and $Pt_3Co(111)$ slabs are different to those in the cobalt standards and in molecular oxygen. Furthermore, the O *K* fine structure from the calculations were different to those from experimental spectra, suggesting that the experimental O *K*-edges arise from bulk-like bonded oxygen atoms within the nanoparticle rather than on the surface. Apart from the top site on Pt(111), all surface site spectra were similar. The top site fine structure resembled that of molecular oxygen the most, also inferring that the O atom in the top site prefers to be molecular. While the other three sites were similar, the fine structure from the fcc site on the $Pt_3Co(111)$ slab was most distinct, evidencing that the oxygen binding on the alloy is distinguishable from that on pure platinum. Comparison of the spectra from the bulk oxides with those from the sites suggested that the symmetry was more influential on the fine structure than oxidation state. In addition, the consistently dominant feature in the calculated spectra on all sites was found to be the onset peak, suggesting hybridisation between the O2*p* and metal 3*d* orbitals is more prominent than between the O2*p* and metal 4*sp* orbitals in the oxygen binding on the surface of the slabs.

10.5 References

[229] Davey W P 1925 Precision measurements of the lattices of 12 simple metals *Phys. Rev.* **25** 753–761

[230] O'Shea V A D, de la Piscina P R, Homs N, Aromi G and Fierro J L G 2009 Development of Hexagonal Closed-Packed Cobalt Nanoparticles Stable at High Temperature *Chem. Mater.* **21** 5637–5643

[231] Morozkin A V 2012 Gd-Co-Ge system at 870/1070 K *Intermetallics* **25** 126–138

[232] Sutton L E 1958 *Tables of Interatomic Distances and Configuration in Molecules and Ions* (London: The Chemical Society)

[233] Pickard C J, Winkler B, Chen R K, Payne M C, Lee M H, Lin J S, White J A, Milman V and Vanderbilt D 2000 Structural Properties of Lanthanide and Actinide Compounds within the Plane Wave Pseudopotential Approach *Phys. Rev. Lett.* **85** 5122–5125

[234] Liu W and Dolg M 1998 Benchmark calculations for lanthanide atoms: Calibration of ab initio and density-functional methods *Phys. Rev. A* **57** 1721–1728

[235] Laasonen K, Pasquarello A, Car R, Lee C and Vanderbilt D 1993 Benchmark calculations for lanthanide atoms: Calibration of ab initio and density-functional methods *Phys. Rev. B* **47** 10142–10153

[236] Jang J, Kim J, Yang-Hee L, Kim I Y, Park M, Yang C, Hwang S and Kwon Y and Vanderbilt D 2011 One-pot synthesis of core–shell-like Pt_3Co nanoparticle electrocatalyst with Pt-enriched surface for oxygen reduction reaction in fuel cells *Energy Environ. Sci.* **4** 4947–4953

[237] Wang, Guofeng. SISGR: Theoretically relating the surface composition of Pt alloys to their performance as the electrocatalysts of low-temperature fuel cells. United States. https://doi.org/10.2172/1105984

[238] Seriani N and Mittendorfer F 2008 Platinum-group and noble metals under oxidizing conditions *J. Phys. Condens. Matter* **20**, 497–522

[239] Li R, Li H and Jifeng Liu J 2016 First Principles Study of O_2 Dissociation on Pt(111) Surface: Stepwise Mechanism *Int. J. Quantum Chem.* **116**, 908–914

[240] Eichler A and Hafner J 1997 Molecular Precursors in the Dissociative Adsorption of O_2 on Pt(111) *Phys. Rev. Lett.* **79**, 4481–4484

[241] Verga L G, Aarons J, Sarwar M, Thompsett D, Russell A E and Skylaris C K 2018 DFT calculation of oxygen adsorption on platinum nanoparticles: coverage and size effects *Faraday Discuss.* **208**, 497–522

[242] Yang Z, Yu X and Ma D 2009 Adsorption and Diffusion of Oxygen Atom on $Pt_3Ni(111)$ Surface with Pt-Skin *Acta Phys. Chim. Sin.* **25** 2329–2335

[243] Jacob T, Merinov B V, Goddard W A 2004 Chemisorption of atomic oxygen on Pt(1 1 1) and Pt/Ni(1 1 1) surfaces *Chem. Phys. Lett.* **385** 374–377

[244] Xu Y, Ruban A V and Mavrikakis M 2004 Adsorption and Dissociation of O_2 on Pt-Co and Pt-Fe Alloys *J. Am. Chem. Soc.* **126** 4717–4725

[245] Ellaby T, Briquet L, Sarwar M, Thompsett D and Skylaris C 2019 Modification of O

and CO binding on Pt nanoparticles due to electronic and structural effects of titania supports *J. Chem. Phys.* **151** 1–11

[246] Ma Y and Balbuena P B 2008 Surface Properties and Dissolution Trends of Pt_3M Alloys in the Presence of Adsorbates *J. Phys. Chem. C* **112** 14520–14528

[247] Han B C and Ceder G 2006 Effect of coadsorption and Ru alloying on the adsorption of CO on Pt *Phys. Rev. A* **74** 1–7

[248] Getman R B and Schneider W F 2007 DFT-Based Characterization of the Multiple Adsorption Modes of Nitrogen Oxides on Pt(111) *J. Phys. Chem. C* **111** 389–397

[249] Gu Z and Balbuena P B 2007 Absorption of Atomic Oxygen into Subsurfaces of Pt(100) and Pt(111): Density Functional Theory Study *J. Phys. Chem. C* **111** 9877–9883

[250] Deskins N A, Lauterbach J and Thomson K T 2005 Absorption of Atomic Oxygen into Subsurfaces of Pt(100) and Pt(111): Density Functional Theory Study *J. Chem. Phys.* **122** 1–8

[251] Kolb M J, Calle-Vallejo F, Juurlink L B F and Koper M T M 2014 Density functional theory study of adsorption of H_2O, H, O, and OH on stepped platinum surfaces *J. Chem. Phys.* **140** 1–6

[252] EELS INFO 2020. *EELS Atlas: Oxygen. https://eels.info/atlas/oxygen*

11 Conclusions and Future Work

11.1 Overview

The main aim of this thesis is to locate oxygen on PtCo catalyst nanoparticles and study the influence of an alloying metal, cobalt, on the oxygen binding in the nanoparticles. To begin with, a review of how the structure, composition and morphology of a catalyst affects the ORR and thus catalytic activity in the hydrogen fuel cell, was discussed. In addition, the benefits of a core-shell design on Pt alloys have been highlighted. Out of several experimental techniques reviewed, a combination of STEM and EELS proves to be most suitable for the required nanoscale study of the catalyst. Furthermore, the modelling techniques of AMT and DFT have been used to simulate cobalt and oxygen fine structure, with the purpose of linking the local oxygen environment to the surface binding of oxygen to the metals. The work presented has been in three parts. The first is the investigation of cobalt oxidation states and their variation between the four PtCo sample types, using STEM-EELS. Secondly, AMT was used to calculate Co $L_{2,3}$-edges and analysing possible crystal field and charge transfer effects. Lastly, O *K*-edges at various metal sites were simulated using DFT, and their fine structure compared and analysed. Limitations and future improvements in each part are discussed hereafter.

11.2 Improvement in Oxidation State Analysis

All cobalt oxidation states found on the nanoparticles lay between Co(0) and Co 2.67+. In literature, the known stable oxidation states are between Co(0) and Co 3+. No Co 3+ states were found on the nanoparticles. The EEL spectra from the nanoparticles showed majority of the oxide states to be Co 2+ and Co 2.67+, suggesting the oxygen atoms were bonded to Co atoms mainly in octahedral sites and some tetrahedral sites. In addition, on most of the oxidation states >2+ in the nanoparticles, the O *K*-edge pre-peak intensity, representative of 1*s* transitions into the O2*p*–Co3*d* hybridised orbital, were significantly lower than the main peak

intensity. This means there was more Co 2+ than any oxide state in the nanoparticles. A total of eighty nanoparticles of various sizes were analysed. The measurement volumes ranged from as little as 2 nm to 16 nm laterally and in depth. The measurements for the standards were four times as much. In terms of pixel dimensions, this ranged 7 x 5 pixels for smallest particle to 80 x 74 pixels largest, unbinned.

There are four major types of oxygen distribution seen across the sample matrix. The first is where oxygen is mainly at the core and this tends to be where cobalt is located. The second is on certain rows/facets. The third is around the edges of the particle, however not all the way around. It was found that the oxygen was mainly in places the cobalt was not, although this type of oxygen distribution was only found on a few particles. The fourth type of oxygen distribution is where oxygen bound to specific pockets where cobalt had been leached out – mainly observed on the $PtCo_3$ leached particles. In terms of catalytic activity, the first type of oxygen distribution ensures that the surface stays Pt-rich, where it is needed for catalysis. This is because the oxygen is predominantly bonded to the oxygen. However, if the oxygen binds too strongly, 0.2 eV more than pure Pt, then desorption from the Co atoms becomes problematic. As the Co atoms also introduce compressive strain, this modifies the Pt-*d* band vacancies such that it increases ORR activity. The second type of oxygen distribution favours binding to facets, planes or terraces which may be more thermodynamically favourable for ORR, as evidenced by computational work. This type of oxygen binding keeps large parts of the catalyst surface free of intermediates which could inhibit sites for reversible oxygen adsorption-desorption kinetics. The third type of oxygen distribution shows preferential binding towards the Pt-rich surface. This is type of oxygen binding would one that would be preferred post-cycling because the oxygen is bonded to nearly no Co atoms, which is the noble metal needed to draw some charge away from the Pt atoms for the ORR. Lastly, the fourth type of oxygen distribution is almost the opposite of the previous. The oxygen is bound and leaches

out specific pockets of Co atoms, leaving a Pt rich shell, which has been seen to enhance catalytic activity the most.

The $PtCo_3$ samples were generally seen to have higher oxidation states as well as larger areas of oxidation compared to Pt_3Co samples. Across the sample matrix, the oxygen distribution in the cores were 30%, 29%, 58% and 85.3% for the $PtCo_3$ unleached, $PtCo_3$ leached, Pt_3Co unleached and Pt_3Co leached particles, respectively. Across all 80 particles measured, more than half had over 50% oxygen distribution in the core of the particle. It has further been shown that smaller particles have a more even distribution of oxygen coverage over the surface compared to larger particles, which have their oxygen coverage mostly in the shell of the particles. It is also concluded that leached particles show a higher degree of oxidation compared to the unleached particles.

The oxidation states should inform on the ability of the metal to bind oxygen, as well as the location of such sites. However, the Co $L_{2,3}$ ratios from the nanoparticles were not all within the oxidation state calibration curve, hindering the assignment of absolute oxidation states to all particles. The metallic standard had a higher ratio than ratios calculated from the nanoparticles and as such, metallic regions from the nanoparticles were used as reference. While the ratios were 30% lower than the metallic standard, they still did not enable assignment of all oxidation states. Furthermore, a low SNR affected fine structure interpretation, especially in particles with low cobalt content such as in Pt_3Co samples. This is more of an issue when extracting fine structure from the shells of the particles as they have a lot less signal than the cores of the particles.

The problem of the SNR could be alleviated, using multiframe spectroscopy, where multiple passes over the SI are summed up to give a higher SNR. However, the trade-off is sample drift and possible in-situ oxidation of the nanoparticles the longer the beam is kept at the same probe position. The discrepancy between the ratios is slightly more complicated. Ratios between the

Co (0) and Co 2+, the blue oxidised states, seems to be the most affected. More time could have been spent looking for a purer metallic standard. However, giving the large differences in the ratios, a study should be done into the effect of particle size on the white line ratios. This is because the particles used for the standards were micron-sized while the nanoparticles are much smaller. Lastly, albeit to a lesser degree, changing dispersions affected the ratios and energy onsets. While the latter could be explained by bad calibration of the spectrometer, the former is more difficult to explain. As mentioned in chapter 7, methods such as the 'HT-adjust protocol' by Webster *et al.* can alleviate the onset issue. However it is not clear if the dispersion binning is affected and hence, will give congruent ratios at different dispersions.

11.3 Cobalt Multiplet Calculations

The modelling of the Co $L_{2,3}$-edge was done at all oxidation states, excluding the metallic cobalt and the mixed valence state, Co 2.67+. The CTM4XAS code used has no option to include the former, or the calculation of mixed states, eliminating the latter. The integer cobalt oxidation states, Co+ – Co4+, were modelled fairly well. However, a linear combination of the Co 2+ and Co 3+ states did not give the mixed state, Co 2.67+. This was confirmed from the linear combination of the experimental Co 2+ and Co 3+ standard spectra. The source of this discrepancy is unknown but may be due to insufficient experimental parameters inputted into the CTM4XAS code. The physical form of the Co 2.67+ standard is where the Co 2+ atoms sit in tetrahedral sites and Co 3+ atoms in octahedral sites. A linear combination of separate calculated spectra of Co 2+ in tetrahedral symmetry and Co 3+ in octahedral symmetry showed a closer match to the experimental spectrum of the Co 2.67+ standard than when both cations are in octahedral symmetry. However, there were still discrepancies with the experimental spectrum of the Co 2.67+ standard.

It was necessary to add crystal field and charge transfer effects to reproduce the cobalt fine structure for the cobalt standards. This implied that the symmetry of the metallic site, and not

just the metal oxidation state, strongly effected the fine structure. Some evidence of crystal field and charge transfer was also found, mostly on the $PtCo_3$ leached particles. However, their assignments are not very reliable due to low SNR. The biggest limiting factor in the multiplet calculations was the inability to retrieve term symbols that represent energy transitions and orbital interactions in the fine structure. This was coded into the software for lanthanides but not for transition metals. This feature is important for linking electron configurations to hybridisation and charge transfer effects in the cobalt fine structure. Comparisons can then be made to possible features from experimental data, illuminating on the nature of the cobalt bonding in the nanoparticles.

It is also apt to mention that the CTM4XAS code used for the calculations uses atomic basis sets and semi-empirical parameters. The CI method, which is *a priori* method, uses molecular orbitals as basis sets. This means that effects of multiple transition metal sites and the effect of molecular bonding can be studied. Some of these effects are in Quanty, and updated version of the CTM4XAS code, however the details are not fully clear. The CI method is still relatively new but would be an improvement for the purposes of the study carried out in this work.

11.4 Robustness of DFT calculations

The restricting factor with the DFT calculations was time. It was not computationally feasible to run all of the oxygen simulations on the different slabs from the sample set. The top, hcp and fcc sites on Pt(111), of which the fcc site was found to be most stable, with the top site as the least. Only the fcc site on a Co atom could be run on the $Pt_3Co(111)$ slab. Other sites run were the bridge site on the Pt(111) and the top site on the $Pt_3Co(111)$ slab, however, they did not converge. Out of all the sites run on the slab, the fcc site on the $Pt_3Co(111)$ slab was found to be the most stable. It only bound the O atom 0.6 eV and 0.2 eV more than the hcp and fcc sites in Pt(111), respectively, making it the most favourable site for the ORR outside of the Pt(111) hollow sites. Comparison of the spectra from the bulk oxides with those from the sites

suggested that the symmetry was more influential on the fine structure than oxidation state, giving that spectra from the sites looked very different to those from the bulk oxides and experiment. Furthermore, the spectra from the experiment were more congruent with the calculated bulk oxide spectra rather than surface oxygen spectra. However, what was common in all spectra was the strong intensity of the onset O *K* peak, suggesting that the dominant hybridisation in the O-metal bond was that between the O2*p* and metal 3*d* orbitals.

The next logical step in this work is to model the rest of the missing sites, including those on a $PtCo_3$(111) slab. After which an investigation into functional groups on the particle surface, using phonon EELS seems appropriate. The advent aloof beam microscopy together with new levels of resolution achieved by monochromation would illuminate species present on the pristine samples as well as the acid leached samples. This would illuminate possible species that may aggregate on the particles before and after cycling, helping to optimise catalyst design. As of writing, there does not appear to be any study in this area which would make very useful new science in the field.

12 Appendices

12.1 Appendix A: Imaging and Spectroscopy Setup

12.1.1 Microscope alignment and spectrum imaging

1. Before working on the alloy nanoparticles, a specimen with similar dark-field scattering is required for calibrating and aligning the microscope. The standard for this setup is the use of Au particles and this placed in a single-tilt holder and inserted into the microscope for alignment.
2. The optics of the microscope need to be centred correctly and this is optimised by changing the Gun Tilt and Anode wobbler in the X and Y directions.
3. The microscope is aligned under normal imaging conditions. The beam spot size, camera length, MAG and emission current need to be noted and kept consistent with every experiment. Once a beam is obtained on the microscope screen, the holey carbon film is used to correct coma and astigmatism, using the Beam Align and COR CRS STIG deflector knobs, respectively. Scrolling in and out of focus at the point of infinite magnification i.e. the ronchigram should be homocentric.
4. A CL2,3 aperture is inserted and it is allowed to stabilise for at least 2 minutes. This is because sometimes, the aperture may vibrate and drift. When this occurs, the project lens shift can be used to re-centre the aperture using the PLA knobs.
5. The ADF detector is inserted and ready for aberration correction. The correction is implemented using CEOS correction software. The main aberrations are the defocus and 2-fold astigmatism, however higher order aberrations may also be corrected. During correction, the coma and astigmatism on the ronchigram has to be iteratively checked and corrected if required.
6. In *Digital Micrograph*, the waveform are adjusted with the amplifier gain and level settings to a liner regime of 20–80% so as to avoid non-linear scattering and

oversaturation of the detector. At this stage, the imaging conditions are at sufficient optimisation to acquire data.

7. A live image of the nanoparticles should now be visible on screen and ready for EELS alignment.
8. A vacuum region, a hole in the carbon grid, is found and zoomed into using the MAG selector. The beam is parked there to avoid energy losses from the specimen during EELS alignment.
9. The camera length to be used for spectrum imaging is chosen. The ADF detectors are retracted and the beam is aligned to centre on the EELS GIF aperture on the screen.
10. The next step is to choose the EELS parameters from the user interface in *Digital Micrograph* shown below.



11. The DUAL EELS is option is chosen and values for parameters such as the dispersion, the exposure time and the energy range are chosen. Once that is done, clicking VIEW under the EELS panel brings up an image of the GIF CCD on the screen.
12. The zero-loss beam is displayed on the CCD and is aligned to zero energy. The aperture is set to optimise the view on the CCD. The counts are maximised by repeated movements of the mouse while watching the spectrum displayed on the user interface in *Digital Micrograph*. The shape of the beam is tuned to allow for uniform spreading of the beam without aberrations.
13. After tuning for aberrations, the beam often shifts and so the PLA knobs are used to re-align the beam. The width of the ZLP is determined by the width of the zero-loss beam and this is checked again, followed by another alignment of the zero-loss beam.
14. The ADF detectors are put in and the beam is 'un-parked' to yield a live image of the nanoparticles.
15. In choosing a particle for spectrum imaging, the particle has to be isolated on the carbon film. In other words, the particle should not be on top of or coalesced into another. This is mainly to avoid channelling and multiple scattering. For best results, a particle 'hanging' over a hole is best because it reduces the contribution of the carbon film to the particle, which can be problematic in EEL spectral background subtraction.
16. Once a particle is chosen, a ROI box is drawn around the image and SI recorded. This is repeated for all particles studied. The settings remain fairly constant, however, depending on the size of the particle and sample drift, the exposure times and pixel array can be changed before the SI is recorded on the particle.

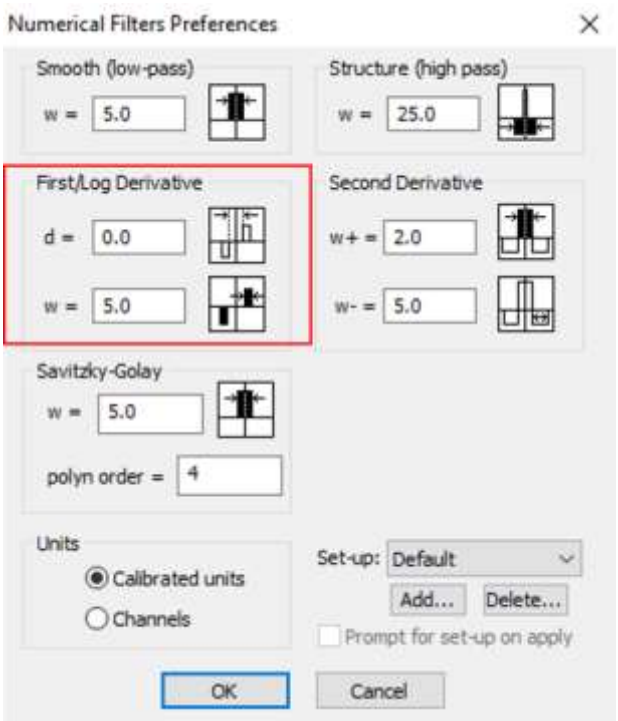
12.1.2 Derivative parameters for obtaining spectrum energies

First derivative

In *Digital Micrograph*, the data is smoothed over an interval *w* (width between peaks) eV wide, then it calculates the difference between values d*E* (width within peak) eV apart and places the result in the channel midway between two. The parameters *w* and d*E* are set under 'Preferences' in the 'Numerical Filters' tab. Finally, the spectrum is divided by *w* + d*E* to yield an approximation of the first derivative with respect to energy.

Second derivative

This averages over an interval *w*+ eV wide and subtracts half the averages in two adjacent "wings" of width *w*-, as illustrated in the GUI in the previous slide. Finally, the spectrum is divided by the squared sum of *w*+ and *w*- to yield an approximation of the second derivative with respect to energy. This is a different method to the just taking the first derivative and this is why the second derivative is not equivalent to the first derivative of the first derivative in *Digital Micrograph*. Note that the latter is used to compute the second derivative in the methodology.



12.2 Appendix B: Python PCA and Core-shell Code

12.2.1 PCA denoising script

```
import hyperspy.api as hs
%matplotlib qt
import os
import math
import logging
import numpy as np
import scipy as sp
import gc
gc.collect()
EELSSI1 = hs.load("EELS Spectrum Image (high-loss) (aligned)_XRYRMVD.dm4")
gc.collect()
EELSSI1.plot()
gc.collect()
EELSSI1 = EELSSI1.rebin((74,39,2041))
gc.collect()
EELSSI1
EELSSI1.change_dtype(float)
import numpy as np
EELSSI1.data = EELSSI1.data.clip(min = 0)
EELSSI1.decomposition()
scree_plot = EELSSI1.get_explained_variance_ratio()
EELSSI1.change_dtype(float)
import numpy as np
EELSSI1.data = EELSSI1.data.clip(min = 0)
EELSSI1.decomposition(True)
gc.collect()
ax = hs.plot.plot_spectra([scree_plot.isig[0:20],
                           EELSSI1.get_explained_variance_ratio().isig[0:20]],
```

```
                legend=("Std", "Normalized"))
ax.set_yscale('log')
ax.lines[0].set_marker("o")
ax.lines[1].set_marker("o")
ax.figure
gc.collect()
EELSSI1.plot_decomposition_loadings(20)
EELSSI1_PCA = EELSSI1.get_decomposition_model(7)
gc.collect()
hs.plot.plot_spectra([EELSSI1.inav[25,22],
EELSSI1_PCA.inav[25,22]],legend=(["Original", "PCA"]), color=("red", "black"))
EELSSI1_PCA.save("EELSSI1_PCA.rpl")
```

12.2.2 Core-shell creation script

```
import hyperspy.api as hs
import scipy.io as sio
import os
import gc
from skimage.io import imshow
import numpy as np
from tqdm import *
from matplotlib import pyplot as plt
from skimage.filters import threshold_otsu
import scipy.misc
import skimage.morphology as morph
import glob
sample_name = 'G_Pt3Co_unleached\\'
current_working_directory =
'C:\\Users\\James\\Documents\\randomz\\CoStds_and_Matrix4_Exp_050918_TT\\'
file_list = glob.glob(current_working_directory+sample_name+"SI-*")
gc.collect()
file_name_ADF = '\\HAADF Image.dm4'
```

```
def plot_image(data):
    plt.figure()
    imshow(data)
    plt.axis('off')
    plt.show()

def threshold(image):
    #------------------------------global thresholding-------------------------
    thresh = threshold_otsu(image)
    binary_image = image > thresh
    binary_image = morph.binary_dilation(binary_image)
    #binary_image = morph.binary_erosion(binary_image)
    return binary_image

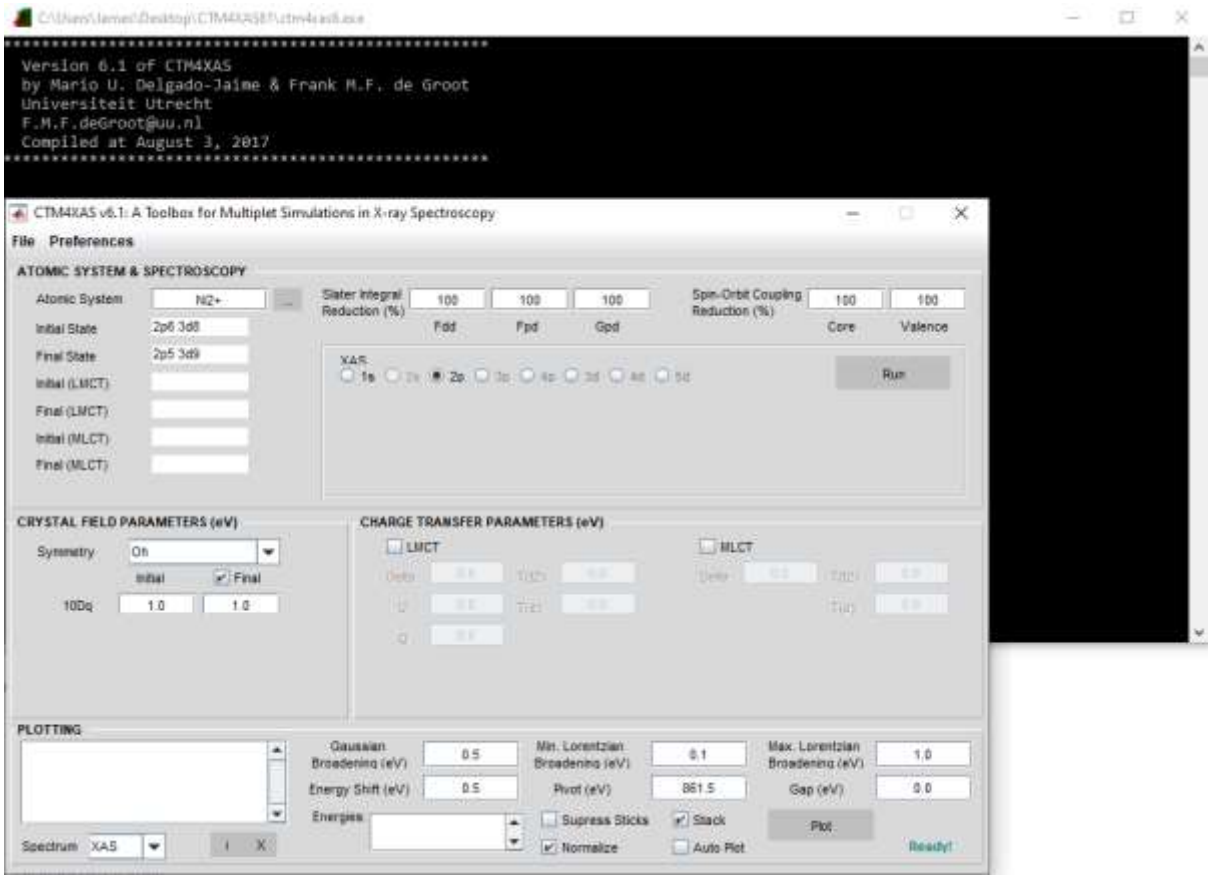
def threshold_shell(binary_image):
    mask_core = binary_image
    mask_core_1 = morph.binary_erosion(mask_core)#1
    mask_core_2 = morph.binary_erosion(mask_core_1)#2



    mask_shell_2 = mask_core_1 - mask_core_2
    return mask_core_2, mask_shell_2
gc.collect()
ADF = hs.load(file_list[0]+file_name_ADF)
        file_name_EELS = '\\EELSSI'+'1'+'_PCA.dm4'
        EELS = hs.load(file_list[0]+file_name_EELS)
        X = ADF.axes_manager[0].size * 0.5
        Y = ADF.axes_manager[1].size * 0.5
        ADF = ADF.rebin((X,Y))
        FADF = ADF.data
        binary_ADF_image = threshold(FADF)
```

```
    mask_core_2, mask_shell_2 = threshold_shell(binary_ADF_image)
    EELS_core = EELS.deepcopy()
    EELS_shell = EELS.deepcopy()
    for j in range(0,EELS_core.axes_manager[2].size):
        EELS_core.data[:,:,j] = EELS_core.data[:,:,j] * mask_core_2
        EELS_shell.data[:,:,j] = EELS_shell.data[:,:,j] * mask_shell_2
    EELS_core.save(filename =
file_list[0]+"\\individual_core_3rdshell"+"\\EELS_core.rpl",overwrite=True)
    EELS_shell.save(filename =
file_list[0]+"\\individual_core_3rdshell"+"\\EELS_shell.rpl",overwrite=True)
    scipy.misc.imsave(file_list[0]+"\\individual_core_3rdshell"+"\\EELS_shell.jpg",
mask_shell_2)
    gc.collect()
    print ("done")
ADF = hs.load(file_list[0]+file_name_ADF)
file_name_EELS = '\\EELSSI'+'1'+'_PCA.dm4'
EELS = hs.load(file_list[0]+file_name_EELS)
ADF.plot()
EELS.plot()
X = ADF.axes_manager[0].size * 0.5
Y = ADF.axes_manager[1].size * 0.5
ADF = ADF.rebin((X,Y))
FADF = ADF.data
binary_ADF_image = threshold(FADF)
plot_image(binary_ADF_image)
mask_core_2, mask_shell_2 = threshold_shell(binary_ADF_image)
plot_image(mask_shell_2)
plot_image(mask_core_2)
```

12.3 Appendix C: Multiplet Software and Atomic Inputs



The atomic parameters firstly require an input for the element to be calculated, Co in this case, and its formal charge – this defines the ground state *d* electron configuration. Several interactions are represented by two-electron Slater integrals and these are split into three parts: the F_{dd}, F_{pd} and G_{pd} integrals. The F_{dd} (F^2 and F^4) terms are the two-electron integrals coupling the 3*d* electrons and core [146], where F^2 and F^4 are the *B* and *C* Racah parameters, respectively. Racah paramters are parameters conceived to account for the effects of electron-electron repulsion which occur in metal complexes. The F_{pd} integral is responsible for the core-valence state electron coupling, while G_{pd} (G^1 and G^3) controls the 2*p*-3*d* core-valence electron coupling; G^1 being the spin-spin part and G^3 the core-valence exchange interaction [146,147,157].

There are a few approximations that make the code semi-empirical and a large part is due to the use of 80% of the Hartree-Fock integrals in the model [146,147,157]. This percentage has been determined to give the best estimation of the values in the free atom [146,147,157]. The Hartree-Fock values are two-electron Slater determinant matrices of electron spin orbitals, which attempts to solve the Schrodinger equation using the mean-field approximation. However, the result gives a weak approximation of electron-electron repulsion and omits electron correlation and exchange interaction. The Slater determinants can also combine and interact, giving configuration interactions [146,147,157]. This 20% atomic reduction of the Hartee-Fock values was used mainly to account for configuration interactions not included in the atomic result; these interactions are generally not included due to the high computational demand.

The values inputted into the software for the Slater integrals are 1.0 for each parameter and represent 80% of the Hartree-Fock. These can be changed between 0 and 1.5 to simulate various multiplets effects, however after various calculations, the values of 1.0 Slater integrals have been found to sufficiently describe the experimental spectra and so have not been changed. There is a separate spin-orbit coupling parameter, which is also related to the Slater integrals and takes the same values. This parameter is mainly to mimic the core spin-orbit coupling in experiment and so its value is never really changed. Rather than just using these parameters blindly, calculations were also carried out for congruence with experimental spectra. While Gaussian and Lorentzian broadening were also included to simulate experimental spectra, separate broadening of each of the cobalt white lines to account for the large uncertainty on the L_2 peak was not done. This was mainly for simplicity, but also, nuance differences between the L_2 peak in experiment spectra and calculated spectra were more conspicuous than any effect of separate broadening of the white lines.

12.4 Appendix D: DFT Input Files and Executables

12.4.1 CASTEP input – example cell file

%block LATTICE_ABC

ang

11.2277770920 11.2277770920 30.0000000000

90.0000000000 90.0000000000 120.0000000000

%endblock LATTICE_ABC

%block POSITIONS_FRAC

O	0.000000000000000	0.000000000000000	0.368539652177522
Pt	0.166666666666667	0.333333333333333	0.000233926085711
Pt	0.000000000000000	0.000000000000000	0.077250485492032
Pt	0.330925681233189	0.165462840616595	0.152744352490356
Pt	0.166662827001265	0.333325654002530	0.228250282859717
Pt	0.000000000000000	0.000000000000000	0.307588017311225
Pt	0.166666666666667	0.083333333333333	0.000233926085711
Pt	-0.000000000000000	0.250000000000000	0.077250485492032
Pt	0.333128168709065	0.416595633425389	0.152658291252685
Pt	0.165032538238068	0.082516269119033	0.230157447356451
Pt	-0.000045154939214	0.255270513591095	0.304880104836127
Pt	0.416666666666667	0.083333333333333	0.000233926085711
Pt	0.250000000000000	0.250000000000000	0.077250485492032
Pt	0.083467464716323	0.416595633425389	0.152658291252685
Pt	0.416960090002534	0.083761847094306	0.227838430902288
Pt	0.255315668530309	0.255270513591095	0.304880104836127
Pt	0.416666666666667	0.333333333333333	0.000233926085711
Pt	0.250000000000000	0.000000000000000	0.077250485492032
Pt	0.082930400276612	0.165860800553225	0.153298931813866
Pt	0.416960090002534	0.333198242908226	0.227838430902288
Pt	0.255315668530309	0.000045154939214	0.304880104836127

Pt	0.666666666666667	0.333333333333333	0.000233926085711
Pt	0.500000000000000	-0.000000000000000	0.077250485492032
Pt	0.834537159383405	0.165462840616595	0.152744352490356
Pt	0.666666666666667	0.333333333333333	0.228249381998243
Pt	0.499888948861152	-0.000222102277697	0.305519762462341
Pt	0.666666666666667	0.083333333333333	0.000233926085711
Pt	0.500000000000000	0.250000000000000	0.077250485492032
Pt	0.833247512023717	0.416623756011859	0.152736948598253
Pt	0.666801757091774	0.083761847094306	0.227838430902288
Pt	0.501275895106350	0.250637947553175	0.305426582937247
Pt	0.916666666666667	0.083333333333333	0.000233926085711
Pt	0.750000000000000	0.250000000000000	0.077250485492032
Pt	0.583376243988141	0.416623756011859	0.152736948598253
Pt	0.917483730880967	0.082516269119033	0.230157447356451
Pt	0.749362052446825	0.250637947553175	0.305426582937247
Pt	0.916666666666667	0.333333333333333	0.000233926085711
Pt	0.750000000000000	0.000000000000000	0.077250485492032
Pt	0.583376243988141	0.166752487976283	0.152736948598253
Pt	0.916238152905694	0.333198242908226	0.227838430902288
Pt	0.744729486408905	0.000045154939214	0.304880104836127
Pt	0.166666666666667	0.833333333333333	0.000233926085711
Pt	0.000000000000000	0.500000000000000	0.077250485492032
Pt	0.333333333333333	0.666666666666667	0.152776528843577
Pt	0.166662827001265	0.833337172998735	0.228250282859717
Pt	0.000222102277697	0.500111051138849	0.305519762462341
Pt	0.166666666666667	0.583333333333333	0.000233926085711
Pt	-0.000000000000000	0.750000000000000	0.077250485492032
Pt	0.333128168709065	0.916532535283677	0.152658291252685
Pt	0.166390731496838	0.583195365748419	0.228263828665127
Pt	-0.000045154939214	0.744684331469691	0.304880104836127
Pt	0.416666666666667	0.583333333333333	0.000233926085711

Pt	0.250000000000000	0.750000000000000	0.077250485492032
Pt	0.082930400276612	0.917069599723388	0.153298931813866
Pt	0.416804634251582	0.583195365748419	0.228263828665127
Pt	0.250572291063811	0.749427708936189	0.305599126196666
Pt	0.416666666666667	0.833333333333333	0.000233926085711
Pt	0.250000000000000	0.500000000000000	0.077250485492032
Pt	0.083467464716323	0.666871831290935	0.152658291252685
Pt	0.416804634251582	0.833609268503162	0.228263828665127
Pt	0.250572291063811	0.501144582127622	0.305599126196666
Pt	0.666666666666667	0.833333333333333	0.000233926085711
Pt	0.500000000000000	0.500000000000000	0.077250485492032
Pt	0.834537159383405	0.669074318766811	0.152744352490356
Pt	0.666674345997470	0.833337172998735	0.228250282859717
Pt	0.499888948861152	0.500111051138849	0.305519762462341
Pt	0.666666666666667	0.583333333333333	0.000233926085711
Pt	0.500000000000000	0.750000000000000	0.077250485492032
Pt	0.834139199446775	0.917069599723388	0.153298931813866
Pt	0.666801757091774	0.583039909997466	0.227838430902288
Pt	0.498855417872378	0.749427708936189	0.305599126196666
Pt	0.916666666666667	0.583333333333333	0.000233926085711
Pt	0.750000000000000	0.750000000000000	0.077250485492032
Pt	0.583404366574611	0.916532535283677	0.152658291252685
Pt	0.916238152905694	0.583039909997466	0.227838430902288
Pt	0.744729486408905	0.744684331469691	0.304880104836127
Pt	0.916666666666667	0.833333333333333	0.000233926085711
Pt	0.750000000000000	0.500000000000000	0.077250485492032
Pt	0.583404366574611	0.666871831290935	0.152658291252685
Pt	0.917483730880967	0.834967461761932	0.230157447356451
Pt	0.749362052446825	0.498724104893651	0.305426582937247

%endblock POSITIONS_FRAC

%block CELL_CONSTRAINTS

0 0 0

0 0 0

%endblock CELL_CONSTRAINTS

!FIX_COM : true

%block IONIC_CONSTRAINTS

1	Pt	1	1.0000000000000000	0.0000000000000000	0.0000000000000000
2	Pt	1	0.0000000000000000	1.0000000000000000	0.0000000000000000
3	Pt	1	0.0000000000000000	0.0000000000000000	1.0000000000000000
4	Pt	2	1.0000000000000000	0.0000000000000000	0.0000000000000000
5	Pt	2	0.0000000000000000	1.0000000000000000	0.0000000000000000
6	Pt	2	0.0000000000000000	0.0000000000000000	1.0000000000000000
7	Pt	6	1.0000000000000000	0.0000000000000000	0.0000000000000000
8	Pt	6	0.0000000000000000	1.0000000000000000	0.0000000000000000
9	Pt	6	0.0000000000000000	0.0000000000000000	1.0000000000000000
10	Pt	7	1.0000000000000000	0.0000000000000000	0.0000000000000000
11	Pt	7	0.0000000000000000	1.0000000000000000	0.0000000000000000
12	Pt	7	0.0000000000000000	0.0000000000000000	1.0000000000000000
13	Pt	11	1.0000000000000000	0.0000000000000000	0.0000000000000000
14	Pt	11	0.0000000000000000	1.0000000000000000	0.0000000000000000
15	Pt	11	0.0000000000000000	0.0000000000000000	1.0000000000000000
16	Pt	12	1.0000000000000000	0.0000000000000000	0.0000000000000000
17	Pt	12	0.0000000000000000	1.0000000000000000	0.0000000000000000
18	Pt	12	0.0000000000000000	0.0000000000000000	1.0000000000000000
19	Pt	16	1.0000000000000000	0.0000000000000000	0.0000000000000000
20	Pt	16	0.0000000000000000	1.0000000000000000	0.0000000000000000
21	Pt	16	0.0000000000000000	0.0000000000000000	1.0000000000000000
22	Pt	17	1.0000000000000000	0.0000000000000000	0.0000000000000000
23	Pt	17	0.0000000000000000	1.0000000000000000	0.0000000000000000

24	Pt	17	0.0000000000000000	0.0000000000000000	1.0000000000000000
25	Pt	21	1.0000000000000000	0.0000000000000000	0.0000000000000000
26	Pt	21	0.0000000000000000	1.0000000000000000	0.0000000000000000
27	Pt	21	0.0000000000000000	0.0000000000000000	1.0000000000000000
28	Pt	22	1.0000000000000000	0.0000000000000000	0.0000000000000000
29	Pt	22	0.0000000000000000	1.0000000000000000	0.0000000000000000
30	Pt	22	0.0000000000000000	0.0000000000000000	1.0000000000000000
31	Pt	26	1.0000000000000000	0.0000000000000000	0.0000000000000000
32	Pt	26	0.0000000000000000	1.0000000000000000	0.0000000000000000
33	Pt	26	0.0000000000000000	0.0000000000000000	1.0000000000000000
34	Pt	27	1.0000000000000000	0.0000000000000000	0.0000000000000000
35	Pt	27	0.0000000000000000	1.0000000000000000	0.0000000000000000
36	Pt	27	0.0000000000000000	0.0000000000000000	1.0000000000000000
37	Pt	31	1.0000000000000000	0.0000000000000000	0.0000000000000000
38	Pt	31	0.0000000000000000	1.0000000000000000	0.0000000000000000
39	Pt	31	0.0000000000000000	0.0000000000000000	1.0000000000000000
40	Pt	32	1.0000000000000000	0.0000000000000000	0.0000000000000000
41	Pt	32	0.0000000000000000	1.0000000000000000	0.0000000000000000
42	Pt	32	0.0000000000000000	0.0000000000000000	1.0000000000000000
43	Pt	36	1.0000000000000000	0.0000000000000000	0.0000000000000000
44	Pt	36	0.0000000000000000	1.0000000000000000	0.0000000000000000
45	Pt	36	0.0000000000000000	0.0000000000000000	1.0000000000000000
46	Pt	37	1.0000000000000000	0.0000000000000000	0.0000000000000000
47	Pt	37	0.0000000000000000	1.0000000000000000	0.0000000000000000
48	Pt	37	0.0000000000000000	0.0000000000000000	1.0000000000000000
49	Pt	41	1.0000000000000000	0.0000000000000000	0.0000000000000000
50	Pt	41	0.0000000000000000	1.0000000000000000	0.0000000000000000
51	Pt	41	0.0000000000000000	0.0000000000000000	1.0000000000000000
52	Pt	42	1.0000000000000000	0.0000000000000000	0.0000000000000000
53	Pt	42	0.0000000000000000	1.0000000000000000	0.0000000000000000
54	Pt	42	0.0000000000000000	0.0000000000000000	1.0000000000000000

55	Pt	46	1.0000000000000000	0.0000000000000000	0.0000000000000000
56	Pt	46	0.0000000000000000	1.0000000000000000	0.0000000000000000
57	Pt	46	0.0000000000000000	0.0000000000000000	1.0000000000000000
58	Pt	47	1.0000000000000000	0.0000000000000000	0.0000000000000000
59	Pt	47	0.0000000000000000	1.0000000000000000	0.0000000000000000
60	Pt	47	0.0000000000000000	0.0000000000000000	1.0000000000000000
61	Pt	51	1.0000000000000000	0.0000000000000000	0.0000000000000000
62	Pt	51	0.0000000000000000	1.0000000000000000	0.0000000000000000
63	Pt	51	0.0000000000000000	0.0000000000000000	1.0000000000000000
64	Pt	52	1.0000000000000000	0.0000000000000000	0.0000000000000000
65	Pt	52	0.0000000000000000	1.0000000000000000	0.0000000000000000
66	Pt	52	0.0000000000000000	0.0000000000000000	1.0000000000000000
67	Pt	56	1.0000000000000000	0.0000000000000000	0.0000000000000000
68	Pt	56	0.0000000000000000	1.0000000000000000	0.0000000000000000
69	Pt	56	0.0000000000000000	0.0000000000000000	1.0000000000000000
70	Pt	57	1.0000000000000000	0.0000000000000000	0.0000000000000000
71	Pt	57	0.0000000000000000	1.0000000000000000	0.0000000000000000
72	Pt	57	0.0000000000000000	0.0000000000000000	1.0000000000000000
73	Pt	61	1.0000000000000000	0.0000000000000000	0.0000000000000000
74	Pt	61	0.0000000000000000	1.0000000000000000	0.0000000000000000
75	Pt	61	0.0000000000000000	0.0000000000000000	1.0000000000000000
76	Pt	62	1.0000000000000000	0.0000000000000000	0.0000000000000000
77	Pt	62	0.0000000000000000	1.0000000000000000	0.0000000000000000
78	Pt	62	0.0000000000000000	0.0000000000000000	1.0000000000000000
79	Pt	66	1.0000000000000000	0.0000000000000000	0.0000000000000000
80	Pt	66	0.0000000000000000	1.0000000000000000	0.0000000000000000
81	Pt	66	0.0000000000000000	0.0000000000000000	1.0000000000000000
82	Pt	67	1.0000000000000000	0.0000000000000000	0.0000000000000000
83	Pt	67	0.0000000000000000	1.0000000000000000	0.0000000000000000
84	Pt	67	0.0000000000000000	0.0000000000000000	1.0000000000000000
85	Pt	71	1.0000000000000000	0.0000000000000000	0.0000000000000000

86 Pt 71 0.0000000000000000 1.0000000000000000 0.0000000000000000
87 Pt 71 0.0000000000000000 0.0000000000000000 1.0000000000000000
88 Pt 72 1.0000000000000000 0.0000000000000000 0.0000000000000000
89 Pt 72 0.0000000000000000 1.0000000000000000 0.0000000000000000
90 Pt 72 0.0000000000000000 0.0000000000000000 1.0000000000000000
91 Pt 76 1.0000000000000000 0.0000000000000000 0.0000000000000000
92 Pt 76 0.0000000000000000 1.0000000000000000 0.0000000000000000
93 Pt 76 0.0000000000000000 0.0000000000000000 1.0000000000000000
94 Pt 77 1.0000000000000000 0.0000000000000000 0.0000000000000000
95 Pt 77 0.0000000000000000 1.0000000000000000 0.0000000000000000
96 Pt 77 0.0000000000000000 0.0000000000000000 1.0000000000000000
%endblock IONIC_CONSTRAINTS

kpoints_mp_spacing 0.04

symmetry_generate

12.4.2 CASTEP input – example param file

task : GeometryOptimization

GEOM_PRECONDITIONER : ID

xc_functional : PBE

spin_polarized : true

continuation : default

opt_strategy : Default

page_wvfns : 0

cut_off_energy : 800.000000000000000

!grid_scale : 1.750000000000000

!fine_grid_scale : 2.100000000000000

finite_basis_corr : 0

elec_energy_tol : 1.000000000000000e-006

max_scf_cycles : 200

fix_occupancy : false

metals_method : dm

mixing_scheme : Pulay

mix_charge_amp : 0.500000000000000

mix_charge_gmax : 1.500000000000000

mix_history_length : 20

nextra_bands : 41

smearing_width : 0.100000000000000

num_dump_cycles : 0

geom_energy_tol : 1.000000000000000e-005

geom_force_tol : 0.030000000000000

geom_stress_tol : 0.050000000000000

geom_disp_tol : 1.000000000000000e-003

geom_max_iter : 200

geom_method : LBFGS

fixed_npw : false

geom_modulus_est : 500.000000000000000 GPa

calculate_ELF : false

calculate_stress : false

popn_calculate : true

calculate_hirshfeld : true

calculate_densdiff : false

popn_bond_cutoff : 3.000000000000000

pdos_calculate_weights : false

write_cell_structure : true

12.4.3 OptaDOS input – example odi file

task = dos core

legacy_file_format = false

broadening = adaptive

!fixed_smearing = 0.2

efermi = optados

!set_efermi_zero = true

output_format = xmgrace

dos_spacing = 0.01

dos_min_energy = -5.0

dos_max_energy = 30.0

adaptive_smearing = 0.6

compute_band_gap : T

core_lai_broadening : true

lai_gaussian_width : 1.0

lai_lorentzian_scale : 0.1

!core_geom : polarised

!core_qdir : 1 1 0

12.4.4 OptaDOS auxiliary files

1. Pt_111_slab_O_top.bands
2. Pt_111_slab_O_top.dome_bin
3. Pt_111_slab_O_top.elnes_bin
4. Pt_111_slab_O_top-out.cell